CRANFIELD UNIVERSITY

Lampros Papagiannis

Simulations of high speed, low angle, structural impacts with water

School of Engineering
PhD Thesis

PhD
Academic Year: 2010 – 2016

Supervisor: Dr. James Campbell
June 2016

CRANFIELD UNIVERSITY

School of Engineering
PhD Thesis

PhD

Academic Year 2010 - 2016

Lampros Papagiannis

Simulations of high speed, low angle, structural impacts with water

Supervisor: Dr. James Campbell
June 2016

© Cranfield University 2016. All rights reserved. No part of this publication may be reproduced without the written permission of the copyright owner.

ABSTRACT

The improvement of the numerical capabilities of predicting the structural loading of high speed, low angle impacts, such as an aircraft during ditching, is addressed in this thesis. Research into the phenomenon of ditching, has shown that specific flow phenomena occur, which influence the structural loading of the aircraft as well as its general dynamics. These phenomena are cavitation, suction and the presence of air. The simple water model that is used in vertical simulations does not provide accurate enough predictions, when considering impacts characterised by high forward velocities. The meshless Smoothed Particle Hydrodynamics (SPH) method, known for its ability to model large deformations, was enhanced with the addition of cavitation and aeration, in order to improve the fluid model used for fluid-structure interactions with forward velocities, such as ditching. With the use of a homogeneous mixture model, a more realistic transient cavitation model was implemented, considering the presence of vapour nuclei in the fluid. It considered the vapour pressure, the growth and reduction evolution of the phenomenon with the use of the Rayleigh-Plesset equation and the change in the properties of the fluid. Initial 2D investigation captured the phenomenon and compared well with published results. Further investigation of plate impacts showed the sensitivity of the approach on the number of nuclei present in the fluid, as well as the influence of the boundary and the potential wave reflection interference on the free surface. The presence of air in the water model was implemented with a mixture approach, governed by the change of the properties of the air. Investigation of plate impacts and a fuselage section showed that the pressures decrease, according to theory, with increasing levels of aeration. In the case of the fuselage section, the results showed little influence in the overall behaviour and highlighted the importance of the phenomenon of suction. Finally, the numerical investigation of ricochet, a phenomenon also characterised by high forward velocities and with available experimental results, was considered as a means of assessing the overall capabilities of the SPH method. Sphere and cylinder results compared favourably for the lower velocity impacts but proved inaccurate for the higher velocities range. This was attributed to a lower deceleration experienced by the projectiles combined with a frictionless contact. The computational cost of such simulations was also considered prohibitive for further investigation within this project.

Keywords: Ditching, Cavitation, Aeration, Fluid-Structure Interaction, SPH, Ricochet

ACKNOWLEDGEMENTS

To my parents, Maria and Andreas.

I would like to thank my supervisor, Dr. James Campbell, for his continued support and patience during my years as a PhD student.

My gratitude goes to Professor Rade Vignjevic, for the advice and help over the last 4 years.

Finally, all the fellow PhD colleagues that have contributed to my development as a person and as a researcher.

TABLE OF CONTENTS

ABSTRACT i
ACKNOWLEDGEMENTS ii
LIST OF FIGURES v
LIST OF TABLES xvii
1 Introduction 1
1.1 Aims and Objectives 2
1.2 Thesis Structure 3
2 Ditching Theory and Accident Review 5
2.1 Characteristics of Water Impact 5
2.2 Water Impact Theories 6
2.3 Accident Review 8
2.4 Experimental Tests Review 15
2.5 Conclusions 23
3 Numerical Investigations 25
3.1 Vertical Impacts 25
3.2 Horizontal Impacts 32
3.3 Conclusions and Limitations 37
4 Air Cushioning, Suction and Cavitation 39
4.1 Air Cushioning 39
4.2 Suction 43
4.3 Cavitation 48
4.3.1 Types of Cavitation 49
4.3.2 Nucleation 51
4.3.3 Liquid Tensile Strength 53
4.3.4 Cavitation Growth and Collapse 55
4.3.5 Mixture Properties 63
4.3.6 Cavitation Parameter 64
4.3.7 Cavitation Numerical Modelling 65
4.4 Conclusions 69
5 The MCM Code 71
5.1 SPH General Description 71
5.2 MCM Structure 78
5.3 Inclined Plate 81
5.3.1 1 m Depth Tests 83
5.3.2 2 m Depth Tests 86
5.4 Conclusions 89
6 Cavitation Modelling 90
6.1 Methodology Assumptions 90
6.2 Vapour Pressure 91
6.3 Growth Phase 93
6.4 Reduction Phase 96
6.5 Methodology Implementation 96
6.6 Methodology Verification 104
6.6.1 Initial Verification 104

6.6.2 2D Venturi Case 108
6.6.3 2D Step Case 113
6.6.4 2D Tube Case 117
6.7 Inclined Plate Impact 125
6.8 Conclusions 138
7 Aerated Water Modelling 141
7.1 Theory and Methodology 141
7.2 Methodology Implementation 147
7.3 2D Test Case 155
7.4 Drop Test 169
7.4.1 Simulation Model 170
7.4.2 Simulation Results 172
7.5 Inclined Plate 175
7.5.1 4° Inclination 176
7.5.2 10° Inclination 183
7.6 NACA2929 J-Body 192
7.7 Conclusions 205
8 Ricochet Modelling 208
8.1 Ricochet Theory and Experimental Data 208
8.2 Initial 3D Sphere Ricochet 220
8.3 Cylinder Mesh Sensitivity Analysis 227
8.3.1 Water Domain Model 228
8.3.2 2D Cylinder Model 230
8.3.3 2D Cylinder Ricochet Simulations 238
8.4 Final 3D Sphere Ricochet 244
8.5 Conclusions 247
9 Conclusions and Future Work 250
9.1 Conclusions 250
9.2 Future Work 253
REFERENCES 255
Appendix A SPH Derivations 266
Appendix B Rayleigh-Plesset Equation 274
Appendix C Mixture Speed of Sound 276

LIST OF FIGURES

Figure 2-1: Loading of a structure during a hard surface impact (left) and a soft/fluid surface (right). Figure reproduced from Zimmermann et al. [24]. 5

Figure 2-2: Stages of the ditching event of a fixed-wing aircraft. 6

Figure 2-3: Vertical impact of a 2D wedge with semi-cylinder area depicting the added mass. Figure reproduced from Mayo [25]. 6

Figure 2-4: Classification of the water entry accidents taking place between 1959-1979. The majority of the fatalities occurred when there was a break in the fuselage. The survival rate is increased significantly when the fuselage does not rupture. Figure reproduced from Widmayer et al. [35]. 12

Figure 2-5: Comparison of ground and water accidents with respect to fatalities per total passenger loading. Comparison shows that the percentage of fatalities per total passenger load is smaller for water impacts. Figure reproduced from Johnson [31]. 13

Figure 2-6: B-24D Liberator aircraft. Figure reproduced from Steiner [5]. 17

Figure 2-7: Sequence of ditching event of a 1/16-scale model DC-6 aircraft with a 12° pitch angle. Initial tail strike followed by a nose dive and potential severe damage. Figure based on Fisher et al. [11]. 18

Figure 2-8: Comparison of the damage on the underside of the fuselage of a 1/16-scale model DC-4 aircraft with a 12° pitch angle: a) calm waters, b) rough waters (6-ft waves). Scale-strength was achieved with balsa wood and aluminium sheets placed in key locations of the underside of the scale model. Figure based on Fisher et al. [11]. 19

Figure 2-9: General behaviour of an upswept rear fuselage during ditching in calm waters. Initial aft body contact followed by nose diving. Figure based on McBride et al. [2]. 20

Figure 2-10: Area of removable sections used to model failure on a 1/30-scale model. Balsa wood, aluminium foil and cardboard were used for the scale-strength of the shaded areas. Figure reproduced from Thompson [6]. 22

Figure 2-11: Damage sustained in calm (left) and rough water impacts (right) for an attitude of 7°, with flaps extended, the main landing gear fully extended and a speed of 71 m/s. Figure based on Thompson [6]. 22

Figure 3-1: Vertical drop of rigid wedge in a water domain consisting of SPH particles with variable smoothing length. Figure reproduced from Oger et al. [19]. 25

Figure 3-2: Evolution of the horizontal velocity for a wedge of 20° dead-rise angle during water impact using the SPH method. Figure based on Pentecote et al. [43]. 26

Figure 3-3: Coupled FE-SPH simulation for helicopter subfloor impact. Water defined by finite elements further away from the structure and with SPH particles in the immediate vicinity of the subfloor. Figure based on Pentecote et al. [43]. 27

Figure 3-4: ALE (left) and SPH (right) simulation of a panel with a cut impacting water. Figure based on Francesconi et al. [18]. 28

Figure 3-5: Vertical drop test simulations for an aluminium box with L-stiffeners. SPH (left) and EFG model (right). Velocities ranging from 3.1 to 7.7 m/s. Figure based on Anghileri et al. [15]. 28

Figure 3-6: SPH (left) and EFG (right) simulation of aluminium box with L-stiffeners impacting water. Reduced splash is evident for the SPH simulations due to the coarse particle distribution. Figure based on Anghileri et al. [15]. 29

Figure 3-7: Initial set-up of the triangular and semi-circular sections. Rigid structures were considered with impact velocities ranging between 4 m/s and 9 m/s. Figure based on Anghileri et al. [14]. 30

Figure 3-8: General impact of the triangular and semi-circular sections [14]. For both cases the accelerations matched the experimental results. Figure based on Anghileri et al. [14]. 30

Figure 3-9: Vertical impact of space capsule at 9 m/s with no inclination included. Figure reproduced from Candy et al. [16]. 31

Figure 3-10: Subfloor overview with 18 points that constrained the global motion in lateral and horizontal translation. Figure reproduced from Hughes et al. [44]. 31

Figure 3-11: Impact evolution of subfloor showing the extreme distortion of the Lagrangian water elements in the vicinity of the structure 35 ms after impact. Figure reproduced from Hughes et al. [44]. 32

Figure 3-12: Evolution of the ditching of the generic aircraft. SPH and finite elements used for the water domain. Figure based on Pentecote et al. [43]. 33

Figure 3-13: Ditching of A321 at 60 m/s forward velocity and 8° inclination. Highest pressures and deformations observed at the rear of the aircraft. Structural deformation visible on the lower section of the aft section. Figure based on Ortiz et al. [46]. 34

Figure 3-14: Evolution of rotorcraft water impact computed using the generic FE code MSC/DYTRAN. Figure reproduced from Wittlin et al. [47]. 35

Figure 3-15: EADS-CASA CN-235-300M aircraft. Figure reproduced by Climent et al. [42]. 35

Figure 3-16: Impact of CN-235-300M scale model with the use of finite elements and SPH particles for water modelling. Figure reproduced by Climent et al. [42]..... 36

Figure 3-17: The three models used for the simulation in the hybrid and RANS solvers. All models are based on the experimental investigation by Mc Bride et al. [2]. Figure based on Streckwall et al. [26]..... 36

Figure 3-18: Simulations for general body of revolution A, D and J respectively. Initial horizontal velocities were set at 9.14 m/s. Figure based on Streckwall et al. [26].37

Figure 4-1: Pressure distribution (in MPa) upon impact of an Airbus A321 model. Top figure water model with two-phase ALE method and bottom figure water model with SPH method. Figure based on Ortiz et al. [45]. 41

Figure 4-2: Ventilation at the trailing edge of a wedge upon impact with an impact angle of 0°. Impact direction from left to right. Figure reproduced from Judge et al. [22]. 42

Figure 4-3: Areas where ventilation can take place. Top figure shows the bottom view of the scale model. Red area (forward section of the fuselage) shows the air being transported towards the low-pressure areas that the aircraft experienced towards the aft section. The blue and yellow section in the top figure also indicate areas of low pressure that the air can be sucked in. Figure based on Busch et al. [10]..... 43

Figure 4-4: Water flow phenomena including cavitation, ventilation and suction during the impact phase of a ditching event. Figure reproduced from Siemann et al. [21]. 44

Figure 4-5: Moment caused by suction forces (purple pressure distribution) leading to the pitching up motion of the fuselage. Figure reproduced from Siemann et al. [21]..... 44

Figure 4-6: Ditching sequence of generic aircraft with upswept aft fuselage and corresponding pressure distribution along the fuselage. Pressure distribution graphs (LHS of the figure) are taken with respect to the water surface. Figure based on Allen [23]. 45

Figure 4-7: Numerical results for an Airbus A321 with (top) and without (bottom) suction modelling using the commercial software PAM-CRASH. With suction modelling active, the fuselage of both models pitches up as expected. Figure reproduced from Siemann et al. [21]. 47

Figure 4-8: Numerical results for an Airbus Military CN235 with (left) and without (right) suction modelling using the commercial software PAM-CRASH. With suction modelling active, the fuselage of both models pitches up as expected. Figure reproduced from Siemann et al. [21]. 48

Figure 4-9: Pressure vs temperature for onset of cavitation. Figure reproduced from Franc [59]..... 49

Figure 4-10: Travelling, attached and vortex cavitation (left to right). Figure based on Franc [59]..... 50

Figure 4-11: Nuclei radius distribution function. Figure reproduced from Brennen [62]. 52

Figure 4-12: Typical distribution of nuclei population for three different measurement methods. Figure reproduced from Franc et al. [64]..... 53

Figure 4-13: Andrew Isotherms. Figure reproduced from Franc et al. [64]..... 54

Figure 4-14: Nucleus in fluid. Figure reproduced from Franc et al. [64]. 56

Figure 4-15: Liquid tension vs radius for nuclei containing both gas and vapour for various gas contents at constant temperatures. Curves are based on bubble equilibrium equation (4-16) [58]. The locus of the peaks, shown by the dashed line, represents the critical radius equation (4-19). Figure reproduced from Brennen [62]. 59

Figure 4-16: Generalised equilibrium curve for nuclei containing both vapour and gas. Curve represents equation (4-19). Liquid pressure vs critical radius. Figure reproduced from Franc [59]. 60

Figure 4-17: Spherical cavitation bubble behaviour (based on the Rayleigh – Plesset method) in the absence of any viscous effects [U is the growth/collapse velocity of the bubble, R and R_0 are the bubble's current and initial size and t is time]. Figure reproduced from Brennen [62]. 62

Figure 4-18: Material erosion on ship propellers caused by vortex cavitation collapse. Figure reproduced from Senocak [73]. 63

Figure 4-19: Variations in liquid and mixture density [77]. 64

Figure 5-1: Support domain of smoothing kernel W. Figure reproduced from Liu et al. [75]. 73

Figure 5-2: Air water mixture with air at the top (left) and pressure distribution of the domain under gravity. Fringe levels show pressure in Pa. 75

Figure 5-3: Density difference between the continuity form of density (left) and the summation form (right). Fringe levels show density in kg/m^3. 76

Figure 5-4: Pressure distribution results for the box under gravity with the use of the summation form of the density. Fringe levels show pressure in Pa. 77

Figure 5-5: Structure of the MCM code. Figure reproduced from De Vuyst et al. [92].. 78

Figure 5-6: Structure of the Solution phase of the MCM code. Figure reproduced from Vuyst et al. [96]. 79

Figure 5-7: Grid representation of the linked list approach. Figure reproduced from Liu et al. [75]. 80

Figure 5-8: Search for neighbouring particles with the linked list approach for 2D cases. Figure reproduced from Liu et al. [75]. 80

Figure 5-9: Symmetry planes concept. Figure reproduced from Liu et al. [75]. 81

Figure 5-10: FE structure under consideration. Left figure shows overall impact test case and right figure shows zoomed in area with structure detail. 82

Figure 5-11: Position of the nodes that time histories were recorded at (bottom view). 83

Figure 5-12: Inclined plate impact with coarser particle density shown on the top figure and finer particle density on the bottom. Results obtained at 0.8 s. Depth of water domain is 1 m. Forward velocity is 30 m/s and vertical velocity is 1.5 m/s. 84

Figure 5-13: Vertical acceleration for the fine and coarse particle distribution for node 265 and 1 m deep water domain. 85

Figure 5-14: Vertical acceleration for the fine and coarse particle distribution for node 342 and 1 m deep water domain. 85

Figure 5-15: Inclined plate impact with coarser particle density shown on the top figure and finer particle density on the bottom. Results obtained at 0.8 s. Depth of water domain is 2 m. Forward velocity is 30 m/s and vertical velocity is 1.5 m/s. 87

Figure 5-16: Vertical acceleration for the fine and coarse SPH distribution for node 265 and 2 m deep water domain. 88

Figure 5-17: Vertical acceleration for the fine and coarse SPH distribution for node 342 and 2 m deep water domain. 89

Figure 6-1: Set of particles for code verification. 104

Figure 6-2: Pressure drop during cavitation and pressure growth after reduction. Initial pressure of 101325 Pa. 106

Figure 6-3: Comparison of critical pressure for varying initial bubble radii and constant nuclei number density. Initial pressure of 101325 Pa. Graph shows the zoomed in area of interest. The smallest the initial bubble radius the stronger the effect of surface tension. This shows that the pressure needs to drop to a lower level in order to reach the cavitation critical pressure. 106

Figure 6-4: Void fraction comparison for varying initial bubble radii and constant nuclei number density. 107

Figure 6-5: Density variation for varying initial bubble radii and constant nuclei number density. Higher void fractions lead to a larger percentage of the particle to the vapour properties and a reduced mixture density. 108

Figure 6-6: 2D venturi model with SPH particles. Green particles indicate the fluid and the red particles indicate the venturi shape. The venturi particles are constrained in translations. The black line indicates the presence of symmetry plane to avoid particles moving upwards. 110

Figure 6-7: Void fraction results in the venturi region at 0.255 s. Fringe levels show void fraction. High concentration of cavitation is indicated at the throat of the venturi. 111

Figure 6-8: Fluid density results in the venturi region at 0.255 s. Fringe levels show density in kg/m^3. Drop in density is located at the throat of the venturi as a result of cavitation. 111

Figure 6-9: Density reduction downstream of the venturi by Coutier-Delgosha et al. [100]. Results show the variation of density as a fraction of the reference water density (1000 kg/m^3). 112

Figure 6-10: Cavitation evolution by Zhang et al. [76]. Attached cavitation shown in white. 114

Figure 6-11: Water (red) and step (blue) composed of SPH particles. Step particles are fixed in translations and rotations. The black lines indicate the presence of symmetry planes. 115

Figure 6-12: Pressure distribution at 0.042 s for the liquid domain. Fringe levels show pressure in Pa. 116

Figure 6-13: Void fraction behind the pressure wave at 0.042 s. Fringe levels show void fraction. 117

Figure 6-14: Zoomed in area of the void fraction at the flow step interface at 0.04 s. Fringe levels show void fraction. 117

Figure 6-15: SPH particles for 2D tube experiment showing initial velocity applied in opposite directions. Fringe levels show velocity in the x direction in m/s. 119

Figure 6-16: Symmetry planes shown in black indicate the restriction in the y-direction. The symmetry planes are applied at half the inter-particle distance (0.0125 m) on top and at the bottom of the water domain. 120

Figure 6-17: Pressure and density results at 0.2 ms at the centre of the 2D tube as obtained by Liu et al. [86]. Cut-off model considers only the presence of water with a cut-off pressure of 0 Pa and it does not take into account the effect of vapour in the water. The present model is the barotropic model used by Liu et al. in their implementation of cavitation. 121

Figure 6-18: Pressure distribution for 2D tube at 0.2 ms. Fringe levels show pressure in Pa. The pressure drops in the middle of the 2D tube as the particles move apart (going into tension), leading to the occurrence of cavitation. 122

Figure 6-19: Pressure comparison between cut-off and new model at 0.2 ms. Pressure taken at the centre of the 2D tube. The cut-off model simply caps the pressure at 0 Pa, whereas the new model takes into account the effect of the “tensile strength” of the liquid, radius of initial nuclei and the vapour pressure. 122

Figure 6-20: Density variations in the 2D tube at 0.2 ms. Fringe levels show density in kg/m^3. The pressure drops in the centre of the 2D tube as the particles move apart (going into tension), leading to a reduction in pressure. 123

Figure 6-21: Density comparison at the centre of the 2D tube between cut-off and the new model at 0.2 ms. The new model considers the effect of vapour leading to a reduced density at the centre of the 2D tube when compared to the simpler cut-off model. The cut-off considers the fluid to be pure water. 124

Figure 6-22: Density variation at the centre of the 2D tube for an arbitrary set of initial radii and nuclei number densities (given per m^3). 125

Figure 6-23: Void fraction evolution for a) $n=6x10^8/m^3$ and b) $n=7x10^8/m^3$ for 1 m deep water domain. Fringe levels show void fraction. Side plane cut view of 3D impact evolution. Direction of travel from left to right. 126

Figure 6-24: Void fraction evolution for a) $n=8x10^8/m^3$ and b) $n=9x10^8/m^3$ for 1 m deep water domain. Fringe levels show void fraction. Side plane cut view of 3D impact evolution. Direction of travel from left to right. 127

Figure 6-25: Void fraction evolution for $n=8x10^8/m^3$ for 2 m deep water domain. Fringe levels show void fraction. Side plane cut view of 3D impact evolution. Direction of travel from left to right. Results shown at 0.04 s, 0.058 s and 0.074 s. 129

Figure 6-26: Void fraction evolution for $n=8x10^8/m^3$ for 2 m deep water domain with symmetry planes applied. Side plane cut view of 3D impact evolution. Direction of travel from left to right. Results shown at 0.04 s, 0.058 s and 0.074 s. The black line indicates the boundary symmetry plane. 130

Figure 6-27: Void fraction evolution for $n=8x10^8/m^3$ for 1 m deep water domain with symmetry planes. Side plane cut view of 3D impact evolution. Direction of travel from left to right. Results shown at 0.04 s, 0.058 s and 0.074 s. The black line indicates the boundary symmetry plane. 131

Figure 6-28: SMAES plate and trolley components. Figure based on Aparici [101]... 132

Figure 6-29: Overall description of the model. On the left is the water domain and the structure and on the right is a view through the vertical symmetry of the structure. 135

Figure 6-30: Void fraction evolution for n=2.5x10^8 /m^3 for 0.4 m water depth. Fringe levels show void fraction. Side plane cut view of 3D impact evolution. Direction of travel from left to right. Results shown at 0.04 s and 0.08 s..... 136

Figure 6-31: Void fraction evolution for n=2.5x10^8 /m^3 for 1.6 m water depth. Fringe levels show void fraction. Side plane cut view of 3D impact evolution. Direction of travel from left to right. Results shown at 0.04 s and 0.08 s..... 137

Figure 6-32: Void fraction evolution for n=1x10^8 /m^3 for 1.6 m water depth. Fringe levels show void fraction. Side plane cut view of 3D impact evolution. Direction of travel from left to right. Results shown at 0.04 s and 0.08 s. 138

Figure 7-1: Variation in the pressure with and without consideration of the liquid's (water) compressibility. 144

Figure 7-2: Speed of sound of a mixture of water and gas for a volume fraction of 10% up to 70%..... 146

Figure 7-3: Pure water pressure results at t=0.0012 s. Maximum pressure corresponds to the theoretical value for a quasi-compressible fluid like water. Fringe levels show pressure in Pa..... 156

Figure 7-4: Change in pressure distribution along the length of the column for pure water. Theoretical wave propagation pressure of 1483 Pa for particle 18526 shows that the simulation follows the theoretical estimate..... 157

Figure 7-5: Pressure distribution for aerated water model in 2D column with ideal gas equation of state. Fringe levels show pressure in Pa. initial velocity of 0.001 m/s. Initial gas volume fraction of 10%..... 159

Figure 7-6: Change in pressure distribution along the length of the column for aerated water model with the ideal equation of state (7-11). Theoretical wave propagation pressure of 36 Pa for particle 18526 shows that the simulation follows the theoretical estimate. Initial velocity of 0.001 m/s and initial gas volume fraction of 10%. 159

Figure 7-7: Gas volume fraction evolution in 2D column with ideal gas equation of state for the pressure evaluation. Fringe levels show gas volume fraction values. Initial gas volume fraction of 10% 160

Figure 7-8: Gas fraction at various points along the length of the 2D column with the ideal gas equation of state. 160

Figure 7-9: Pressure distribution for initial pressure of zero with offset in the adiabatic formula. The results show the correct behaviour and no particles are detached at the top from the main fluid column. Fringe levels show pressure in Pa. Note: the pressure levels are in gauge terms as opposed to the pressure results of Figure 7-5. Initial velocity of 0.001 m/s. 162

Figure 7-10: Change in pressure distribution along the length of the column for aerated water model with the adiabatic equation of state (7-2). Theoretical wave

propagation pressure of 36 Pa for particle 18526 shows that the simulation follows the theoretical estimate. Initial velocity of 0.001 m/s and initial gas volume fraction of 10%..... 163

Figure 7-11: Pressure evolution (left) and gas fraction evolution (right) for 2D column at 1 m/s with adiabatic equation of state and initial gas volume fraction of 10% (plot taken at t=0.028 s). Fringe levels on the left show pressure in Pa and on the right the gas volume fraction. 164

Figure 7-12: Pressure (left figure) and gas volume fraction (right figure) along various points for 2D column at 1 m/s and initial gas volume fraction of 10% with adiabatic equation of state. Gas fraction reduction is more severe than in the previous case, as expected for more severe impacts. 164

Figure 7-13: Pressure evolution (left) and gas evolution (right) for 2D column at 1 m/s with ideal equation of state (plot taken at t=0.028 s). Fringe levels on the left show pressure in Pa and on the right the gas volume fraction. Initial gas volume fraction of 10%..... 166

Figure 7-14: Pressure points for 2D column at 1 m/s with adiabatic equation of state and initial gas fraction of 20%. The pressure peaks are lower when compared to the peak values for an initial gas content of 10%. Initial velocity of 1 m/s. 167

Figure 7-15: Gas fraction points for 2D column at 1 m/s with adiabatic equation of state and initial gas fraction of 20%. 168

Figure 7-16: Gas fraction reduction for velocities of 5 m/s (left) and 10 m/s (right) for the 2D column test with the adiabatic equation of state and an initial gas content of 20%. The particles compress more with the 10 m/s impact case leading to a reduction in the gas content. 169

Figure 7-17: Overall drop test set-up for aeration validation case..... 170

Figure 7-18: Relative SPH particle – finite element spacing. 170

Figure 7-19: Top view of pressure plots at 0.00074 s. Plots neglect the plate in order to show the pressure results. Results show a reduced peak pressure as the aeration levels increase. Fringe levels show pressure in Pa. 173

Figure 7-20: Pressure evolution for circular plate impact on water. Pure water, 5% aeration and 10% aeration cases were considered and compared to experimental results by Walkden [104]. Comparison shows good agreement, especially for the 10% aeration case. 174

Figure 7-21: Top view of gas volume fraction plots at 0.00074 s. Plots neglect the plate in order to show the pressure results. Results show a reduction in gas content as the particles compressed. Fringe levels show gas volume fraction..... 175

Figure 7-22: Global behaviour for pure water model at 4° inclination. Side view of model at 0.09 s. Forward velocity of the structure is 40 m/s and vertical velocity of the structure is -1.5 m/s. Fringe levels show pressure in Pa. Top figure shows complete set-up and bottom figure shows pressure levels for the water domain only. 177

Figure 7-23: Global behaviour of structure for aeration levels of 5% for 4° inclination. Side view of model at 0.09 s. Forward velocity of the structure is 40 m/s and

vertical velocity of the structure is -1.5 m/s. Fringe levels show pressure in Pa. Top figure shows complete set-up and bottom figure shows pressure levels for the water domain only. 178

Figure 7-24: Global behaviour of structure for aeration levels of 10% for 4° inclination. Side view of model at 0.09 s. Forward velocity of the structure is 40 m/s and vertical velocity of the structure is -1.5 m/s. Fringe levels show pressure in Pa. Top figure shows complete set-up and bottom figure shows pressure levels for the water domain only. 179

Figure 7-25: Global behaviour of structure for aeration levels of 20% for 4° inclination. Side view of model at 0.09 s. Forward velocity of the structure is 40 m/s and vertical velocity of the structure is -1.5 m/s. Fringe levels show pressure in Pa. Top figure shows complete set-up and bottom figure shows pressure levels for the water domain only. 180

Figure 7-26: Vertical force acting on the structure for the original (pure water) model, 5%, 10% and 20% aeration models for impact of plate at 4° inclination. 181

Figure 7-27: Pressure acting on the centre of the plate for the pure water model, 5%, 10% and 20% aeration models 182

Figure 7-28: Global behaviour for pure water model at 10° inclination. Side view of model at 0.09 s. Forward velocity of the structure is 40 m/s and vertical velocity of the structure is -1.5 m/s. Fringe levels show pressure in Pa. Top figure shows complete set-up and bottom figure shows pressure levels for the water domain only. 184

Figure 7-29: Global behaviour of structure for aeration levels of 5% for 10° inclination. Side view of model at 0.09 s. Forward velocity of the structure is 40 m/s and vertical velocity of the structure is -1.5 m/s. Fringe levels show pressure in Pa. Top figure shows complete set-up and bottom figure shows pressure levels for the water domain only. 186

Figure 7-30: Global behaviour of structure for aeration levels of 10% for 10° inclination. Side view of model at 0.09 s. Forward velocity of the structure is 40 m/s and vertical velocity of the structure is -1.5 m/s. Fringe levels show pressure in Pa. Top figure shows complete set-up and bottom figure shows pressure levels for the water domain only. 187

Figure 7-31: Global behaviour of structure for aeration levels of 20% for 10° inclination. Side view of model at 0.09 s. Forward velocity of the structure is 40 m/s and vertical velocity of the structure is -1.5 m/s. Fringe levels show pressure in Pa. Top figure shows complete set-up and bottom figure shows pressure levels for the water domain only. 188

Figure 7-32: Vertical force acting on the structure for the original (pure water) model, 5%, 10% and 20% aeration models for impact of plate at 10° inclination. 189

Figure 7-33: Pressure results for four elements (4156, 5608, 6934 and 7273) at the centre of the impacting plate for pure water (top figure) and 5% (bottom figure) aeration at 10° inclination. 190

Figure 7-34: Pressure results for four elements (4156, 5608, 6934 and 7273) at the centre of the impacting plate for 10% (top figure) and 20% (bottom figure) aeration at 10° inclination. 191

Figure 7-35: Pressure results for an element at the trailing edge of the plate for the pure water model, 5%, 10% and 20% aeration models for impacting plate at 10° inclination. 192

Figure 7-36: Initial set-up of fuselage structure. 195

Figure 7-37: Impact evolution for the pure water case at 0.04 s. Fringe levels show pressure in Pa. Peak pressure was 190 kPa 196

Figure 7-38: Impact evolution for the 5% aerated water at 0.04 s. Fringe levels show pressure in Pa. Peak pressure was 129 kPa. 197

Figure 7-39: Impact evolution for the 10% aerated water at 0.04 s. Fringe levels show pressure in Pa. Peak pressure was 93.6 kPa. 197

Figure 7-40: Impact evolution for the 20% aerated water at 0.04 s. Fringe levels show pressure in Pa. Peak pressure was 90.5 kPa. 198

Figure 7-41: Impact evolution of fuselage on pure and aerated water (5%, 10% and 20%) at 0.12 s. The fuselage does not experience any pitching up motion, which is the expected experimental behaviour [2]. This is due to the lack of suction modelling. 199

Figure 7-42: Gas content at t=0.24 s for 5% (top left), 10% (top right) and 20% (bottom) aeration. Top view with fuselage section blanked. Direction of travel from right to left. 200

Figure 7-43: Vertical velocity comparison for pure water, aerated cases (5%, 10% and 20%) and TUHH simulations with no suction. 201

Figure 7-44: Horizontal velocity comparison of pure water, aerated cases (5%, 10% and 20%), experimental data [2] and TUHH simulations with no suction. 202

Figure 7-45: Zoomed in section of the horizontal velocity comparison of pure water, aerated cases (5%, 10% and 20%), experimental data [2] and TUHH simulations with no suction. 203

Figure 7-46: Pitch attitude comparison for pure water, aerated cases (5%, 10% and 20%), experimental data [2] and TUHH simulations with no suction. 204

Figure 7-47: CG (Centre of Gravity) height comparison for pure water, aerated cases (5%, 10% and 20%), experimental data [2] and TUHH simulations with no suction. 205

Figure 8-1: Different cases of water impact. Case a) describes the phenomenon of ricochet, case b) the phenomenon of broaching and cases c) and d) the phenomenon of sinking. Figure reproduced from Johnson [108]. 209

Figure 8-2: Partially submerged projectile during oblique impact. v is the velocity of impact and line of forward motion, dS is the surface area and $\boldsymbol{\beta}$ is the angle of the outward normal of the surface area with respect to the line of forward motion... 210

Figure 8-3: Experimental results for ricochet and sink cases depending on velocities and angles (left) and dependency of depth on ricochet (right). Tests carried out in a tank with steel spherical projectiles. The maximum angle at which ricochet can be achieved was determined to be approximately 6°. Figure reproduced from Soliman et al. [107]. 213

Figure 8-4: Generalised case of a partially submerged sphere and the wetted area angles. Left figure shows the elevation view and right figure shows a plan view. $\boldsymbol{\Phi}$ and $\boldsymbol{\Psi}$ indicate the longitude and latitude at the element dA respectively. Figure reproduced from Hutchings [106]. 214

Figure 8-5: Elevation view of partially submerged cylindrical projectile with backspin. $\boldsymbol{\omega}$ is the angular velocity of the spinning projectile, $\boldsymbol{v}$ is the velocity of the centre of mass, $\boldsymbol{v'}$ is the velocity of the surface element relative to the water, $\boldsymbol{\alpha}$ is angle between $\boldsymbol{v'}$ and the surface of the cylinder, $\boldsymbol{\gamma}$ is the angle between $\boldsymbol{v}$ and $\boldsymbol{v'}$ and $\boldsymbol{\Phi}$ is the angle between the vertical axis and the surface element dA. 215

Figure 8-6: Theoretical critical angle as a function of velocity for a sphere and a cylinder with no spin. Theoretical results for a sphere are taken from Soliman et al. [107]. 219

Figure 8-7: Initial pressure distribution for the water domain under gravity. Fringe levels show pressure in Pa. 222

Figure 8-8: Side view of FE sphere and SPH water particles set-up. 223

Figure 8-9: Stiffness variations: a) K=0.01 kg/m^4 s^2, b) K=0.1 kg/m^4 s^2, c) K=1 kg/m^4 s^2. Particle penetration shown for the lower values of the contact stiffness. Figure shows a cut across the FE structure and the SPH particles in order to show potential particle penetration. 223

Figure 8-10: Water impact simulations of a rigid steel sphere: a) 40 ft/s at 2°, b) 60 ft/s at 3°, c) 70 ft/s at 4° and d) 100 ft/s at 5°. Direction of travel from left to right. ... 224

Figure 8-11: Cross sectional cut of sphere impact with initial velocity of 10 ft/s and an impact angle of 5°. 225

Figure 8-12: Water impact simulations of a rigid steel sphere: a) 40 ft/s at 5°, b) 40 ft/s at 6°, c) 80 ft/s at 6.5° and d) 100 ft/s at 7.5°. Results suggest that the sphere will ricochet contrary to experimental evidence that suggest that the sphere should sink. Direction of travel from left to right. 226

Figure 8-13: Complete set of 3D sphere water impact simulations. Comparison between experimental [107] and simulation results. Experimental and theoretical curves have been taken from Figure 8-3. 227

Figure 8-14: Side view. Pressure distribution on the water domain under gravity. Fringe levels show pressure in Pa. 229

Figure 8-15: Side view of steel cylinder. Finite Element mesh sizes for a) 0.002 m, b) 0.001 m, c) 0.0005 m particle spacing. 231

Figure 8-16: Side view. Cylinder impact on the water for the three different particle spacing at initial velocity of 30 ft/s and an inclination of 7°. Top figure is for 0.002 m, middle for 0.001 m and bottom for 0.0005 m of particle spacing. Direction of travel from left to right. 232

Figure 8-17: Side view. Cylinder impact on the water with initial velocity of 30 ft/s and an inclination of 7°. Water particle spacing of 0.00025 m. Direction of travel from left to right. 233

Figure 8-18: Cylinder impact on the water for the three different particle spacing at initial velocity of 30 ft/s and an inclination of 7°. Vertical displacement analysis for

the different particle spacing options. Results show a convergence for the finer particle distribution of 0.0005 m and 0.00025 m. 234

Figure 8-19: Cylinder impact on the water for the three different particle spacing at initial velocity of 30 ft/s and an inclination of 7°. Vertical velocity analysis for the different particle spacing options. Results show a convergence for the finer particle distribution of 0.0005 m and 0.00025 m. 235

Figure 8-20: Vertical contact force comparison for the finer particle spacing options. 236

Figure 8-21: Theoretical vertical velocity for a cylinder with diameter of 0.0254 m and an initial velocity of 9.144 m/s (30 ft/s) at 7° inclination. 238

Figure 8-22: Overall set of water impact of 2D steel cylindrical projectiles. Comparison is made to the theoretical curve for ricochet for a 2D cylinder. Good comparison can be made for the low velocity impacts. Deviation from the theoretical curve occurs for high velocity cases. 240

Figure 8-23: Side view. Water impact of 2D steel cylindrical projectile: top: 15 ft/s at 6° (indicating sinking), bottom: 40 ft/s at 7° (indicating ricochet). Direction of travel from left to right. 241

Figure 8-24: Initial pressure distribution for the 3D model. Fringe levels show pressure in Pa. 242

Figure 8-25: Side view. Water impact of 3D steel cylindrical projectile at 30 ft/s and an inclination of 7°. Direction of travel from left to right. 242

Figure 8-26: Horizontal component of the contact force on the 3D steel cylinder. Results indicate that there is no significant forward deceleration to slow the projectile down. As a consequence, the projectile maintains its momentum that leads to ricochet. 243

Figure 8-27: Initial position of the 3D steel sphere and the water domain with a particle spacing of 0.001 m. 246

Figure 8-28: Overall results for the water impact of a 3D steel sphere and a water particle spacing of 0.001 m. Comparison is made with experimental and theoretical results taken from Figure 8-3 [107]. 246

Figure 8-29: Side view cut. Cross section of 3D steel sphere impacting water domain at 20 ft/s and 6° inclination. The sphere sinks as the simulation progresses following the theoretical and experimental results by Soliman et al. [107]. 247

LIST OF TABLES

Table 2-1: Water accidents between 1959-1979. Table reproduced from Patel et al. [30]. 10

Table 2-2: Fatalities for water impact accidents between 1959-1979. Table reproduced from Patel et al. [30]. 11

Table 2-3: Recommendations and actual configuration of A320 aircraft of the Hudson River landing. Table based on NTSB [36]. 14

Table 4-1: Selected review of various methods for cavitation modelling. 68

Table 5-1: Input data for FE material model 82

Table 5-2: Murnaghan EOS input data. 83

Table 6-1: Coefficients for the Antoine equation depending on temperature. Table reproduced from Zardoni [60]. 93

Table 6-2: Input parameters for cavitation model 98

Table 6-3: Initial input data. 104

Table 6-4: Gruneisen EOS input data. 105

Table 6-5: Gruneisen EOS input data. 109

Table 6-6: Initial input data. 110

Table 6-7: Initial input data. 114

Table 6-8: Gruneisen EOS input data. 115

Table 6-9: Initial data for the 2D tube experiment. 118

Table 6-10: Gruneisen EOS input data. 119

Table 6-11: Initial radius and nuclei number density sensitivity cases. 120

Table 6-12: Overview of test cases 125

Table 6-13: Description of trolley and plate components. Table based on Aparici [101]. 133

Table 6-14: Initial input for SMAES plate impact. 133

Table 6-15: Material properties for FE structure. 134

Table 6-16: Initial input for water domain for SMAES plate impact. 134

Table 6-17: Murnaghan EOS input data. 135

Table 6-18: Symmetry plane coordinates. 135

Table 7-1: Input parameters for mcm_calcmass.f90 148

Table 7-2: Initial input example 149

Table 7-3: Input parameters for aerated water model and description..... 151

Table 7-4: Input data for 2D water column tests. 155

Table 7-5: Five particles and their corresponding vertical distance from the bottom of the column. Used for pressure readings. 156

Table 7-6: Aerated water model input parameters for 2D column..... 158

Table 7-7: Estimated pressure peaks for the pure water and aerated models. 161

Table 7-8: Estimated pressure peaks for the aerated model for 1m/s impact velocity and initial gas volume fraction of 10%. 165

Table 7-9: Initial density and speed of sound variation depending on the initial gas volume fraction. 167

Table 7-10: Estimated pressure peaks for the aerated model for 1m/s impact velocity and initial gas volume fraction of 10%. 168

Table 7-11: General input data for circular plate for drop test in aerated water. 171

Table 7-12: General input data for water domain for drop test in aerated water. 171

Table 7-13: Aerated water model input parameters for drop test in aerated water. ... 172

Table 7-14: General input data for water domain for plate impact at 4° inclination. ... 176

Table 7-15: Murnaghan EOS input data. 176

Table 7-16: Aerated water model input parameters for plate impact tests at 4° inclination. 177

Table 7-17: General input data for water domain for plate impact at 10° inclination. . 183

Table 7-18: Aerated water model input parameters for plate impact tests at 10° inclination. 185

Table 7-19: General input data of the structure for fuselage water impact. 194

Table 7-20: General input data of the water domain for fuselage water impact. 194

Table 7-21: Murnaghan EOS input data. 195

Table 7-22: Aeration parameters for fuselage water impact. 196

Table 8-1: Dimensions and properties of the 3D sphere for the water impact simulations. 220

Table 8-2: Combination of velocities and angles tested for water impact of 3D sphere simulations. 221

Table 8-3: Water domain dimensions and properties for water impact of the 3D sphere simulations. 222

Table 8-4: Impact and exit angles for the various ricochet simulations. 225

Table 8-5: Particle spacing options used for the cylinder mesh sensitivity analysis. .. 228

Table 8-6: Input values for evaluation of true compressibility. 229

Table 8-7: Pressure extremes for the 3 different particle spacing options for the water under gravity. 229

Table 8-8: Dimensions and material properties for steel cylinder. 230

Table 8-9: Material properties for steel cylinder for refined case with particle spacing of 0.00025 m. 233

Table 8-10: Discreet distances, times and vertical velocities for theoretical vertical velocity calculation of cylinder with diameter of 0.0254 m. Initial velocity of 9.144 m/s (30 ft/s) at 7° inclination. 237

Table 8-11: Dimensions and properties of 2D cylinder for water impact simulations. 239

Table 8-12: Dimensions and properties of water domain for water impact of 2D cylinder simulations. 239

Table 8-13: Dimensions and properties of 3D sphere for water impact simulations... 245

Table 8-14: Dimensions and properties of water domain for water impact of 2D cylinder simulations. 245

1 Introduction

This project is focused on the structural response of high speed, low angle impacts of structures, such as during an aircraft ditching event. A ditching event is described as the planned water landing of an aircraft, while the crew is in control of the aircraft. As part of the aircraft certification process, manufacturers are obliged to show that following a ditching, the aircraft will be able to stay afloat in order to allow for the safe disembarkation of passengers [1].

Aircraft manufacturers have defined some basic characteristics that an aircraft must attain for an optimum ditching event, in order to show compliance to ditching certification as given by EASA CS 25.801 emergency provisions [1]:

- “Each practicable design measure, compatible with the general characteristics of the airplane, must be taken to minimize the probability that in an emergency landing on water, the behaviour of the airplane would cause immediate injury to the occupants or would make it impossible for them to escape.”
- “The probable behaviour of the airplane in a water landing must be investigated by model tests or by comparison with airplanes of similar configuration for which the ditching characteristics are known.”
- “It must be shown that, under reasonably probable water conditions, the flotation time and trim of the airplane will allow the occupants to leave the airplane and enter in the life rafts required by CS 25.1415. If compliance with this provision is shown by buoyancy and trim computations, appropriate allowance must be made for probable structural damage and leakage. If the aeroplane has fuel tanks (with fuel jettisoning provisions) that can reasonably be expected to withstand a ditching without leakage, the jettisonable volume of fuel may be considered as buoyancy volume.”

Current industry needs include the introduction of novel designs and materials. However, the methods employed in ditching analysis mean that these new designs would be expensive and time consuming to process. Extensive research in the past fifty years has tried to identify the behaviour of aircraft of various profiles and a multitude of configurations [2] [3] [4] [5] [6]. Current designs, in principle, still use similar fuselage profiles to tested configurations.

Initial investigations into ditching, included analytical and semi-analytical methods that used simple geometries and scale model test results of conventional fuselages shapes, in order to obtain the pressure loading on the fuselage [7] [8] [9] [10] [11] [12] [13].

Numerical methods have been introduced in ditching analysis with the improvement of computing technology. However, the focus has been on relatively simple structures dropped in a simplified water model [14] [15] [16] [17] [18] [19] [20]. Even though there has been progress in the field of finite element structural modelling, water modelling has seen less improvement.

1.1 Aims and Objectives

This project is a contribution to a European initiative (SMAES project, funded by FP7 Programme), with a focus on the flow phenomena that are present during a typical water landing. These phenomena are air cushioning and aeration, suction and cavitation [21]. It has been established, through experimental data, that these flow phenomena can affect the overall behaviour of the fuselage upon impact and also the structural response (pressure distribution and deflection) of the fuselage [22] [10] [23].

This project aims to improve the numerical capability to predict the structural loading on an aircraft during ditching. This process is much more complex than vertical impacts of simple structures. Specifically, the aim is to improve the meshless SPH code, owned by Cranfield University, in order to improve the fluid model used for fluid-structure interactions with forward velocities such as ditching. This will be achieved by:

- Understanding the phenomenon of ditching. This will include a review of accidents, experimental work and the state-of-the-art in the numerical analyses of aircraft ditching and fluid-structure interaction simulations. The main factors that influence the accurate prediction of the loading of the structure will be assessed.
- Developing a more detailed understanding of how cavitation, suction and the presence of air affect the flow and the structural loading in such cases.
- Developing and implementing a physical cavitation model that can improve the predictions for the loading of the structure and investigating the parameters that can influence these predictions.
- Developing and implementing an aerated water model in order to investigate the effect of air on the loading of the structure.

- Investigating angled water impact cases that will allow the assessment of the water model.

1.2 Thesis Structure

Chapter 2 provides an overview of ditching research. It includes the initial theories applied to relatively simple structures impacting the water vertically. Moreover, an accident review is considered from the past decades, including discussions of the major ditching events. Finally, a review has been undertaken, of the experimental investigation and the effects of fuselage shape, velocities and other aircraft configurations on the water impact of more modern airliners.

Chapter 3 progresses to the numerical investigation of ditching with examples of both vertical (helicopter and simple shapes) and fixed-wing simulations, demonstrating the current numerical capabilities in modelling water and introducing the limitations that existing water models have.

Chapter 4 provides a detailed description of the water flow phenomena of air cushioning, ventilation, cavitation and suction. Particular interest lies with cavitation, since it is further developed. Cavitation growth and collapse are introduced along with a review of numerical attempts to model the phenomenon.

Chapter 5 provides the essential information on the meshless Smoothed Particle Hydrodynamics approach that is used for the water modelling. Moreover, the MCM code, Cranfield University's SPH code, is described and an initial plate impact with high forward velocity is discussed, as a coupled example of the code.

Chapter 6 details the development and application of a homogeneous cavitation model. Initial validation cases are considered, which demonstrate the correct implementation of the current model. Further test cases of plate impacts under high forward velocity are considered, providing an understanding into the applicability of the approach in the context of ditching and assess the limitations of the approach.

Chapter 7 investigates the influence of air in the water in more detail, and provides an implementation for a homogeneous mixture of water and gas. The main effect of aerated water, which is the reduced pressure profiles, is validated with simple 2D test cases, followed by plate and fuselage runs. Comparison of the fuselage runs with other numerical results is also made.

Chapter 8 details the theory behind the phenomenon of ricochet of spheres and cylinders, a high forward velocity scenario with a less complicated structure. An equation that relates the critical angle of impact of a non-spinning cylinder with its velocity is derived, based on previous theories for spheres and numerical simulations are performed, in order to evaluate the accuracy of the ricochet prediction for both the new theoretical value and the experimental results for spheres.

2 Ditching Theory and Accident Review

In this chapter, the main differences between water and hard landings are described, along with the main stages of ditching of a fixed-wing aircraft. Furthermore, the original theories of water impact, initially considered for seaplane designs, will be discussed. An accident review with the major ditching accidents is detailed. Experimental results from model tests of aircraft and the influence of a variety of parameters are finally provided as part of this review.

2.1 Characteristics of Water Impact

Even though there has been considerable research in the field of helicopter crashworthiness, fixed-wing aircraft ditching assessment has attracted less interest, mainly due to the complexities of the water-structure interaction imposed by the high forward velocity. It is well known that for vertical water impacts, characteristic of helicopter behaviour, the structural loading is different from hard soil landings. The distribution of loading in vertical water impacts varies along the fuselage and the impact pulse is longer. As a consequence, fuselage skin rupturing can allow water to enter the aircraft, thus reducing the floatation time [18]. Moreover, from a structural point, the elements of the fuselage that are designed to fail during impact and absorb energy fail to collapse, party or entirely due to the nature of the load distribution. In doing so, the load path can reach weak points of the fuselage leading to damage. Finally, higher levels of energy need to be absorbed by the occupants. Figure 2-1 illustrates the differences.

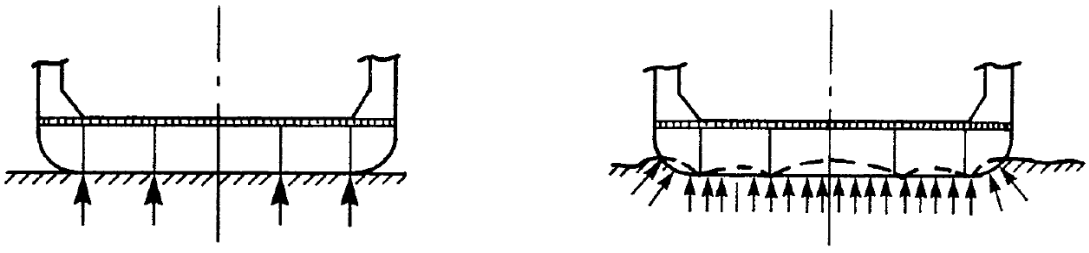

Figure 2-1: Loading of a structure during a hard surface impact (left) and a soft/fluid surface (right). Figure reproduced from Zimmermann et al. [24].

For fixed-wing aircraft characterised by high forward velocities, ditching can be categorised in four phases, as shown in Figure 2-2. During the approach phase, the aircraft is configured in a similar way to a normal landing, but with the landing gear retracted. For a successful ditching, it is assumed that the first point of contact is the

rear part of the fuselage. Pressure loads on that area of the fuselage can be significant, leading to deformations of the skin and potential rupture. As the aircraft decelerates during the landing phase, there can be a strong pitch-up moment, caused by suction forces on the aircraft, resulting in a more severe second impact of the forward fuselage and potential nose diving [4]. This behaviour can lead to further damage in the centre and forward sections. Finally, after a successful ditching the aircraft enters the floatation phase, where the safe exit of passengers takes place [10]. From a structural point of view, the most severe loading and thus the most dangerous period for water penetration is during the impact and landing phases.

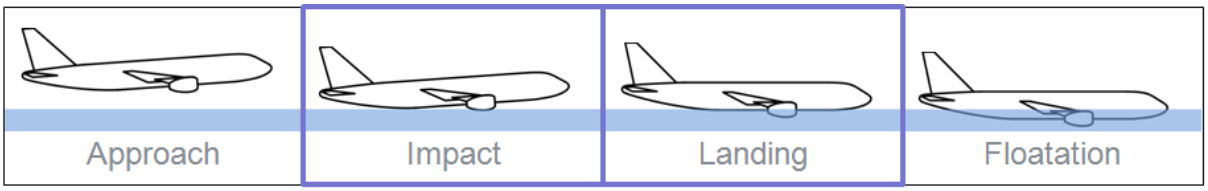

Figure 2-2: Stages of the ditching event of a fixed-wing aircraft.

2.2 Water Impact Theories

Research into water impact started in 1929 with the work of von Karman and the vertical impact of a wedge, as part of the research of that era for the design of seaplanes [7]. The objective of that research was to establish an analytical solution for the pressure on a simple non-deformable structure. Figure 2-3 shows a wedge during partial immersion.

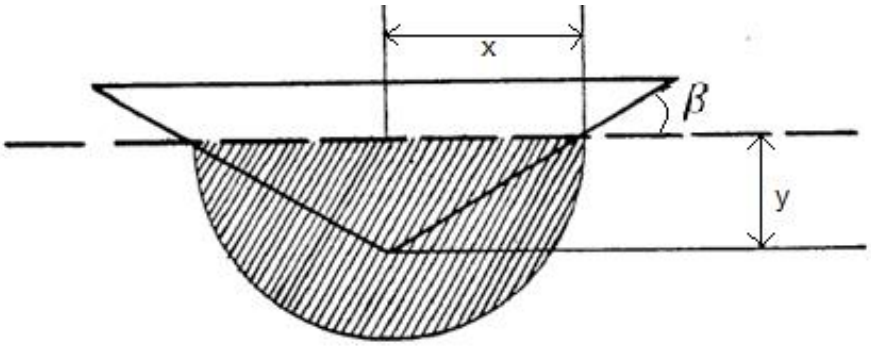

Figure 2-3: Vertical impact of a 2D wedge with semi-cylinder area depicting the added mass. Figure reproduced from Mayo [25].

To derive the pressure solution, von Karman started by assuming that the added mass of the plate, which is the mass of a displaced volume of fluid, is equal to the mass of water that is present in half a cylinder. Starting from the momentum, *M*:

$$\mathrm{M} = \frac{W}{g} v + 0.5\rho\pi v x^2 = \frac{W}{g} v_0 , \tag{2-1}$$

where *W* is the weight of the body per unit length, *x* is the width of the wetted wedge. For a dead-rise angle *β,* the vertical velocity can be written as:

$$\mathrm{v} = \frac{dy}{dt} = tan\beta \frac{dx}{dt}, \tag{2-2}$$

which, after substitution and rearranging of equation (2-1), gives:

$$\frac{dx}{dt} = \frac{v_0 cot\beta}{1 + \frac{q\pi x^2}{2W}}, \tag{2-3}$$

where *q=gρ.*

Using the fact that:

$$\frac{d^2x}{dt^2} = \frac{d}{dx}\left[0.5\left(\frac{dx}{dt}\right)^2\right], \tag{2-4}$$

equation (2-3) becomes:

$$\frac{d^2x}{dt^2} = -\frac{v_0^2 cot^2\beta}{\left(1 + \frac{q\pi x^2}{2W}\right)^3} \frac{q\pi x}{W}. \tag{2-5}$$

The force per unit length can then be expressed as:

$$F = \frac{W}{g}\frac{d^2y}{dt^2} = \frac{v_0^2 cot\beta}{\left(1 + \frac{q\pi x^2}{2W}\right)^3} \rho\pi x , \tag{2-6}$$

which gives an average pressure per unit length of:

$$P = \frac{F}{2x} = \frac{v_0^2 cot\beta}{2\left(1 + \frac{q\pi x^2}{2W}\right)^3} \rho\pi . \tag{2-7}$$

It follows from equation (2-7) that the maximum pressure would be in the centre of the wedge which means that for *x=0*:

$$P_{max} = \frac{v_0^2}{2}\,\rho\pi cot\beta. \tag{2-8}$$

The above derivation suffers from the fact that, as the dead-rise angle, β, reaches zero, the pressure becomes infinite, suggesting that it is not valid for flat plates.

Wagner proposed, in 1931, that the displaced water from the sides of the wedge would lead to a greater width and virtual mass values compared to the von Karman analysis. The virtual mass of a wedge similar to the previous theory is greater by a factor of $\left(\frac{\pi}{2}\right)^2$ [25]. According to Wagner, the pressure distribution is not uniform. The highest pressures are located on the top edges of the wedge, whereas the pressure is more evenly distributed at the bottom of the wedge [9]. The maximum pressure was found to be towards the top edges of the wedge, where the water forms a spray:

$$p_{max} = \frac{\rho}{2}\frac{1}{u^2}\frac{v_0^2}{(1+\mu)^2}, \tag{2-9}$$

where μ is defined as:

$$\mu = \frac{\pi\rho x^2}{2m}, \tag{2-10}$$

and u is the ratio of the velocity over the rate of increase of the wetted surface:

$$u = v/\frac{dx}{dt}. \tag{2-11}$$

The analytical solutions above represent the original investigations into the vertical water impact of simple non-deformable shapes. These solutions are still used today as part of semi-analytical methods [26]. Further improvements to the above solutions have been proposed and an overview of these is found in [20] and [25].

2.3 Accident Review

Data from the US and the UK show that 88% of ditching events are survivable with minimum injuries to the crew or the passengers [27]. The trend is the same for both

high wing and low wing aircraft. Statistics show that up to 50% of the survivors drown after the impact [27].

A ditching event is described as the planned water landing of an aircraft. It is categorised as a consequential factor to the accident, since in most cases it is the result of fuel exhaustion or crew error [28] [29]. Furthermore, a ditching event assumes that the pilot has some control over the aircraft. These parameters, along with the fact that the passengers have time to prepare, increase the survival rates for planned water landing events, compared to unplanned ones [30] [31]. Next, some accident data are discussed. This will provide evidence of the significance of a safe water landing with no water penetration in the fuselage and also provide some details of the structural damage sustained by modern passenger airliners. Unfortunately, to this point, there are no collective data specifically for planned water impacts (ditching events) from the latest decades and there is no distinction between planned landings on water and land in recent publications. From 1959-1979 there were 16 accidents involving water, of which only in 11 of them water was a major factor in the survival of the occupants [30]. Table 2-1 shows the accidents that occurred for this period collectively.

Table 2-1: Water accidents between 1959-1979. Table reproduced from Patel et al. [30].

Accident	Year	Hull Loss	On-Board	Fatal-ities	Serious Injuries	Flight Phase	Fire	Occupant Survivability[1]
092461 720 Boston	1961	NO	71	0	2	LDG	YES	YES
082062 DC8 Rio De Janiero	1962	YES	105	15	NA	T/O	NO	YES
040764 707 JFK	1964	YES	145	0	7	LDG	NO	YES
063067 CVL Hong Kong	1967	YES	80	17	5	APP	NO	YES
110567 880 Hong Kong	1967	YES	137	1	NA	T/O	NO	YES
011369 DC8 Los Angeles	1969	YES	45	15	17	APP	NO	YES
050270 DC9 St. Croix, V.I.	1970	YES	63	25	25	LDG	NO	PARTIALLY
072770 DC8 Naha, Okinawa	1970	YES	4	4	0	APP	NO	PARTIALLY
121877 CVL Madeira, Spain	1977	YES	57	36	13	LDG	NO	YES
050878 727 Pensacola	1978	YES	58	31	1	APP	NO	YES
122378 DC9 Palermo, Italy	1978	YES	129	108	NA	LDG	NO	UNKNOWN

From the list above, only one can be classified as a ditching event. That is the DC9 accident at St. Croix. AML 980 was a flight that ditched outside Virgin Islands in 1970, where 40 of the 63 passengers and crew survived the event, giving a 63.5% survival rate. According to the NTSB report poor weather, failed landing attempts and fuel exhaustion were the main factors that contributed to this accident. The ditching attitude was a general nose up position with flaps between 5° and 6°. The DC-9 did not sustain great damage and stayed afloat for about 10 minutes [32]. The aircraft is estimated to have experienced decelerations of the region of 8-12 g, based on the time it took the aircraft to come to a stop and the fact that several seats, with a design limit of 9 g, experienced failure [33]. Another accident, not mentioned in Table 2-1, is the ditching of a Lockheed Constellation 1049H in 1962, in the North Atlantic that suffered total engine failure in 3 out of the 4 engines, leading to a controlled landing in the sea 560 nautical miles west of Shannon, Ireland. Out of the 76 passengers and crew, 28 perished giving a survival rate of 61.5%. According to the accident report, the pilot landed in the face of the swell, a procedure which is not recommended as it can lead to severe structural damage. Even though the aircraft did not experience any skipping

after the initial impact, it suffered from the loss of the left wing, along with the externally located life rafts. Based on passengers' accounts, the aircraft suffered from one severe deceleration that led to seat and seatbelt failure. As a consequence, several passengers were thrown out of the seats and sustained injuries that hampered their safe egress from the aircraft [34]. Occupant survivability means that there is at least one survivor, there is a way for passengers to exit the aircraft, the impact forces are within survivable limits and there is enough occupant space, within the airframe, for the passengers to move [30]. With respect to the fatalities, Table 2-2 shows that the majority of the fatalities are due to drowning and not direct trauma from the impact. Fatalities due to direct force trauma represent a significantly smaller percentage of fatalities.

Table 2-2: Fatalities for water impact accidents between 1959-1979. Table reproduced from Patel et al. [30].

Accident Group	Occupants	Fatalities	**Percent Occupant Fatality**	Trauma	**Percent Occupant Fatality**	Drowned	**Percent Occupant Fatality**
High Energy	507	206	40.6	4	0.79	202	39.8
Slide/Roll	387	16	4.1	1	0.26	15	3.9

Care must be taken with these data, because the author does not explicitly define ditching in the accident categories. Slide or roll events most likely do not fall under the category of ditching and most likely many of the high-energy accidents were performed with insufficient preparation or control. It is suggested that when the fuselage tears, which is the case in 7 out of the 11, the fatalities from drowning reach 36.8%, whereas for accidents where the fuselage crushes but does not tear, the fatalities from drowning reduce to 25.9% of the passenger load [30]. The displacement of the floor was evident in 4 accidents involved in deep water entry and the fatality rate due to the displacement was 13.8% of the total occupants [35]. Figure 2-4 makes the distinction and shows the causes of the 11 water entry accidents.

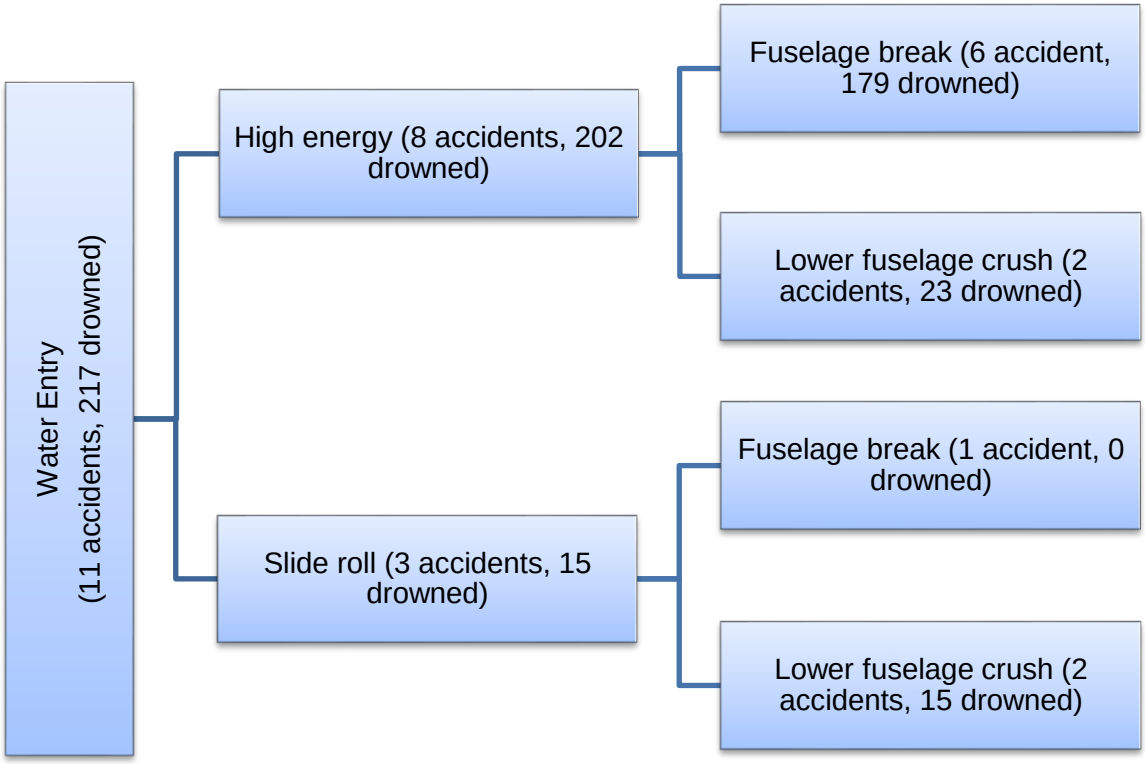

Figure 2-4: Classification of the water entry accidents taking place between 1959-1979. The majority of the fatalities occurred when there was a break in the fuselage. The survival rate is increased significantly when the fuselage does not rupture. Figure reproduced from Widmayer et al. [35].

From Figure 2-4 it is found that 82.5% of fatalities occurred when there was a break in the fuselage and only 17.5% when the fuselage is just crushed.

Comparing these data with ground accidents in Figure 2-5, it is suggested that the percentage of fatalities per total passenger load is smaller for water impacts [31].

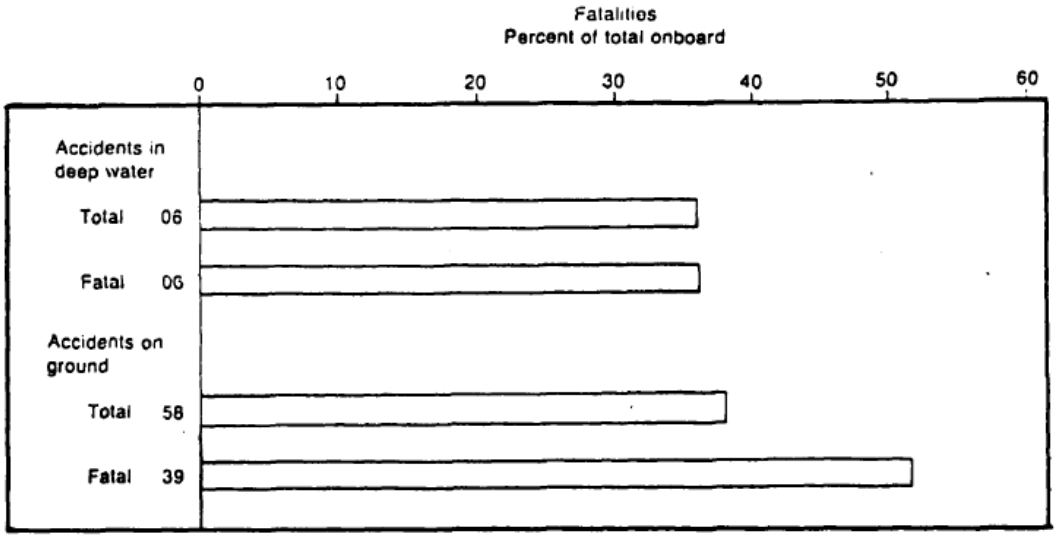

Figure 2-5: Comparison of ground and water accidents with respect to fatalities per total passenger loading. Comparison shows that the percentage of fatalities per total passenger load is smaller for water impacts. Figure reproduced from Johnson [31].

From 1980 until 1996 there were 30 reported fatal accidents, where the aircraft performed a forced landing, but the data does not distinguish between landing on land or water [28]. Similarly, for the period between 1997 and 2006 there were 22 similar reports [29]. From what is mentioned so far, those latest figures cannot be used since the percentage of commercial aircraft that are forced to land on water are far less than those that land on hard soil. This gives an indication of the difficulty to collect data for ditching events, due to the scarcity of their occurrence.

However, some general conclusions can be drawn from the above data. Firstly, the occurrence of a ditching event is far rarer compared to the rest of the accident types. This is the main reason why data for ditching events are not easily gathered. As far as the passenger survivability is concerned, Table 2-2 and Figure 2-4 clearly indicate that most fatalities do not result directly from the impact but from drowning. It is important to notice that in the 11 accidents that are recorded above, four of them are classified as survivable and further three as partially survivable, if the actions and the training of the crew were better.

More recent events include the Hudson River landing in 2009 and the Tuninter Mediterranean ditching. The aircraft in the Hudson ditching accident was a US Airways Airbus A320. It was forced to ditch in the river after dual engine failure, due to bird

ingestion. There were no fatalities in this event and only 5 serious injuries, out of the 155 passengers and crew. Table 2-3 provides a comparison of the recommendations that Airbus suggests for a safe ditching and the actual configuration of the accident aircraft.

Table 2-3: Recommendations and actual configuration of A320 aircraft of the Hudson River landing. Table based on NTSB [36].

	Certification	Accident
Pitch, deg	11	9.5
Airspeed, knots	118	125
Glideslope, deg	-1	-3.5
Descent rate, m/s	1.07	3.81

The accident investigation reported that the prescribed conditions of Table 2-3 could not have been practically achieved in this case, mainly due to the timing of the engine failure, during the climb phase.

One could argue that this accident should be classified as an impact, since the descent rate (sink rate) is much higher than the regulations define. On the other hand, NTSB suggests that due to the difficulty of maintaining the certification parameters during a flight with minimal engine power and also because there was sufficient time to go through parts of the relevant checklists, prepare the cabin and the passengers, this accident can be categorised as a successful ditching [36].

As far as the structural damaged is concerned, it was focused on the rear part of the fuselage. The water pressures imparted on the aft fuselage led to the collapse of frames, the cargo door and the passenger floor struts. Furthermore, the bottom fuselage skin cracked and water rushed in the aircraft. Further pressures and suction forces resulted in the failure of the lower fuselage skin and the pressure bulkhead. These post-impact damages are due to the forward motion of the aircraft and the flow of water in the aircraft [36].

The second accident, which happened in the Mediterranean Sea in 2005, involved an ATR-72. It was forced to ditch after fuel starvation and shut down of both engines. There were 16 fatalities, 16 serious injuries and 7 minor injuries.

The accident report [37] states that the aircraft sustained severe damage and was broken apart into three pieces. The rear of the fuselage detached at first impact. All three parts remained afloat for 20-30 minutes after ditching. Subsequently, the forward and aft sections of the fuselage sank, while the central section along with the engines and the wings (high wings) remained afloat. Due to the configuration of the ATR-72, the wings and engines did not impact the water surface and they suffered very little damage.

The lower part of the fuselage was dented in places, with many breaks due to the impact. In the rear of the aircraft there was a large opening, as well as severe damage on the pressure bulkhead. Generally, the rear part was completely collapsed, however the occupant space was maintained. Strong bending stresses caused the rear section to detach at the time of impact and also allowed the central part of the fuselage to detach from the wing. The front section, including the cockpit, was severely damaged and compressed [37].

As far as the recommended ditching configuration is concerned, it is similar to the Airbus case above but the optimum pitch angle is 9° [37]. The main outside parameter that needs to be considered when ditching, irrespective of the aircraft, is the sea state. In calm seas, it is recommended to land into the wind in order to reduce the aircraft's speed, whereas if there is a swell, ditching parallel to the swell (parallel to wave crests) is preferable. Finally, it is considered best practice for the wings to be level in order to avoid yawing [37].

2.4 Experimental Tests Review

A number of experiments, including full scale and scale models of aircraft and aircraft components, have been performed by NACA and NASA since the late 1920s. Initial tests involved the use of simple shapes in water and were focused on the design of hulls and seaplane bottoms. These experimental tests provide the benchmark for the general understanding of the influence of aircraft design and ditching configuration that forms modern standard practices.

Sottorf [38] performed a variety of tests on planing surfaces with flat rectangular plates, describing the pressure distribution on a flat plate when impacting the water. At the front part (leading edge) of the plate, the pressure peaks to its maximum at the moment of impact and then drops steadily. It was found that when dealing with relatively small angles of attack, the pressure becomes zero at the trailing edge.

Shoemaker [39] conducted experiments with V-shaped planing bottoms of various dead-rise angles in order to determine the drag of the wetted surface to the flow. It was found that, for small dead-rise angles, the resistance of the V-shaped bottom decreases with increasing speed. These observations follow from the fact that the resistance of a flat body reduces with increasing speed, due to the lift that is generated, allowing for a smaller wetted area.

Mayo [13] tested a prismatic float at a dead-rise angle of 22.5°, with varying flight parameters establishing the loading of the floats. It was determined that, when landing with a small flight path angle (angle with respect to the horizontal), then the planing forces are significant, causing a more severe impact. On the other hand, landing with a high flight path angle tends to reduce the effect of planing, leading to milder impacts and reduced forces.

A full ditching test of a B-24D Liberator bomber has also been conducted (Figure 2-6) [5]. The pressures and accelerations at the bottom of the aircraft were recorded. The overall dynamics of the impact included an initial impact of the tail section, before skipping out of the water for a brief period of time. The second impact led to a nose dive and a deep-water fuselage run. The tail section experienced the highest pressures during the first impact, while during the second impact the forward section experienced the highest pressures. The highest decelerations recorded were 2.7 g [5].

Figure 2-6: B-24D Liberator aircraft. Figure reproduced from Steiner [5].

Fisher et al. [11] performed scale model ditching tests of the DC-4 and DC-6 airliners. These tests are the first that apply directly to the ditching behaviour of an aircraft that resembles the needs of this project. The experiments took place in both calm and rough waters for various speeds and attitudes. The results of those tests provide the first understanding as to the effect of the different structural elements on the ditching behaviour of an aircraft. In order to reproduce damage on the underside of the fuselage, replaceable scale-strength sections, made from balsa wood frames and aluminium sheets, were used.

Firstly, the effect of the position of control surfaces, such as the flaps, was investigated. It was determined that their extension or retraction is not important, as far as the impact sequence is concerned, but it was observed that when the flaps were fully retracted the aircraft took longer to come to a stop. This is expected since the main aim of the flaps is to reduce the aircraft's speed. As a result of the higher speed the impact was more severe, leading to more pronounced decelerations. Thus, it was suggested that the flaps should always be lowered for a ditching event.

Next the effect of the attitude was considered. It was found that the pitch angle (angle of the aircraft to the horizontal, including the angle of attack) of the aircraft can influence the decelerations and the damage of the fuselage. According to the experimental results and for that specific type of aircraft, the most favourable pitch angle was 12°, producing the lowest decelerations and the least damage.

Finally, the effect of the state of the sea was discussed and it was concluded that in rough seas, as expected, the damage and decelerations are more severe. If the aircraft

lands parallel to the wave crests it will not be severely damaged [11]. Figure 2-7 shows the ditching testing performed on a scale model of a DC-6 airliner. The two most important aspects of the impact are the initial tail strike on the surface of the water and the subsequent nose dive.

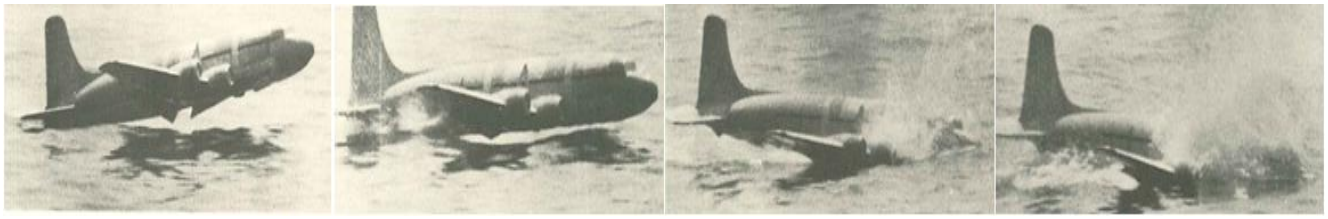

Figure 2-7: Sequence of ditching event of a 1/16-scale model DC-6 aircraft with a 12° pitch angle. Initial tail strike followed by a nose dive and potential severe damage. Figure based on Fisher et al. [11].

A comparison of the damage of the underside of the fuselage is shown in Figure 2-8, for calm and rough water ditching. This experiment shows the influence of the state of the water on the damage, especially on the forward section of the model. This can be attributed to the fact that the model may have suffered from low pressures at the aft fuselage leading to a pitching up moment, followed by a more severe impact at the front.

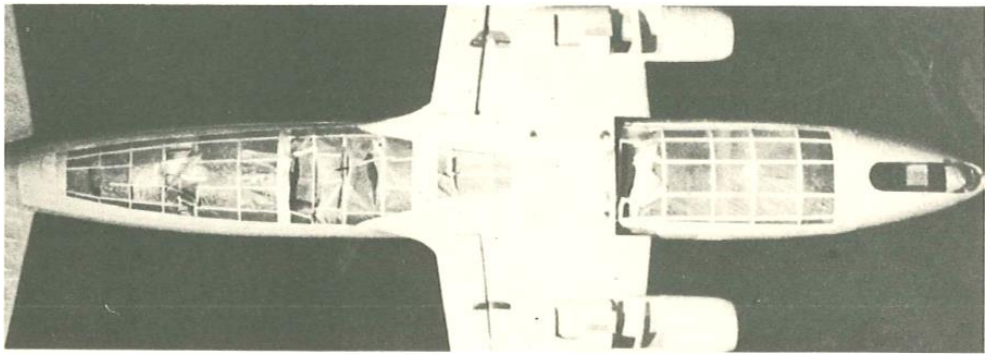

a)

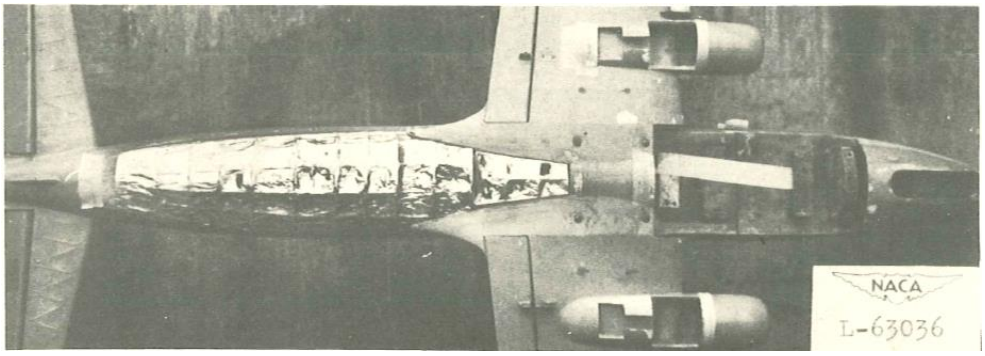

b)

Figure 2-8: Comparison of the damage on the underside of the fuselage of a 1/16-scale model DC-4 aircraft with a 12° pitch angle: a) calm waters, b) rough waters (6-ft waves). Scale-strength was achieved with balsa wood and aluminium sheets placed in key locations of the underside of the scale model. Figure based on Fisher et al. [11].

An important area of research was conducted by McBride et al. [2] and it raises the question of the influence of the cross section of the aircraft's fuselage on the overall behaviour during a ditching event. A variety of impact speeds were tested for a total of nine different cross sections. The experiments showed that, if the rear cross section is flat then the tendency for a high-attitude response and high suction forces is decreased. Moreover, this kind of aircraft fuselage could lead to skipping after the initial impact. For an upswept rear fuselage, there can be significant suction forces during the landing phase, leading to the behaviour similar to that of Figure 2-9. When dealing with lower impact velocities, the flat cross section is better, whereas for higher impact velocities a rounded fuselage is preferable, in order to reduce the effect of suction forces. Another finding of these experiments was that aircraft with high fineness ratio are prone to skipping and reduced suction forces. The importance of this research lies

in the fact that modern aircraft manufacturers still use these results in order to make design choices for new models.

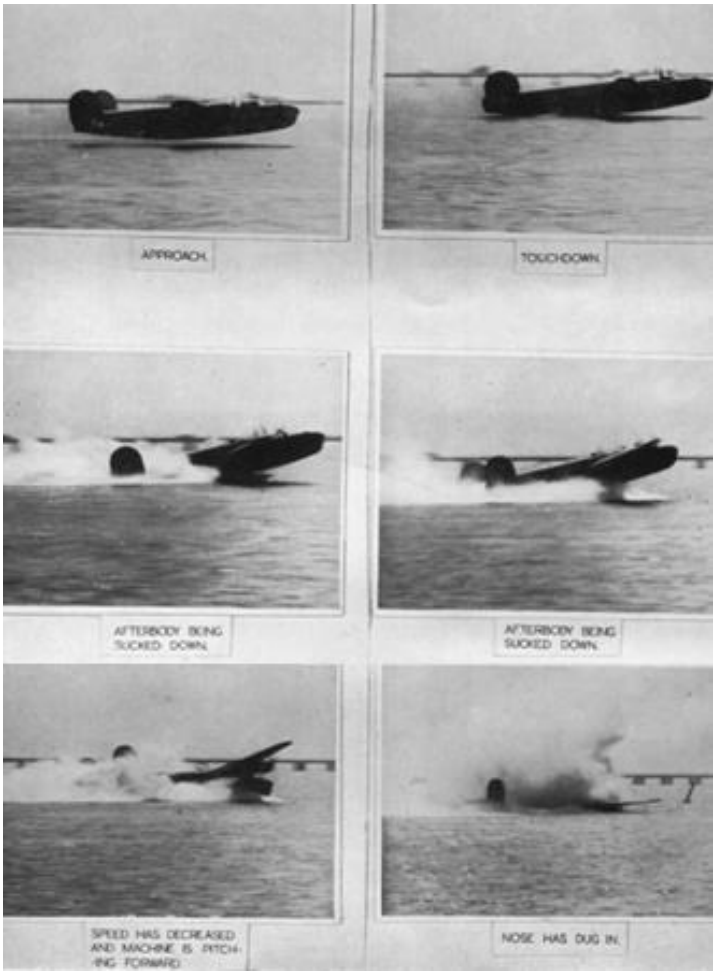

Figure 2-9: General behaviour of an upswept rear fuselage during ditching in calm waters. Initial aft body contact followed by nose diving. Figure based on McBride et al. [2].

Fisher et al. [12] provided a more comprehensive report on a number of bomber fighter and transport models, in order to establish the influence of different structural elements on their ditching behaviour. As far as the wings are concerned, they suggest that the best position is marginally higher than the bottom of the fuselage. This will allow for a clearance during ditching, so that the engines and the flaps will not interfere with the ditching but also allow for the wings to act as a means of buoyancy. A high wing will not be affected by significant impact pressures, suggesting that the bottom of the fuselage will need to absorb most of the impact energy and thus sustain more extensive damage

[4]. For the flaps the extended position is preferred. The trade-off between extended and retracted flaps is that the deployed flaps can lead to diving of the airplane, whereas the flaps-up configuration can lead to significantly more damage due to the higher impact velocities. The ability of the flaps to break off during ditching was considered to reduce the risk of diving, caused by the moments generated by their extension. With respect to the engine nacelles, they must be above the bottom of the aircraft to avoid rapid deceleration. The landing gear should always be retracted.

Next the effect of the shape of the fuselage was investigated. It was observed that high longitudinal and lateral curvature can lead to suction forces and subsequently a trim-up attitude. This is similar to the experimental observations of [2] [12].

Further publications include experiments on fuel tank positions [3] and engine positions [40], which have been shown to have negligible influence on the overall ditching behaviour. Moreover, the extension of the landing gear can increase the risk of diving [41].

Thompson [6] investigated the ditching behaviour of a scale model of a jet transport in various sea conditions. In order to allow for damage in the model, sections of the bottom of the fuselage were made of cardboard, balsa wood and aluminium foil, as shown in Figure 2-10. A combination of different flap settings, landing speeds and landing attitudes were considered, as well as a combination of landing gear configurations. The outcome of these experiments suggested that the optimum configuration would be a medium landing attitude (7°) with the flaps extended, as this would lead to reduced accelerations. An interesting observation in these experiments was that the bottom of the fuselage experienced less damage with the main landing gear extended, a fact that is disputed by other experimental data. However, the different position of the landing gear on this model, compared to a typical airliner could be the reason for this discrepancy. Additionally, the undercarriage of this model consists of 24 wheels, suggesting that they can absorb higher levels of energy than a typical airliner.

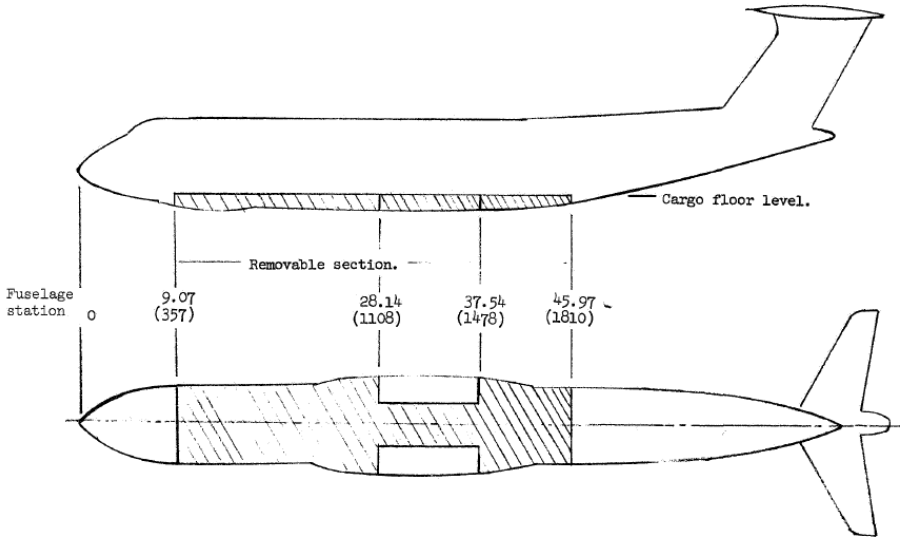

Figure 2-10: Area of removable sections used to model failure on a 1/30-scale model. Balsa wood, aluminium foil and cardboard were used for the scale-strength of the shaded areas. Figure reproduced from Thompson [6].

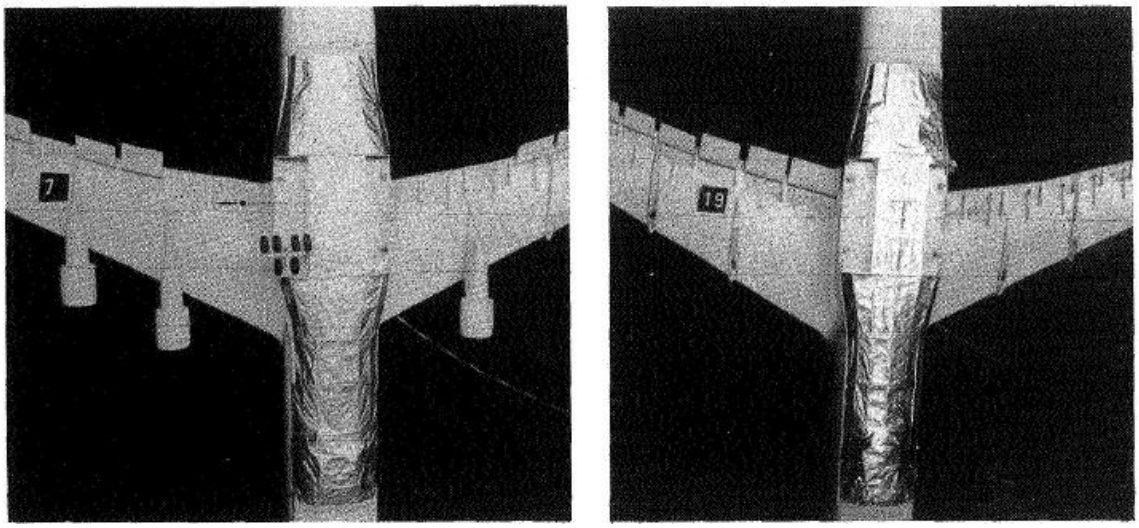

Figure 2-11: Damage sustained in calm (left) and rough water impacts (right) for an attitude of 7°, with flaps extended, the main landing gear fully extended and a speed of 71 m/s. Figure based on Thompson [6].

Figure 2-11 shows the damage sustained for a moderate attitude at impact and the main gear extended. As it is could be expected, the rough water impact shows the whole of the main gear system and half the flaps being torn away. The damage on the structural elements, which are supposed to fail and are covered with the aluminium foil, do not show any significant differences. The observation that the landing gear

extension provides a better ditching configuration could be due to the higher energy absorption of the landing gear structure during the impact. This observation, however, stands alone against the majority of research, which suggests that for a smooth ditching the landing gear should be fully retracted.

The above review provides a description of the most significant ditching experiments with the most important results. A detailed investigation into forced water landing tests was done by Smith et al. [4]. This report outlines testing techniques (tower drop tests, controlled launch of aircraft models) and data acquisition methods up to 1948, along with some additional experiments performed in the UK. The report provides clear guidelines for a variety of parameters that would allow a successful ditching. With respect to the velocity of the aircraft a low landing velocity is preferred. This will lead to reduced impact forces and pressures and avoid instabilities in the longitudinal direction.

As far as the angle of descent is concerned, it is suggested that a relatively small angle will produce lower pressures, thus allowing for a more successful ditching scenario. In the case of high angle of descent, the aircraft would be prone to diving in the water, leading to significant structural failure and reduced flotation time [4].

The attitude of the aircraft at touchdown is another aspect that has been discussed by many researchers. It is established that a tail down attitude is best for a smooth contact with the water. As it has been recommended in the accident reports, ditching parallel to the swell is ideal. If ditching occurs on a rising wave front the impact forces increase due to the increase in the wetted area of fuselage [4].

2.5 Conclusions

In this chapter, the initial analytical solutions of von Karman and Wagner were described, which provided the basis for the initial seaplane design. Their limitations with regards to modern fixed-wing airliners are apparent in the fact that these early theoretical developments dealt with simple rigid structures impacting the water surface vertically. An accident review was discussed along with the most important experimental investigations, which demonstrated that the aircraft needs to be in a similar position to landing in order to perform a successful ditching. A variety of parameters from sea state to fuselage shape and wing position has also been discussed.

Current ditching methods include a combination of scale model testing along with the use of numerical analyses, as demonstrated by Climent et al. [42] with the test case of an EADS-CASA CN235 model. This leads to the next chapter, where more recent investigations into water impacts and ditching, with the use of computer simulations, will help provide the background into the research that has been done so far in the field. Moreover, the limitations that the engineering community faces with respect to ditching will become clear.

3 Numerical Investigations

In this chapter, a review of the numerical analyses of water impacts performed in the past is given. Both vertical impacts (helicopter and sections), as well as simulations that consider forward velocities are reviewed. The purpose of this chapter is to showcase the state-of-the-art in the field but also to demonstrate the limitations that are present.

3.1 Vertical Impacts

There has been considerable research into the numerical analysis of water impacts, with particular interest in vertical drop tests of simple shapes. The reason for this is that computationally it is less expensive and also it served towards the ditching investigation of helicopters and helicopter subfloor sections. As it will be discussed later, the loading predictions for vertical impacts are considered to be generally adequate. However, the following review shows the implications on the loading predictions caused by the use of a simplified water model and primarily by the lack of any air present in the simulations. Since the focus of this project is in ditching attempts, which are characterised by forward velocities, the description that follows is by no means exhaustive. A more complete review is provided by Seddon et al. [20]. Oger et al. [19] performed 2D simulations of wedge water entry using the SPH method. The SPH model was developed with a variable smoothing length as seen in Figure 3-1. The variable smoothing length allows the SPH model to be refined in a particular area of interest (in this case it is the SPH region closer to the wedge for the initial impact pressures), while keeping a coarser particle spacing in the rest of the fluid domain. This set-up allows for a smaller overall fluid domain and thus reduced computational costs.

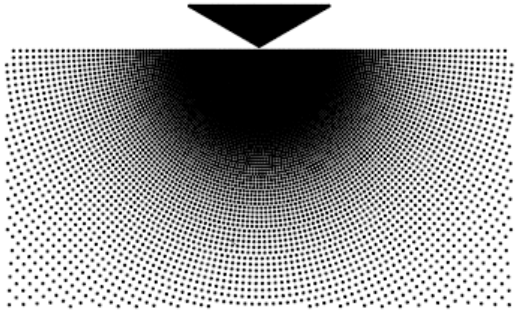

Figure 3-1: Vertical drop of rigid wedge in a water domain consisting of SPH particles with variable smoothing length. Figure reproduced from Oger et al. [19].

The authors used the Murnaghan equation of state for modelling the water which is given by:

$$p = B\left(\left(\frac{\rho}{\rho_0}\right)^{\gamma} - 1\right), \tag{3-1}$$

where *B* is the bulk modulus and relates to the speed of sound *c* as:

$$B = \frac{\rho_0 c_0^2}{\gamma}. \tag{3-2}$$

The above equation of state is widely used, mainly due to its simplicity. It relates the pressure to the density of the liquid. The main findings of the above simulations were concerned with the effect of the variable smoothing length. It was found that there are pressure peaks at the interface between the fine and the coarse smoothing length, which were attributed to inner wave reflection. Moreover, the initial pressure peaks at impact were comparable to experimental results. However, for dead-rise angles lower than 20° they were slightly higher. This discrepancy was thought to be caused by the lack of any air in the model and thus any air cushioning effects were neglected.

Pentecote et al. [43] used the SPH method in PAM-CRASH in order to perform similar 2D simulations of wedges of varying dead-rise angle. For the water model a polynomial equation of state was used and for the wedges the dead-rise angles were 10°, 20° and 30°. The vertical accelerations recorded in the simulations for the higher dead-rise angles compared well with the experimental results that the authors provide. As it is expected results for the flatter wedge, with a dead-rise angle of 10°, proved less accurate, again due to the lack of any air modelling. Figure 3-2 shows the horizontal velocity during the impact of a wedge with a 20° dead-rise angle.

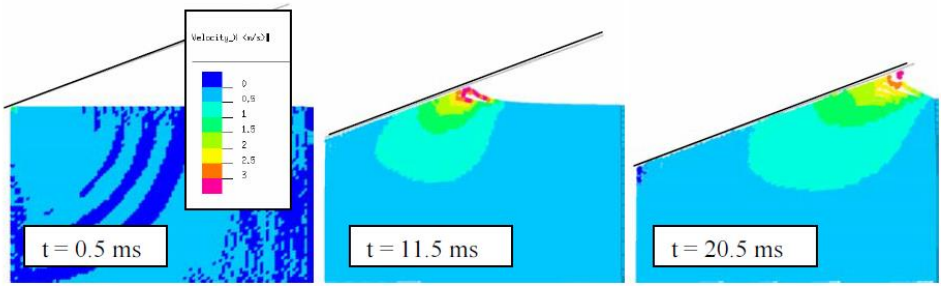

Figure 3-2: Evolution of the horizontal velocity for a wedge of 20° dead-rise angle during water impact using the SPH method. Figure based on Pentecote et al. [43].

A more complex analysis was also performed by Pentecote et al. [43] for a helicopter subfloor, modelled with aluminium. The SPH particle spacing was similar to the finite element size. As it is shown in Figure 3-3, the water domain was modelled with a combination of SPH particles in the vicinity of the impact and finite elements in the rest of the domain. The pressure results obtained did not agree well with experimental data. The duration of the initial pressure peaks was shorter and the peak values considerably higher. The authors suggested that accurate recordings of pressures can be quite cumbersome to achieve during experiments, primarily due to the high sensitivity of the transducers. However, it must be noted that the fact that the pressure peaks were higher and the pulses shorter in the simulations can also be due to the neglect of any air in the simulations. As with the flatter wedge components, this can be a significant problem when dealing with flatter surfaces, such as a helicopter subfloor.

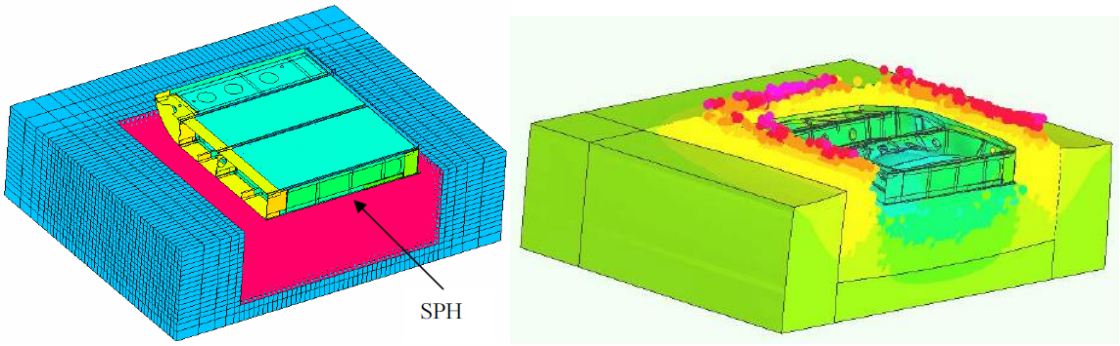

Figure 3-3: Coupled FE-SPH simulation for helicopter subfloor impact. Water defined by finite elements further away from the structure and with SPH particles in the immediate vicinity of the subfloor. Figure based on Pentecote et al. [43].

Francesconi et al. [18] performed drop tests of aluminium alloy panels of various thicknesses and compared the experimental results to simulations, performed with the SPH and ALE methods in LS-DYNA. The focus of these studies was to investigate the accuracy of the acceleration prediction by the two different methods.

Both modelling techniques captured the general behaviour of the water at the point of impact. However, the ALE model failed to capture the splash to the extent that the SPH did (Figure 3-4). As far as the accelerations are concerned, both methods agreed with the results of the drop tests. However, the impact pulse was more accurate for the SPH model. The main difference between the models is that for the SPH case the penetration of particles through the cut was less pronounced due to the coarser particle

spacing. However, the reduced computational cost of the coarser SPH model outweighs this discrepancy.

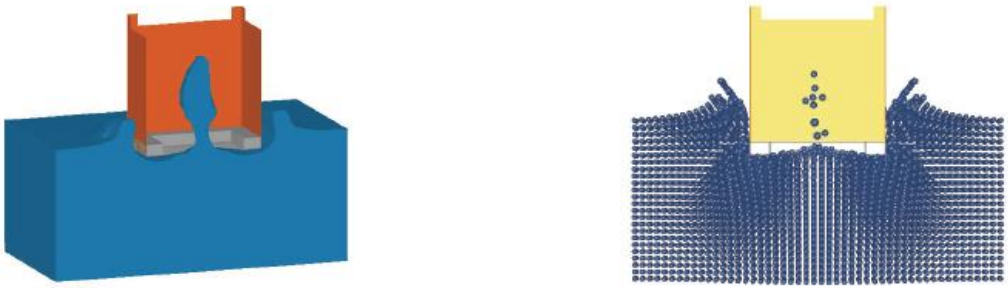

Figure 3-4: ALE (left) and SPH (right) simulation of a panel with a cut impacting water. Figure based on Francesconi et al. [18].

Similar vertical drops of aluminium skin panels were simulated by two meshless methods, SPH and EFG [15]. The models are shown in Figure 3-5. The test specimens consisted of deformable panels, which were attached to L-shaped stiffeners. The main difference to the previous models is that these panels do not have any opening at the bottom. The impact velocities that were tried ranged from 3.1-7.7 m/s and the accelerations were recorded. The refinement of the models was the same for both the SPH and the EFG approach.

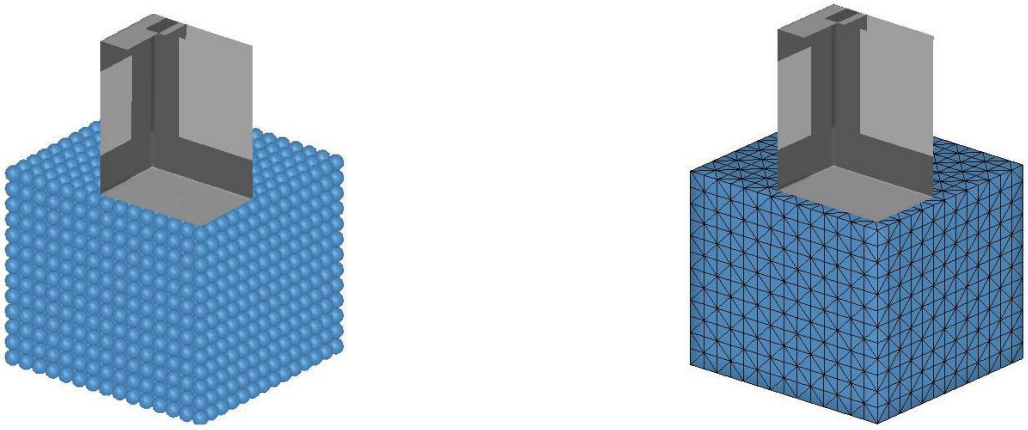

Figure 3-5: Vertical drop test simulations for an aluminium box with L-stiffeners. SPH (left) and EFG model (right). Velocities ranging from 3.1 to 7.7 m/s. Figure based on Anghileri et al. [15].

The authors suggest that both models give an accurate physical representation of the impact with respect to the experiments. Figure 3-6 shows that the SPH simulation fails

to capture any of the splash that is clearly evident in the EFG simulation. Comparing the numerical results of the two models, the authors suggested that both models were acceptable in capturing the initial deformation and deceleration peaks. Finally, it was observed that the SPH model led to a longer pulse.

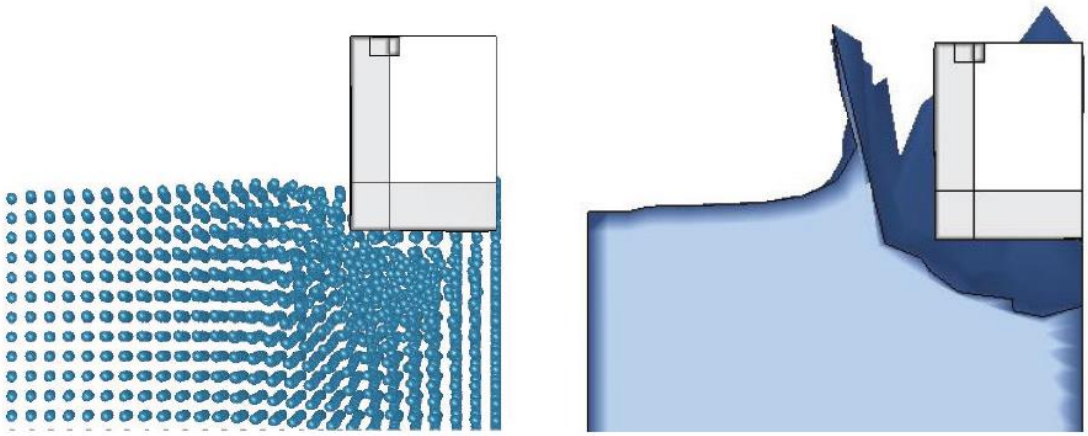

Figure 3-6: SPH (left) and EFG (right) simulation of aluminium box with L-stiffeners impacting water. Reduced splash is evident for the SPH simulations due to the coarse particle distribution. Figure based on Anghileri et al. [15].

Additional experimental and numerical investigations were performed with an interest in helicopter ditching crashworthiness by Anghileri et al. [14]. Triangular and semi-circular sections were considered and impact pressures and accelerations were recorded through experiments and compared to numerical results. The numerical method used was SPH in the commercial LS-DYNA package. The structure was modelled with conventional finite elements, while the water domain was modelled with SPH particles. A uniform coarser model and varying particle spacing were considered. Figure 3-7 and Figure 3-8 show the initial set-up of the simulations and the overall behaviour during impact.

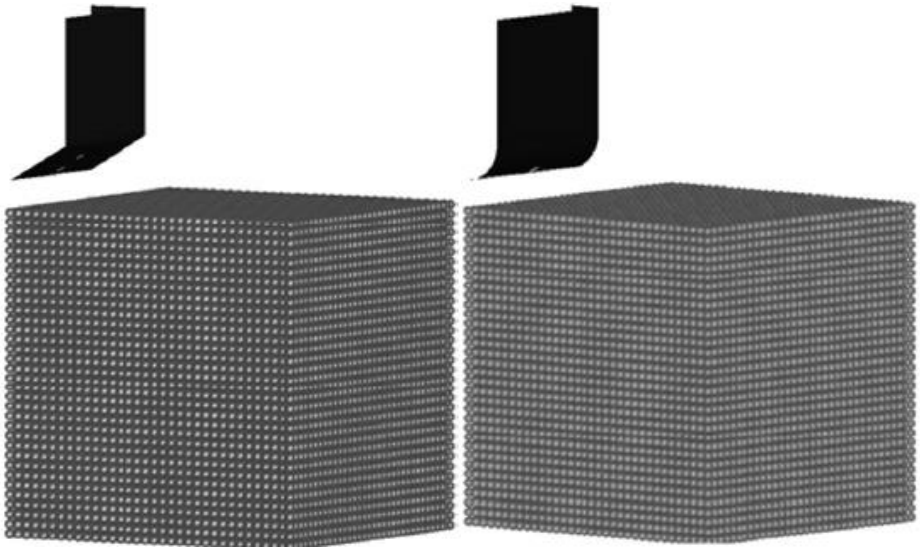

Figure 3-7: Initial set-up of the triangular and semi-circular sections. Rigid structures were considered with impact velocities ranging between 4 m/s and 9 m/s. Figure based on Anghileri et al. [14].

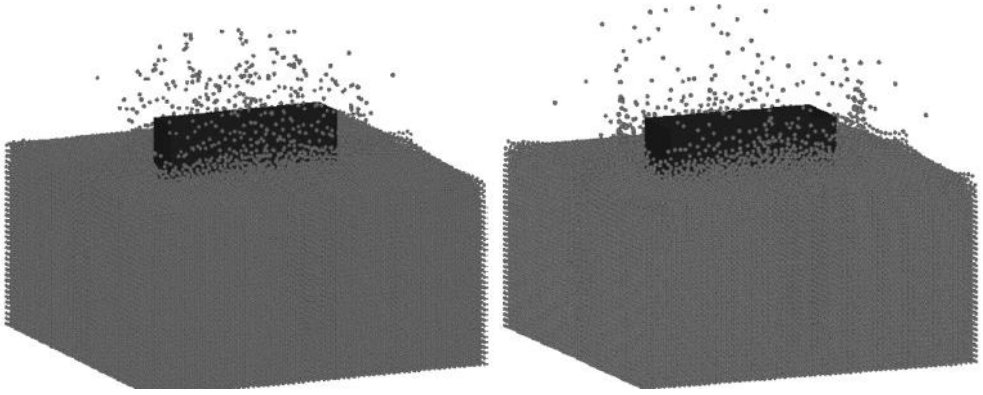

Figure 3-8: General impact of the triangular and semi-circular sections [14]. For both cases the accelerations matched the experimental results. Figure based on Anghileri et al. [14].

According to the authors, the accelerations and pressure results compared well with the experimental data and captured the peak magnitudes and trends accurately. As a general modelling advice, the authors suggested that the accurate material description and adequate particle spacing between the structure and the fluid are paramount for the accurate simulations of such test cases.

The numerical analysis of the water impact of a space capsule was also investigated by Candy et al. [16]. Both a Lagrangian and an Eulerian approach were used for the water modelling and the accelerations and pressures were recorded. The capsule

(Figure 3-9) was modelled as a rigid body, as experimental results showed no significant deformations occurring during impact. The acceleration and displacement results compared well with respect to the experiments, however it must be noted that the Lagrangian approach, which is computationally less expensive, provides less accurate displacement results as the simulation progresses. This is attributed to the extreme distortion of the elements as the capsule penetrates the water domain.

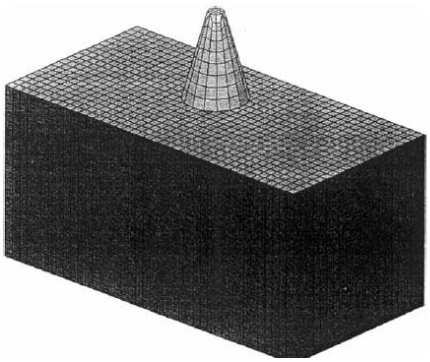

Figure 3-9: Vertical impact of space capsule at 9 m/s with no inclination included. Figure reproduced from Candy et al. [16].

A detailed review of the capabilities of the Finite Element method with respect to the response of a helicopter subfloor vertically impacting the water has been done by Hughes et al. [44]. A detailed model of a helicopter subfloor was modelled with finite elements in LS-DYNA consisting of aluminium panels, composite sections and rivets. The water domain was also modelled with finite elements, given the fact that the interest in the study was only for the initial stages of the impact. Figure 3-10 shows the subfloor with nodal constraints used for the impact simulations.

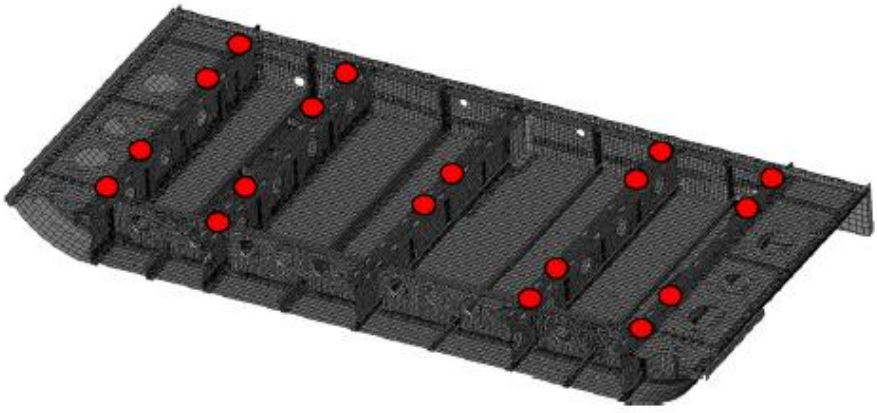

Figure 3-10: Subfloor overview with 18 points that constrained the global motion in lateral and horizontal translation. Figure reproduced from Hughes et al. [44].

The lack of any air modelling led to higher pressure predictions than in the experiments. It is concluded that the purely Lagrangian water model can provide an acceptable correlation to experimental results for the initial stages of the impact. It is not the best option for longer fluid-structure interactions due to the extreme distortion of the elements, that can lead to numerical instabilities. It is suggested that other options, such as SPH and ALE should be investigated with regards to helicopter ditching analysis. Figure 3-11 shows the evolution of the impact and the extreme distortion of the water elements close to the boundary.

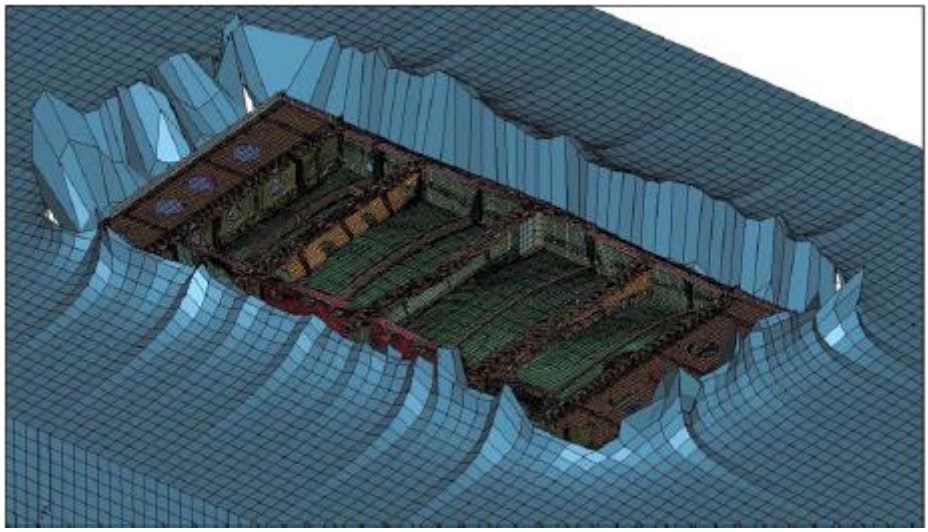

Figure 3-11: Impact evolution of subfloor showing the extreme distortion of the Lagrangian water elements in the vicinity of the structure 35 ms after impact. Figure reproduced from Hughes et al. [44].

3.2 Horizontal Impacts

The numerical investigation of impacts that are characterised by high forward velocity has attracted less interest than the vertical impacts described above. One of the attempts to simulate the ditching of an aircraft was performed by Pentecote et al. [43]. A generic aircraft model was used and the water domain was modelled with both SPH particles and finite elements, allowing for a reduced computational cost. The middle section of the water, where the aircraft impacts, was modelled with SPH particles, whereas the rest was modelled with solid finite elements.

Figure 3-12 shows the evolution of the ditching. Generally, the impact followed the patterns that was observed in experiments and also gave a representation of the spray that surrounds the aircraft. High contact forces were experienced at the first point of

impact (rear section) and also during the impact of the forward fuselage. However, no further details are provided and the generic model used for the aircraft does not allow for any conclusions with respect to the accuracy of these simulations.

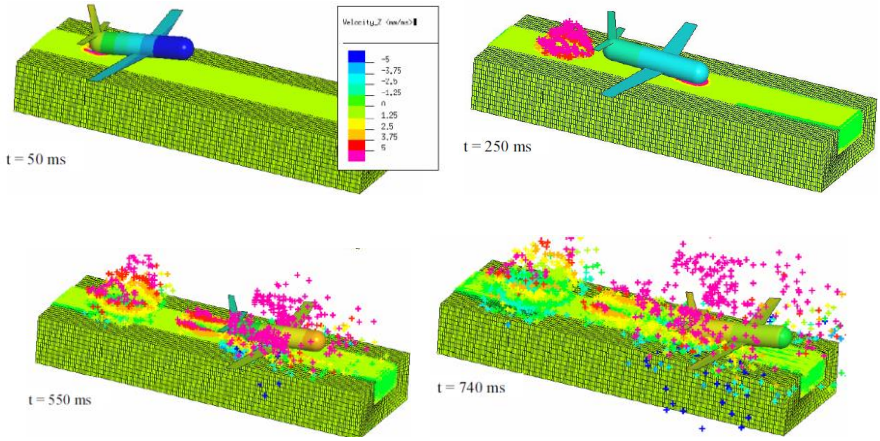

Figure 3-12: Evolution of the ditching of the generic aircraft. SPH and finite elements used for the water domain. Figure based on Pentecote et al. [43].

A detailed model of an Airbus A321 during ditching was modelled by Ortiz et al. [45] [46]. Two different aircraft configurations were considered, one at 9° inclination and a forward velocity of 50 m/s and the second at 8° and 60 m/s. For both cases, the vertical velocity was kept at 1.5 m/s, which the authors considered a typical sink rate. For the first case both ALE and SPH were used for the water model. The ALE model used a two-phase model that can allow for the presence of air, whereas the SPH modelled used a one-fluid model (only water). Pressure results showed that the ALE model was able to capture lower pressures due to the inclusion of air. The above simulations were compared to a hard soil impact which, as expected, differs in both the distribution of deformations and also in the magnitude and duration of accelerations experienced by the fuselage. However, this set of simulations showcases the ability of the ALE and SPH methods in modelling a full aircraft ditching scenario.

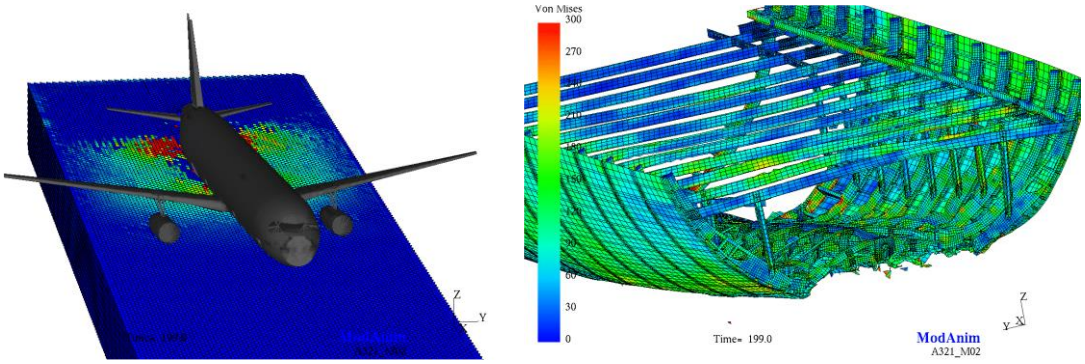

Figure 3-13: Ditching of A321 at 60 m/s forward velocity and 8° inclination. Highest pressures and deformations observed at the rear of the aircraft. Structural deformation visible on the lower section of the aft section. Figure based on Ortiz et al. [46].

Wittlin et al. [47] performed simulations of rotorcraft impacts with vertical and horizontal velocities using both a FE code and a hybrid approach. The Finite Element method was used in order to record pressures, forces and accelerations, whereas the hybrid method was used as a less computationally intensive approach for design evaluation and parametric studies. For the water model, an Eulerian approach was used, which included a layer of air. Figure 3-14 shows the general evolution of the impact. The accelerations and pressure results were of comparable magnitudes to test cases.

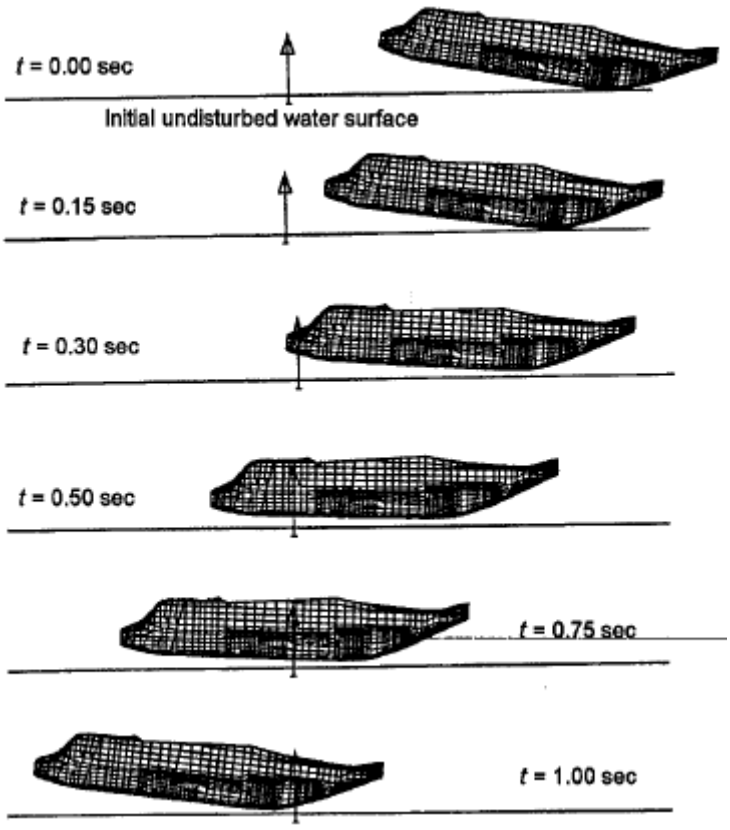

Figure 3-14: Evolution of rotorcraft water impact computed using the generic FE code MSC/DYTRAN. Figure reproduced from Wittlin et al. [47].

Another ditching simulation was performed by Climent et al. [42]. A coupled FE-SPH approach was used by EADS-CASA, in order to evaluate the capabilities of the coupled approach in modelling the vertical impact of a helicopter subfloor, similar to the one performed by Hughes et al. [44]. Next, the ditching simulation of a CN-235-300M aircraft (Figure 3-15) was considered.

Figure 3-15: EADS-CASA CN-235-300M aircraft. Figure reproduced by Climent et al. [42].

The numerical simulations were able to represent the skipping motion of the aircraft, however the predicted pressures did not agree with the experiments. They demonstrated a much sharper profile compared to the experiments. This can be attributed to the lack of any air modelling between the structure and the water. Figure 3-16 shows the last step of the impact of the aircraft on the SPH particles. To reduce computational cost the water particles were modelled with a thin layer, which at an initial assessment appears too small for the scale of the simulation.

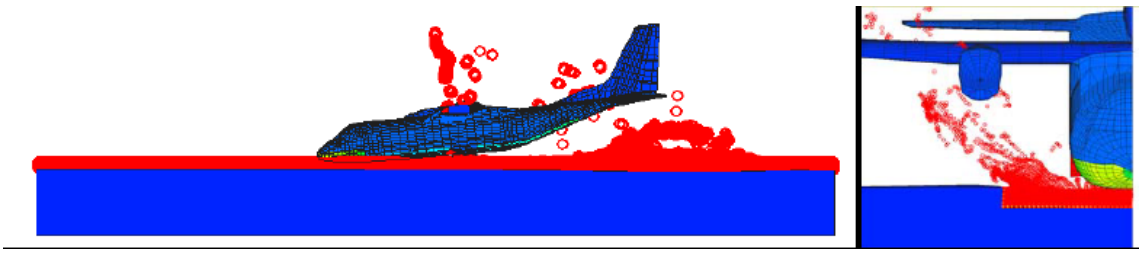

Figure 3-16: Impact of CN-235-300M scale model with the use of finite elements and SPH particles for water modelling. Figure reproduced by Climent et al. [42].

Streckwall et al. [26] used generic aircraft models to simulate ditching events. A hybrid approach was used in order to estimate the forces on a section, using an enhanced momentum method, based on the von Karman and Wagner theories. The authors also made use of a RANS solver in order to model the interaction of the structure with the free surface and the subsequent behaviour of the fuselage. For both the hybrid and the RANS simulations three general bodies of revolution were used provided by [2], shown here in Figure 3-17.

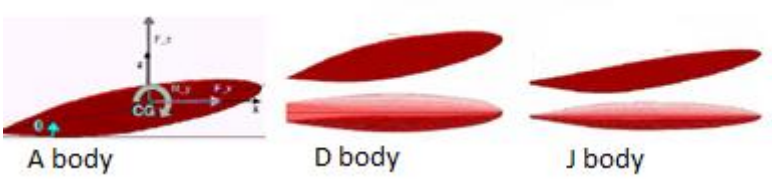

Figure 3-17: The three models used for the simulation in the hybrid and RANS solvers. All models are based on the experimental investigation by Mc Bride et al. [2]. Figure based on Streckwall et al. [26].

The results show high pressures developing at the front of the submerged part and negative pressures at the rear. The results for the A, D and J bodies correlate well with respect to test results for the pitch angle and position of the centre of gravity. Figure 3-18 shows the general behaviour of the different fuselage bodies.

Figure 3-18: Simulations for general body of revolution A, D and J respectively. Initial horizontal velocities were set at 9.14 m/s. Figure based on Streckwall et al. [26].

3.3 Conclusions and Limitations

An overview of the numerical attempts at modelling of ditching has been provided. The main limitations in the methods above are related to the ditching scenarios that are considered and the methods with which the water is modelled. As far as the ditching scenarios are concerned, the majority of research is focused on vertical impacts of simple shapes (box structures or wedges). With respect to helicopter ditching crashworthiness, these simplified attempts can produce accurate predictions for pressures and accelerations for the initial stages of the impact. Any discrepancies in the results are mainly due to the lack of air modelled between the structure and the water surface and the distortions of the finite element water model. Numerically, both Lagrangian and Eulerian methods have been tried. It has been shown that a combination of computational cost and length of run should be taken into account when deciding the modelling approach.

Considering the simulations of structures with forward velocities, such as in the fixed-wing aircraft, the numerical attempts are less developed. The numerical attempts either use a generic model for the aircraft, that can only describe the general behaviour of the model to experimental results, or more importantly, the water model is not accurate enough. During these impacts, there are phenomena in the water flow that occur which can significantly influence the pressures imparted on the structure, as well as the general behaviour of the structure. The most important of them are the effect of air, cavitation and suction. However, current explicit FE codes fail to incorporate any of them, or their representation is not accurate enough. Examples of cavitation modelling are applied in commercial CFD codes with good accuracy, however in these software applications the interest lies in the flow over rigid symmetric structures and do not provide any local deformations or accelerations of the structures.

Moreover, literature indicates the difficulty in comparing numerical simulations with experimental results due to the scarcity of these tests and the low levels of repeatability of such complex experiments.

The literature review so far has helped to develop an understanding of the phenomenon of ditching by reviewing experimental test cases, investigating the state-of-the-art with respect to the numerical analyses performed, as well as through the review of some major and recent ditching accidents. In the next chapter the flow phenomena, for cases of high forward velocity water impacts, will be described along with various attempts in modelling them.

4 Air Cushioning, Suction and Cavitation

In this chapter, the main physical phenomena that occur in the water during the impact and landing phases of ditching will be described, with respect to their influence on the loading of a structure. Furthermore, the influence of these phenomena for the case of high forward velocity impacts, such as a ditching event, will be assessed.

4.1 Air Cushioning

In the numerical attempts described in Chapter 3 there have been a number of cases where the pressure and acceleration predictions failed to provide good correlation with experiments, due to the lack of air modelling. The effect of air in fluid-structure interaction problems is further analysed in this chapter. For high velocity water impacts, there is considerable mixing between air and water.

Where entrapment of air is present in an area between the structure and the fluid, it is known as an air cushion. The air cushioning effect is of particular interest in vertical water impacts and it can influence the pressure duration and distribution [48]. Initially, during an impact there is a peak pressure, followed by a lower and more constant pressure [49]. With the presence of air, the peak pressure is reduced and its pulse is longer, providing a milder impact profile. The smaller the amount of trapped air, the higher the peak pressure and the shorter the pulse will be [49]. Typically, this phenomenon is more pronounced with structures that have small deadrise angles, such as hull section and wedges [50] [51]. This means that the vertical drop of a flat plate will be influenced far more from the trapped air compared to a similar drop of a wedge that has a large dead-rise angle. In these cases, air cushioning appears in the form of a single cavity filled with air. The body motion of a flat structure being dropped into a water tank depends on the velocity, gravity and the presence of air. As a result of the compressibility of the air, the pressure in the air cushion will deform the free surface of the water and the structure prior to the actual impact [52].

The majority of the research is focused on the water impact of simple shapes, such as wedges, as a means of understanding the phenomenon of slamming in hull design processes. Korobkin [53] performed the analysis of the elastic response of a beam impacting the water vertically and determined that the stresses and pressures are lower for thicker layers of air. An interesting observation made by both Korobkin [53] and Lewison [54] is that, the effect of air and the potential reduction in the pressure

does not necessarily mean that the stresses and strains on deformable structures will lead to a more favourable design. This is due to the fact that the duration of the initial impact is longer. For the case of a fixed-wing aircraft, the shape of the lower fuselage can influence whether an air cushion will occur and also determine its severity. This follows closely from the numerical attempts reviewed in Chapter 3.

Peseux et al. [55] performed simulations of wedge drops. The pressure results followed similar patterns. However, the peaks recorded were considerably higher for the wedges with the smaller dead-rise angle. This discrepancy was attributed to the lack of air in the water model. Panciroli et al. [56] also investigated the vertical impact of wedges with the SPH method excluding air, reaching the same conclusion as Peseux et al. [55]. These simple tests complement the general water impact simulations described in Chapter 3 and follow closely with their findings.

The use of the ALE method has shown to provide a reduced pressure peak upon the impact of an Airbus A321 model. Inherently, the ALE method allows for the use of a two-phase approach. This means that the presence of air can be taken into consideration. This approach provides lower pressures when compared to the single phase SPH method as shown in Figure 4-1 [45].

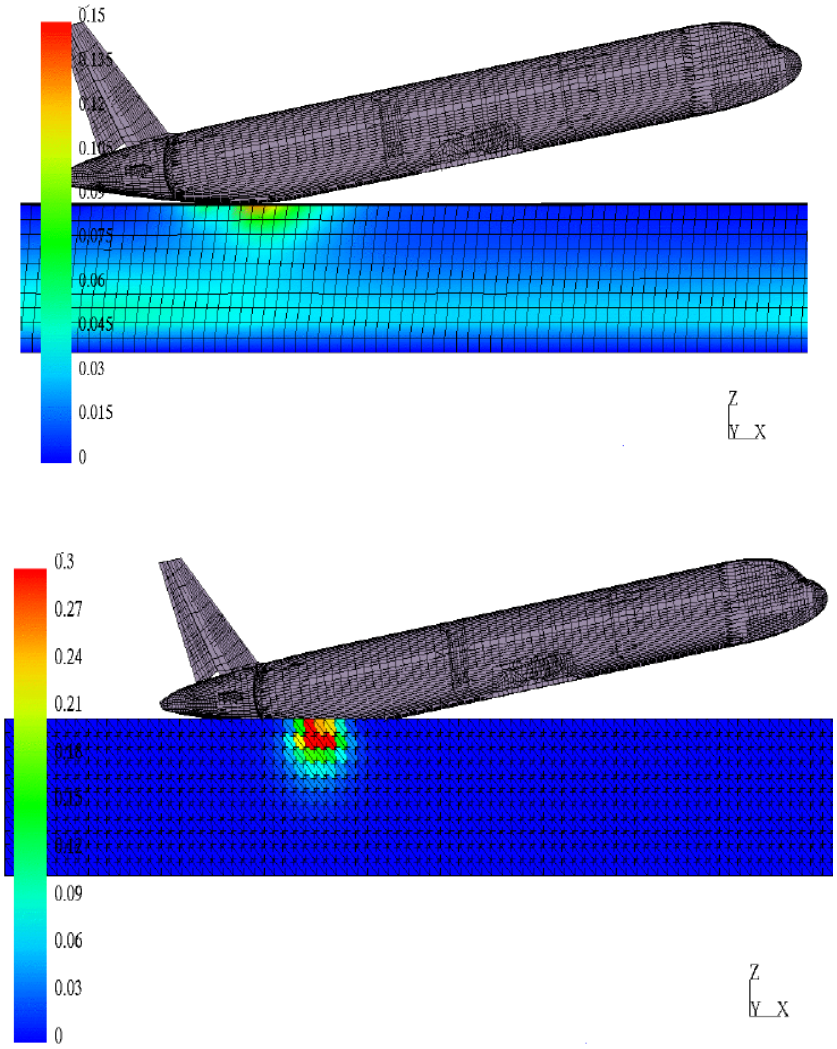

Figure 4-1: Pressure distribution (in MPa) upon impact of an Airbus A321 model. Top figure water model with two-phase ALE method and bottom figure water model with SPH method. Figure based on Ortiz et al. [45].

When a body impacts the water with a forward velocity component present, there is a possibility that low pressure areas will develop in that region of the fluid. This will allow the surrounding air to be sucked between the fluid and the structure, leading to the ventilation of the low-pressure regions. This, in turn, will lead to an increase of the pressure to atmospheric levels [51].

Judge et al. [22] performed a series of tests in order to investigate the flow separation and subsequent ventilation that can occur, when simple wedge shaped structures are impacting the water with forward velocity. It was found that the geometry and velocity of the structure affects the degree of ventilation. For the case of small dead-rise angles

for wedge impact, the horizontal velocity needs to be considerably higher than the vertical one for ventilation to take place. Moreover, the angle of impact relative to the free surface of the liquid is also influential. The effect of air, due to ventilation, becomes more important for higher angles, while maintaining a constant ratio of forward and vertical velocity. Figure 4-2 shows the effect of ventilation on the trailing edge of a wedge penetrating the water with forward velocity. The separation of the flow at the trailing edge allows the air to be sucked in and alter the pressure distribution.

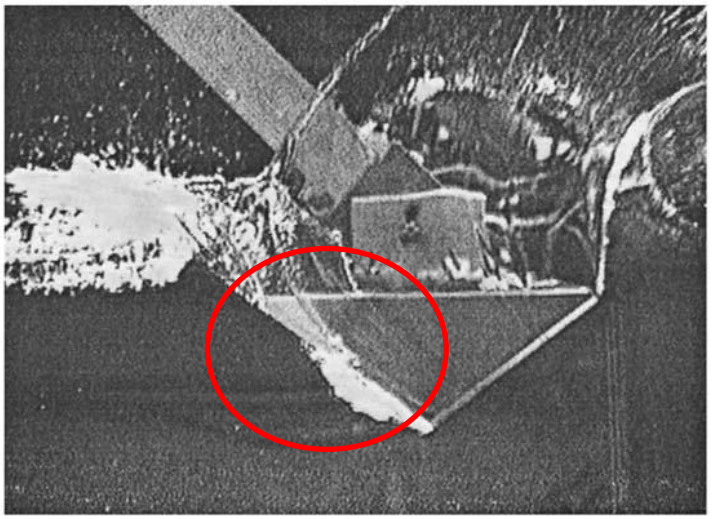

Figure 4-2: Ventilation at the trailing edge of a wedge upon impact with an impact angle of 0°. Impact direction from left to right. Figure reproduced from Judge et al. [22].

With respect to aircraft impacts, ditching scale model tests indicate that air is sucked under the wetted fuselage from the sides and the rear causing ventilation [10]. Initially, as the aircraft touches down with the aft section the pressure can drop below atmospheric, thus allowing air to be sucked under and fill the cavity that has formed. As the event progresses, the middle and forward sections of the fuselage come into contact with the water. As a result, areas at the front and the sides of the fuselage can also experience a low enough pressure that will allow air to be drawn inwards from the sides and also to be transported from the front section. Figure 4-3 shows the possible areas where the effects of air can be experienced.

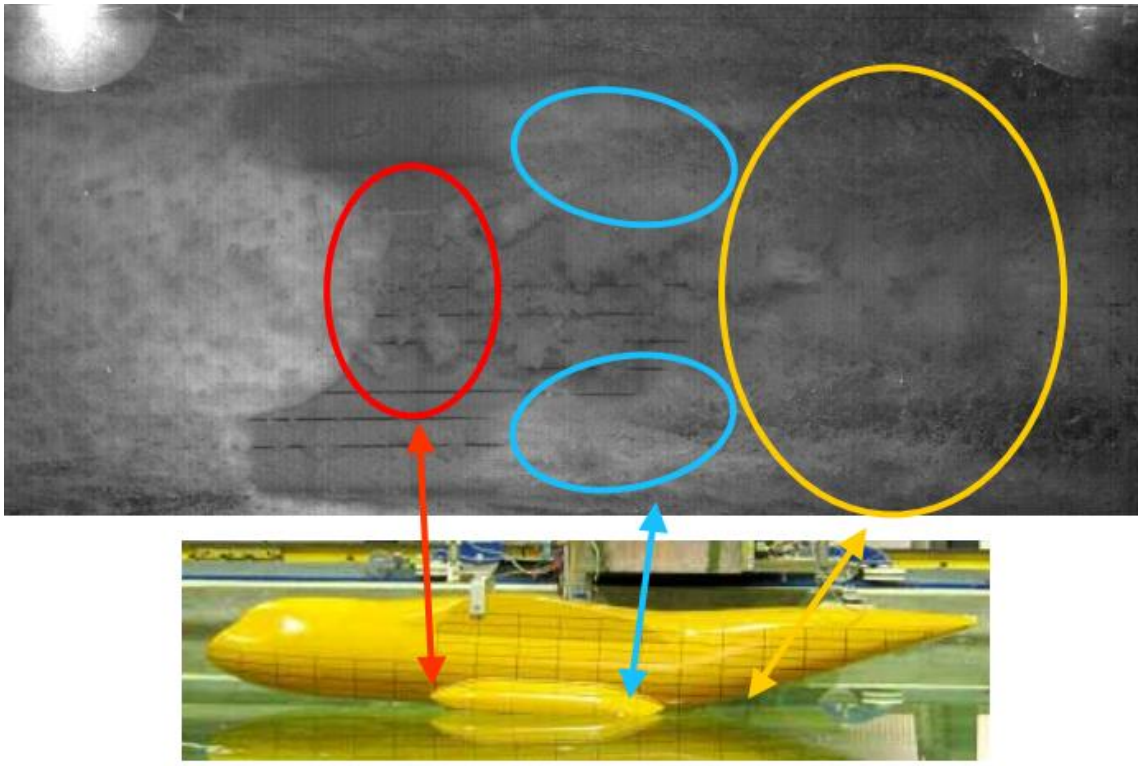

Figure 4-3: Areas where ventilation can take place. Top figure shows the bottom view of the scale model. Red area (forward section of the fuselage) shows the air being transported towards the low-pressure areas that the aircraft experienced towards the aft section. The blue and yellow section in the top figure also indicate areas of low pressure that the air can be sucked in. Figure based on Busch et al. [10].

4.2 Suction

Suction forces can influence both the local and global dynamics of an aircraft when ditching. During the impact phase of an aircraft, a low-pressure area under the rear of the fuselage can develop, allowing for the formation of a suction force, which acts as a downwards force that pulls the fuselage skin further into water [8].

As was described in Chapter 2, experimental research has shown that the shape of the rear of the fuselage can affect the global behaviour of the aircraft, due to the presence of these suction forces. For a general shaped aircraft, the flow phenomena that occur during a ditching event are shown in Figure 4-4.

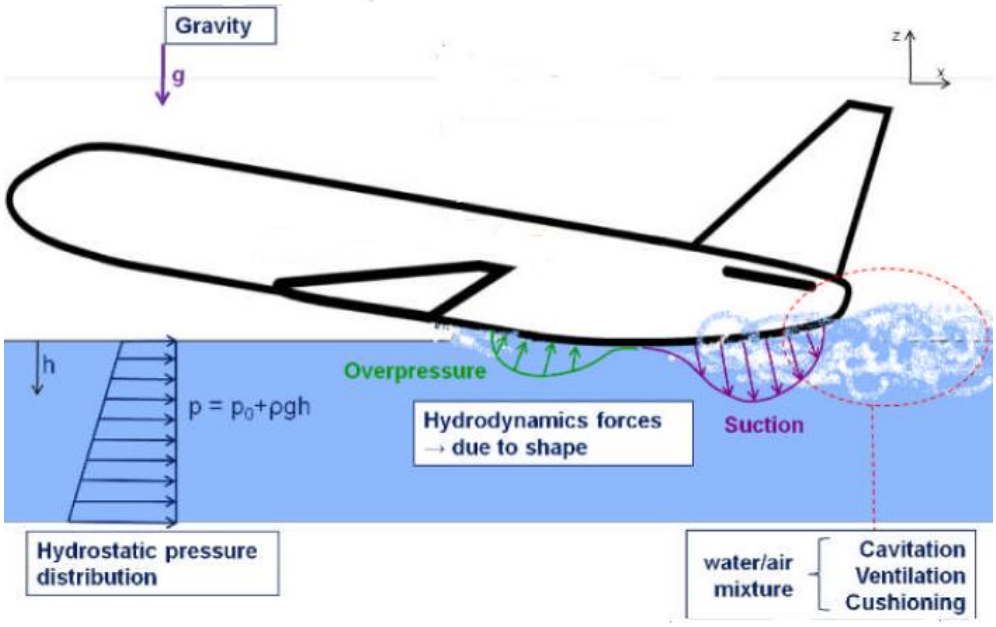

Figure 4-4: Water flow phenomena including cavitation, ventilation and suction during the impact phase of a ditching event. Figure reproduced from Siemann et al. [21].

Looking into the aft part of the fuselage, there is the potential for a force to develop that can submerge the rear part even more than in a usual water impact. This immersion can cause extended local deformations on the rear section of the fuselage.

The suction of the fuselage will eventually lead to a reduced velocity and a subsequent wing stall, leading to a change in the global behaviour of the aircraft. Figure 4-5 shows the overpressure that can occur close to the centre of the fuselage (green), which can lead to a pitching down moment. The suction force is located further behind (purple), leading to a strong pitching up moment [21].

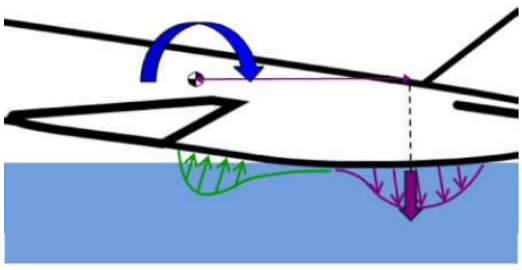

Figure 4-5: Moment caused by suction forces (purple pressure distribution) leading to the pitching up motion of the fuselage. Figure reproduced from Siemann et al. [21].

Following the wing stalling and during the landing phase, global deformations can occur with particular focus on the forward section of the aircraft. This is due to the fact that the aircraft will experience a pitching down moment after the stalling, with potential deep diving of the nose. The diving can cause severe damage to the forward section, increasing the risk of skin rupturing. It has been found that fuselages with upwards-curved rear sections are the most susceptible to experience suction [4].

Allen [23] performed experiments on a generic aircraft with an upswept aft section thus providing a good example of the expected flow behaviour around the fuselage. The structure was guided in the water, so its dynamics could not show any change in attitude.

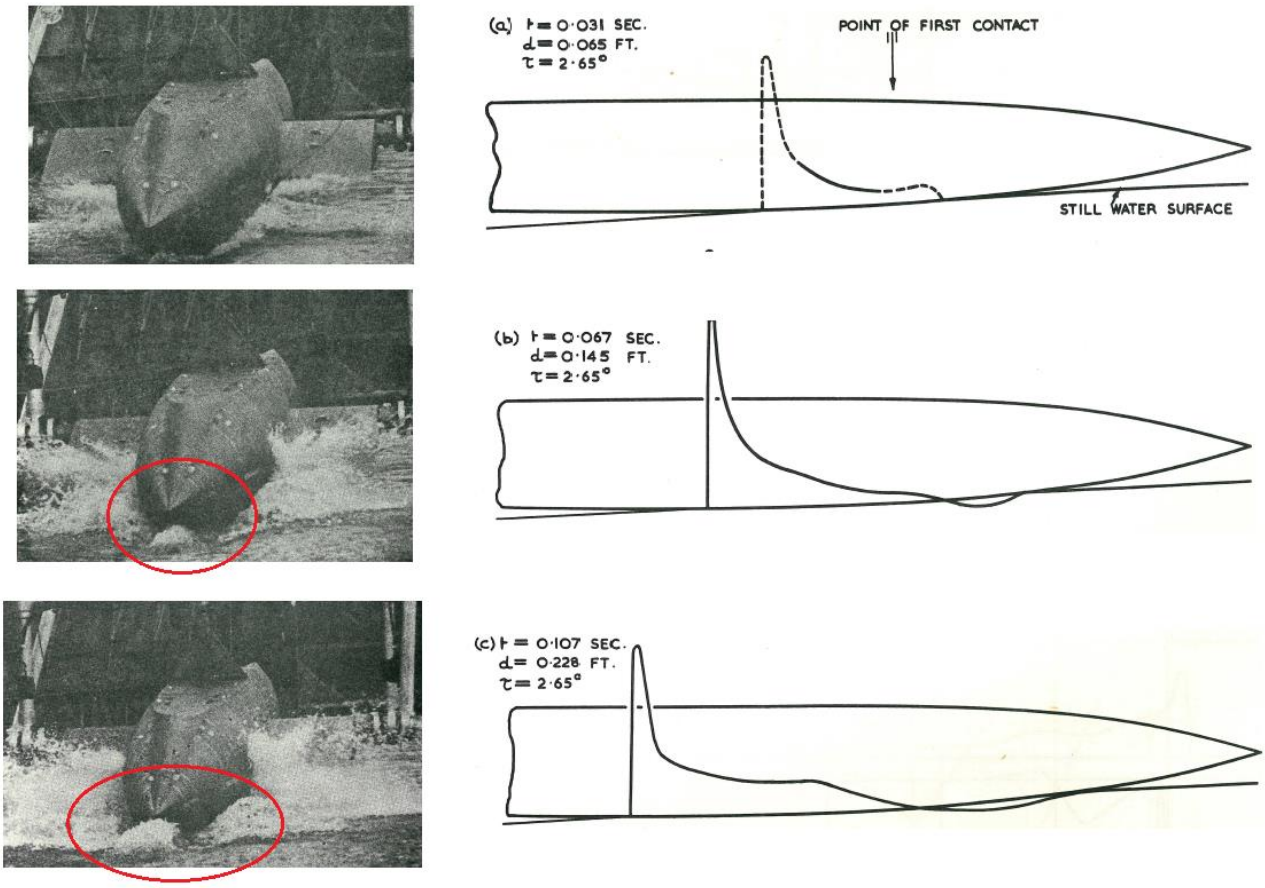

Figure 4-6: Ditching sequence of generic aircraft with upswept aft fuselage and corresponding pressure distribution along the fuselage. Pressure distribution graphs (LHS of the figure) are taken with respect to the water surface. Figure based on Allen [23].

From Figure 4-6 it is evident that, as the ditching progresses the water at the rear of the fuselage, highlighted with the red circle, fails to detach from the structure. Looking at the pressure distribution, this corresponds to the negative pressures indicated by the relative dip of the curve.

Numerical investigations [21] have shown the importance of modelling suction when dealing with ditching. Figure 4-8 shows the results of two full aircraft ditching simulations. In both cases, the fuselage models are rigid and so the interest is in the global behaviour of the structure. For both cases, the water model is a combination of finite elements and SPH particles, similar to the numerical attempts discussed in Chapter 3. For suction to be modelled naturally, it would be essential to have a large section of air with an initial atmospheric pressure covering the simulation domain, however this is not straightforward in the case of the SPH approach, since the large density variations in the interface would lead to numerical instabilities. Instead, suction in the simulations of Figure 4-7 and Figure 4-8 was modelled with a modified contact algorithm that allows the structure and the water to remain in contact, if the penalty force is less than a specified value.

The numerical attempts showed that ditching simulations without suction produce a run that is characterised by a steady decline of the pitch attitude. On the other hand, the inclusion of suction captured the pitching up moment of the aircraft and provided improved attitude profiles, when compared to experiments.

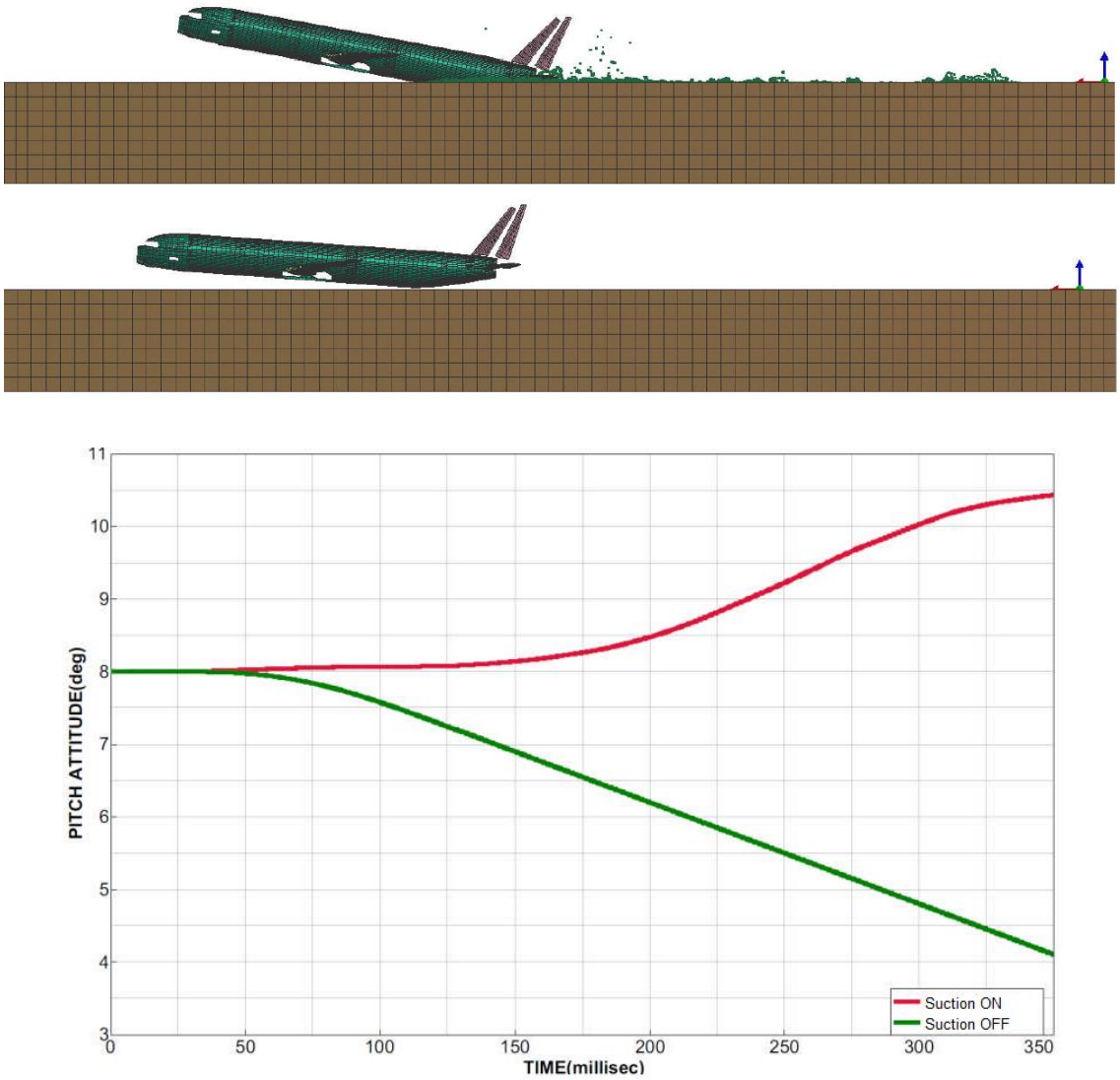

Figure 4-7: Numerical results for an Airbus A321 with (top) and without (bottom) suction modelling using the commercial software PAM-CRASH. With suction modelling active, the fuselage of both models pitches up as expected. Figure reproduced from Siemann et al. [21].

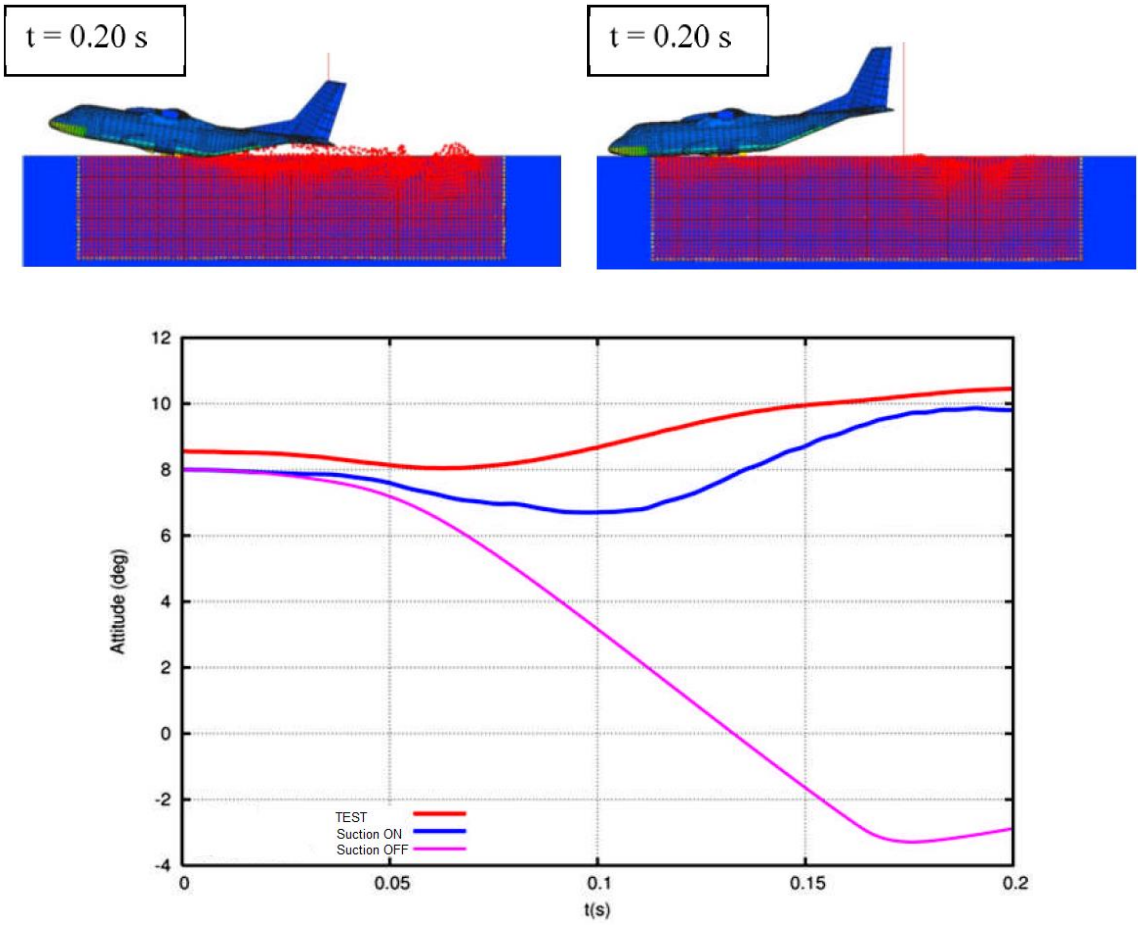

Figure 4-8: Numerical results for an Airbus Military CN235 with (left) and without (right) suction modelling using the commercial software PAM-CRASH. With suction modelling active, the fuselage of both models pitches up as expected. Figure reproduced from Siemann et al. [21].

4.3 Cavitation

Cavitation is described as the formation of bubbles in a fluid as a result of a phase change of the fluid from liquid to vapour [57]. Cavitation can alter the pressure and force distribution between the structure and the flow. This is due to the discontinuity that appears in the fluid, as cavitation takes place [58]. The onset of cavitation occurs when the liquid pressure drops below its vapour pressure, while maintaining a constant temperature and the collapse of cavitation occurs when the cavitating fluid reaches an area of high pressure [59]. Cavitation is not easy to assess through experimental investigation of model aircraft, due to scaling consideration discussed in Section 4.3.6.1. Hence, the more accurate representation of this phenomenon can improve the overall assessment of aircraft ditching loading with respect to the numerical analyses,

which are currently considered to complement the experimental tests, such as in [42]. Figure 4-9 shows the difference between cavitation and a similar phenomenon, boiling.

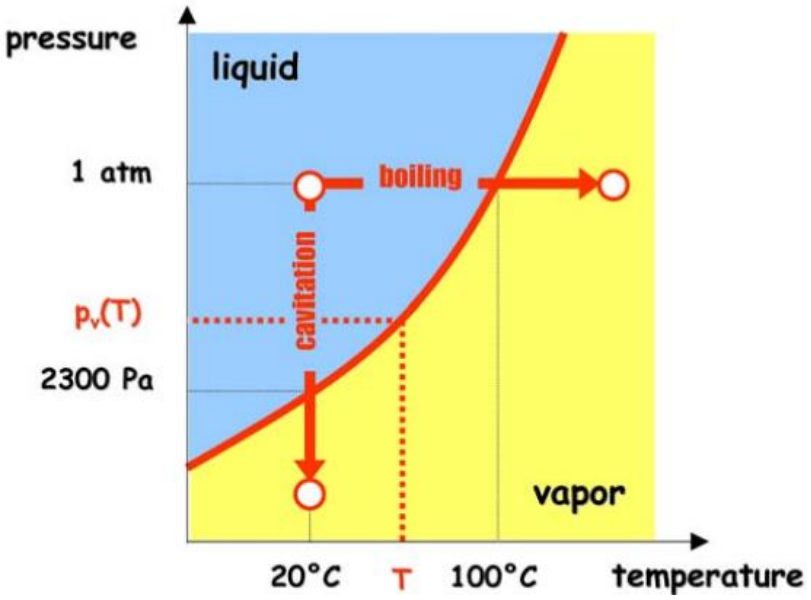

Figure 4-9: Pressure vs temperature for onset of cavitation. Figure reproduced from Franc [59].

4.3.1 Types of Cavitation

Cavitation can be classified based on the method by which it is initiated [57]. Hydrodynamic cavitation is the result of pressure changes in a liquid. This can be the result of a sharp interface or a rarefaction wave. When dealing with high velocity impacts there will be two pressure waves at impact. The first is the compression wave and behind it is a rarefaction wave, which can have low enough pressure to induce cavitation [60] [61]. Next, acoustic cavitation can develop through sound waves in the flow that alter the pressure. More specialised methods of cavitation include optic cavitation, which occurs when high intensity photons break down the cohesion of the liquid and particle cavitation, where a particle causes liquid instability and loss of liquid cohesion. In this project, the focus is on hydrodynamic cavitation and the “rupture” of the fluid under certain conditions.

Hydrodynamic cavitation can be found in the form of travelling nuclei (voids) of almost spherical shape, which initially are microscopic in size and can be found in a volume of liquid. Once these nuclei reach a low-pressure area, they expand and become large cavitating bubbles. These cavitating bubbles are called transient since their duration is very small. Next, there is the attached or fixed cavitation, which is a more stable

phenomenon and occurs when there is separation of flow such as in the cases of flow over a hydrofoil or a step. A cavity is formed at the boundary between the flow and the object. Moreover, transient cavitating bubbles form around this cavity. The steady-state nature of the attached cavitation can best be described by a cyclical behaviour. For example, the flow over a hydrofoil will lead to a cavitation region over the leading edge, followed by the collapse of the cavitation region at the trailing edge and the appearance of a jet that travels towards the leading edge and causes the cavitation region to partly shed away. This process continues to occur for as long as the flow and the structure remain under the same conditions [57] [58] [59] [62]. The main effects of this type of cavitation, usually found on hydrofoils, are the loss of lift and increase of drag. This is out of the scope of this project.

Finally, vortex cavitation is the creation of cavitation due to the variation in pressure between the pressure and suction sides of an object. This is usually found in propellers [59] [58]. Figure 4-10 shows these three main types of hydrodynamic cavitation.

Figure 4-10: Travelling, attached and vortex cavitation (left to right). Figure based on Franc [59].

The majority of interest, as it will be discussed later on, in hydrodynamic cavitation lies in two main areas. The first one is related to the effects that attached cavitation has on streamlined bodies. Specifically, cavitation is known to increase the drag and reduce the lift on hydrofoil surface [63]. An additional area of interest is in the damage that cavitation can cause during collapse. This is a particular problem in propeller induced cavitation, where severe material degradation can occur due to cavitation bubble collapse on the suction (low pressure) surface of the propellers. In high velocity impact phenomena, such as in the case of aircraft ditching, transient cavitation is known to take place. Material erosion and hydrodynamic performance is out of the scope of this

project. Instead, an accurate description of the pressure distribution and structural loading is necessary to capture the phenomenon of aircraft ditching.

4.3.2 Nucleation

For the onset of cavitation it is thought that there are microscopic voids in the liquid. These voids are also called nuclei and they can be described as the “weak points” of the liquid. These nuclei can be found in an arbitrary distribution within a certain volume of liquid. These nuclei can contain vapour or gas or a mixture of both [64]. The term “weak points” refers to the fact that cavitation inception starts from these nuclei, once the pressure in that area of the liquid drops to critical value. The existence of these nuclei can occur in two ways. These are called homogeneous and heterogeneous nucleation [62]:

- Homogeneous nucleation occurs when thermal motions in a liquid give rise to void formation, which are the “weak points” of the liquid.
- Heterogeneous nucleation takes place when there are gas micro nuclei trapped in areas of a solid boundary or due to the existence of suspending nuclei.

The amount of nuclei present in water has been investigated, however precise data are hard to record, mainly due to the non-repeatability of the experiments, as well as the fact that the liquid conditions, such as the standing time of the water, can affect the results. Moreover, in water volumes that have not been degassed or decontaminated, cavitation can occur due to contaminant nuclei destabilisation, rather than gas and/or vapour nuclei destabilisation [62]. The importance of the nuclei population is the fact that their response varies depending on their initial size, as well as the overall population within a water volume. Relatively large nuclei grow smoothly, while smaller nuclei experience a more violent change in size [64]. This behaviour can alter the flow dynamics and consequently the structural loading. The nuclei population is usually given as a radius distribution function *dN(r)*, defined as a function n(r), such that the number of nuclei present in a cubic metre of water with a radius in the range of [r, r+dr], is given by [65]:

$$dN(r) = n(r)dr\,, \tag{4-1}$$

where $n(r) = \frac{B}{r^4}$.

In the above equation *r* is the radius of the nuclei, *dr* is the increase in the radius range and B is an experimental parameter which is dependent on the type of water. This parameter is an estimate of the number of nuclei with the specified radius.

Figure 4-11 shows a typical distribution function based on various water conditions and the scatter depending on whether the measurements were performed in a laboratory environment or at sea.

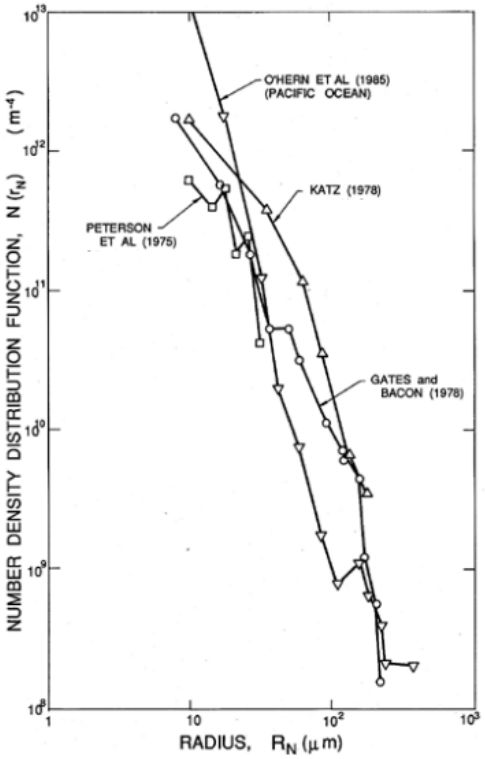

Figure 4-11: Nuclei radius distribution function. Figure reproduced from Brennen [62].

Even though the population of nuclei can vary between different water volumes, there is a general trend when considering the size of the nuclei. The population of nuclei decreases as their size increases. Figure 4-12 shows the number of nuclei/cm^3 as a function of diameter for three methods of nuclei population measurements.

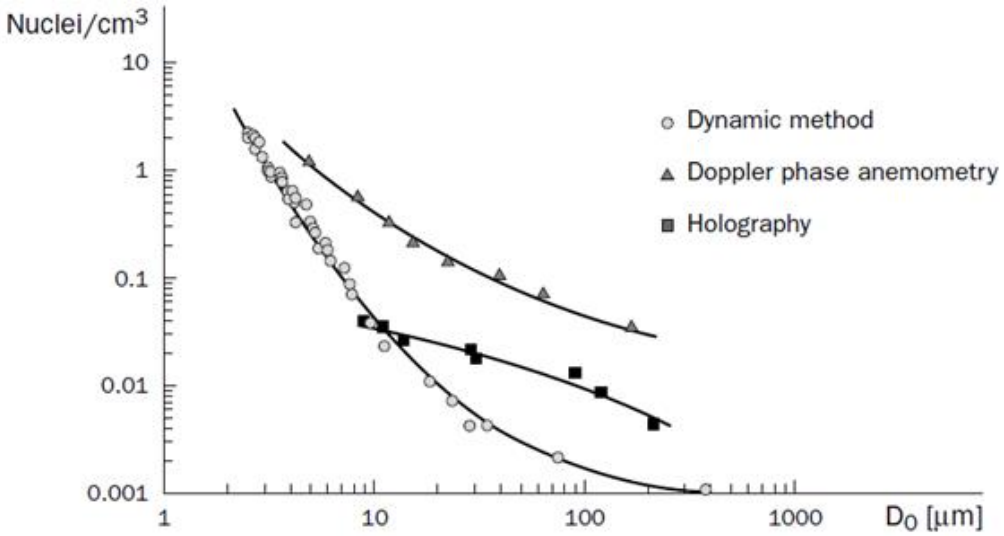

Figure 4-12: Typical distribution of nuclei population for three different measurement methods. Figure reproduced from Franc et al. [64].

The above measurements are valid for the specific set of conditions, such as contamination, standing time and salinity of the body of fluid, that the water was tested and does not provide any guide as to the nuclei contents used in the next chapter.

4.3.3 Liquid Tensile Strength

So far it has been established that cavitation occurs when the liquid pressure drops to or below the vapour pressure of the liquid. For most engineering purposes the onset of cavitation occurs when:

$$P = P_v \, . \qquad \textbf{(4-2)}$$

In the case of water however, the cohesive forces are strong due to surface tension [66]. Figure 4-13 shows that, in some cases, the fluid can withstand negative pressures (metastable condition), which prevent the fluid from changing phase, even at pressures lower than the vapour pressure. The difference between the pressure, at which the fluid actually cavitates and the vapour pressure is called static delay [64] [67].

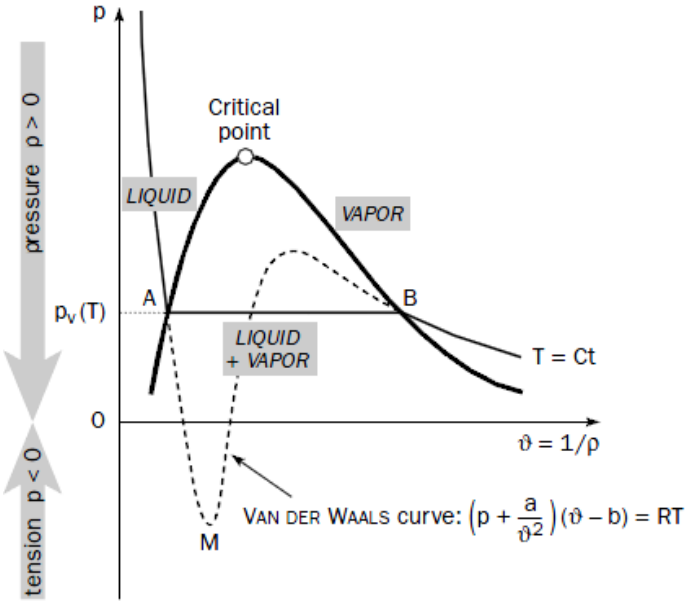

Figure 4-13: Andrew Isotherms. Figure reproduced from Franc et al. [64].

Investigating Figure 4-13, it is evident that for certain paths the pressure can even reach negative absolute values (point M). Experimental work has shown that water can reach high tensions (negative absolute pressures) in the region of 50-200 bar. However, these results took place in carefully controlled environments which are rarely encountered in typical fluid-structure interactions. These pressures are not encountered in the applications relevant to this thesis. For more details on these experiments the reader is directed to the work of Sedgewick et al. [68] and Trevena [69].

The difference between the vapour pressure and the lowest pressure that the fluid can sustain prior to cavitation is called the ultimate tensile strength [68]. This term was derived because of the effect that surface tension has on delaying the inception of cavitation, especially in the case of water.

Assuming that the liquid is populated with spherical nuclei (necessary for hydrodynamic cavitation) then its tensile strength, otherwise known as the Young-Laplace equation, is related to the surface tension and the nuclei radius. For purely vaporous nuclei the tensile strength is [62]:

$$\Delta P = \frac{2S}{R}, \tag{4-3}$$

where S is the surface tension and R is the nuclei radius.

In the case of a fluid with nuclei containing a mixture of vapour and gas then the tensile strength is given as:

$$\Delta P = \frac{4S}{3R}. \quad \textbf{(4-4)}$$

The presence of gas is considered to be an impurity in the fluid domain. Experimental data have shown that the presence of gas (air) led to significantly lower tensile strength of the liquid and that the reduction in the presence of gas can lead to a lower critical pressure for cavitation inception, as a consequence of the higher tensile strength of the liquid. This relates to the static delay, described previously. The purer the water, the lower the pressure can drop before the onset of cavitation. The existence of gas also represents a rupture in the continuity of the liquid and thus a “weak spot” for cavitation to occur. This is more pronounced with undissolved gas being present in water [58]. The above equation is given for completeness. In this project, it is assumed that the presence of gas is neglected. The emphasis is on transient cavitation characterised by liquid vaporisation. The short life time of these transient nuclei, along with the generally small amount of gas present in them, allows for the gas content to be neglected.

The surface tension of water at ambient conditions is approximately 0.073 N/m. Assuming an initial nuclei radius of 50 μm then the tensile strength of a purely vaporous bubble is 2880 Pa.

4.3.4 Cavitation Growth and Collapse

Cavitation growth can be described in three steps, all occurring very rapidly. First, there is the breakdown of the liquid and the increase in the size of the nuclei into larger cavitation bubbles. Next, these bubbles are filled with vapour. Finally, almost instantaneously with the second step, the bubbles are saturated with vapour.

Initially, the cavitation nuclei are assumed spherical due to surface tension and their dimension varies between a few micrometres and a few hundred micrometres. It is assumed that, at microscopic level, the nuclei are in equilibrium with the surrounding liquid, as shown in Figure 4-14, satisfying the following equation [64]:

$$p_v + p_g - \frac{2S}{R} = p_\infty , \quad \textbf{(4-5)}$$

where p_v is the vapour pressure, p_g is the gas pressure, p_∞ is the pressure in the liquid at infinity, *S* is the surface tension and R is the nuclei radius.

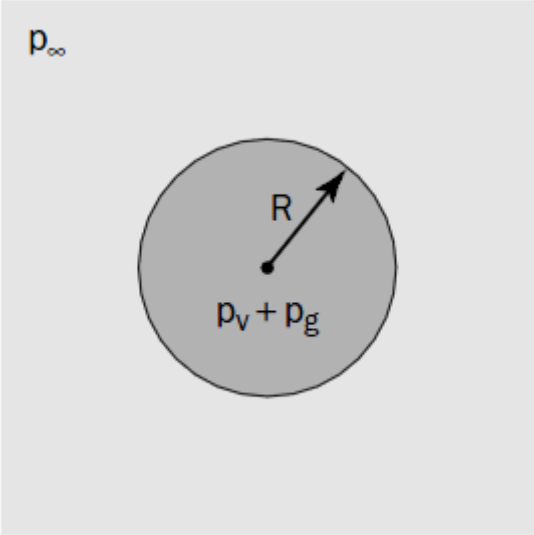

Figure 4-14: Nucleus in fluid. Figure reproduced from Franc et al. [64].

As the surrounding pressure decreases, the initially microscopic nuclei begin to increase in size in a stable manner without cavitation. As discussed above the pressure can only drop as low as the vapour pressure and tensile strength will allow it to.

Consider a spherical vaporous bubble with radius R, an internal pressure p_v and an external pressure p_∞. The surface tension acts inwards, trying to reduce the size of the drop. For the bubble to increase in size, as is expected during cavitation, the external pressure must reach a critical value, p_c, so that the pressure difference, $p_v - p_c$, is acting outwards, trying to increase the volume of the bubble [70]. The corresponding radius of the bubble for a critical pressure is also called critical radius, R_c.

Considering a hemispherical cut of the bubble, the surface tension is [70]:

$$2\pi R_c S\,, \tag{4-6}$$

where $2\pi R_c$ is the circumference of the hemisphere. The force due to the difference in pressure, on the projected area of the hemisphere is [70]:

$$\pi R_c^2 (p_v - p_c)\,. \tag{4-7}$$

The equilibrium is given when equation (4-6) is equal to equation (4-7):

$$\pi R_c^2 (p_v - p_c) = 2\pi R_c S\,. \tag{4-8}$$

Rearranging equation (4-8), leads to the critical pressure for a purely vaporous bubble:

$$p_c = p_v - \frac{2S}{R_c}. \tag{4-9}$$

The above can also be deduced from equation (4-5) by neglecting the presence of gas.

In the case of a nucleus that contain both vapour and gas then [58]:

The velocity potential for an irrotational flow is:

$$\varphi = \frac{R^2}{r}\frac{dR}{dt}, \tag{4-10}$$

where R is the nucleus radius, *r* is the radial distance from the centre of the nucleus and *t* is time.

The radial velocity can be given, with respect to the nuclei centre, as [58]:

$$u = -\frac{\partial \varphi}{\partial r} = \frac{R^2}{r^2}\frac{dR}{dt}. \tag{4-11}$$

Neglecting gravity, the equation of motion of the liquid is given as the Bernoulli's equation of unsteady potential flow [58]:

$$-\frac{\partial \varphi}{\partial t} + \frac{u^2}{2} + \frac{p}{\rho} = F(t) = \frac{p_\infty}{\rho}, \tag{4-12}$$

where p is the local pressure in the liquid and p_∞ is the pressure in the liquid at infinity ($u = 0$ and $\varphi = 0$).

At the nuclei wall the equation of motion (4-12) leads to (for *r* = *R*) [58]:

$$-R\frac{\partial U}{\partial t} - \frac{3U^2}{2} = \frac{p_\infty - P}{\rho}, \tag{4-13}$$

where *P* is the pressure of the liquid at the nuclei wall.

The equilibrium for nuclei possessing both gas and vapour is given as [58]:

$$p_v + \frac{NT}{R^3} - \frac{2S}{R} = P, \tag{4-14}$$

where p_v is the vapour pressure, N is constant for fixed mass of a specific gas, T is the temperature, P is the pressure at the bubble wall and *S* is the surface tension.

The above equation is similar to the generalised equilibrium equation given in (4-5).

Substituting equation (4-14) into (4-13):

$$\rho\left(R\frac{\partial U}{\partial t}+\frac{3U^2}{2}\right)=-\left(p_\infty-p_v+\frac{2S}{R}-\frac{NT}{R^3}\right)=f(R,T)\,, \tag{4-15}$$

where, $f(R,T)$ is the force required for change in the nuclei radius. A positive value indicates growth and a negative value indicates collapse of cavitating nuclei. For equilibrium, and radius $R=R_c$, equation (4-15) becomes [58]:

$$\left[-\left(p_\infty-p_v+\frac{2S}{R}-\frac{NT}{R^3}\right)\right]_{R=R_c}=f(R,T)=0\,. \tag{4-16}$$

Assuming constant temperature, *T* and constant N, the critical radius is [58]:

$$R_c=\sqrt{\frac{3NT}{2S}}=0\,. \tag{4-17}$$

Equation (4-17) is based on the stability conditions of the equilibrium of a bubble, which states that the equilibrium is stable when $\frac{df}{dR}<0$ and unstable when $\frac{df}{dR}\geq 0$. As such, the critical radius for the onset of cavitation is when $\frac{df}{dR}=0$ [58].

Using equation (4-17) in equation (4-16) and considering that the pressure at the nuclei wall is the critical pressure for cavitation to occur, leads to:

$$R_c=\frac{-4S}{3(p_c-p_v)}\,. \tag{4-18}$$

Rearranging, the critical pressure is given as [58] [62] [64]:

$$p_c=p_v-\frac{4S}{3R_c}\,. \tag{4-19}$$

Subscript c denotes the critical state of both the pressure and the radius. Once the pressure drops to p_c, the nuclei start expanding in an unstable way. At this point, the fluid breaks down and cavitation takes place. The most important parameter in equation (4-9) and (4-19) is the critical radius. Any nuclei with size above that critical radius will expand explosively into a cavitating bubble.

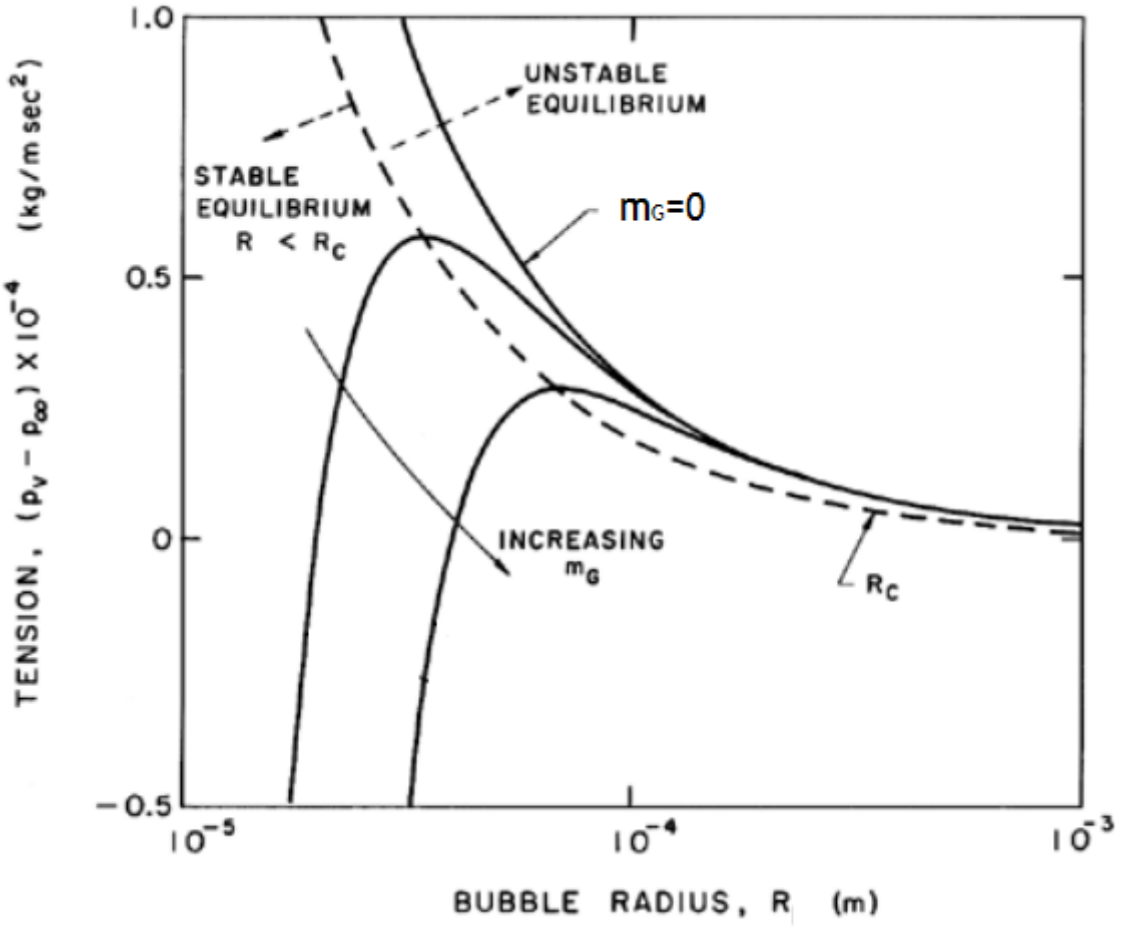

Figure 4-15: Liquid tension vs radius for nuclei containing both gas and vapour for various gas contents at constant temperatures. Curves are based on bubble equilibrium equation (4-16) [58]. The locus of the peaks, shown by the dashed line, represents the critical radius equation (4-19). Figure reproduced from Brennen [62].

The graph of Figure 4-15 shows the equilibrium conditions based on the rate of change of the equation (4-16) with respect to the radius of the nuclei, for different fixed gas contents. The radius of the nuclei increases in a stable manner, as the liquid pressure p_∞ decreases, until it reaches the locus of curves, which represents the critical radius. As the liquid pressure decreases, the nuclei (with fixed gas content) increase in size until they reach the particular critical pressure, at the maximum of the curve. Until this point the nuclei are under stable conditions, passing through a number of equilibrium states. Once the liquid pressure drops below the value corresponding to the maximum of the curve, cavitation will take place and the nuclei will increase into cavitating bubbles. The locus of the different curves represents equation (4-19) [62].

Figure 4-16 shows the generalised graph of the stable and unstable conditions for bubble growth with respect to critical radius and pressure for equation (4-19).

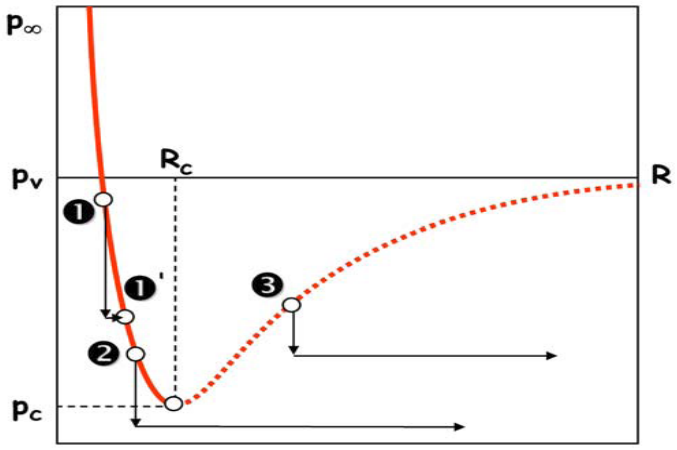

Figure 4-16: Generalised equilibrium curve for nuclei containing both vapour and gas. Curve represents equation (4-19). Liquid pressure vs critical radius. Figure reproduced from Franc [59].

At point 1, the nucleus has an initial radius less than the critical one. If the pressure drops but remains above the critical pressure, then the nucleus will increase in size but it will remain in equilibrium. At point 2, the pressure has decreased further but is still higher than the critical pressure. As a result, the nucleus increases in size further, maintaining equilibrium with the surrounding liquid. If the pressure is lowered to the critical pressure, then the microscopic nucleus will develop into a cavitating bubble. Finally, at point 3, the nucleus has reached a radius greater than the critical radius. This means that even a small drop in the liquid's pressure will lead to further growth of the cavitating bubble [59].

The critical radius has two main side-effects in cavitation. The first one is evident from equations (4-9) and (4-19). The smaller the critical radius of the nucleus, the higher the influence of the tensile strength and surface tension is to the critical pressure. As a result, the static delay for cavitation will be prolonged [64].

For an initial radius of 5 μm and surface tension of S= 0.073 kg/s^2 the critical tension is equivalent to:

$$\frac{4S}{3R_c} = 19466.667 \text{ Pa.}$$

Using the Antoine equation (see Chapter 6) for room temperature, the saturated vapour pressure is close to:

$$p_v = 3166 \text{ Pa}.$$

Using equation (4-19) the critical pressure is:

$$p_c = -16300.667\ Pa = 85024.333\ \text{Pa}_{\text{abs}}.$$

For an initial radius of 30 μm the critical tension is:

$$\frac{4S}{3R_c} = 3244.444\ \text{Pa}.$$

This gives a critical pressure of:

$$p_c = -78.444\ Pa = 101246.556\ \text{Pa}_{\text{abs}}.$$

The example above shows the effect of the critical radius of the nuclei on the critical pressure. It shows that, for small enough initial radii of the microscopic nuclei, the pressure can drop considerably, before the onset of cavitation, due to the effect of the tensile strength of the liquid.

The second effect is related to the extent and severity of the cavitation. If the critical radius is small then there are more nuclei that will explode into cavitating bubbles, thus affecting the flow dynamics [62]. This is based on Figure 4-12, which shows that for a specified volume of liquid, it is more likely to have a larger number of small nuclei. This means that there are more "weak points" in the fluid that will expand into cavitating bubbles as the pressure drops.

In most practical cases the initial size of the nuclei varies, which means that the "weakest point" of the liquid is usually taken as the largest nucleus present in the area of the fluid that will experience cavitation. Since the largest nucleus is considered as the critical radius, the effects of the tensile strength of the liquid are usually neglected and the assumption that the critical pressure is the same as the vapour pressure is used [64]. For most numerical cases however, it is always assumed that the size of the nuclei is the same throughout the water domain at the start of the simulation [71].

Once the fluid reaches an area with a pressure higher than the critical one, the nuclei that have developed into cavitation bubbles start to collapse in a violent manner. As the cavitating bubbles reduce in size there are complex phenomena that take place,

including very high implosion velocities. For a purely vaporous cavitation bubble compressibility is considered to be of less significance during the initial stages, due to the low velocities that the bubble experiences. During collapse however, the vapour in the bubble will act as a gas because there is not sufficient time for condensation to occur. This will affect the inward collapse velocity of the bubble, as well as its pressure. This means that the compressible nature of the flow should be considered [59] [64] [58].

Typically, the initial collapse is followed by rebounds and subsequent collapses. In the case of a non-viscous flow these rebounds do not attenuate but can keep appearing indefinitely as it is shown in Figure 4-17 [62].

Finally, another difference between growth and collapse is the spherical nature of the cavitating bubbles. Usually for cavitation growth, the nuclei are considered spherical. However, as cavitation collapse progresses, the spherical nature of the cavitating bubbles is no longer valid [72].

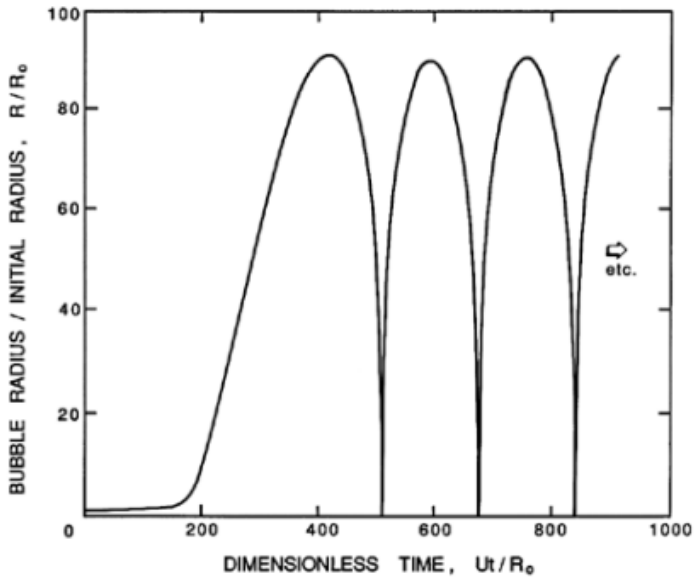

Figure 4-17: Spherical cavitation bubble behaviour (based on the Rayleigh – Plesset method) in the absence of any viscous effects [U is the growth/collapse velocity of the bubble, R and R_0 are the bubble's current and initial size and t is time]. Figure reproduced from Brennen [62].

The importance of cavitation collapse is related to possible material erosion caused by high pressures and velocities. Vaporous cavitating bubbles exhibit a fragmentation

behaviour as their size reduces to orders smaller than their maximum [62]. As the bubbles collapse a jet appears through them leading to fragmentation.

Given the presence of a solid boundary near the fluid, there would be a difference in the inward acceleration of the bubbles present in the cavitating fluid. This would cause one side of the bubbles to collapse faster than the other leading to the appearance of this jet with a direction towards the solid boundary.

Cavitation damage is significant in structures that experience repeated cavitation collapse, such as ship propellers. The severe pressures close to the boundary lead to surface fatigue, as shown in Figure 4-18. Moreover, for softer materials, such as aluminium, cavitation collapse can lead to pitting of the surface, which is directly linked to the formation of the jet discussed above.

Figure 4-18: Material erosion on ship propellers caused by vortex cavitation collapse. Figure reproduced from Senocak [73].

The above is a brief description of the effects of cavitation collapse. In this project, the focus is on the effects of cavitating bubbles during the ditching of an aircraft, which does not experience repeated cavitation collapse exposure and so it is not necessary to investigate any potential material damage caused by it.

4.3.5 Mixture Properties

The phenomenon of cavitation is a problem that involves a mixture of liquid, vapour and gas. Generally, the amount of gas present in water is small so the focus here is on a liquid-vapour mixture.

The introduction of vapour into the liquid will alter both its density and its speed of sound. Initially, the density of water is considered to be $\rho_l = 1000\,\mathrm{kg/m^3}$ and the density of vapour is $\rho_v = 0.023\,\mathrm{kg/m^3}$. The ratio of the liquid density to that of the vapour is larger than 40,000 [74]. As cavitation progresses and the vapour inside the cavitating bubbles increases, there is a severe reduction in the mixture density [75]. Figure 4-19 shows the changes that the flow is undergoing with respect to its density. As separate entities both water and vapour are considered incompressible for low velocities. However, the mixture is compressible when the pressure is close to the saturated vapour pressure [76].

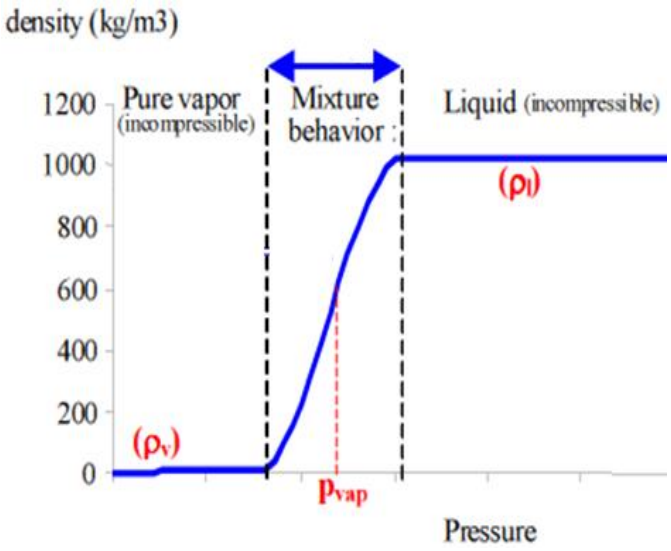

Figure 4-19: Variations in liquid and mixture density [77].

The second property that changes due to the presence of the vapour is the speed of sound. The speed of sound of the water in liquid form is $c_l = 1482.9\,\mathrm{m/s}$. Generally, it is acceptable to use the speed of sound of an ideal gas so $c_v = 340.26\,\mathrm{m/s}$ for the vapour part. The result of the phase change is that the speed of sound of the mixture can be lower than either of the individual components [78].

4.3.6 Cavitation Parameter

Cavitation parameter is a flow similarity number that can provide a quantitative comparison of cavitation, which is particularly helpful but not limited to the attached cavitation cases. Considering a flow over a structure would lead to a pressure difference between a point close to the body and a point further away in the flow. This

difference is proportional to the dynamic pressure and is given as the negative of the pressure coefficient [58]:

$$-C_p = \frac{P_0 - P}{0.5\rho v_0^2}, \tag{4-20}$$

where P_0 is the pressure of the fluid, P is the pressure at a point close to the structure, ρ is the density of the fluid and v_o is the velocity of the flow with respect to the structure.

The cavitation parameter is equal to equation (4-20) and cavitation inception occurs when $P = P_c$ and is given as:

$$\sigma_c = \frac{P_c - P_v}{0.5\rho v_0^2}. \tag{4-21}$$

If the surrounding pressure is high enough, then there will not be any cavitation inception but as the pressure reduces to P_c the extent of cavitation increases. It should be noted that the above parameter is a relatively crude approach for obtaining cavitation flow similarity, since it is assumed that the fluid cannot sustain any tensions unlike the theory described previously [62].

4.3.6.1 Scale Models

When dealing with scale modelling of a structure, its Reynolds number will be different from the full scale structure, unless the velocity is altered in order to match the Reynolds number of the full scale and model structure. By changing the velocity, the cavitation number will change [62]. This simple explanation is the reason why scale model tests fail to capture cavitation.

4.3.7 Cavitation Numerical Modelling

There have been numerous attempts to model cavitating flows in the past. In what follows is a description of the most common approaches along with their limitation. The applications that these methods are used in, are also described.

4.3.7.1 Interface Tracking Method

The interface tracking method provides a clear distinction between the vapour and liquid part of the flow. It is most commonly used in order to simulate stable cavitation

occurrences, such as attached cavitation, because in those types of cavitation there is a clearly defined closed area of pure vapour or gas [79] [80] [75]. The limitation in its applicability to transient cavities is due to the fact that, even though it can track two distinct interfaces as they interact with each other, it does not allow for the creation of new interfaces [81].

4.3.7.2 Homogeneous Method

The most common approach in the literature involves homogeneous or continuum models. The major difference to the interface approach is that there is no interest to track the cavitating bubbles, but instead the flow is treated as a mixture of vapour and liquid [75]. These models are usually employed for transient cavitation. Homogeneous models are used under the assumption that the relative velocity between the nuclei and the liquid is zero. This is commonly referred to as the slip velocity [80].

Homogeneous models can include a two-fluid or a one-fluid approach. The two-fluid model assumes that the liquid and vapour phases co-exist in the flow and every phase is governed by its own set of differential equations. This method is used to model compressible multi-phase flows, taking into account the physical details of the mixture, such as the effects of mass exchange and surface tension [75]. The problem with this approach is that it usually requires data which are difficult to know a priori.

The one-fluid approach uses one set of differential equations under the concept that the flow is treated as a mixture. The most common application of this approach relates to the definition of steady cavitation over streamlined bodies. For this method, the use of mass transfer equations between the liquid and the vapour are employed [75] [82].

The one-fluid approach is the most widely used, primarily due to its simplicity in modelling the growth and collapse of the cavitating nuclei. The cut-off and the vacuum models are the simplest one-fluid models. Both these techniques treat the flow as a pure fluid, neglecting the phase changes and any changes in the properties of the liquid. The cut-off model does not allow the liquid pressure to drop below a predefined threshold. Currently this method is used in transient FE codes, such as LS-DYNA. For simulations where cavitation is of interest, a cut-off pressure value of zero is chosen, whereas when cavitation is neglected this value is set to a very high negative value [75] [83]. The vacuum model treats the cavitation region as an area of no mass [81].

In addition to the one-fluid method, a bubble dynamics approach is usually employed in order to account for the evolution of the cavitating bubbles. This approach allows for

the consideration of bubble collapse and can be used for cavitation erosion; however, it can lead to numerical instabilities, because it cannot provide accurate enough results for high void fractions. This is due to the fact that the majority of bubble dynamics methods use the Rayleigh-Plesset equation, which does not account for interaction between bubbles [80]. The Rayleigh-Plesset equation is applicable to transient phenomena and it is possible to include the effects of surface tension and viscosity. The shortcomings of the Rayleigh-Plesset approach is the fact that it does not account for the potential non-spherical nature of the bubbles and that the mass transfer between the vapour and the liquid are not considered. This means that the accuracy of this method for steady-state cavitating phenomena, such as the attached cavitation over hydrofoils is not acceptable [84]. Table 4-1 gives an overview of some methods and their applications. The majority of the research is focused on the steady-state behaviour around axisymmetric bodies and hydrofoils.

With respect to aircraft ditching, the areas where cavitation is expected to appear is in the areas of low pressure and, as described before, these are likely to occur at the rear section of the fuselage. Accurate cavitation modelling has the effect of reducing the permissible pressures imparted on the aircraft, since the onset of the phenomenon is based on the tensile strength of the liquid. By reducing the pressures on the fuselage, the local deformations will also be reduced. If the arbitrary cut-off model is not used, the liquid pressure would drop lower than the liquid tensile strength would otherwise permit. Hence, the inclusion of a more realistic cavitation model is necessary in order to achieve more accurate loading predictions during ditching.

Table 4-1: Selected review of various methods for cavitation modelling.

Authors	Method	Applications
Huang et al. [85]	Homogeneous approach with a density model including phase exchange rates.	Steady-state cavitation for axisymmetric bodies and hydrofoils.
Kubota et al. [71]	Homogeneous approach with the Rayleigh Plesset equation and Poisson's equation.	Cloud cavitation on hydrofoils.
Zhang et al. [76]	Homogeneous approach with phase exchange method.	Steady-state axisymmetric cylinders and hydrofoils.
Xie et al. [81]	Homogeneous pressure based approach (use of barotropic equations).	Transient cavitation in pressure induced cases.
Tamura et al. [80]	Modified Rayleigh-Plesset for higher void fractions and use of convection-diffusion techniques.	Steady-state hydrofoil cavitation.
Liu et al. [86]	Homogeneous one-fluid barotropic pressure approach.	Transient cavitation in pressure induced cases and underwater explosions.
Singhal et al. [74]	Homogeneous approach with the use of phase exchange rates based on Rayleigh-Plesset equations and the use of turbulence modelling.	Steady-state in orifice and hydrofoils.
Chen et al. [87]	Barotropic model and turbulence modelling.	Steady-state in venturi and hydrofoils.

4.4 Conclusions

This chapter provided a more detailed understanding of the flow phenomena occurring during a ditching event.

The water phenomena present during fluid-structure interactions have been introduced, along with their influence on both simple structures and aircraft models. It is important in this project to identify which of these phenomena are more likely to influence the structural response of a ditching event of a fixed-wing aircraft with high forward velocity.

As far as the air cushioning in the form of a distinct cavity is concerned, it has been found to have a significant influence on the pressure and decelerations of a structure. Having said that, it must be argued that it is more profound when the contacting surface is large with small angles with respect to the water surface. Furthermore, its influence depends on the direction of the impact. For fixed-wing water landing, where the forward velocity is high, and the geometry of the structure is not as flat, it is expected that it will not play as an important role as in vertical drops of square boxes. The computational cost of introducing air particles would not provide significant benefits. However, the effect of suspended particles within the fluid should be investigated further (Chapter 7) and compared to available published results.

Suction can influence the pressure distribution and loading of an aircraft, depending on the fuselage shape, suggesting that its omission can compromise the accuracy of the simulations. Modelling of suction forces would allow for more accurate simulation of the motion of the aircraft, either through the presence of air at atmospheric pressure or by a contact definition, as described before. However, it is considered more appropriate to establish the capabilities of the current meshless method (SPH code) with respect to cavitation and also aeration; the last being a mixture approach accounting for the presence of air in the liquid which is described in Chapter 7.

With respect to cavitation the review identified the different types of cavitation that exist. Furthermore, the nucleation procedure was established and the influence of the nuclei on the flow has been defined. Next, the cavitation pressure and the concept of liquid tensile strength was briefly introduced, which shows the strong cohesive nature of water and how this can affect the cavitation pressure. The cavitation growth and collapse were discussed including the importance of the nuclei size and the significance of compressibility during the later stages of collapse. Finally, the effect of

cavitation on the density and speed of sound was discussed, showing that they can be far smaller than the individual components of the flow.

Cavitation modelling methods have also been described. It is evident that, depending on the nature (steady-state or transient) of cavitation, a different approach is employed. The majority of literature deals with steady-state occurrence of axisymmetric bodies and hydrofoils thus a mass transfer approach is preferred. However, for transient phenomena a mixture approach linking pressure to density and subsequently to void fraction is preferred. This is achieved with the use of a mixture density function accounting for vapour and liquid. Finally, the Rayleigh-Plesset bubble dynamics model has been briefly outlined. This model is used in conjunction with the mass transfer approaches. The Rayleigh-Plesset approach will be used for transient cavitation in this project and will be discussed in more detail in Chapter 6.

Next, information about the SPH code will be provided, as it is the method used for the modelling of the fluid. Moreover, an initial test case of a high forward velocity impact will be discussed, showing the current capabilities of the code.

5 The MCM Code

In this chapter, a description of the code used for the water modelling is given. Cranfield University's code implementation of the Smoothed Particle Hydrodynamics (SPH) method will be explained and an initial forward velocity example will be described. This example is the impact of an inclined plate with both forward and vertical velocity.

5.1 SPH General Description

Smooth Particle Hydrodynamics (SPH) was first developed for astrophysical problems due to the need for a meshless approach into simulations [88]. The basis of the SPH method is the use of approximations for the solution of differential equations. It is a Lagrangian method, allowing for the tracking of the properties of discreet elements as they move in time. In the Lagrangian method the grid, or mesh, is fixed on the material as it moves. In this way, the properties of each material point can easily be tracked. The main difference between the Finite Element and the SPH methods, is the fact that SPH uses particles (interpolation points) instead of mesh defined elements. Each of these particles is characterised by velocity, position, mass, stress and internal energy. Since it is a meshless approach, it allows for the simulations of highly distorted material without any of the problems of a mesh defined Lagrangian method. This is particularly important for simulating a free surface fluid under high velocity impact. SPH is based on an arbitrary distribution, the kernel approximation, of interpolation points in order to determine the particle variables [89] [90].

The SPH approach starts from the following integral representation of a function:

$$f(x) = \int_{\Omega} f(x')\delta(x - x')dx' \,, \tag{5-1}$$

where x is the position vector, Ω is the volume domain of interest and $\delta(x - x')$ is the Dirac delta function, which is given by:

$$\delta(x - x') = \begin{cases} 0 & x \neq x' \\ 1 & x = x' \,. \end{cases} \tag{5-2}$$

Next, the Dirac delta function is replaced by a kernel function denoted as $W(x-x',h)$. The interpolation points used for the kernel approximation are defined through the smoothing length h. This parameter determines the domain of particles over which the kernel is applicable [75]. Equation (5-1) then becomes [91]:

$$< f(x) >= \int_{\Omega} f(x')W(x-x',h)dx' , \quad \textbf{(5-3)}$$

where <> represents a kernel approximation.

The kernel usually satisfies the following three criteria [90]:
The kernel is normalised:

$$\int_{\Omega} W(x-x',h)dx' = 1 . \quad \textbf{(5-4)}$$

As a consequence, the kernel function is usually defined as a bell-shaped function, as shown in Figure 5-1. It should be noted that corrected functions, such as Shephard and MLS, are not normalised.

It has compact support:

$$W(x-x',h) = 0 \quad for \quad |x-x'| \geq 2h . \quad \textbf{(5-5)}$$

This suggests that the kernel approximation for a point x occurs only for a support domain of $2h$. The original implementation of SPH used a Gaussian kernel, which did not satisfy this criterion.
When the smoothing length approaches zero, the kernel reduces to the Dirac delta function:

$$\lim_{h\to 0} W(x-x',h) = \delta(x-x') . \quad \textbf{(5-6)}$$

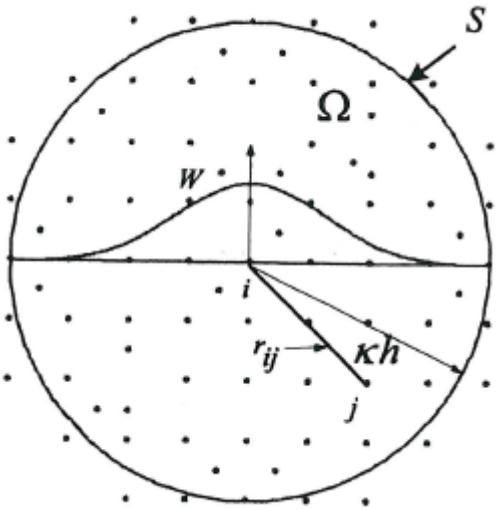

Figure 5-1: Support domain of smoothing kernel W. Figure reproduced from Liu et al. [75].

From this criterion, it follows that as the smoothing length reduces to zero the approximation of function $f(x)$ becomes equal to equation (5-1).

There is a variety of kernel functions available, the most common of which is a cubic B–spline [92]:

$$W(x-x',h) = C\begin{cases} 1-\frac{3}{2}z^2+\frac{3}{4}z^3 & if\ 0 \le z < 1 \\ \frac{(2-z)^3}{4} & if\ 1 \le z < 2 \\ 0 & otherwise\ , \end{cases} \quad \textbf{(5-7)}$$

where:

$$z = \frac{|x-x'|}{h}, \quad \textbf{(5-8)}$$

and C is [90]:

$$C = \begin{cases} \frac{2}{3} & D = 1 \\ \frac{10}{7\pi} & D = 2 \\ \frac{1}{\pi} & D = 3\ , \end{cases} \quad \textbf{(5-9)}$$

where D is the number of spatial dimensions of the problem.

The cubic B-spline kernel has a compact support domain, in contrast to a Gaussian function that never reaches zero.

Since the domain of interest in the SPH method is represented by a set of particles, it is essential to convert the continuous integral representation of the kernel approximation of equation (5-3) into a summation form, accounting for the number of particles, *N,* in the support domain. Consider Figure 5-1, with a support domain around particle *i* and *k=2,* which is a typical value characterising the radius of the support domain. The mass of particle *j* is given as:

$$m_j = \Delta V_j \rho_j \,. \tag{5-10}$$

Then, equation (5-1) can be approximated for particle *i* as [75] [93]:

$$\langle f(x_i) \rangle \cong \sum_{j=1}^{N} f(x_j) W(x_i - x_j, h)\, \Delta V_j$$

$$= \sum_{j=1}^{N} f(x_j) W(x_i - x_j, h) \frac{1}{\rho_j} (\rho_j \Delta V_j) \tag{5-11}$$

$$= \sum_{j=1}^{N} \frac{m_j}{\rho_j} f(x_j) W(x_i - x_j, h)\,.$$

The above derivation means that a variable at a particle *i* is the sum of the contributions of the neighbouring particles *j* within the support domain.

The kernel has units of *1/V*, where *V* is the volume. Defining density ρ as the variable *f* in the final form of equation (5-11), the simplest form of the density equation is derived [75]:

$$\rho_i = \sum_{j=1}^{N} m_j \left(W(x_i - x_j, h) \right). \tag{5-12}$$

Equation (5-12), called the summation form of density, effectively states that the density of particle *i* is equal to the weighted summation of the neighbouring particles located within the support domain. The summation form of the density conserves the

mass exactly however it leads to poor results at the boundaries due to the lack of particles in the whole support domain.

Another form for the evolution of density is given by the following form of the conservation of mass as (full derivation in Appendix A) [75] [94]:

$$\frac{d\rho_i}{dt} = \rho_i \sum_{j=1}^{N} \frac{m_j}{\rho_j} (v_j - v_i) \frac{\partial W(x_i - x_j, h)}{\partial x_i}, \quad \textbf{(5-13)}$$

where $v_j - v_i$ is the velocity difference between particles *j* and *i.*

Equation (5-13), derived from the continuity equation, is usually applied for flow problems that deal with strong discontinuities, because it considers the velocity difference between the particles. The following simulations were performed in order to show the difference in the pressure and density variations, along the interface of an air-water block of particles under the influence of gravity, with the use of the summation equation of the density (5-12) and the density evolution from equation (5-13). The aim is to demonstrate the boundary deficiency of equation (5-12) and also its ability to provide a smoother transition of density between the water and air.

The set-up includes a 2D box of water and air 10 m *x* 10 m with the same amount of particles for the water and air domains, as shown in Figure 5-2. The density of the air is 1.225 kg/m^3 and that of water is 1000 kg/m^3.

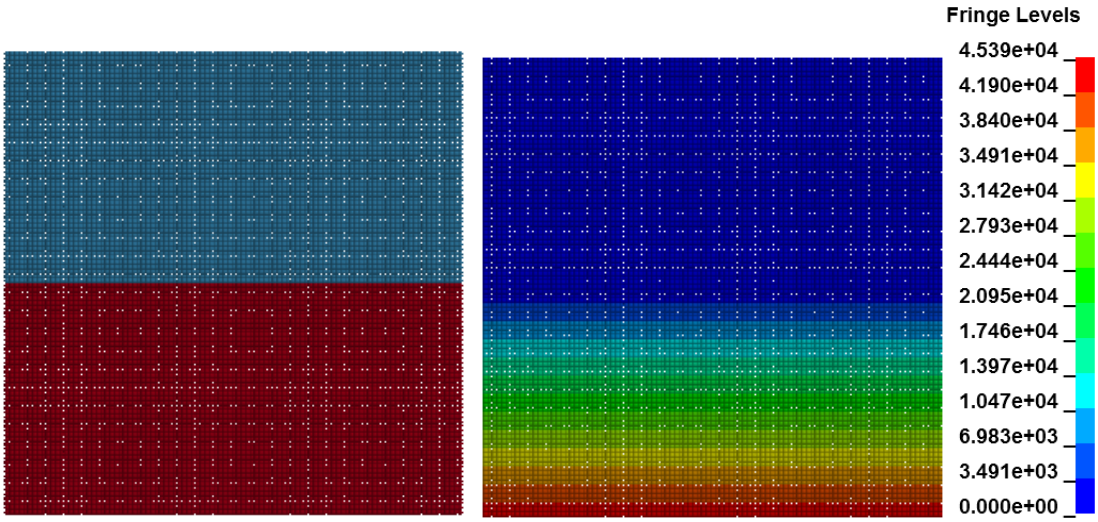

Figure 5-2: Air water mixture with air at the top (left) and pressure distribution of the domain under gravity. Fringe levels show pressure in Pa.

The initial simulation was performed with the use of the continuity equation for the density (equation (5-13)). The pressure at the bottom of the box should be approximately 50,000 Pa. The result of Figure 5-2 yields results close to this value.

Next, equation (5-12) was applied to the entire problem domain. It is expected that it will provide a smoother density transition between the air and the water interface. Figure 5-3 shows a comparison of the densities between the continuity approach and the summation method.

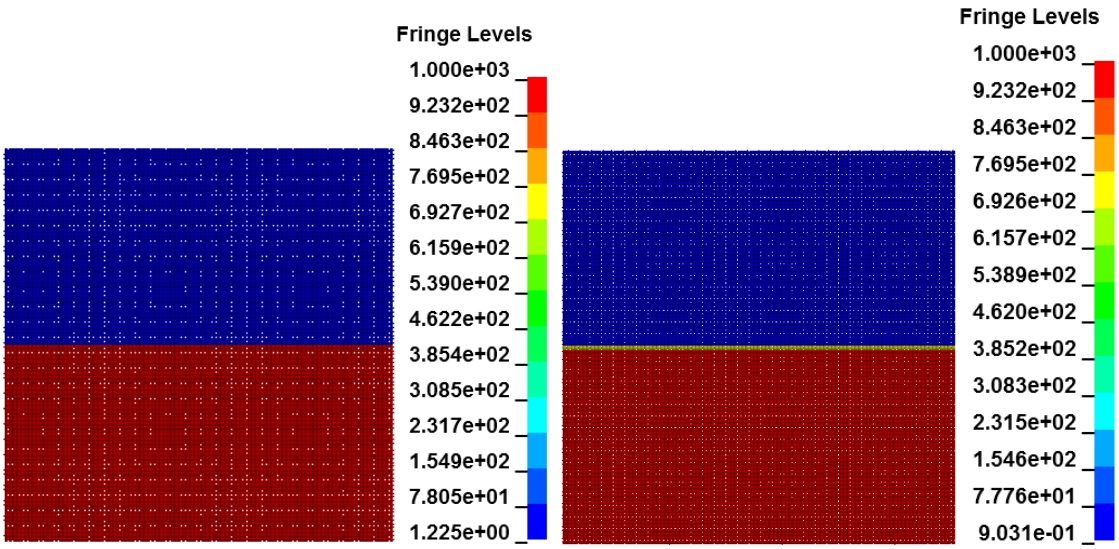

Figure 5-3: Density difference between the continuity form of density (left) and the summation form (right). Fringe levels show density in kg/m^3.

The density at the interface does not transition as abruptly for the summation approach when compared to the continuity one. There is a row of particles that is affected by both the water and the air particles, leading to a smoother density transition. However, the deficiency of the summation form at the boundaries, due to the reduced number of neighbouring particles becomes evident. The density at the top of the air is less than the initial density of air. This deficiency is only present at the top boundary, due to the boundary treatment applied in the current SPH code that will be discussed later.

Finally, the effect of the summation form of the density on the pressure distribution is shown in Figure 5-4. The summation form provides a slightly more accurate pressure distribution as far as the peak value is concerned at the bottom of the water.

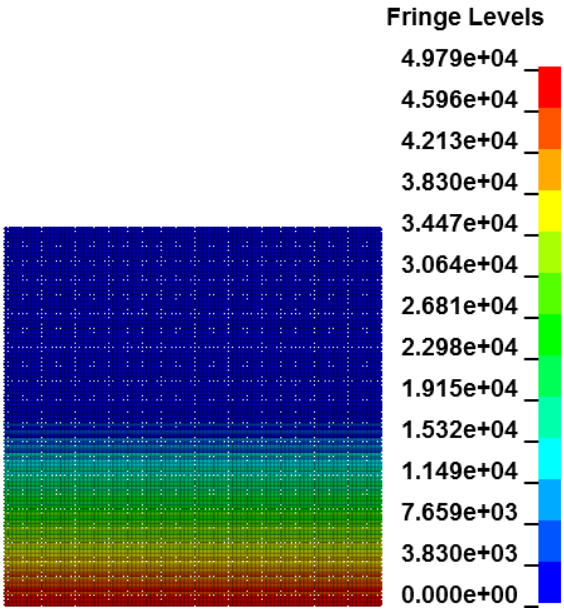

Figure 5-4: Pressure distribution results for the box under gravity with the use of the summation form of the density. Fringe levels show pressure in Pa.

The conservation of momentum and energy are given from the following equations (full derivation in Appendix A) [94]:

$$\frac{dv_i}{dt} = -\sum_{j=1}^{N} m_j \left(\frac{\sigma_j}{\rho_j^2} + \frac{\sigma_i}{\rho_i^2}\right) \frac{\partial W(x_i - x_j, h)}{\partial x_i}, \tag{5-14}$$

$$\frac{dE_i}{dt} = -\frac{\sigma_i}{\rho_i^2} \sum_{j=1}^{N} m_j \left(v_j - v_i\right) \frac{\partial W(x_i - x_j, h)}{\partial x_i}. \tag{5-15}$$

Artificial viscosity was introduced as a means to handle shocks. It is an artificial dissipative term, which effectively smooths the discontinuity present in a shockwave front. The following term was introduced by Monaghan et al. [95]:

$$\Pi_{ij} = \begin{cases} \dfrac{-\alpha c_{ij}\mu_{ij} + \beta\mu_{ij}^2}{\rho_{ij}} & \mu_{ij} < 0 \\ 0 & \mu_{ij} \geq 0 \end{cases}, \tag{5-16}$$

where α and β are viscosity coefficients, $c_{ij} = 0.5(c_i + c_j)$, $\rho_{ij} = 0.5(\rho_i + \rho_j)$ and:

$$\mu_{ij} = \frac{h(v_i - v_j)(x_i - x_j)}{\left|x_i - x_j\right|^2 + \varepsilon h^2},$$

where ε is 0.1 for most cases.

5.2 MCM Structure

The structure of the MCM code is shown in Figure 5-5. During the input phase the data from the input file are imported and the relevant checks, such as correct use of equation of state and boundary conditions are performed. Next, during the initialisation phase, parameters that are not given from the input file are calculated. These include data such as initial pressures/stresses and time step size.

Finally, the output phase provides all the relevant state plots and time history variables for the simulations at intervals specified in the input file.

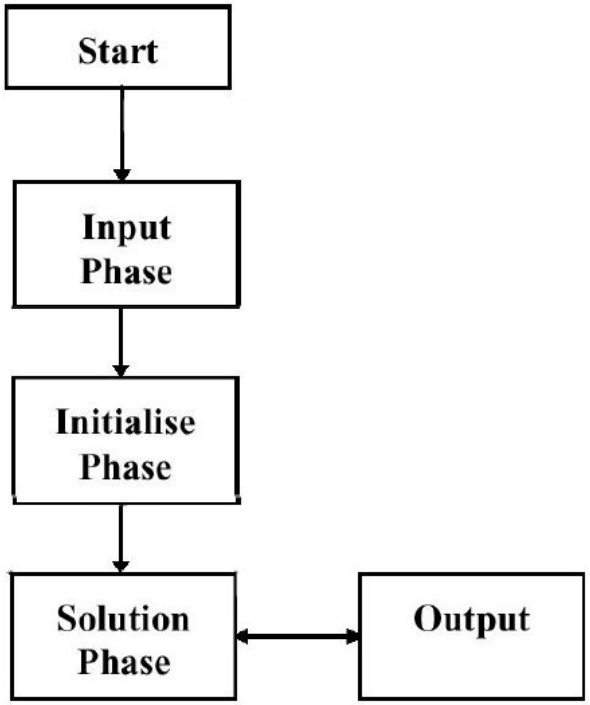

Figure 5-5: Structure of the MCM code. Figure reproduced from De Vuyst et al. [92].

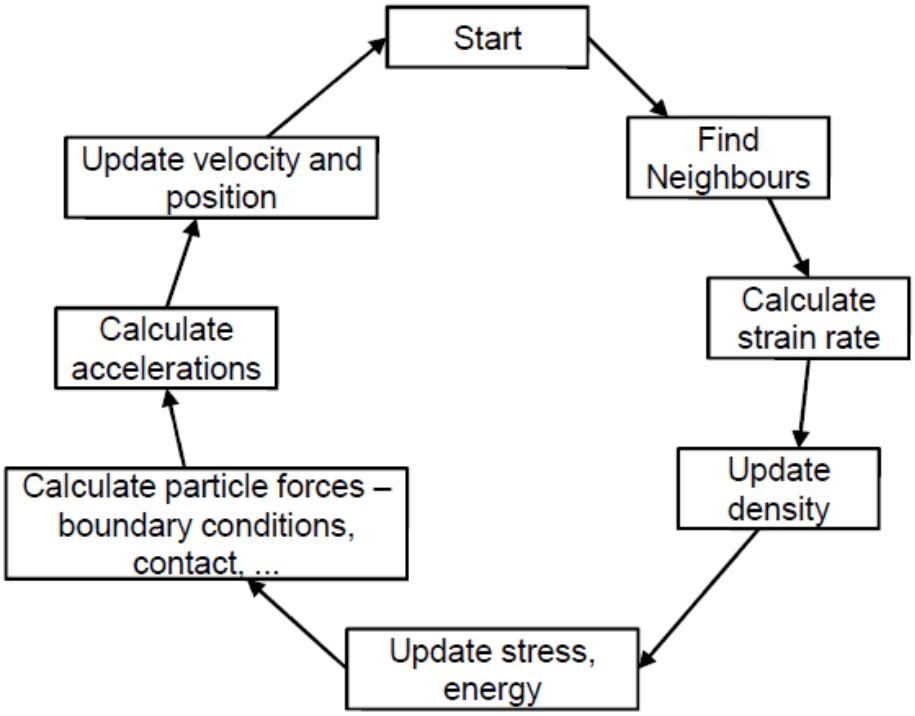

Figure 5-6: Structure of the Solution phase of the MCM code. Figure reproduced from Vuyst et al. [96].

The solution phase is the bulk of the code which performs the time integration. The main routines that it includes are given in Figure 5-6. The first operation that needs to be performed is to determine the neighbouring particles (*j*) for the particle of interest.

The most direct approach to finding the neighbours of particle *i* would be to evaluate the distance between the particles and determine which can classify as neighbours, based on whether they are at a distance less than the support domain. This approach would be computationally expensive so an approach called linked list is employed [94].

With the linked list approach the particles are divided into a grid with dimensions in 3D cases of *2h x 2h x 2h,* which corresponds to the support domain, as shown in Figure 5-7. Then the neighbouring particles of a specific particle can either be in the same grid or the surrounding ones. This means that the search for the neighbour particles takes place in 3, 9 or 27 grid elements for 1D, 2D and 3D cases respectively, as shown in for 2D cases [75].

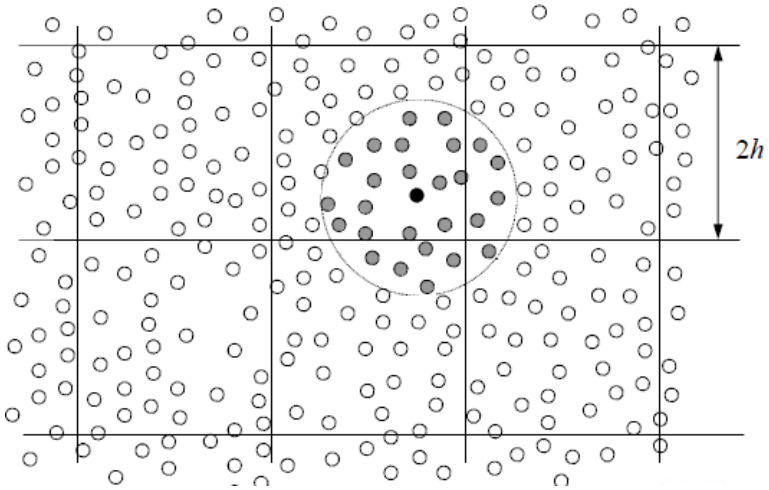

Figure 5-7: Grid representation of the linked list approach. Figure reproduced from Liu et al. [75].

The efficiency of the linked list approach becomes evident as the number of particles increases.

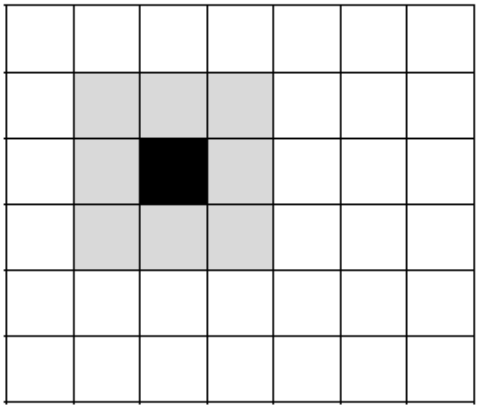

Figure 5-8: Search for neighbouring particles with the linked list approach for 2D cases. Figure reproduced from Liu et al. [75].

Once the neighbour particles are determined, the strain rate and density are evaluated. The MCM code uses the continuity form of the density described above. Next, the constitutive model is applied, which determines the stresses on the particles based on the material model that is used. Then the boundary conditions and body forces are calculated. In order to deal with the particle deficiency at the boundaries a set of ghost particles can be applied at each boundary with the use of symmetry planes, as shown in Figure 5-9. These particles have ghost mass, velocity and pressure as their original

counterpart particles and are included in the neighbours' search, thus avoiding the boundary deficiency issues inherent in SPH [14].

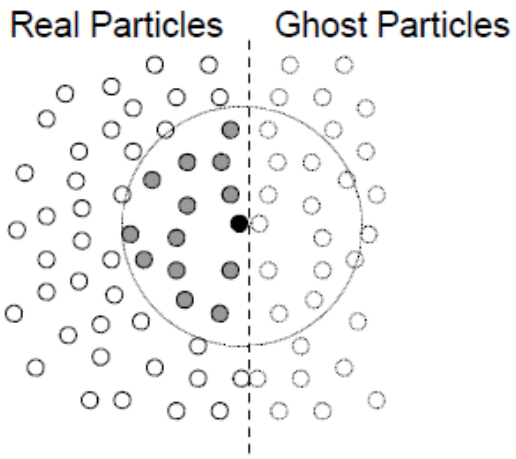

Figure 5-9: Symmetry planes concept. Figure reproduced from Liu et al. [75].

Finally, the accelerations can be computed including body forces, artificial viscosity and any other contact forces based on the momentum equation (5-14). The accelerations are then used to update the velocities and positions of the particles [96].

5.3 Inclined Plate

A test case was developed for a water impact of an inclined plate with high forward velocity, as an initial example of the MCM code coupled with the FE code DYNA3D. This example also represents a simplified version of the experimental tests defined by SMAES. The simulations involve a curved structure, representing a section of the bottom part of the fuselage. By performing these initial simulations, a better understanding of simulating fluid-structure interaction problems with high forward velocity can be achieved. They also contribute towards an assessment of the parameters that influence the simulations and particularly the fluid behaviour modelled with SPH.

The structure under consideration is given in Figure 5-10. It is an elastic plate 1 m long and 0.5 m wide. Under the plate there is a section attached to it with a 1.5 m radius of curvature. Moreover, the structure has been given a 5° inclination with respect to the water surface.

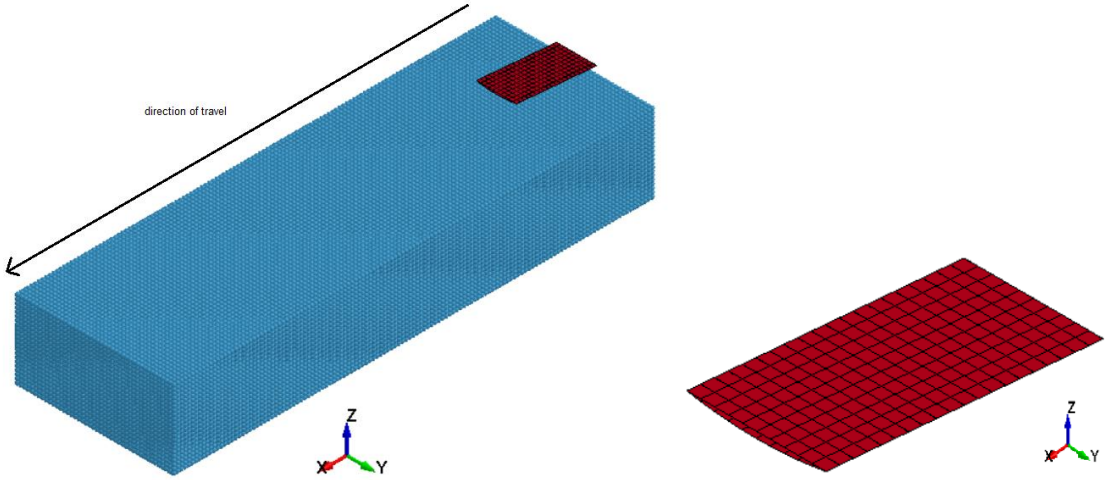

Figure 5-10: FE structure under consideration. Left figure shows overall impact test case and right figure shows zoomed in area with structure detail.

The material used for the plate is aluminium Al 2024-T3 and the input data for the material are given in Table 5-1.

Table 5-1: Input data for FE material model

Density, kg/m^3	2700
Young's Modulus, Pa	7.2x10^9
Poisson's ratio, -	0.33
Yield Stress, Pa	3.45x10^8

The model consists of 422 nodes and 400 shell elements with 10 mm thickness and a total mass of 27 kg. With respect to the initial conditions, the body is assigned a forward velocity of 30 m/s and a vertical velocity of 1.5 m/s. The edges are fully constrained in both rotations and translations. The nodes, selected for time history data plots are shown in Figure 5-11.

Additionally, nodal constraints have been defined for the plate. The "spotweld nodes option" has been applied. This method constrains two nodes of the structure to move along a vector that is internally defined between the two nodes. The nodes are then only able to translate along the direction defined by this vector.

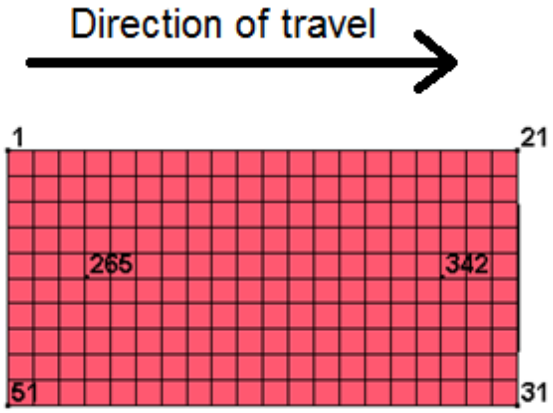

Figure 5-11: Position of the nodes that time histories were recorded at (bottom view).

5.3.1 1 m Depth Tests

The impact test cases in the following two sections describe the impact of a curved structure into a water domain. The water domain varies in depth and consists of SPH particles modelled with the MCM code. The number of particles is also varied in a similar way as conventional mesh refinement in Finite Element simulations. The depth and particle variation allows for an initial comparison of the vertical accelerations experienced by the structure. The water domain was 6 m long and 2 m wide. Two different depths were tested; 1 m and 2 m. For the water domain with 1 m depth there were 128,744 particles with a total mass of 12,000 kg of water and a particle distance of 0.045 m. The smoothing length was 0.585 m.

The finer particle distribution was developed with 255,640 particles and a particle distance of 0.036 m. The smoothing length was 0.0468 m. The comparison between the two impacts is shown in Figure 5-12.

For both models the Murnaghan equation of state was used. The parameters are given below.

Table 5-2: Murnaghan EOS input data.

Bulk Modulus B, MPa	13.0
Parameter γ, -	7.0

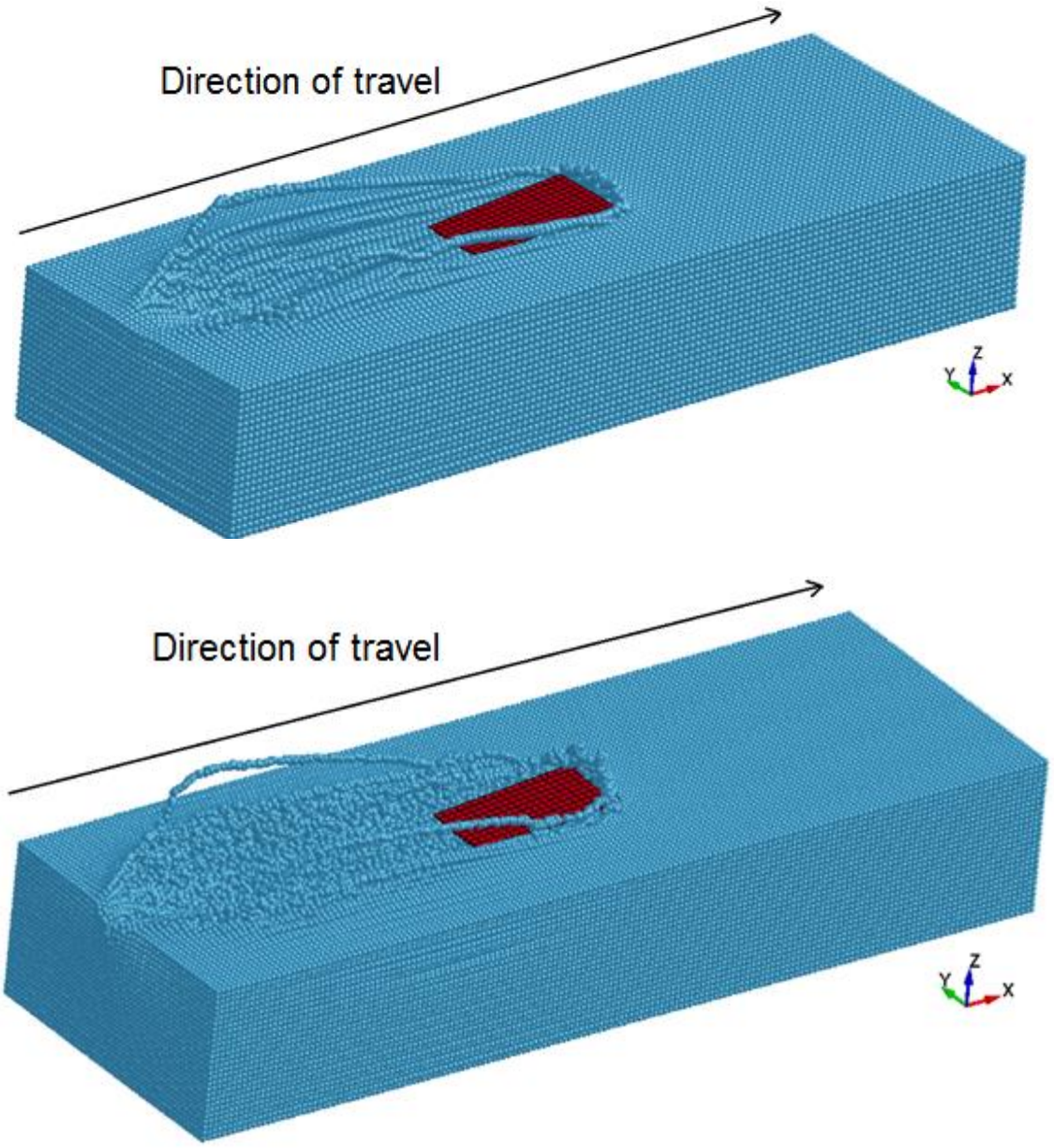

Figure 5-12: Inclined plate impact with coarser particle density shown on the top figure and finer particle density on the bottom. Results obtained at 0.8 s. Depth of water domain is 1 m. Forward velocity is 30 m/s and vertical velocity is 1.5 m/s.

Initial results show that the particle distribution affects the general behaviour. The frames above show that, with increased particle density, the splash in front of the structure is better defined and there is more detail with respect to the water jets from

the sides. A comparison for the vertical accelerations on the nodes 265 and 342 is shown in Figure 5-13 and Figure 5-14 respectively.

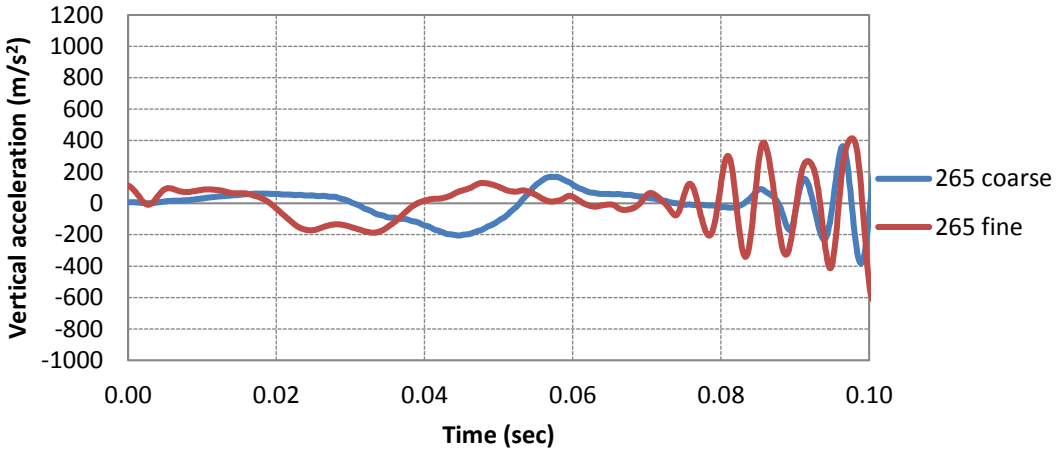

Figure 5-13: Vertical acceleration for the fine and coarse particle distribution for node 265 and 1 m deep water domain.

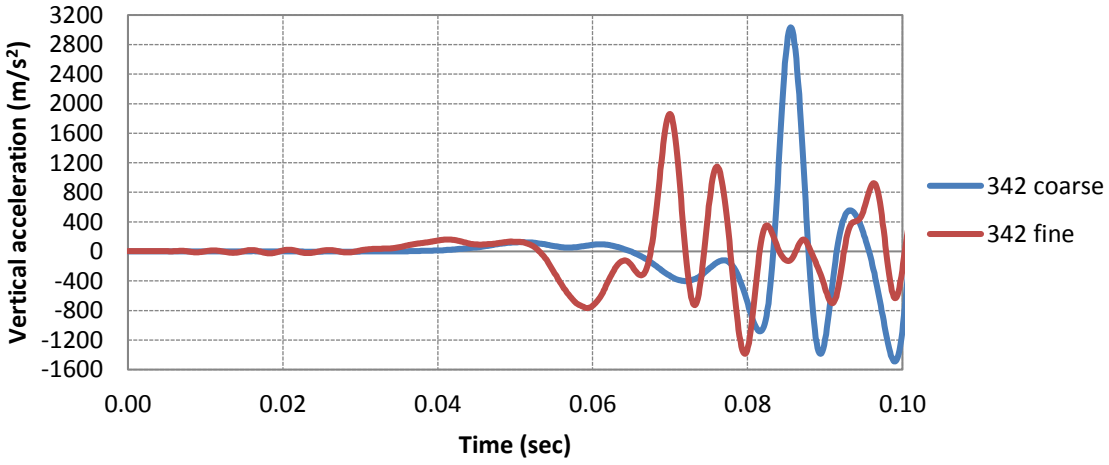

Figure 5-14: Vertical acceleration for the fine and coarse particle distribution for node 342 and 1 m deep water domain.

The acceleration results indicate that there is an initial smooth increase, for as long as the aft section is in contact with the water, followed by a larger secondary deceleration phase as the rest of the structure impacts. For node 265, which is located further back, the initial acceleration peak occurs earlier for the finer particle distribution. This can be attributed to the fact that the contact between the finite elements and the SPH particles depends on the smoothing length (and consequently on the inter particle distance), so

the interaction will start at a different stage in the simulation. The oscillations can be attributed to the elastic material properties of the structure. As the impact progresses, the structure experiences variations in deformations, which lead to the oscillatory nature of the accelerations. Moreover, the oscillatory nature of the results can also be due to wave reflection from the bottom boundaries leading to a noisier signal. For node 342 the initial acceleration peaks do not seem to be significantly affected, however the secondary impact again occurs earlier for the finer particle distribution. The effect of the plate oscillation should also be considered as part of the discrepancies.

5.3.2 2 m Depth Tests

For the 2 m deep test case the water domain consisted of 257,488 particles, with a total mass of 24,000 kg, whereas for the finer particle distribution there are 502,150 particles. The particle distance, smoothing length and equation of state is the same as in the 1 m deep models. The impact is shown in Figure 5-15.

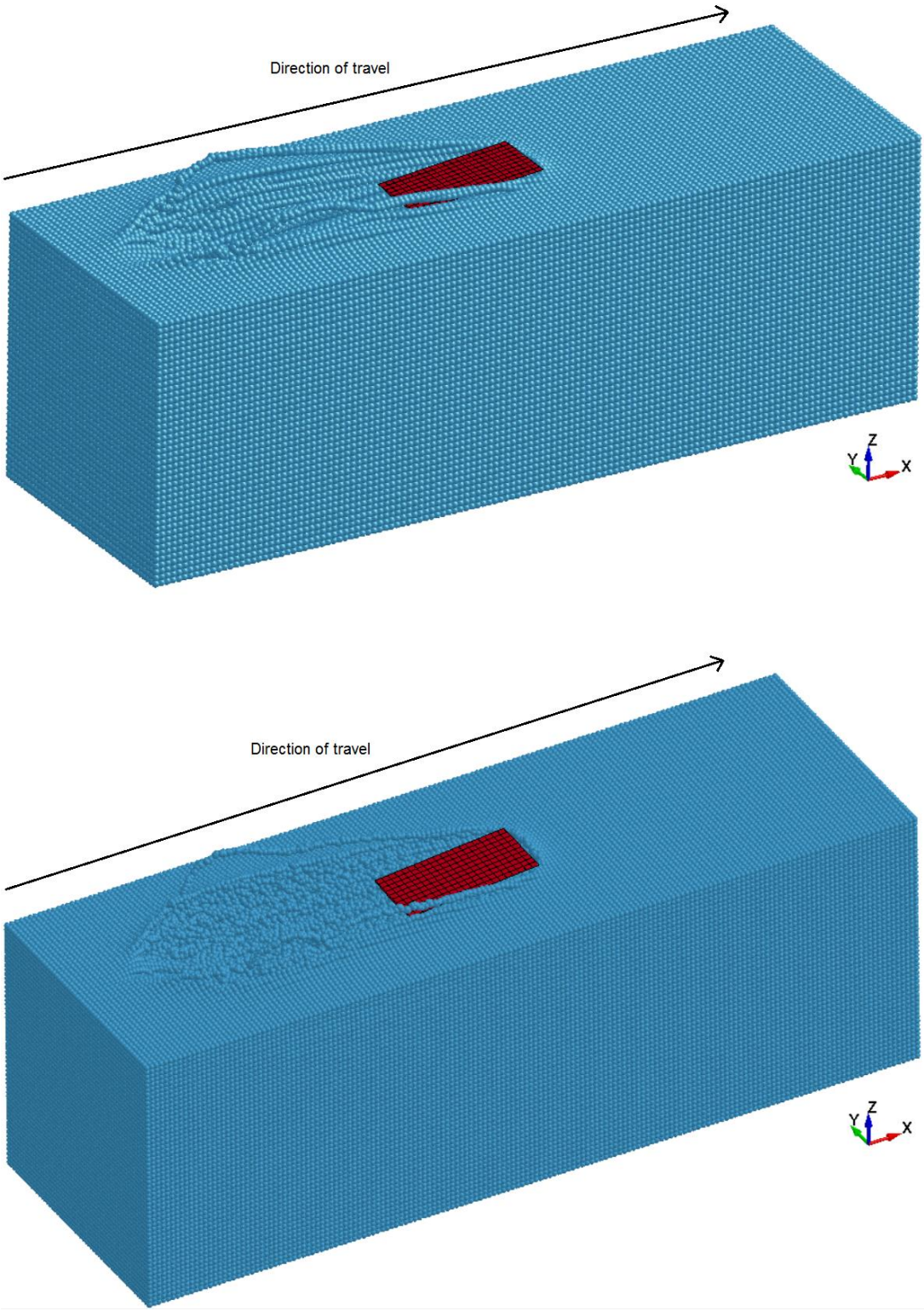

Figure 5-15: Inclined plate impact with coarser particle density shown on the top figure and finer particle density on the bottom. Results obtained at 0.8 s. Depth of water domain is 2 m. Forward velocity is 30 m/s and vertical velocity is 1.5 m/s.

The general behaviour is similar to the 1 m deep simulations. The accelerations in Figure 5-16 and Figure 5-17 follow similar trends to the 1 m deep test case as well, even though the oscillations for node 265 are not as pronounced, meaning that any reflected wave effect takes longer to reach the surface, thus minimises the disturbance on the structure.

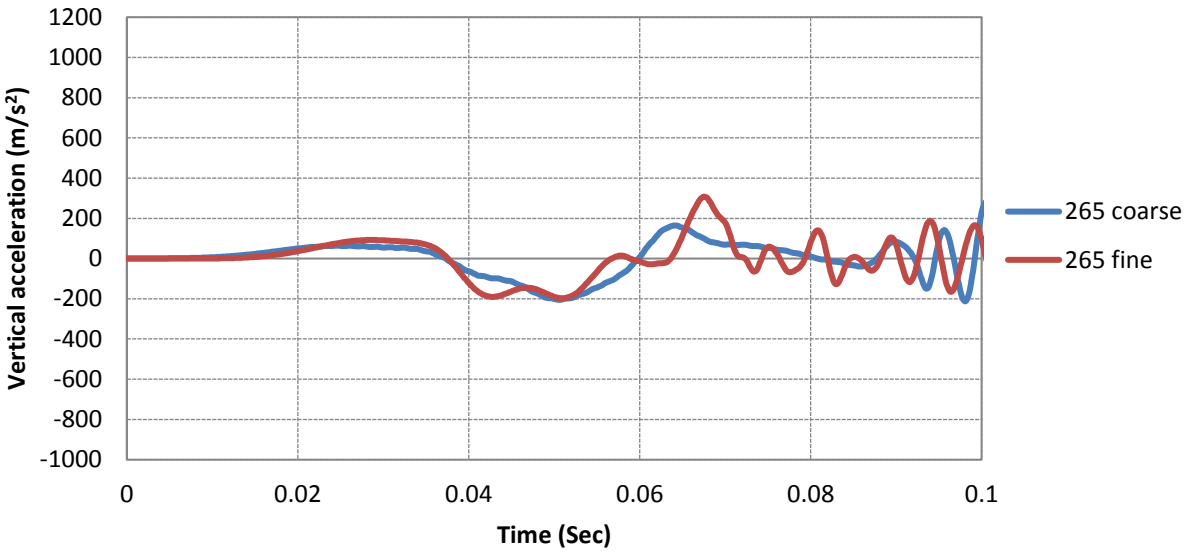

Figure 5-16: Vertical acceleration for the fine and coarse SPH distribution for node 265 and 2 m deep water domain.

With respect to node 342, the increase in depth has not affected the results considerably, suggesting that the results can be caused by the oscillation of the plate.

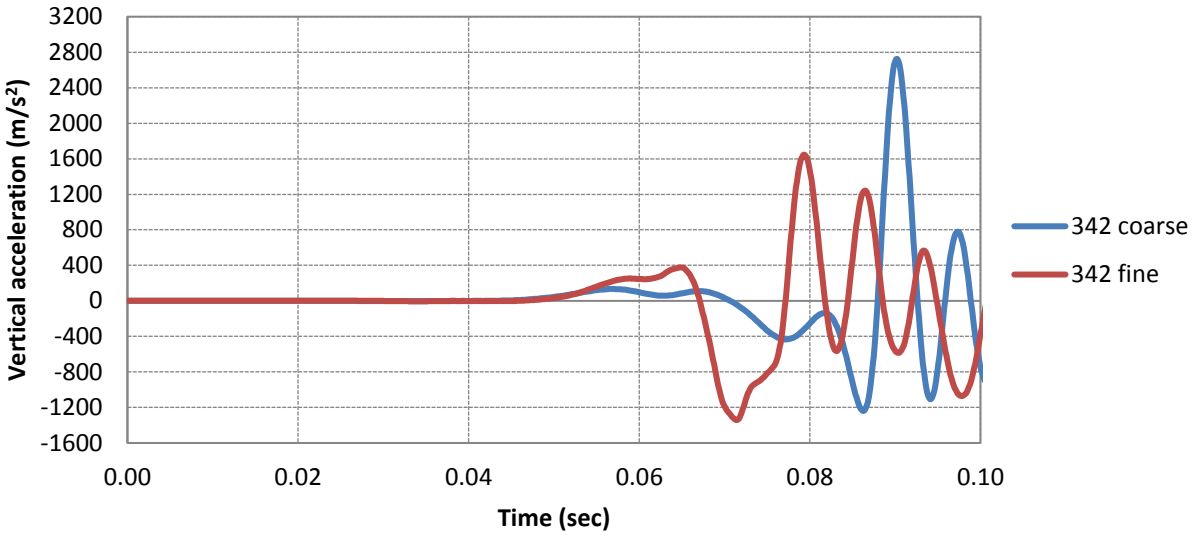

Figure 5-17: Vertical acceleration for the fine and coarse SPH distribution for node 342 and 2 m deep water domain.

The main findings of the simulations are that the particle spacing affects the timing of the maximum recorded accelerations. Moreover, the increased depth of the water domain provides less oscillations in the results, suggesting that there is less disturbance on the structure by unwanted wave reflection. Finally, the oscillation of the plate due to its elastic properties is considered as the main reason for the discrepancies in the forward section of the plate.

5.4 Conclusions

In this chapter, the theory of SPH was described, along with the implementation of the method in the university's MCM code. An initial test case of an inclined plate impacting a water domain with high forward velocity was implemented, that will also be used in subsequent sections. The main findings include the influence of the particle spacing and more significantly the depth of the water domain with respect to the obtained results (accelerations).

In the next chapter the methodology used for the modelling of cavitation will be described and an investigation into the applicability of the method within the MCM code will be performed.

6 Cavitation Modelling

The interest in modelling cavitation is based on the fact that the pressure distribution on the fuselage of an aircraft during ditching is affected by the presence of cavitating regions, thus playing a key role in the structural integrity of the fuselage skin and also due to the scaling difficulties that model aircraft face during experiments, as described in Section 4.3.6.

The majority of the cavitation models shown in Section 4.3.7 include the use of a homogeneous mixture and a range of phase exchange parameters in order to simulate attached cavitation over streamlined bodies. In this project however, the interest is in transient cavitation, which appears in the form of cavitating nuclei in the fluid. Currently, the SPH code uses a simplistic approach for the inclusion of cavitation. It uses the pressure cut-off model, which makes no attempt to alter the physical properties of the flow and does not provide a good approximation of the vapour pressure. The approach that will be used for the cavitation model is a combination of the one-fluid homogeneous model and the bubble dynamics approach presented in Section 4.3. The choice of this approach is based on the fact that the interest in cavitation in this project is from a macroscopic perspective, where each SPH particle is a mixture of both liquid and vapour. Hence, a homogeneous approach is relevant. Furthermore, the fact that the mixture density depends on the amount of vapour present in each particle means that a procedure for determining the size of the cavitating nuclei, and as a consequence the amount of vapour present in them, is necessary. The Rayleigh-Plesset form will thus be introduced and used as it was briefly described in Section 4.3. With respect to the pressure for the onset of cavitation, the new approach will consider not only the vapour pressure of the fluid, which has been the case in previous numerical investigations, but it will also take into account the effect of the tensile strength of the fluid.

6.1 Methodology Assumptions

One of the most important assumptions is that the interest in this project lies with transient cavities. As a consequence, the cavitating nuclei have a very short lifetime and any mass exchange taking place between the liquid and the vapour is negligible. Transient cavities are characterised by the phase change from liquid to vapour. This makes it acceptable to assume that the gas content is neglected, allowing us to consider purely vaporous nuclei.

With respect to the density of the mixture it is essential to consider the influence of both the liquid and the vapour. The liquid in this project is water and, for the temperature ranges considered, its density does not change. Furthermore, it is assumed that the pressure of each particle, remains constant, once it reaches the critical cavitation pressure. This allows the vapour density to remain unchanged as well. This is acceptable for the growth and part of the collapse of cavitating nuclei, while the mixture's velocity is far smaller than the liquid's speed of sound [60].

Next, the pressure inside the SPH particles is considered equal to the critical pressure of equation (4-9). This is different to the usual approach that assumes that the critical pressure is equal to the vapour pressure. It is expected that for small enough nuclei the surface tension will give significantly different critical pressures. In order to have cavitation it is logical to assume that there are microscopic nuclei present in the liquid. The total number of the nuclei present is predetermined and their initial size is the same throughout the liquid.

Finally, the nuclei are assumed to be spherical throughout the phenomenon. This is acceptable for the growth and initial stage of collapse but as the size of the nuclei reduces they can assume a variety of shapes [72].

6.2 Vapour Pressure

There exist several empirical and semi-theoretical equations, which have been developed in the past decades, with respect to the accurate estimation of the vapour pressure of liquids. The most famous one is the Clausius-Clapeyron [97]. This is based on the assumption that the vapour acts as an ideal gas and it is given as:

$$\ln P_v = -\frac{\Delta_{vap}H^0}{RT} + \frac{\Delta_{vap}S^0}{R}, \qquad \textbf{(6-1)}$$

where P_v is the vapour pressure, $\Delta_{vap}H^0$ is the enthalpy of vaporisation, $\Delta_{vap}S^0$ is the entropy of vaporisation, R is the constant of ideal gas and *T* is the temperature.

The above equation assumes that the enthalpy of vapourisation (otherwise known as heat of vapourisation) is constant, which is only acceptable for small temperature ranges. This leads to deviations in the substance's phase diagram and a "bowed" graph instead of a straight line (for pressure vs 1/T). As such, it appears that

extrapolation of the vapour pressure graph over large temperature ranges is not accurate. With respect to the other empirical approaches, a priori knowledge of the required terms, for some of the empirical formulae, is cumbersome making the use of these equations more difficult [97].

The simpler Antoine equation is used instead, which is given as [60]:

$$logP_v = A - \frac{B}{T + C}, \tag{6-2}$$

where *A, B* and *C* are empirically calculated dimensionless parameters, depending on the temperature *T* and are given in Table 6-1. The Antoine equation provides a better fit for the phase diagram compared to the Clausius-Clapeyron equation (6-1). It provides a less pronounced bowing of the P vs 1/T graph, where a straight line is expected. This has been established for temperatures up to 0.75-0.85 of the critical pressure of the liquid, T_{crit}, where the error in the vapour pressure is less than 0.001%. For water T_{crit}=374°C, and as such, the Antoine equation can provide accurate vapour pressure estimations for temperatures up to approximately 300°C. This is within the scope of this project. Additionally, the simplicity and availability of data of the Antoine equation make it an ideal solution for this application.

From Table 6-1 it is obvious that the Antoine equation can be used in a variety of examples, given the wide range of temperatures that it considers.

Table 6-1: Coefficients for the Antoine equation depending on temperature. Table reproduced from Zardoni [60].

Temperature (K)	A	B	C
273-303	5.40221	1838.675	-31.737
304-333	5.20389	1733.926	-39.485
334-363	5.0768	1659.793	-45.854
364-373	5.08354	1663.125	-45.622

Once the pressure of equation (6-2) is computed, it is used for the evaluation of the critical pressure given from equation (4-9). The critical radius of the nuclei and the surface tension are known variables and they do not change during the phenomenon. Once equation (4-9) is evaluated, it is used as the new cut-off value including the tensile strength of the fluid and the temperature dependent vapour pressure. This provides a better approximation from the cut-off model.

6.3 Growth Phase

Once the vapour pressure is reached, the density and speed of sound of the fluid flow will change into a two-phase homogeneous fluid. Using bubble dynamics models will allow for the evolution of the cavitating nuclei to be considered. The most commonly used method is the simplified Rayleigh-Plesset equation. The Rayleigh-Plesset equation provides an approximate method for determining the radius of a spherical bubble [72] [71]. Initially the Rayleigh-Plesset equation is (full derivation in Appendix B):

$$\rho\left[R\ddot{R}+\frac{3}{2}\dot{R}^2\right]=[p_v-p_\infty(t)]+p_{g0}\left[\frac{R_0}{R}\right]^{3\gamma}-\frac{2S}{R}-4\mu\frac{\dot{R}}{R}. \qquad \textbf{(6-3)}$$

Since the nuclei under consideration are only filled with vapour, the second term of the equation can be dropped. Moreover, the assumption of a non-viscous liquid means that the last term is also neglected. This is generally true for small nuclei. Furthermore, the pressure in the fluid p_∞ is constant. The fluid pressure can be considered constant when dealing with small nuclei radii (less than 2.7 mm for water) [59]. In that case, the hydrostatic pressure difference is negligible. Following integration, the nuclei growth velocity can be found as [59]:

$$\dot{R}^2 = \frac{2}{3}\frac{p_v - p_\infty}{\rho_l}\left[1 - \frac{R_0^3}{R^3}\right] - \frac{2S}{R}\left[1 - \frac{R_0^2}{R^2}\right]. \quad \textbf{(6-4)}$$

As the radius increases to many times the initial radius, it can be assumed that the last term of equation (6-4) is sufficiently small to give an asymptotic interface velocity:

$$\dot{R} \cong \sqrt{\frac{2}{3}\frac{p_v - p_\infty}{\rho_l}}, \quad \textbf{(6-5)}$$

where p_∞ is the pressure of the surrounding fluid. Once the pressure of an SPH particle reaches the critical value for cavitation, equation (6-5) can be written as:

$$\dot{R} \cong \sqrt{\frac{2}{3}\frac{\frac{2S}{R_c}}{\rho_l}}. \quad \textbf{(6-6)}$$

Since the method assumes that the initial radius of the nuclei is the critical radius, it follows that $R_c = R_0$. The simplified nuclei interface velocity above depends only on the critical pressure of the SPH particle (i.e. the critical nuclei radius) or in other terms the difference between the vapour pressure and the surrounding pressure [62] [64]. It also shows that for larger initial nuclei the growth velocity reduces, which follows closely with the theory that smaller nuclei explode more violently than the bigger ones.

Once the interface velocity is known the radius of the nuclei will follow the equation:

$$R(t + dt) = R(t) + \dot{R}dt\,. \quad \textbf{(6-7)}$$

The density of the mixture, given in equation (6-8) consists of two parts. The first is the vapour density and the second is the liquid density and is given as [98]:

$$\rho = \alpha\rho_v + (1 - \alpha)\rho_l\,. \quad \textbf{(6-8)}$$

The next step is to define the void fraction α, used in the above equation. The void fraction is a parameter, which determines the amount of vapour in each SPH particle that reaches the critical cavitation pressure. It can assume values ranging from 0 to 1. A value of 0 means that there is only liquid present in the SPH particle and hence no cavitation is present. On the other extreme, a value of 1 means that the SPH particle is saturated with vapour. The vapour volume within a particle is considered to be:

$$\alpha = \frac{V_v}{V} = \frac{V_v}{V_l + V_v}. \quad \textbf{(6-9)}$$

Assuming $V_v \ll V$ and that the total volume of a particle is unity, it follows that equation (6-9) becomes:

$$\alpha = \frac{V_v}{V} = \frac{V_v}{1 + V_v}. \quad \textbf{(6-10)}$$

Considering that the vapour volume is the total volume of the individual spherical nuclei, it follows that equation (6-10) can be written as:

$$\alpha = \frac{\frac{4}{3}\pi n R^3}{1 + \frac{4}{3}\pi n R^3}, \quad \textbf{(6-11)}$$

where n is the number density of nuclei present in a m^3.

As the nuclei increase in size, so does the void fraction. It must be noted that, with bigger nuclei there is potential for more interaction and grouping, however the current method does not allow for these interactions to be considered. As a consequence, the results may not be as accurate as experimental data for high void fraction values. This is one of the most important limitations of the Rayleigh-Plesset approach [80]. As was discussed previously, the nuclei number density present in a flow is an empirical measurement and any changes in that number will alter the extent and behaviour of the cavitation.

The final property that needs to be considered is the speed of sound. As it was discussed earlier, the speed of sound of the mixture can be significantly lower than the liquid's speed of sound. The speed of sound equation uses the mixture density of equation (6-8) and a combination of the void fraction and the speed of sound of the individual components and is given as [78] (full derivation given in Appendix C):

$$C = \left\{ [\alpha\rho_v + (1-\alpha)\rho_l] * \left[\frac{\alpha}{\rho_v c_v^2} + \frac{1-\alpha}{\rho_l c_l^2} \right] \right\}^{-1/2}, \quad \textbf{(6-12)}$$

where c_v is the speed of sound of vapour and c_l is the speed of sound of the liquid.

6.4 Reduction Phase

Once the SPH particles are in a high pressure region they should start to reduce in size. It should be noted that the interest in this project is in the continuum field and as such moving into the actual collapse phase will only complicate the modelling attempts. Moreover, cavitation collapse is focused on material damage and degradation, a phenomenon associated with cavitation in propellers and pumps due to the cyclical occurrence of the phenomenon. This is also out of the scope of this project.

The reduction of cavitating nuclei follows a similar method to the growth described above, with the exception that the nuclei reduction velocity is [64]:

$$\dot{R} = \sqrt{\left|\frac{2}{3}\frac{p_v - p_\infty}{\rho_l}\left[1 - \frac{R_0^3}{R^3}\right]\right|}. \qquad \textbf{(6-13)}$$

Following the same procedure as above the nuclei reduction velocity can be rewritten as:

$$\dot{R} = \sqrt{\left|\frac{2}{3}\frac{\frac{2S}{R_c}}{\rho_l}\left[1 - \frac{R_0^3}{R^3}\right]\right|}. \qquad \textbf{(6-14)}$$

In contrast to the growth phase, the reduction velocity is influenced by the current nuclei radius as well as the pressure difference (tensile strength of the liquid). Once equation (6-14) is evaluated, the reduction in the nuclei size should occur. This is given as:

$$R(t + dt) = R(t) - \dot{R}dt\,. \qquad \textbf{(6-15)}$$

6.5 Methodology Implementation

In this section, the essential input parameters and the structure of the method within the MCM code will be discussed.

The main structure of the MCM code includes the following main routines.

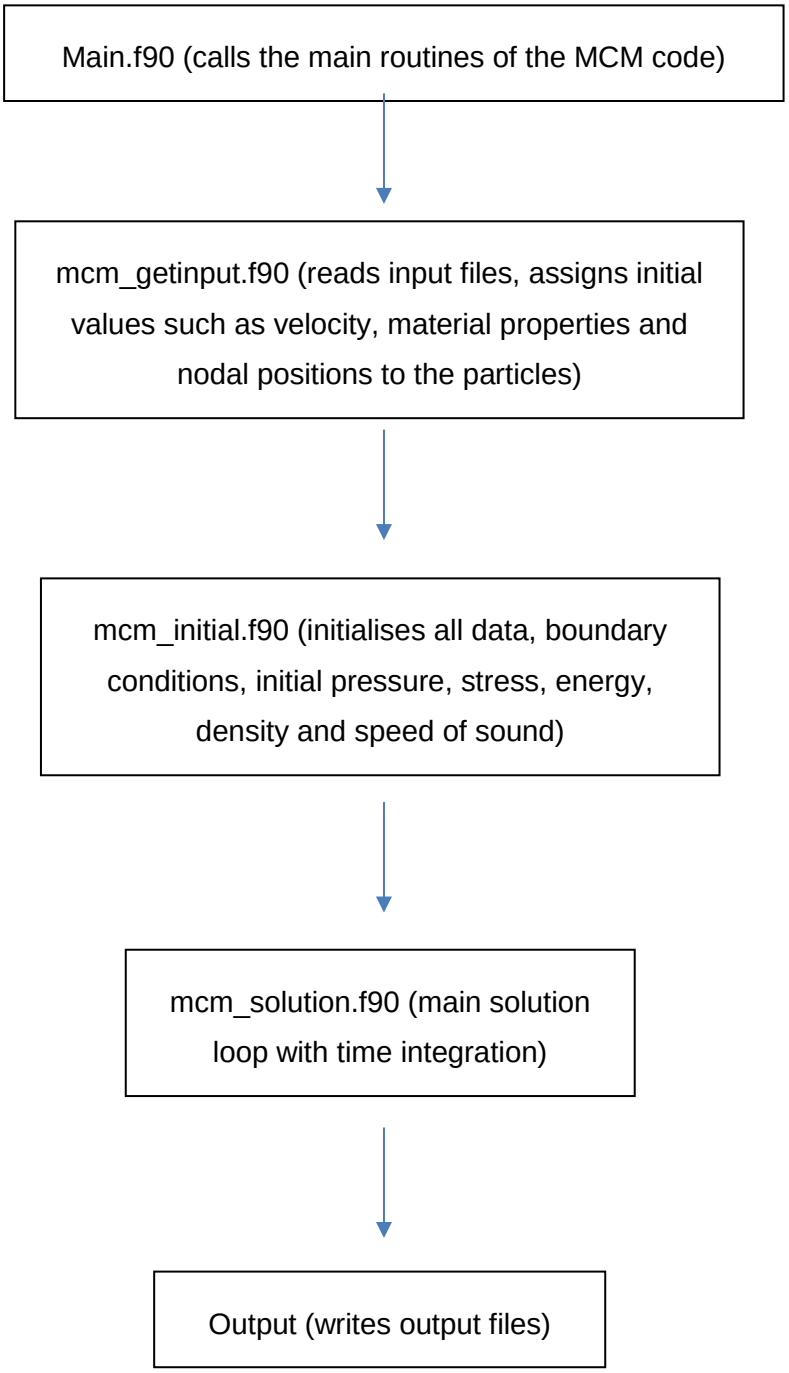

For the cavitation model implementation the following subroutines have been modified.

- Mcm_initial.f90
  - Mcm_initialise_database.f90
- Mcm_solution.f90
  - Mcm_f3dm9.f90

- Mcm_voidfraction.f90
- Mcm_eos28c.f90
- Mcm_eos4c.f90

mcm_initialise_database.f90 initialises the input data. All of the parameters that are used in the MCM code are initialised in this subroutine and are usually given an original value of zero. The input parameters of the method within the MCM code are given in Table 6-2.

Table 6-2: Input parameters for cavitation model

Input Parameter	**Description**
Pref	Reference value of 0 or 1 to assess if the problem has an initial pressure or not.
tempcav	Temperature used for the evaluation of the Antoine Equation.
rmin	Minimum radius of the nuclei (same as critical radius)
nuclei	Nuclei number density of nuclei/m^3
cl	Speed of sound of the liquid

The implementation of cavitation in the MCM code considers the theory described in sections 6.1-6.4. Since the cavitation model considers a homogeneous approach, there is no attempt to distinguish between the water and the vapour interface. Instead, the method assumes that each SPH particle is a mixture of water and vapour under one criterion. If the pressure drops to the critical cavitation pressure, then the SPH particle is no longer pure liquid but a combination of liquid and vapour. This means that each SPH particle is assumed to be populated by microscopic nuclei. The number density of the nuclei is user defined input.

mcm_ f3dm9.f90 is the subroutine that defines the fluid material model. This routine has been modified so that the Antoine equation (6-2) is incorporated. Based on the temperature, initial pressure defined by the user in the input file and equation (4-9), the subroutine calculates the critical pressure for cavitation. This is stored and compared against the pressure of each SPH particle for each timestep later in the solution. If the

pressure of the particle drops to or below the critical pressure, then the cavitation model is activated.

mcm_voidfraction.f90, is a new subroutine that has been included in the MCM code. This subroutine is used only for each SPH particle with pressure equal to the critical cavitation pressure. As long as the SPH particle has a pressure equal to the critical cavitation pressure then equations (6-6), (6-7), (6-8) and (6-11) are employed. In the implementation of the code the void fraction has been capped at 0.7. In SPH density ratios of up to 0.1 can be handled with no particular numerical difficulties, however for smaller density ratios, particles at the interface can have large velocities with opposite directions leading to an unstable solution [99]. If the void fraction increases to a maximum of 0.99 then the densities can range from 1000 kg/m^3 in pure liquid form to 10 kg/m^3 for pure vapour. By capping the void fraction at 0.7 with a density ratio of approximately 0.3, it is ensured that any sharp density interfaces will not affect the solution.

Even though the nuclei growth velocity remains constant, the nuclei radius increases at each timestep. The void fraction is updated and this subsequently is used for the SPH particle density, which is a mixture density (water and vapour). In the next timestep the same process is followed, as long as the SPH particle has a pressure still equal to the critical cavitation pressure.

As soon as the pressure of a cavitating SPH particle increases above the critical cavitation pressure, the cavitation reduction phase occurs. As far as the reduction phase is concerned, this is triggered once the particles start to compress and the pressure increases. In that case, equations (6-8), (6-11), (6-14) and (6-15) are employed. The reduction phase remains active, for each SPH particle, in the subsequent timesteps until the nuclei radius or the void fraction reaches their initial value. Then the flow is assigned its original values with respect to the density, nuclei radius and void fraction. Moreover, the growth/reduction velocities are reset to zero. If the pressure of the SPH particle drops to the critical cavitation pressure, then the growth phase is activated once again and the growth of the nuclei is estimated based on the latest void fraction, nuclei radius and mixture density, as described above.

mcm_eos4c.f90 is the subroutine that calculates the speed of sound for each SPH particle when the Gruneisen equation of state is used. If the cavitation model is active, then the speed of sound is estimated based on equation (6-12). This process is used in

order to take into account the effect of both the liquid and the vapour in the calculation of the speed of sound of the mixture.

Similarly, **mcm_eos28c.f90** is the subroutine that calculates the speed of sound for each SPH particle for the case when the Murnaghan equation of state is used. This subroutine is also modified so that the speed of sound uses equation (6-12).

The flow chart below shows the solution loop performed for each MCM particle.

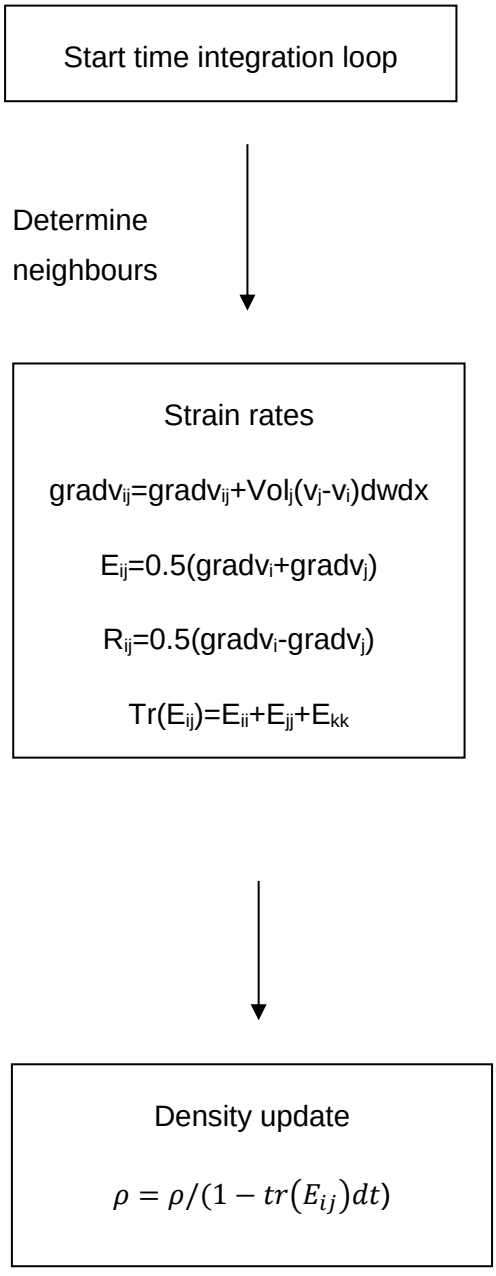

If cavitation is active

Material strength and stress tensor

If cavitation is active:

Estimate Antoine equation in absolute and gauge terms:

$$Pv=10^{(a-(b/T+c))100000}$$

Pvg=Pv-101325

Estimate tensile strength of water in absolute and gauge terms:

Δp=(2s)/rmin

$\Delta p_g = \Delta p$ -101325

Estimate critical pressure if there is an initial pressure:

pcrit= Pvg- Δp_g - pact

Estimate critical pressure if there is no initial pressure:

pcrit=Pvg- Δp_g

pcut=pcrit

The stress tensor for hydrostatic pressure (for water)

$$\begin{bmatrix} \sigma_{ii} - \frac{1}{3}tr(E_{ij}) & 0 & 0 \\ 0 & \sigma_{jj} i \frac{1}{3}tr(E_{ij}) & 0 \\ 0 & 0 & \sigma_{kk} - \frac{1}{3}tr(E_{ij}) \end{bmatrix}$$

Void fraction calculation

If the pressure is less than the cut-off pressure, pcut, and the $Tr(E_{ij})>0$ then calculate the bubble growth velocity and update the bubble radius rmax. Then update the void fraction and the density.

$$v= ((0.67\Delta p/\rho_0))^{0.5}$$

$$rmax=rmax+(vdt)$$

$$\alpha=(n\pi 1.33(rmax^3))/(1+(n\pi 1.33(rmax^3)))$$

$$\rho=((\alpha\rho_v)+((1- \alpha)(\rho_0)))$$

If the void fraction reaches 0.7 then,

$$v=0.0$$

$$rmax=rmax+(vdt)$$

$$\alpha=0.7$$

$$\rho=((\alpha\rho_v)+((1- \alpha)(\rho_0)))$$

If the pressure increases above the cut-off pressure then calculate the bubble reduction velocity and update the bubble radius, rmax. Then update the void fraction and the density.

$$a=rmin^3$$

$$b=rmax^3$$

$$v=((0.67\Delta p/ \rho_0)(1-(a/b)))^{0.5}$$

$$rmax= rmax-(vdt)$$

$$\alpha=(n\pi 1.33(rmax^3))/(1+(n\pi 1.33(rmax^3)))$$

$$\rho=((\alpha\rho_v)+((1- \alpha)(\rho_0)))$$

Speed of sound

If the cavitation model is active and for as long as the pressure is less than the cut-off pressure, pcut, the speed of sound is calculated by the following:

$$c=(\alpha\rho_v +(1- \alpha)\rho_0)((\alpha/(\rho_v(c_v^2)))+((1- \alpha)/(\rho_0 c_l^2)))^{-0.5}$$

Calculate trial value for internal energy

Update pressure and internal energy:

Select the appropriate Equation of state. For the Murnaghan EOS:

$$p = b((\rho/\rho_0)^{\gamma} - 1.0)$$

If the cavitation model is active check if the pressure is less than the cut-off pressure, pcut. If valid then:

$$p = pcut$$

$$\rho = \rho(1 – tr(E_{ij})dt)$$

Then update the internal energy:

$$e = e_{try} - 0.5p\Delta V$$

Update stress tensor with pressure and calculate critical timestep, calculate acceleration, update boundary conditions, calculate total energy and update velocity and position of particle

End of time integration loop

6.6 Methodology Verification

In this section, the above methodology is tested on simple 2D simulations, namely a set of constrained particles, a more realistic step simulation, a venturi flow simulation and a 2D tube test.

6.6.1 Initial Verification

Initial trials in the MCM code for a 2D set of particles in tension were performed in order to check if the code works properly. The 2D simulation was performed with 15 particles. The particles were fully constrained in both translation and rotation and were assumed to be pre-seeded with microscopic nuclei. The strain rate was prescribed for all the particles as shown in Table 6-3. Figure 6-1 shows the simple set-up of the experiment and Table 6-3 shows the relevant input data.

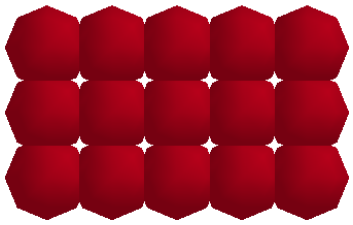

Figure 6-1: Set of particles for code verification.

Table 6-3: Initial input data.

Initial Pressure, Pa	101325
Liquid density, kg/m^3	1000
Vapour density, kg/m^3	0.023
Nuclei number density (n), /m^3	3.7x10^7
Initial radius of nuclei, m	5x10^{-5}
Temperature, K	298.15
Strain rate, /s	$\pm$1

The model is fully constrained in translations in x and y displacements. The length of the model is 0.352 m and the height is 0.176 m. The particle spacing was set at 0.088 m and the smoothing length was 0.1144 m. The total mass of the water domain is 116.16 kg. The equation of state that was used is the Gruneisen EOS and the inputs are given in the table below.

Table 6-4: Gruneisen EOS input data.

Velocity Curve Intercept, *C*, m/s	1482.9
First slope coefficient, S_1, -	2.0367
Second slope coefficient, S_2, -	0
Third slope coefficient, S_3, -	0
Gruneisen coefficient, γ_0, -	1
First order volume correction coefficient, α, -	0.5
Initial relative internal energy, ε_0, kg/ms^2	101325
Initial relative volume, V_0, -	1

Of particular interest are the results for the pressure, density and void fraction. The graph in Figure 6-2 shows the drop of the pressure during cavitation. The critical pressure, according to equation (4-9), should be approximately 246 Pa, which means that this is the lowest pressure that the liquid can sustain prior to cavitation. Indeed, the code did not allow the fluid to drop below that threshold. A closer look at the result of Figure 6-2 is shown in Figure 6-3.

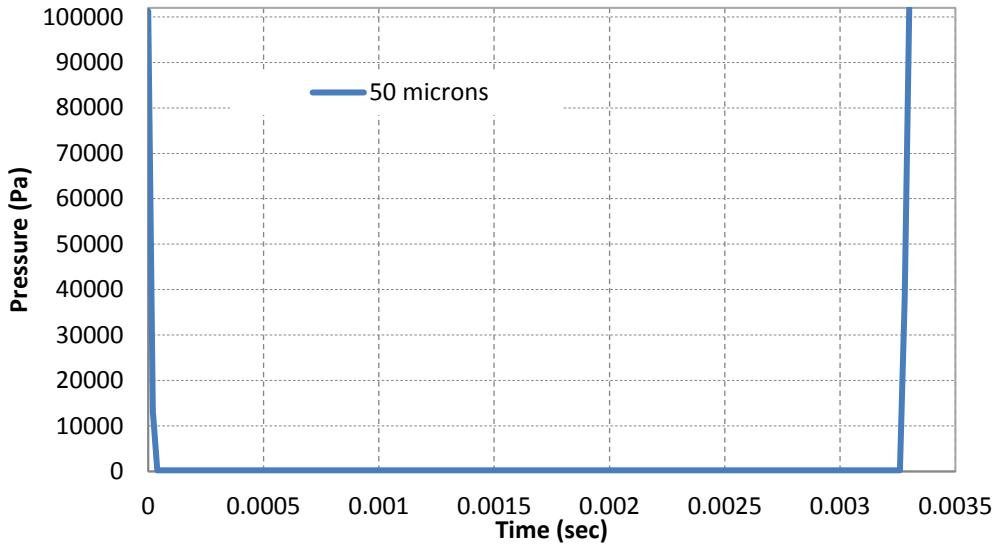

Figure 6-2: Pressure drop during cavitation and pressure growth after reduction. Initial pressure of 101325 Pa.

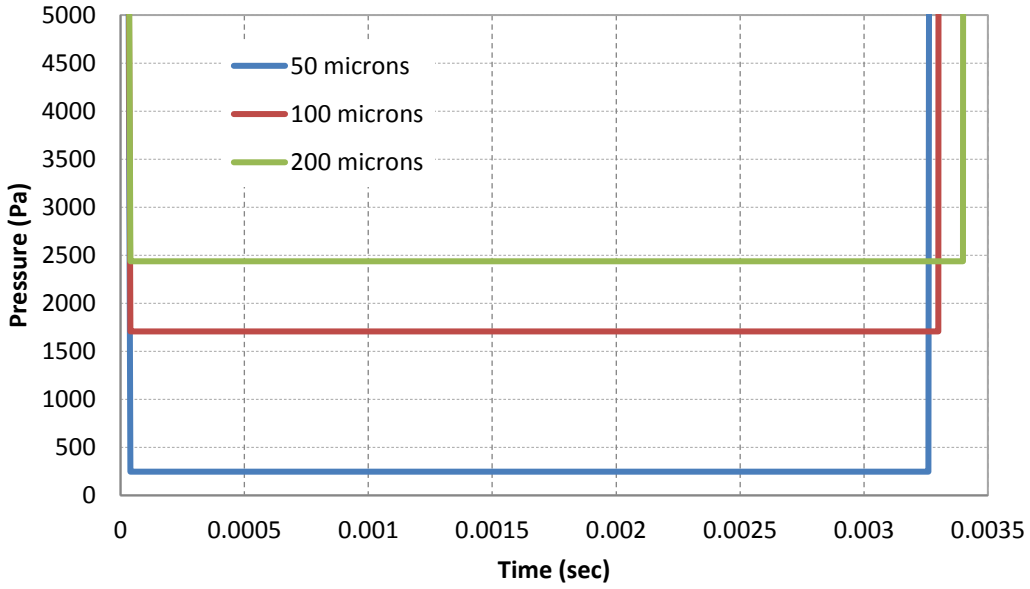

Figure 6-3: Comparison of critical pressure for varying initial bubble radii and constant nuclei number density. Initial pressure of 101325 Pa. Graph shows the zoomed in area of interest. The smallest the initial bubble radius the stronger the effect of surface tension. This shows that the pressure needs to drop to a lower level in order to reach the cavitation critical pressure.

Changes in the initial nuclei radius altered the critical pressure. Figure 6-3 shows the variations of the pressure results based on a range of initial radii, while maintaining the rest of the parameters constant. As expected, the pressure drops more when the initial radius is small, showing the influence of the tensile strength of the liquid (surface tension of the nuclei in the liquid). For larger initial radii the effect of the surface tension becomes less important, allowing the critical pressure to reach values closer to the actual vapour pressure, which for a temperature of 298.15 K is 3660 Pa.

The void fraction depends on both the initial radius and the bubble number density. In reality for larger initial radii the number density of initial nuclei should be smaller. However, for comparison purposes and to examine the behaviour of the void fraction the initial nuclei present were assumed constant for this simple test case, while the same radii variations as above were investigated. Figure 6-4 shows the change in the void fraction based on the radii discussed above.

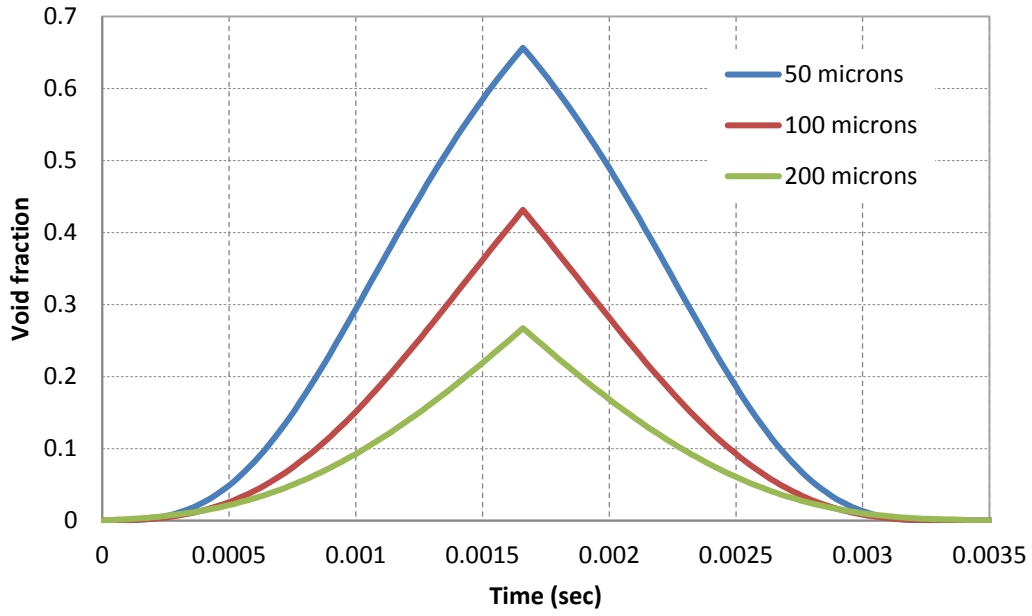

Figure 6-4: Void fraction comparison for varying initial bubble radii and constant nuclei number density.

The reduction in the void fraction is due to the fact that the initial radius governs the nuclei growth velocity, which in turn controls the radius growth and the void fraction of equation (6-11).

The dependence of the density on the void fraction is clearly shown in Figure 6-5. The more pronounced density fluctuations were obtained with the smaller nuclei radius. This is in accordance with the void fraction results obtained in Figure 6-4. The higher values of void fraction will associate a larger percentage of the particle to the vapour properties, thus leading to a much reduced mixture density.

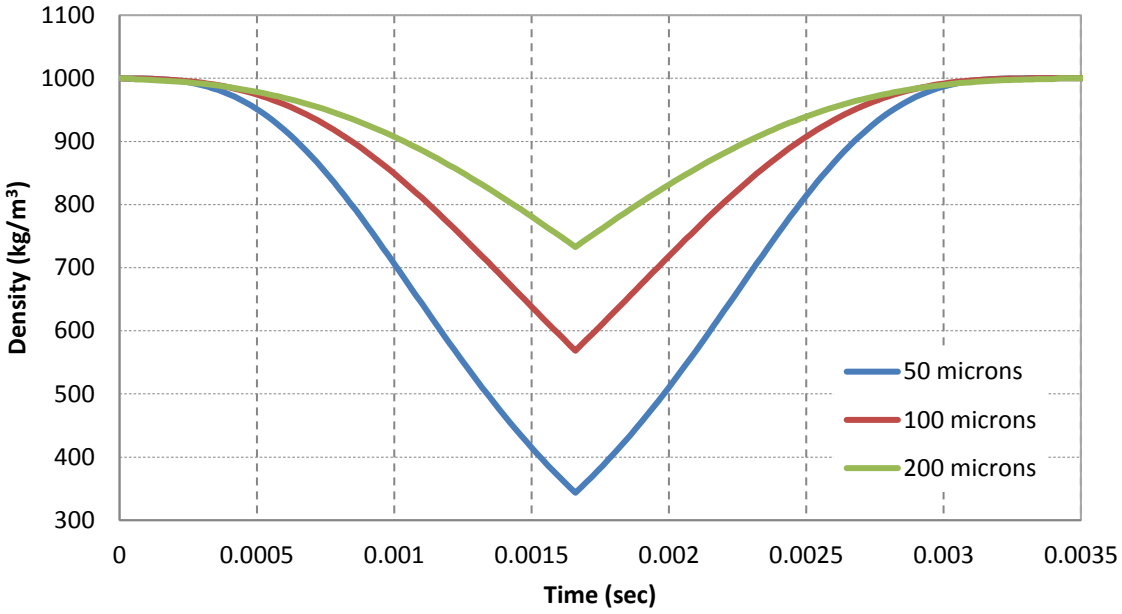

Figure 6-5: Density variation for varying initial bubble radii and constant nuclei number density. Higher void fractions lead to a larger percentage of the particle to the vapour properties and a reduced mixture density.

6.6.2 2D Venturi Case

A 2D venturi case is the first verification simulation. It is known that during the flow of liquid through a constricted area, such as in the venturi throat, the pressure drops and the fluid can experience cavitation. The aim of this example is to show that the fluid will experience cavitation in the vicinity of the venturi throat.

The following example has been modelled, based on the simulation analysis performed by Coutier-Delgosha et al. [100]. The numerical model used by Coutier-Delgosha et al. is an implicit finite volume algorithm, which solves the Reynold's-Averaged Navier-Stokes (RANS) equations and a barotropic law that links density to pressure.

The 2D venturi model is shown in Figure 6-6. The model has been designed with two parts. The first is the fluid, shown in green, which is allowed to translate only in the x-direction. The second part is the venturi shape, shown in red. This has been fully constrained in translations. Symmetry planes have been added at the top of the model at a distance of half the particle spacing, in order to provide the top section of the venturi. The total number of the SPH particles is 58770. The particle distance is 0.04 m and the smoothing length has been set at 0.052 m. The Gruneisen equation of state has been used for all the particles with atmospheric pressure applied to the moving particles. The input parameters for the equation of state are given below.

Table 6-5: Gruneisen EOS input data.

Velocity Curve Intercept, *C*, m/s	1482.9
First slope coefficient, S_1, -	2.0367
Second slope coefficient, S_2, -	0
Third slope coefficient, S_3, -	0
Gruneisen coefficient, γ_0, -	1
First order volume correction coefficient, α, -	0.5
Initial relative internal energy of moving particles, ε_0, kg/ms^2	101325
Initial relative internal energy of fixed boundary particles (venturi shape), ε_0, kg/ms^2	0
Initial relative volume, V_0, -	1

The final boundary condition is that two sets, 4 particles long, have been fully constrained in translations at either side of the moving fluid. These particles act as a barrier on either side of the moving fluid and they translate with the initial velocity assigned to the fluid. This was done in order to avoid leakage from the sides of the fluid model.

One aspect of this model is its length. Considering the inability of the MCM code to include inlet and outlet conditions, it was necessary to create a long enough model to allow the flow to become steady. The main simulation inputs are given in Table 6-6.

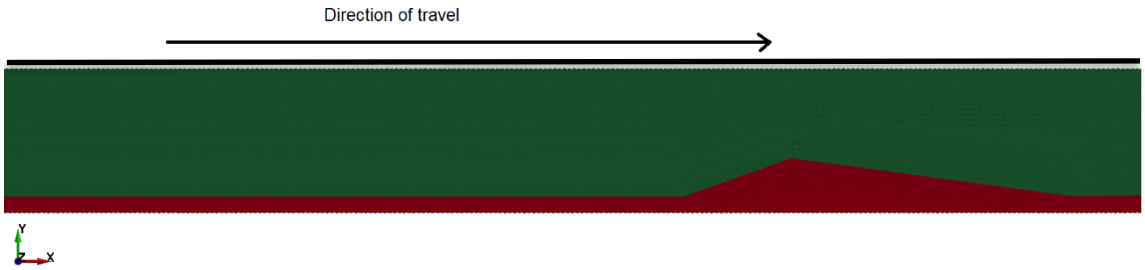

Figure 6-6: 2D venturi model with SPH particles. Green particles indicate the fluid and the red particles indicate the venturi shape. The venturi particles are constrained in translations. The black line indicates the presence of symmetry plane to avoid particles moving upwards.

Table 6-6: Initial input data.

Fluid length, m	74
Fluid height, m	1
Venturi overall length, m	142
Venturi inlet length, m	0.904
Venturi outlet length, m	2.34
Venturi height, m	0.39
Liquid density, kg/m^3	1000
Vapour density, kg/m^3	0.023
Nuclei number density (n), /m^3	8x10^7
Initial nuclei radius, m	5x10^{-5}
Temperature, K	298.15
SPH particles	58770
Mass of fluid, kg	76573
Mass of the venturi shape, kg	17494
Initial pressure of moving fluid, Pa	101325

Particle spacing, m	0.04
Initial velocity, m/s	7.2
Gravitational acceleration, m/s^2	9.81

The simulation results are shown in Figure 6-7 and Figure 6-8. The results were taken once the fluid had reached a steady solution. The steady solution was deemed satisfactory once the fluid showed nearly constant behaviour in the venturi region.

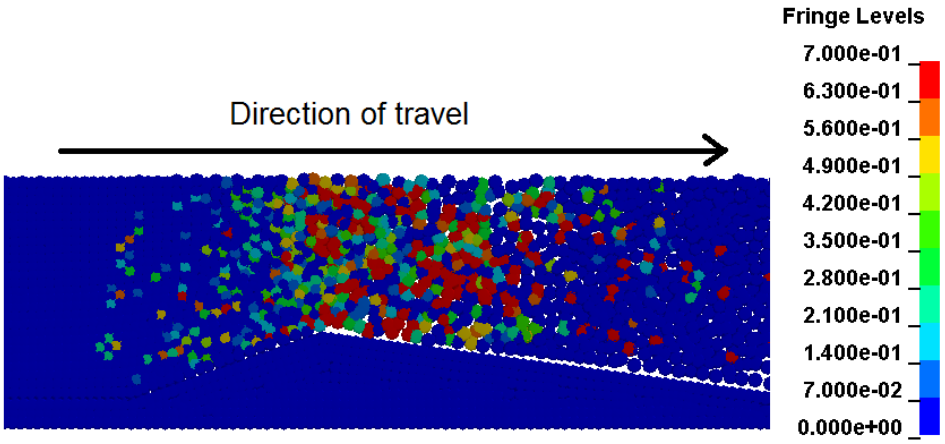

Figure 6-7: Void fraction results in the venturi region at 0.255 s. Fringe levels show void fraction. High concentration of cavitation is indicated at the throat of the venturi.

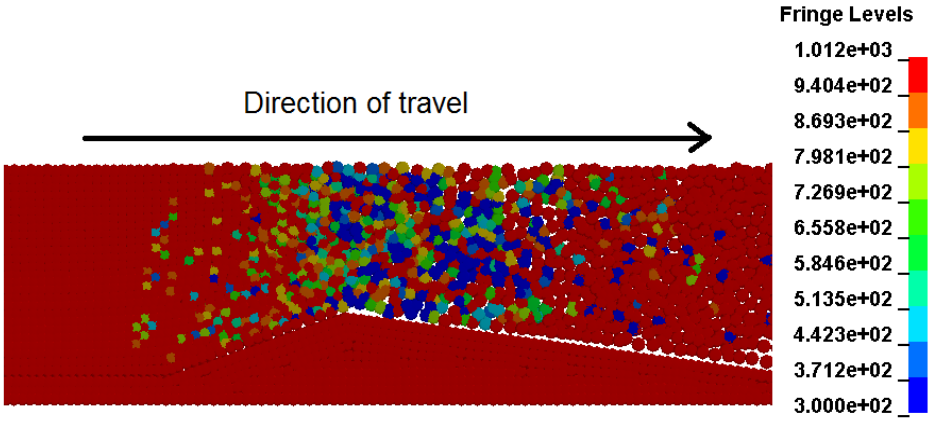

Figure 6-8: Fluid density results in the venturi region at 0.255 s. Fringe levels show density in kg/m^3. Drop in density is located at the throat of the venturi as a result of cavitation.

The results indicate that cavitation takes place in the throat of the venturi, as it is expected. As the SPH particles go through the venturi, the pressure drops and the cavitation model becomes active. The void fraction increases significantly, especially downstream. This leads to a rapid reduction of the density, which at this stage is composed of a liquid and a vapour part. As the void fraction increases, the density reduces further. Figure 6-9 shows the density results obtain by Coutier-Delgosha et al. [100]. The absolute density values compare reasonably well, with density variations in the cavitation regions ranging from 250-600 kg/m^3.

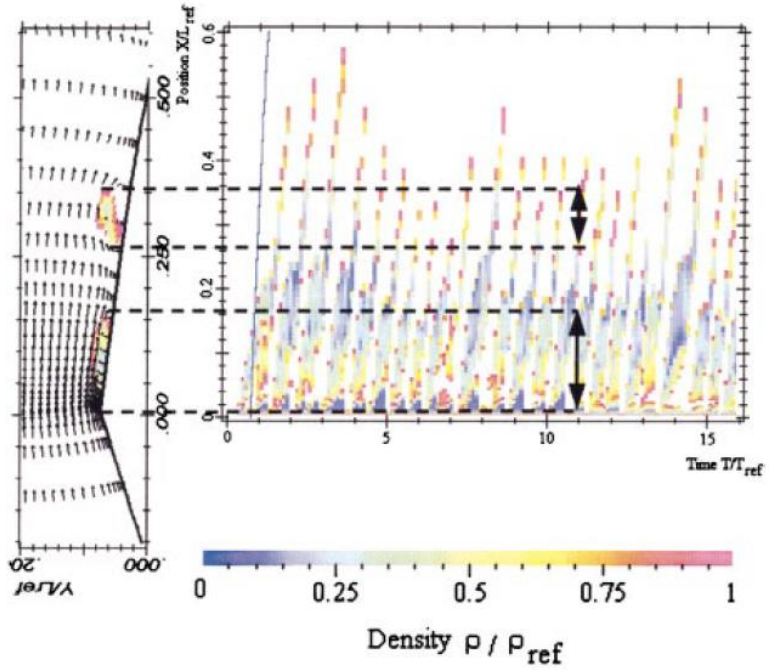

Figure 6-9: Density reduction downstream of the venturi by Coutier-Delgosha et al. [100]. Results show the variation of density as a fraction of the reference water density (1000 kg/m^3).

There are two main discrepancies between the published results and the results shown in Figure 6-7 and Figure 6-8.

The first one is related to the extent of cavitation in the throat of the venturi. In the published results, cavitation appears to be more concentrated near the throat. This difference can be caused by the fact that SPH and the MCM code can lead to high levels of noise especially for coarse particle distribution. This phenomenon is exacerbated by the symmetry plane that is applied at the top of the particles, as shown

in Figure 6-6. As the fluid travels through the throat of the venturi, pressure waves reflect from the symmetry plane resulting in further disturbance of the fluid. One remedy for this is to include a much larger water domain. This would however, be exceptionally expensive in terms of computation time, because the simulation only reaches a steady-state after 0.2 seconds. This means that the height of the water domain will need to be almost 300 m (for typical water speed of sound of 1483 m/s) in order to minimise the effect of reflected pressure waves. Additional remedies would include creating a much finer mesh and reducing the length of the body of water, to partly counteract the added computational costs. Considering that the aim of this verification simulation is to observe the cavitation taking place at the throat of the venturi, the above simulation is deemed to have an adequate particle spacing.

The second discrepancy is related to the occurrence of the cavitation cloud further downstream from the throat. This is caused by the fundamental differences between the MCM capabilities and the Reynolds-Averaged Navier-Stokes approach that was employed by Coutier-Delgosha et al. [100]. The lack of any turbulent modelling in the SPH code is the main reason why the code is not able to predict the re-entrant jet and the subsequent cloud cavitation occurring downstream of the venturi throat. This should not pose any restrictions in this project because the re-entrant jet and cloud cavitation are associated with attached cavitation, which is a cyclical process taking place when fluid passes over a streamlined cross section. In the case of aircraft ditching the interest lies in the transient cavitation, which is best described by the occurrence of cavitation at the throat of the venturi. For a more comprehensive approach to turbulence modelling in cavitation, the reader may refer to the work of Coutier-Delgosha et al. [100] and Singhal et al. [74].

6.6.3 2D Step Case

A 2D step example was also tried, where both attached cavitation and transient cavitation was found to be present in simulations performed by Zhang et al. [76]. The water flow velocity is 20 m/s in the bulk of the liquid and 30 m/s above the step. These velocities have been chosen so that the simulation follows the one performed by Zhang et al. [76]. The region where cavitation occurs in the published results is shown in Figure 6-10.

Figure 6-10: Cavitation evolution by Zhang et al. [76]. Attached cavitation shown in white.

The focus on this simulation is to investigate how well the code can simulate transient cavitation, caused by the low pressure behind the compression wave at the step, as well as the ability to simulate the cavity on top of the step. Table 6-7 shows the initial input data and boundary conditions for the test case.

Table 6-7: Initial input data.

Liquid density, kg/m^3	1000
Vapour density, kg/m^3	0.023
Nuclei number density (n), /m^3	1.2x10^7
Initial nuclei radius, m	0.0001
Temperature, K	298.15
SPH particles	56071
Mass, kg	548870
Initial pressure, Pa	101325
Particle spacing, m	0.1
Smoothing length, m	0.13
Gravitational acceleration, m/s^2	9.81

Symmetry planes have been added at the top and sides of the model at a distance of half the particle spacing. The Gruneisen equation of state has been used for all the particles with atmospheric pressure applied to the moving particles. The input parameters for the equation of state are given below.

Table 6-8: Gruneisen EOS input data.

Velocity Curve Intercept, *C*, m/s	1482.9
First slope coefficient, S_1, -	2.0367
Second slope coefficient, S_2, -	0
Third slope coefficient, S_3, -	0
Gruneisen coefficient, γ_0, -	1
First order volume correction coefficient, α, -	0.5
Initial relative internal energy, ε_0, kg/ms^2	101325
Initial relative volume, V_0, -	1

The final boundary condition is that two sets, 4 particles long, have been fully constrained in translations at either side of the moving fluid. These particles act as a barrier on either side of the moving fluid and they translate with the initial velocity assigned to the fluid. This was done in order to avoid leakage from the sides of the fluid model.

An overview of the model is given below. The step was also modelled with SPH particles, which were fixed in both translation and rotation.

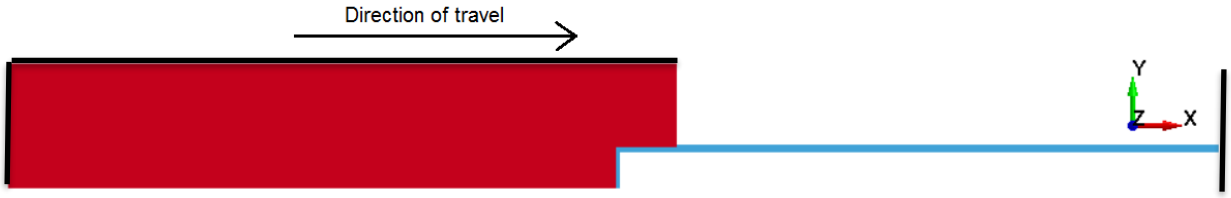

Figure 6-11: Water (red) and step (blue) composed of SPH particles. Step particles are fixed in translations and rotations. The black lines indicate the presence of symmetry planes.

The water domain to the left of the step is 50 m in length and 10 m in height, whereas the length of the water domain over the step is 5 m and the height is 6.6 m.

With respect to the transient cavitation, Figure 6-12 and Figure 6-13 show the pressure and void fraction in the bulk of the liquid. As the pressure wave travelled away from the

step, the pressure started to drop allowing for the creation of cavitation. The extent of the cavitation can be seen in Figure 6-13, where the void fraction increased up to its maximum value of 0.7.

Looking into the steady-state attached cavitation in Figure 6-14, the cavity started to form early on during the simulation. However, steady-state solution would require a large number of particles and additional computational cost. In this simulation there were not enough particles so as to capture possible shedding, as this is not the primary interest of this research. Moreover, particles close to the right wall of the simulation also experienced some cavitation, which is due to the disturbance by the presence of the reflected wave.

It becomes evident that a larger fluid domain is needed in order to reduce the effect of any reflected wave on the evolution of cavitation. In theory, sheet cavitation is usually accompanied by transient cavitation bubbles at its top. The results show that particles close to the sheet cavitation started to act like cavitation bubbles with an increase of void fraction. Based on the simulation results by Zhang et al. [76] the attached cavity should cover approximately 1.9 m. The fully developed attached cavity in this case was 1.8 m.

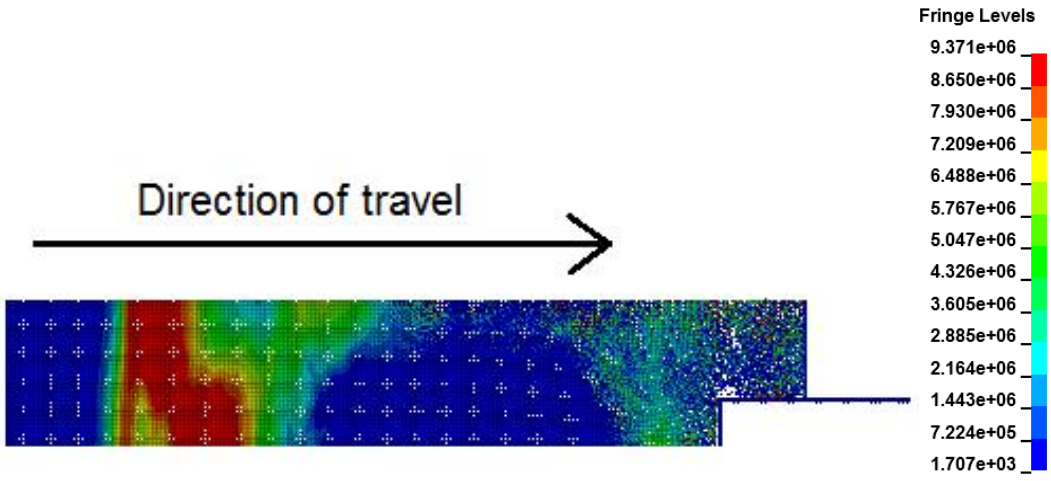

Figure 6-12: Pressure distribution at 0.042 s for the liquid domain. Fringe levels show pressure in Pa.

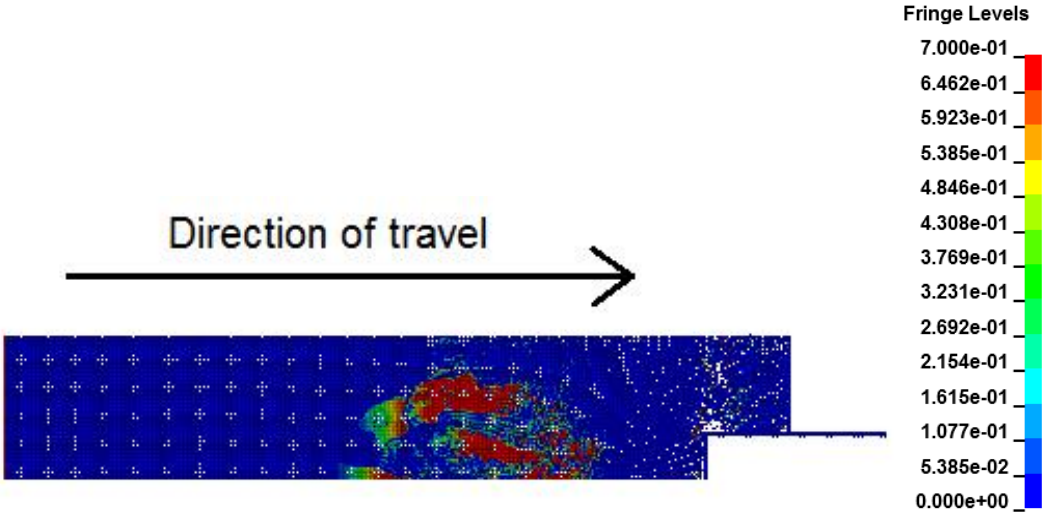

Figure 6-13: Void fraction behind the pressure wave at 0.042 s. Fringe levels show void fraction.

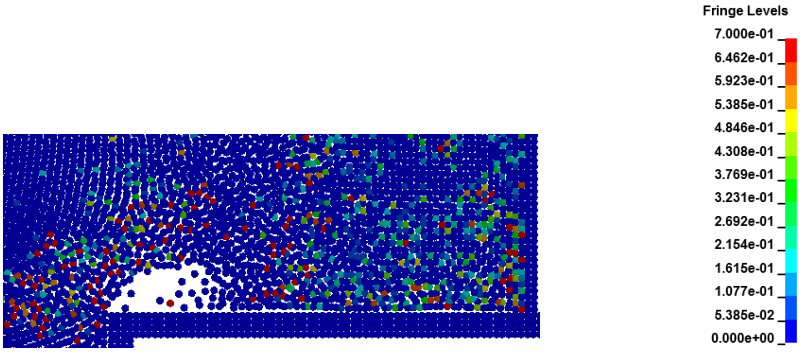

Figure 6-14: Zoomed in area of the void fraction at the flow step interface at 0.04 s. Fringe levels show void fraction.

The initial verification of the code has shown that the code works appropriately. It is evident that the results are dependent on the parameters that the user defines. With respect to pressure variations, the two parameters that can influence the results are the initial nuclei radius and the temperature. With respect to the density of the mixture, the initial radius and the number of nuclei are the most influential parameters. Insufficient number of nuclei can result in less pronounced cavitation and smoother density variations.

6.6.4 2D Tube Case

The following simulation is a 2D block of water particles, which move in opposite directions. This set-up has been implemented with other cavitation algorithms in the past so a comparison of results could provide an insight of whether the current code

provides acceptable results. Moreover, a comparison between the new code and the cut-off approach will be discussed.

The block of water consists of 671 particles spaced at 0.025 m apart with a total mass of 419.375 kg. The length of the model is 1.5 m and symmetry planes have been applied in order to constrain any vertical motion. Table 6-9 shows the initial data used for these simulations while Figure 6-15 shows the initial state of the tube. The Gruneisen equation of state has been used with atmospheric pressure applied to the particles. The input parameters for the equation of state are given in Table 6-10. The various sensitivity cases that were considered are presented in Table 6-11.

Table 6-9: Initial data for the 2D tube experiment.

Initial Pressure, Pa	101325
Density, kg/m^3	1000
Fixed velocity, m/s	+100/-100
Temperature, K	298.15
Length, m	1.5
Height, m	0.25
SPH Particles	671
Mass, kg	419.4
Particles spacing, m	0.025
Smoothing length, m	0.0325

Table 6-10: Gruneisen EOS input data.

Velocity Curve Intercept, *C*, m/s	1482.9
First slope coefficient, S_1, -	2.0367
Second slope coefficient, S_2, -	0
Third slope coefficient, S_3, -	0
Gruneisen coefficient, γ_0, -	1
First order volume correction coefficient, α, -	0.5
Initial relative internal energy, ε_0, kg/ms^2	101325
Initial relative volume, V_0, -	1

The final boundary condition is that two sets, 3 particles long, have been fully constrained in translations at either side of the moving fluid. These particles act as a barrier on either side of the moving fluid and they translate with the initial velocity assigned to the fluid. This was done in order to avoid leakage from the sides of the fluid model.

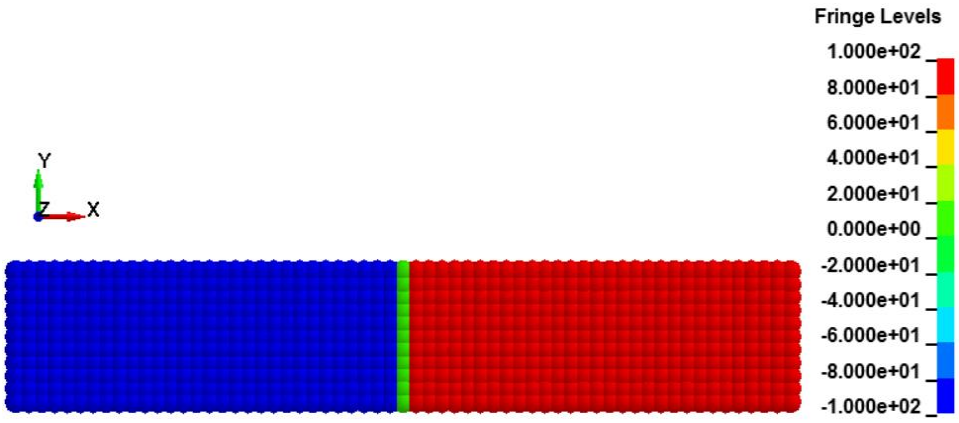

Figure 6-15: SPH particles for 2D tube experiment showing initial velocity applied in opposite directions. Fringe levels show velocity in the x direction in m/s.

Table 6-11: Initial radius and nuclei number density sensitivity cases.

Initial radius *r*	nuclei number density (n) /m^3	
50 μm	$9x10^7$	$2.5x10^{10}$
100 μm	$3.7x10^7$	$8x10^7$
200 μm	$3.7x10^7$	$8x10^7$

The symmetry planes have been applied at the top and bottom of the water domain, at half the particle distance, in order to keep the SPH particles from moving along the y-direction. The symmetry planes are shown in Figure 6-16.

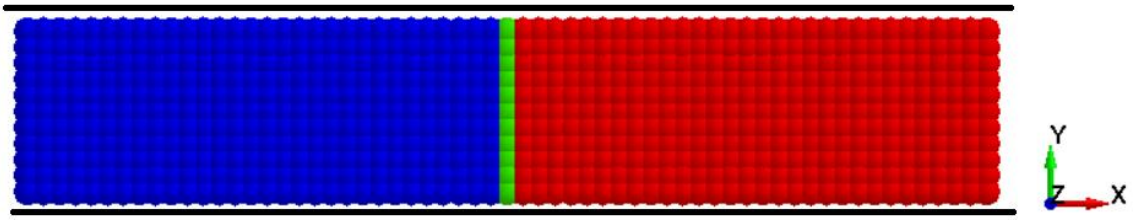

Figure 6-16: Symmetry planes shown in black indicate the restriction in the y-direction. The symmetry planes are applied at half the inter-particle distance (0.0125 m) on top and at the bottom of the water domain.

This simple simulation has been performed by [86] and there is a direct comparison between their results and the cut-off method. The approach that they used is a barotropic relation, so the pressure results do not take into account the tensile strength of the liquid, such as in this project. It must also be noted that the simulation by [86] is for a tube that is 1 m in length compared to the one in this project that is 1.5 m. The parameters that were discussed are the density and the pressure behaviour of the water tube. Figure 6-17 shows the results of their simulations at 0.2 ms and will be the basis of comparison for the method used in this project.

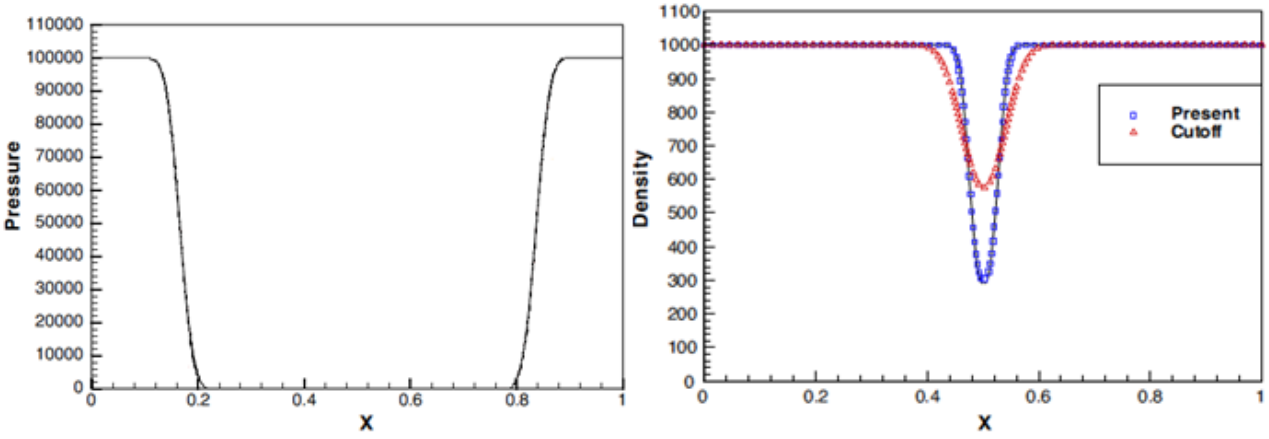

Figure 6-17: Pressure and density results at 0.2 ms at the centre of the 2D tube as obtained by Liu et al. [86]. Cut-off model considers only the presence of water with a cut-off pressure of 0 Pa and it does not take into account the effect of vapour in the water. The present model is the barotropic model used by Liu et al. in their implementation of cavitation.

The combination of radius and nuclei number density that provided similar results as the publications is for 50 microns and n=2.5x10^{10} /m^3. The pressure drop in the middle of the tube is expected as the fluid is stretched under the opposite direction velocity. Figure 6-18 shows the pressure distribution at 0.2 ms as performed with the new cavitation approach. As expected, the pressure drop is symmetric and did not fall below the critical pressure. It follows closely the results by [86]. Figure 6-17 shows that the liquid experienced cavitation between 0.4 m-0.6 m along the length of the tube. For a 1.5 m tube such as in this project this translates to 0.6 m-0.9 m. Indeed, the results from Figure 6-19 captured the phenomenon in this region.

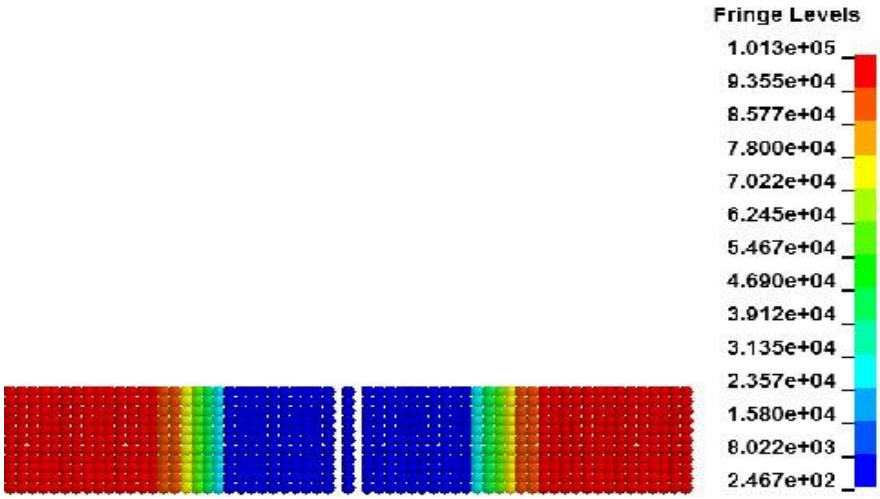

Figure 6-18: Pressure distribution for 2D tube at 0.2 ms. Fringe levels show pressure in Pa. The pressure drops in the middle of the 2D tube as the particles move apart (going into tension), leading to the occurrence of cavitation.

The difference between the simple cut-off model and the new model with respect to the pressure is evident in the close up of Figure 6-19. The difference becomes more apparent in the density comparison that follows.

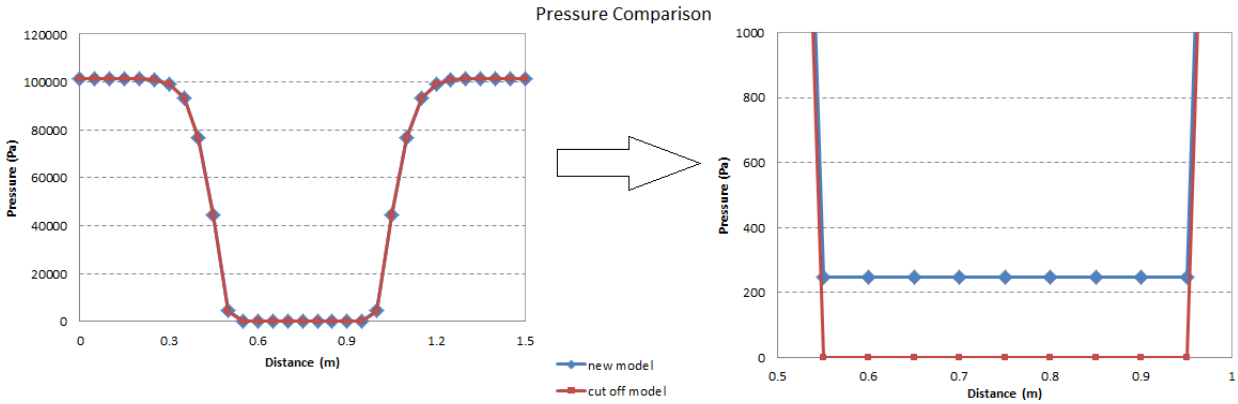

Figure 6-19: Pressure comparison between cut-off and new model at 0.2 ms. Pressure taken at the centre of the 2D tube. The cut-off model simply caps the pressure at 0 Pa, whereas the new model takes into account the effect of the "tensile strength" of the liquid, radius of initial nuclei and the vapour pressure.

The density variation is shown in Figure 6-20. The density dropped in the middle of the tube as the pressure dropped. The sharp reduction in the density occurred when the particles reached the critical pressure and cavitation was initiated.

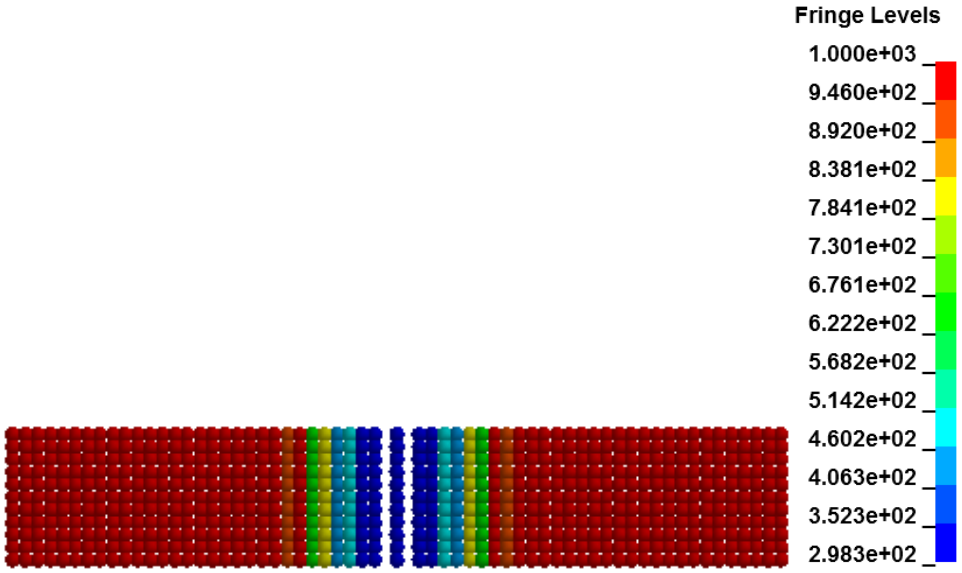

Figure 6-20: Density variations in the 2D tube at 0.2 ms. Fringe levels show density in kg/m^3. The pressure drops in the centre of the 2D tube as the particles move apart (going into tension), leading to a reduction in pressure.

The graph in Figure 6-21 shows the difference between the new cavitation model and the cut-off approach. The results fit fairly well with the published results. The peak densities are captured well, even though density changes for the new cavitation model covered a much wider region. This could be due to the fact that the particle spacing was too coarse, which led to a much bigger interpolation region (smoothing length value). Finer particle distribution would lead to a more localised interpolation region, thus the density variations can be found in a more confined region towards the centre of the 2D tube.

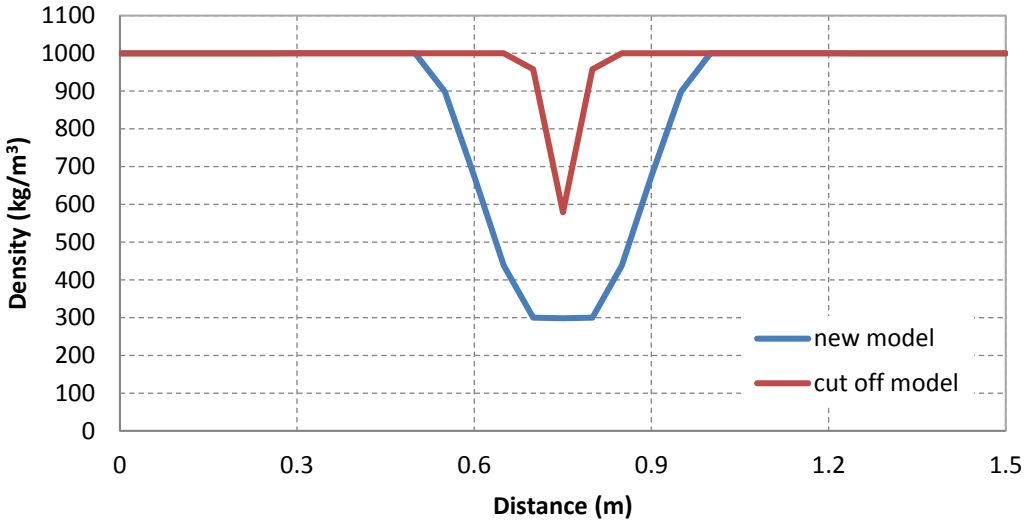

Figure 6-21: Density comparison at the centre of the 2D tube between cut-off and the new model at 0.2 ms. The new model considers the effect of vapour leading to a reduced density at the centre of the 2D tube when compared to the simpler cut-off model. The cut-off considers the fluid to be pure water.

The rest of the test cases shown in Table 6-11 are shown in Figure 6-22. One of the major conclusions is that the density drop is strongly dependent on the nuclei population, *n*. For a given initial radius, it is observed that the increase in *n* reduces the density further, showing that the cavitation severity becomes stronger. A secondary conclusion is that the current methodology is highly sensitive to both the initial radius and the initial number of nuclei. In order to capture the correct results for a specific case, a range of values should be tried. This necessity for a sensitivity analysis can be described as one of the disadvantages of the new cavitation approach.

Further tests included the application of the 2D tube experiment with gauge pressure terms. Appropriate changes have been made in the code to allow the user to decide whether absolute or gauge terms will be used. The results were identical for the density and the magnitude of the pressure drop was the same (even though it goes into negative gauge values).

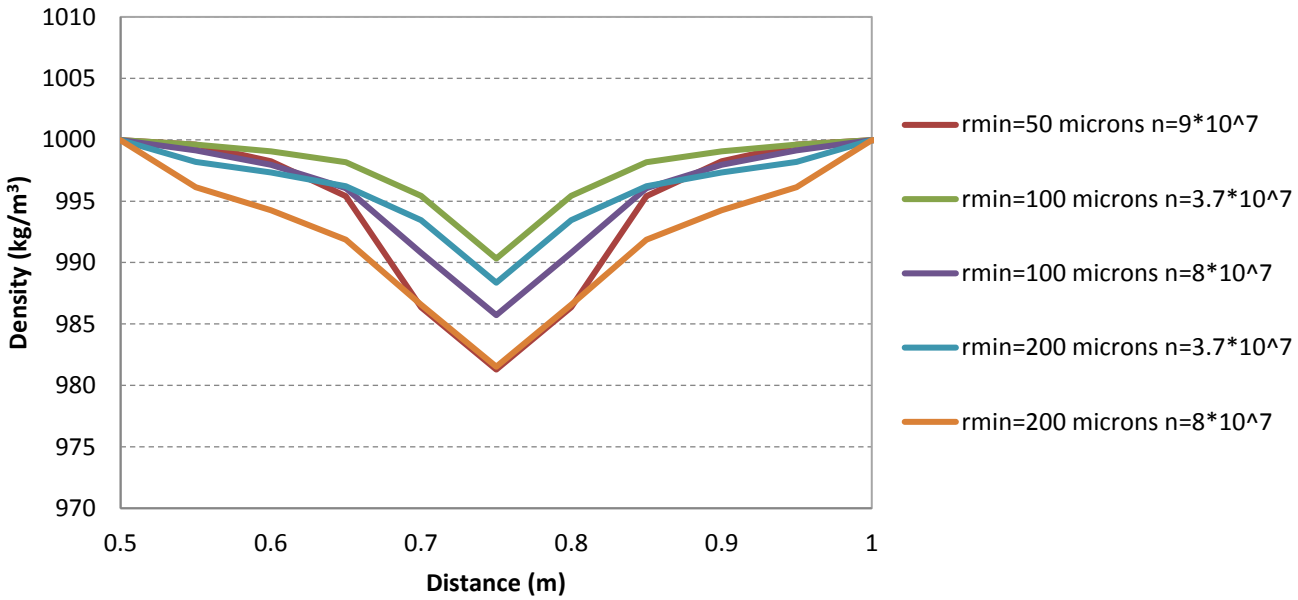

Figure 6-22: Density variation at the centre of the 2D tube for an arbitrary set of initial radii and nuclei number densities (given per m^3).

6.7 Inclined Plate Impact

A set of simulations were performed with the simple inclined plate described in Section 5.3, as it is a one of the SMAES initiative test cases. The purpose of these simulations was to establish the behaviour of the fluid domain in a forward velocity impact case and observe the influence of the cavitation parameters. Table 6-12 shows the complete set of simulations described in this section.

Table 6-12: Overview of test cases

Initial radius *r*	Nuclei number density (n) /m^3
100 µm	$6x10^8$
100 µm	$7x10^8$
100 µm	$8x10^8$
100 µm	$9x10^8$

The initial pressure was set at 101325 Pa. Finally, the temperature, required for determining the coefficients that are used for the Antoine equation, was taken as 298.15K (25°C).

Since there were no experimental results for comparison, the selection of the number of nuclei was based on an iterative procedure, based on the qualitative results shown in Figure 6-23 and Figure 6-24 for a water domain of 1 m depth.

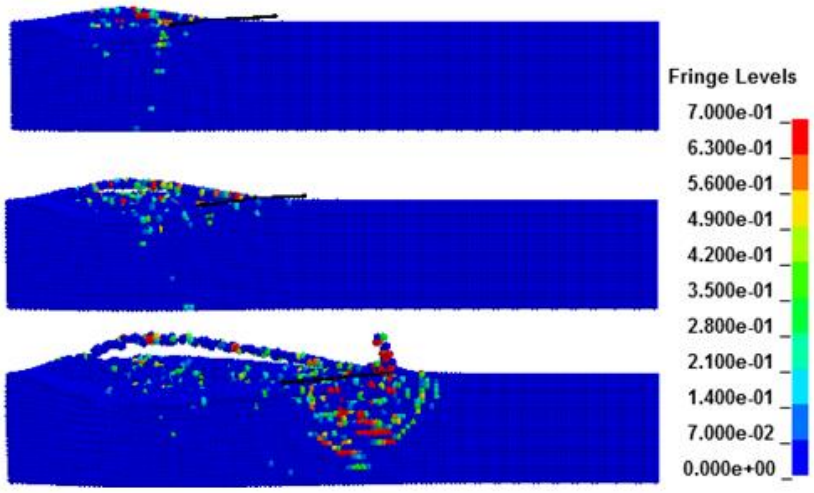

a) Plots at 0.05 s, 0.065 s and 0.084 s

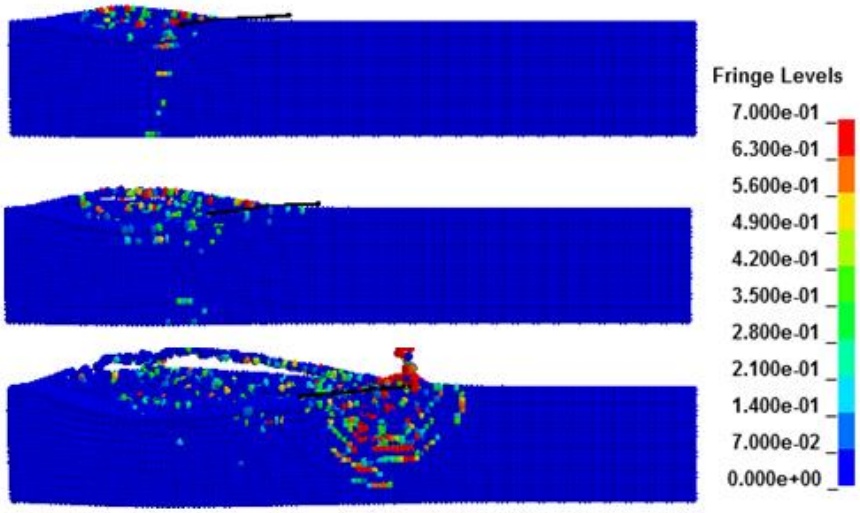

b) Plots at 0.05 s, 0.065 s and 0.084 s

Figure 6-23: Void fraction evolution for a) n=6x10^8 /m^3 and b) n=7x10^8 /m^3 for 1 m deep water domain. Fringe levels show void fraction. Side plane cut view of 3D impact evolution. Direction of travel from left to right.

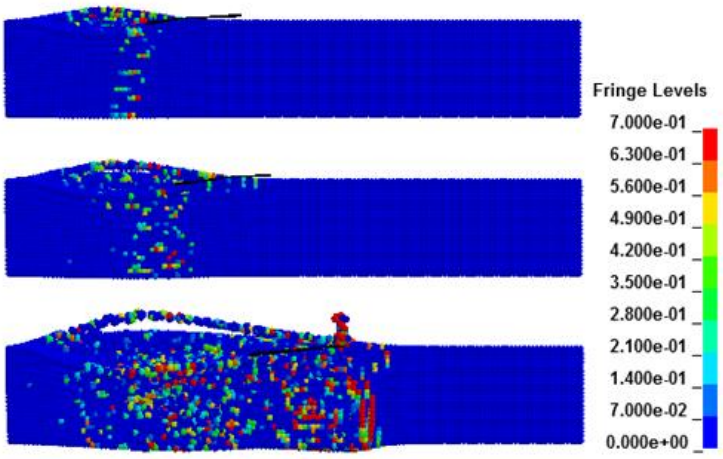

a) Plots at 0.05 s, 0.065 s and 0.084 s

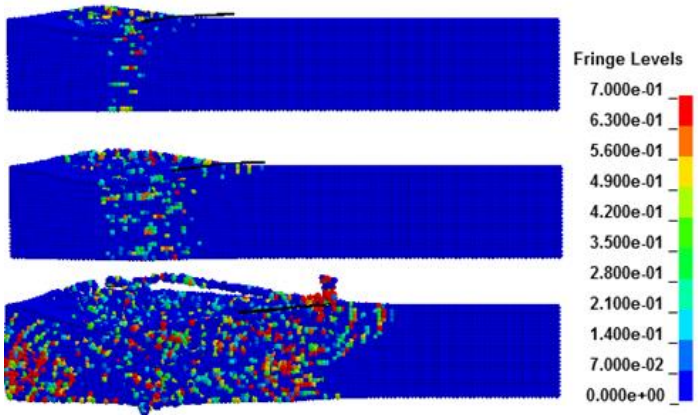

b) Plots at 0.05 s, 0.065 s and 0.084 s

Figure 6-24: Void fraction evolution for a) n=8x10^8 /m^3 and b) n=9x10^8 /m^3 for 1 m deep water domain. Fringe levels show void fraction. Side plane cut view of 3D impact evolution. Direction of travel from left to right.

The results of Figure 6-23 do not show significant differences and the void fraction followed a reasonable pattern, as the pressure wave propagated in a radial direction. The highest level of cavitation was present during the impact of the leading edge of the plate, where the particles in the region reached the maximum allowable void fraction of 0.7. This could be due to the fact that as the particles at the leading edge detached from the free surface they experienced tensions that could possibly reach low enough values for cavitation to occur. Another reason for this behaviour is that the impact of the leading edge is severe enough to produce tension in the fluid that can lead to cavitation

or that the motion of the plate, as in the results of Chapter 5, caused oscillations to the pressure field.

The void fraction results shown in the cross sections above illustrate the severity of cavitation based purely on the nuclei population. The cavitation region increased in size as the number of nuclei increased in number.

For the cases shown in Figure 6-24 the relatively high nuclei population led to cavitation at the bottom boundary, where the particles experienced tension as they moved outwards artificially. The artificial “bulging” of the particles at the bottom can lead to tensions which then propagate radially towards the free surface producing a noisy signal. For the interest of this project, it would be ideal to avoid any noise at least until the leading edge of the plate impacts the water. Hence the depth of the water domain was increased to 2 m and the case of $n=8x10^8$ $/m^3$ was selected in order to evaluate any changes in the water domain behaviour (Figure 6-25).

The most significant change is the fact that the particles at the boundary exhibited a much higher level of disturbance and similar noisy signal were observed. Moreover, it is observed that during the middle stage, the growth of the void fraction is concentrated in a smaller region in comparison to the equivalent results of Figure 6-24. This means that the simulations can provide a qualitatively more accurate representation of cavitation further away from the boundary. Cavitation is expected to occur near the structure and should not influence the entire fluid domain. The boundary effects present in these simulations are less pronounced compared to the shallow water model.

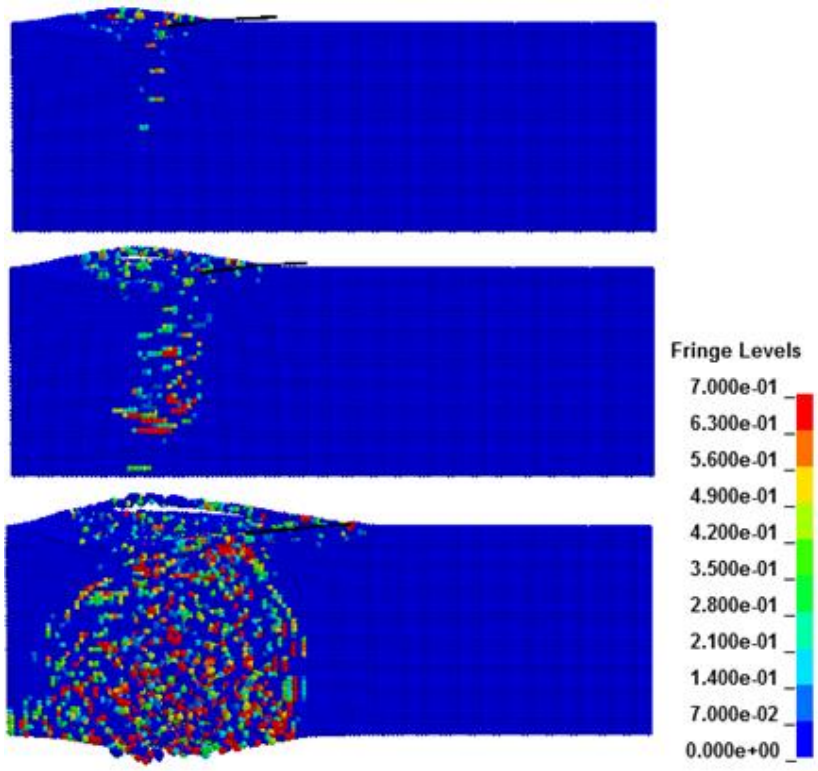

Figure 6-25: Void fraction evolution for n=8x10^8/m^3 for 2 m deep water domain. Fringe levels show void fraction. Side plane cut view of 3D impact evolution. Direction of travel from left to right. Results shown at 0.04 s, 0.058 s and 0.074 s.

In order to avoid the particle disturbance at the bottom boundary, symmetry planes were added. The same test case as in Figure 6-25 is shown in Figure 6-26. The results immediately improved with respect to the disturbance at the boundary, however the noisy signal was still present. Since the symmetry planes act as physical barriers to the water domain the noisy signal was due to the reflected pressure waves. The depth however, was adequate since the noisy signal did not dominate throughout the simulation as it was observed in Figure 6-24 and to a lesser extent in Figure 6-25.

The results so far indicate that the particles at the bottom boundary can lead to noisy signals, either due to the artificial tension which leads to an increase in the void fraction (for the case of no symmetry planes) or due to the reflection of pressure waves caused by the inclusion of symmetry planes. In both cases a water domain large enough should be used so that any noisy signal does not influence the region close to the plate.

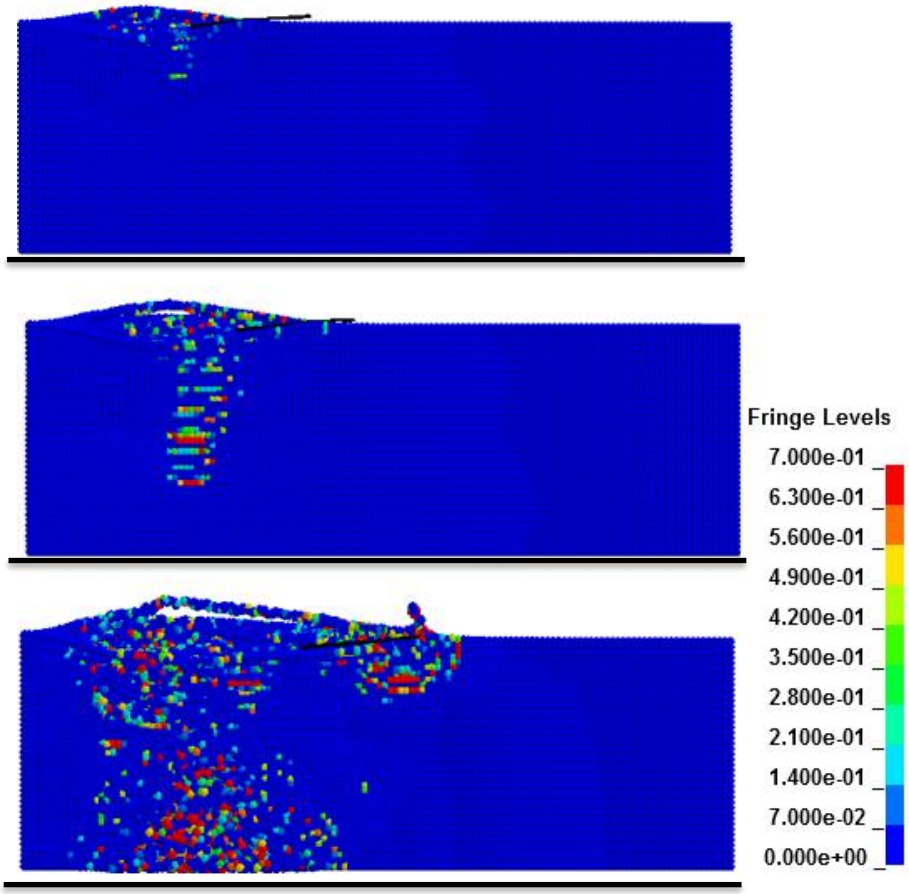

Figure 6-26: Void fraction evolution for n=8x10^8 /m^3 for 2 m deep water domain with symmetry planes applied. Side plane cut view of 3D impact evolution. Direction of travel from left to right. Results shown at 0.04 s, 0.058 s and 0.074 s. The black line indicates the boundary symmetry plane.

It should be noted that the distinct void fraction area at the leading edge, shown in the latest stage of impact of Figure 6-26, is similar to the one of Figure 6-23, further suggesting that a large enough water domain is necessary.

The initial 1 m deep test case was also tried for comparison purposed with the symmetry planes applied and is shown in Figure 6-27. Once again, there was no particle disturbance at the bottom boundary, however the shortcomings of the smaller depth of the water domain for high number of nuclei become evident with the propagation of the noisy signal.

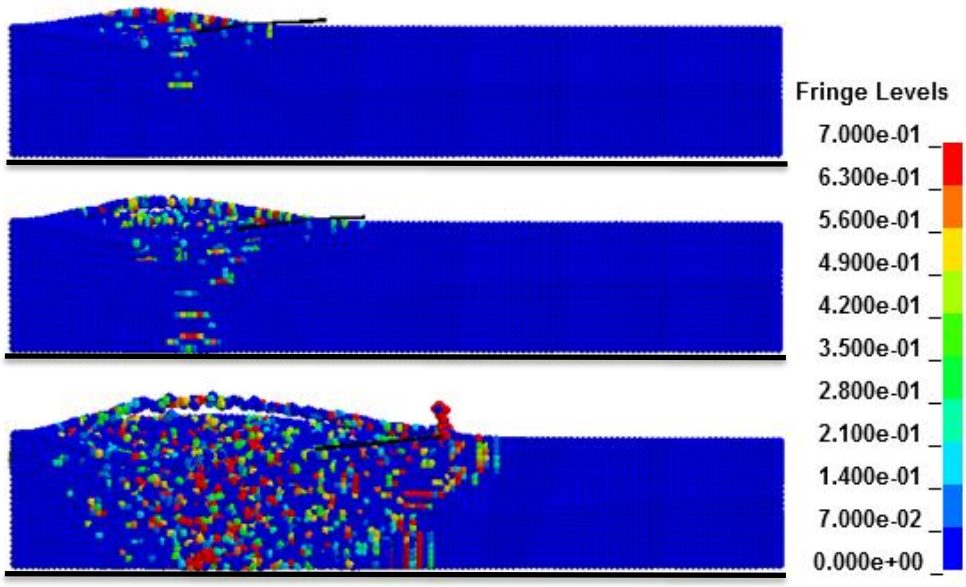

Figure 6-27: Void fraction evolution for n=8x10^{8} /m^{3} for 1 m deep water domain with symmetry planes. Side plane cut view of 3D impact evolution. Direction of travel from left to right. Results shown at 0.04 s, 0.058 s and 0.074 s. The black line indicates the boundary symmetry plane.

In addition to the inclined plate tested above, a more complete model was attempted. This model is representative of the experimental se- up provided as part of the SMAES initiative. The plate represents part of the bottom of the fuselage, whereas the addition of the trolley system is added in order to guide the impact of the plate under the specified initial conditions. The Finite Element model consists of a plate, support structure and trolley system and a full description, including material properties, is given in Figure 6-28. At the time of these simulations experimental results were not yet fully available, so a general description of the applicability of the cavitation method is provided.

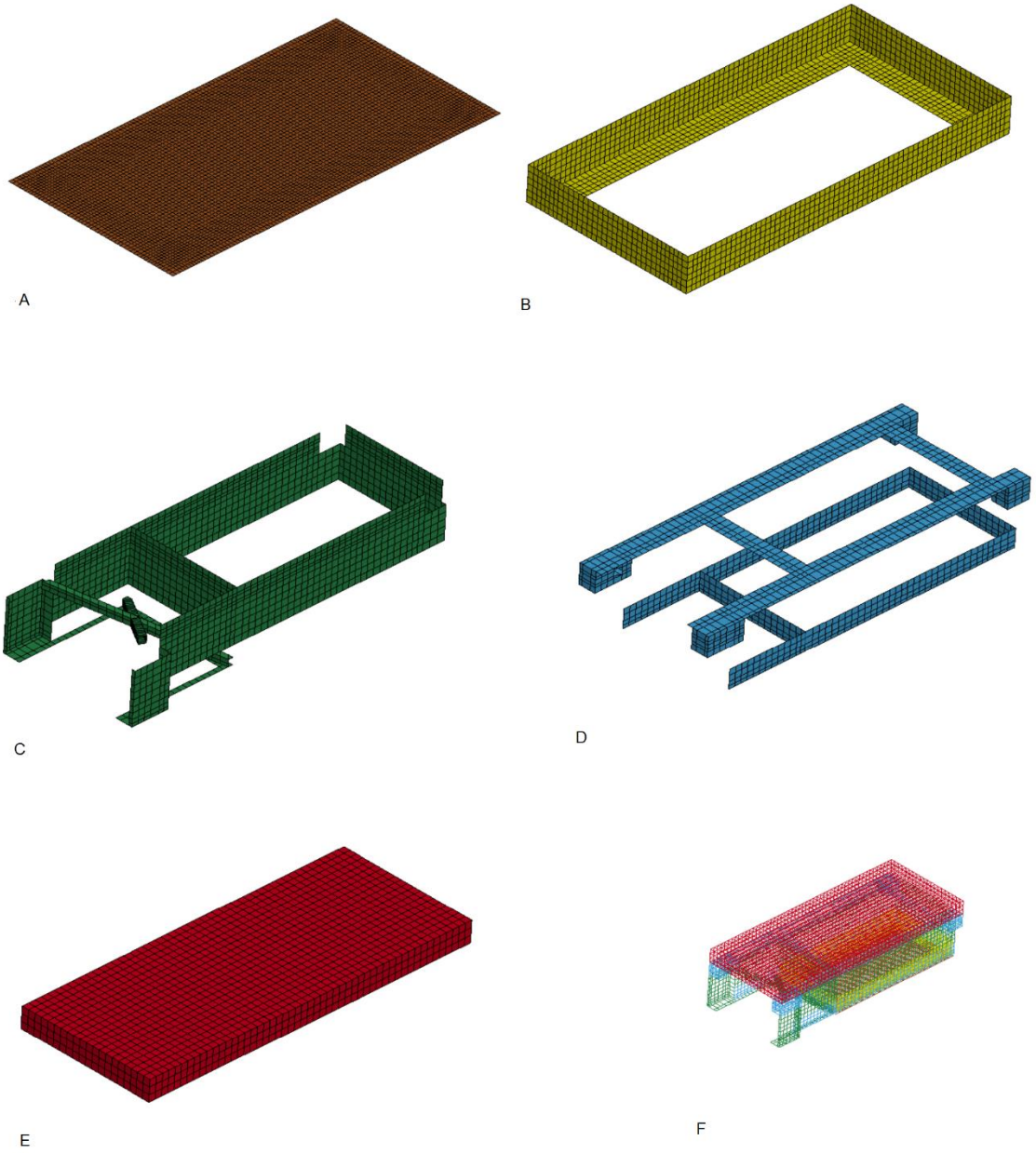

Figure 6-28: SMAES plate and trolley components. Figure based on Aparici [101].

The initial data used for the structure and the water domain and the structure are given in Table 6-13, Table 6-14 and Table 6-16.

Table 6-13: Description of trolley and plate components. Table based on Aparici [101].

Component	Thickness	Shells	Solids	Mass	Material
Plate [A]	1.5 cm	5304	-	20.85 kg	Al Alloy 2024-T351
Frame [B]	1 cm	2144	-	36 kg	Mild Steel
Trolley Skin [C]	0.3 cm	3744	-	27.05 kg	Mild Steel
Support frame [D]	0.6 cm	2434	-	39.89 kg	Mild Steel
Solid mass (also accounting for wheels' mass) [E]	9.1 cm	-	3060	666.21 kg	Mild Steel

The structure has a prescribed horizontal velocity of 40 m/s, a prescribed vertical velocity of 1.5 m/s and acceleration applied at 9.81 m/s^2. The structure has a sliding boundary plane defined, which prescribes the motion of all the elements. In this case, a vector has been defined and all the nodes can only translate along this vector.

Additionally, nodal constraints have been defined for the plate and the frame and also for the trolley skin and the support frame. This allows each of these structures to act as a single rigid body.

Table 6-14: Initial input for SMAES plate impact.

FE plate inclination, °	4
FE plate prescribed forward velocity, m/s	40
FE plate prescribed vertical velocity, m/s	1.5

The material properties for each of the components is given below.

Table 6-15: Material properties for FE structure.

Material	Young's Modulus, Pa	Poisson's ratio, -	Yield stress, Pa
Al Alloy 2024-T351	$7.2x10^{10}$	0.3	$3.24x10^{8}$
Mild Steel	$2.1x10^{11}$	0.3	$4.7x10^{8}$

The input parameters for the water domain are given below.

Table 6-16: Initial input for water domain for SMAES plate impact.

Number of particles	19200
Fluid Length, m	6
Fluid Width, m	1
Fluid Depth, m	0.4
Water density, kg/m^3	1000
Mass, kg	2400
Particle spacing, m	0.05
Smoothing length, m	0.06
Nuclei number density (n), $/m^3$	$2.5x10^{8}$
Initial nuclei radius, m	$5x10^{-5}$
Initial pressure, Pa	101325
Temperature, K	298.15

The overall model is shown in Figure 6-29.

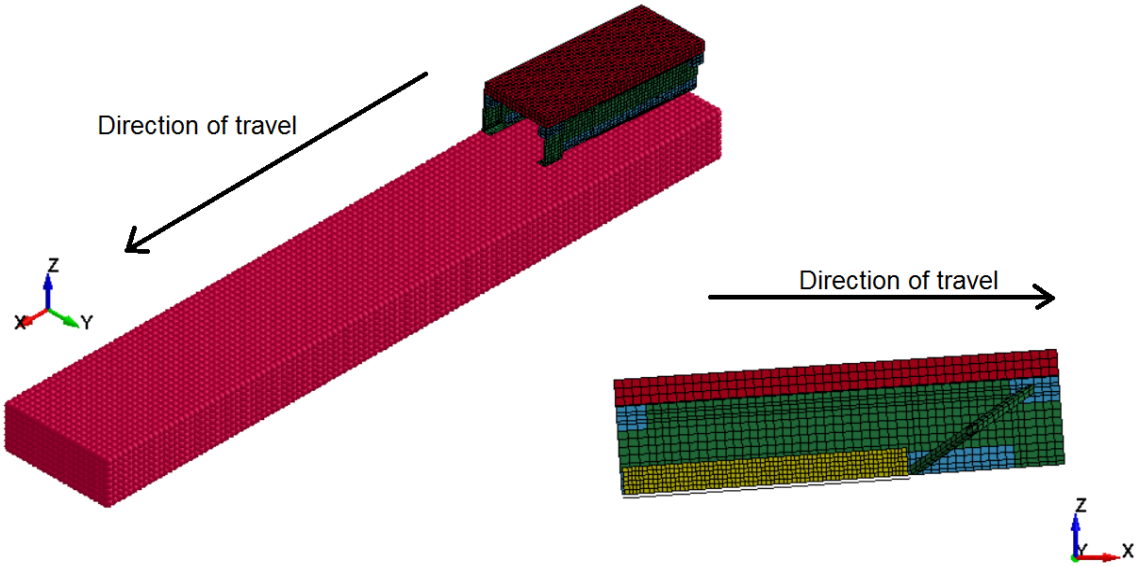

Figure 6-29: Overall description of the model. On the left is the water domain and the structure and on the right is a view through the vertical symmetry of the structure.

The Murnaghan equation of state was used. The parameters are given below.

Table 6-17: Murnaghan EOS input data.

Bulk Modulus B, MPa	550.0
Parameter γ, -	4.0

Finally, symmetry planes have been applied around the model as shown below.

Table 6-18: Symmetry plane coordinates.

Xmin	Xmax	Ymin	Ymax	Zmin	Zman
-2.0 m	8.0 m	-1.5 m	1.5 m	-2.0 m	1.0 m

The above symmetry planes allow for the fluid particles to move freely within the coordinates defined by the symmetry planes, while minimising the potential of numerical instability caused by particles that have moved at great distances and are no longer relevant to the simulations.

Initial results, Figure 6-30, showed that the depth of the water domain is extremely small leading to tension at the bottom boundary, which then propagated to the rest of the water domain in a similar manner to the previous simulations. A depth of four times the initial size, 1.6 m, was also considered with 121,000 particles as shown in Figure 6-31 which still provided a noisy signal. Looking at the effect of the nuclei number density, it is evident that further sensitivity cases should be conducted to find an acceptable level of depth in combination with an acceptable level of nuclei number density. Time constraints however did not allow for a more detailed investigation of this specific set-up.

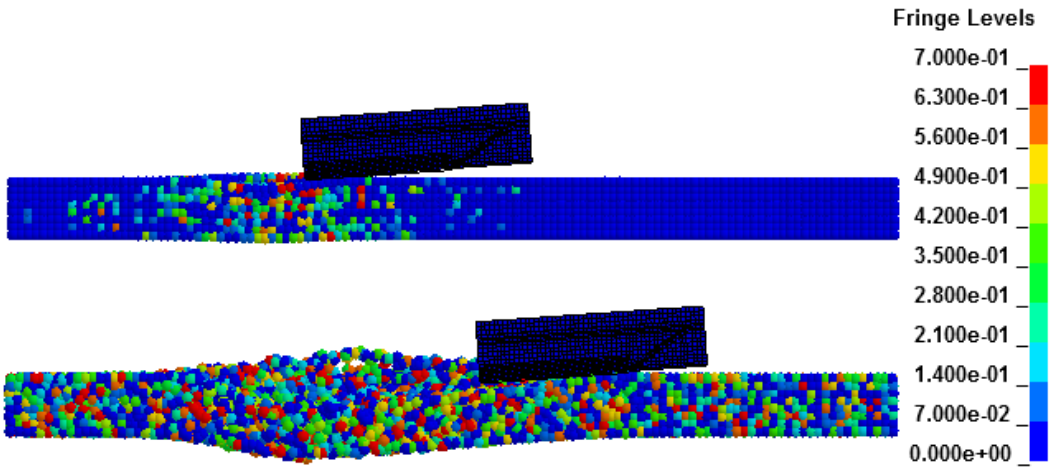

Figure 6-30: Void fraction evolution for n=2.5x10^8 /m^3 for 0.4 m water depth. Fringe levels show void fraction. Side plane cut view of 3D impact evolution. Direction of travel from left to right. Results shown at 0.04 s and 0.08 s.

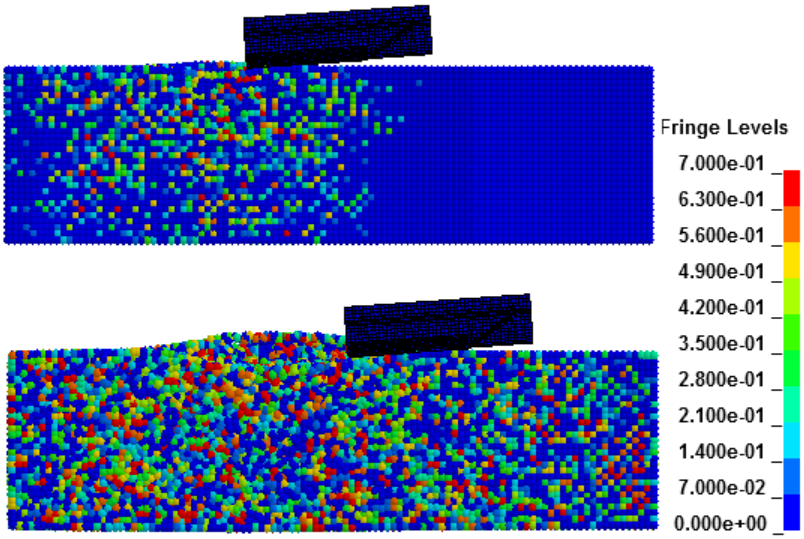

Figure 6-31: Void fraction evolution for n=2.5x10^8 /m^3 for 1.6 m water depth. Fringe levels show void fraction. Side plane cut view of 3D impact evolution. Direction of travel from left to right. Results shown at 0.04 s and 0.08 s.

Deeper water domains were prohibitively expensive to perform, which is one of the main difficulties facing high forward velocity impacts. However, an additional test case with lower nuclei number density was also performed similar to the earlier models, since it was found that it can confine the extent of cavitation. The nuclei number density chosen for this simulation is $n=1x10^8/m^3$ and the results are shown in Figure 6-32.

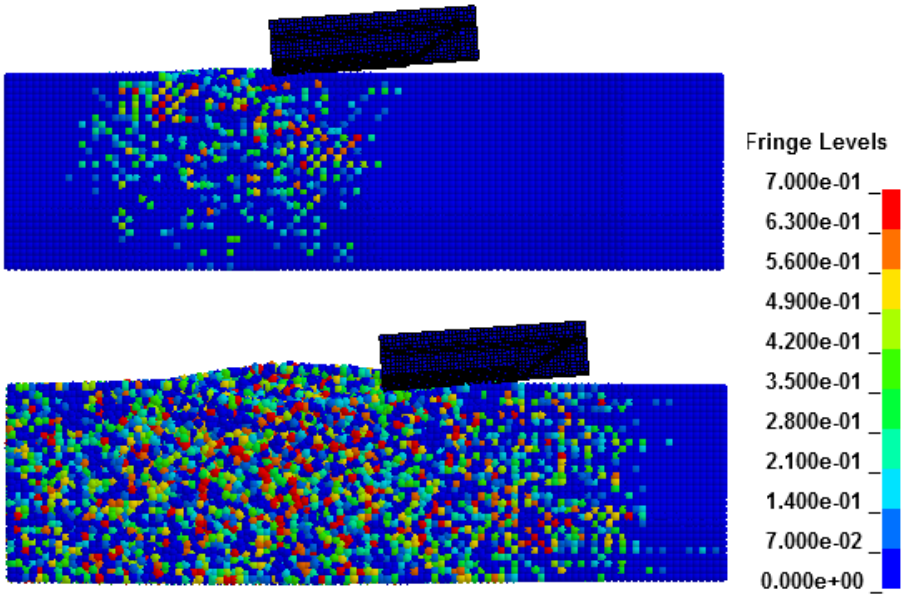

Figure 6-32: Void fraction evolution for n=1x10^8 /m^3 for 1.6 m water depth. Fringe levels show void fraction. Side plane cut view of 3D impact evolution. Direction of travel from left to right. Results shown at 0.04 s and 0.08 s.

The extent of cavitation is evidently restricted; however further increase of the depth is required if the simulation is to provide any meaningful results. The main findings of these simulations are that the size of the water domain, along with the choice of nuclei populations are the most important parameters for simulating ditching test cases. Thus, future analyses should focus on varying the depth even further or at least to the point where there is no pressure wave interaction at the free surface. Moreover, it should be noted that, computationally, these sensitivity analyses will become prohibitively large.

6.8 Conclusions

The methodology for cavitation was described, which includes the use of the Antoine equation for the estimation of the vapour pressure and the use of the tensile strength of the liquid for a better approximation of the critical pressure where cavitation occurs. The method for the growth and reduction of cavitation was detailed with the use of the bubble dynamics approach of Rayleigh-Plesset, a simplified vaporous bubble method that is widely used in cavitation research.

The major changes in the cavitation method, compared to the cut-off model, were the use of the critical pressure instead of an arbitrary cut-off pressure, the introduction of

the void fraction, allowing the code to evaluate the amount of vapour and liquid in the particles and the introduction of a new mixture density and speed of sound.

The Rayleigh-Plesset equation was applied for the ideal case of spherical nuclei in transient conditions, neglecting the compressibility of the mixture, as it is more profound in the later stages of cavitation collapse. The high velocities during collapse invalidate the assumption of incompressibility. The effect of compressibility is more important at the later stages of cavitation collapse because the vapour inside the nuclei undergo cavitation collapse does not condense fast enough. This means that the vapour component starts to act like a gas, at which point compressibility becomes an issue. However, it is necessary to consider the context under which cavitation is studied in this project. The interest is in the phenomenon from a continuum point of view, so investigating bubble radii of the order of less than 10^{-7} m would only lead to a more complicated implementation of the phenomenon. Moreover, cavitation collapse is a phenomenon associated with cavitation damage and material erosion due to the cyclical occurrence of attached, cloud and vortex cavitation. This is not a phenomenon observed in aircraft ditching cases. This means that the issue of compressibility can be avoided if the model is confined in the growth and reduction of the radius to its original value.

The new approach was implemented in the SPH code and a set of 2D simple examples were tried in order to show the applicability, as well as the limitations of the method. The results suggest that the code can adequately provide a new cut-off pressure, which is based on the vapour pressure, the surface tension and the initial radius of the microscopic nuclei. Furthermore, it can simulate the changes in the fluid's properties in a better way compared to the cut-off model, taking into account the amount of vapour.

A 2D venturi test case showed that cavitation will take place at the constriction of the venturi throat as is expected and the density values follow closely the published results. Comparison to published results of a 2D tube test case showed reasonable similarities in both the pressure and density trends and values.

Further test cases included the high forward velocity impact of plates in water, but the lack of any experimental data did not allow for a direct comparison of the simulation predictions. However, they provided a better understanding of the difficulties of the new approach. These difficulties are related to two main areas. The first is the effects that a relatively small water domain can have, which can lead to wave reflection and artificial

cavitation dominating the domain. Larger water domains for the simple plate examples were found to provide less noisy results, however this was not the case for the more detailed plate model where an even larger domain is required. Computationally this can be unacceptable, which leads to the second parameter that can greatly influence the results, the number of nuclei.

The number of nuclei was shown to affect greatly the extent of cavitation and hence a tuning process should be followed. Both the simple and more detailed plate test cases demonstrated that by reducing the number of nuclei, the results suffer from reduced areas of cavitation. The lack of any experimental tests by SMAES does not allow for a direct comparison of any experimental results to the simulations. It must be noted that as part of the future work for this topic, any tuning of the number of nuclei should follow closely the experimental results without missing out any potential cavitation regions.

7 Aerated Water Modelling

The presence of air during ditching was investigated in the literature review in Chapter 4, where it was shown that it can lead to a cushioning effect. Moreover, it was shown that the numerical attempts in fluid-structure interactions did not include air, leading to poor predictions of pressure loads, especially for sections which have a small angle with respect to the water surface. This chapter aims to introduce an aerated water model in order to investigate the effects of air particles on the pressures imparted on a structure impacting the water with forward velocity. A methodology is outlined, that aims to treat the water as a mixture of liquid and gas (air). Four test cases are considered with increased complexity in order to demonstrate the capabilities of the method.

7.1 Theory and Methodology

Unlike cavitation, aerated water is the mixture of two distinct materials, instead of a mixture of one material of different phases. It has previously been discussed how a pocket of air can influence the pressure distribution on an object upon impact with the surface of the water. There are different ways in which air can affect the pressure distribution of the flow on a structure. Apart from a distinctive pocket or layer of air at the water surface, the fluid can become a mixture of liquid and small gas particles. Air can be entrapped between the liquid's surface and the impacting structure and the air content can be split into smaller regions of air particles, also termed air bubbles. This is usually the case in the more severe impact cases [17]. The effect of such division of the air pocket is effectively the same as in the air cushion phenomenon, in that it reduces the high shock pressures at the start of the impact, while the initial pulse of the impact is prolonged.

The fact that the air bubbles lead to the same effect on the overall behaviour of the flow allows the use of a mixture approach for its modelling. Moreover, the interest is to observe the changes of the flow from a macroscopic point of view rather than observing the behaviour of a single gas (air) bubble in a liquid.

When aerated water is treated as a mixture, it is considered to consist of gas bubbles distributed in the fluid. As in the cavitation process detailed in Chapters 4 and 6, the density and speed of sound change significantly. The density of the mixture depends

on both the gas and the liquid component and their relation is governed by the amount of air that is present. The speed of sound also takes into account the mixture nature and it has been found that, for a gas volume fraction of 10%, the speed of sound is 33 m/s, far less than the liquid's or air's speed of sound [102].

Peregrine et al. [48] observed that as the severity of the impact increases and the amount of air increases, due to the more significant mixing, the pressure experienced by a rigid body (such as a wall) reduces.

Another aspect that has been considered is whether the flow with the air bubbles behaves adiabatically or isothermally. Bullock et al. [49] suggested that a straightforward answer does not exist, as depending on the size of the air bubbles, the centre of the bubble can behave in an adiabatic manner, whereas the outer surface that is in contact with the liquid can behave in an isothermal manner. It follows that the smaller gas particles would behave isothermally, whereas larger ones would behave adiabatically. However, considering a mixture approach that does not explicitly distinguish between air and water particles would then complicate the definition of the behaviour even further. Peregrine et al. [48] considered both cases for a mixture approach and while it was determined that the effect in the pressure is negligible, it was suggested that the change in the polytropic index (which is lower for an isothermal process) would alter the speed of sound of the mixture. This means that a lower speed of sound is expected for the isothermal case, leading to supersonic flow regimes for milder impacts. It is suggested that the best description for such a case would be an initially adiabatic process that changes to an isothermal as their size reduces, due to an increase in pressure. Since the above work shows the negligible difference between the two processes, it allows for this complicated heat transfer approach to be simplified to an adiabatic process.

The fact that both air and water are present in the flow means that the compressibility of the mixture should be considered. For the cavitation method the vapour is treated as incompressible, however for the case of aerated water the effects of air compressibility need to be discussed. The density and bulk modulus of air alters significantly with changes in pressure. When dealing with a mixture, then the compressibility is taken as [49]:

$$\frac{1}{K_{aw}} = \frac{\beta}{K_a} + \frac{1-\beta}{K_w}, \qquad \textbf{(7-1)}$$

where *a* and *w* represent air and water phases, *aw* represents the mixture, *K* is the bulk modulus and β is the gas volume fraction, which is the most significant parameter with respect to milder pressure peaks. An increase of 1% in the gas volume fraction has been found to increase the compressibility of the mixture by as much as 65% in typical drop test cases [49]. This has serious implications when trying to predict any realistic water-structure behaviour, as it is very hard to demonstrate such small changes in the gas content on any experimental water tank [49]. Other parameters that can influence the aerated water mixture include the type of water (freshwater or saltwater) and the severity of the impact.

For the methodology in this project it is assumed that each particle is pre-seeded with a percentage of air. The percentage of air, which is defined by the user, will change as the phenomenon progresses. This assumption is not accurate in real life fluids, where the concentration of any gas follows an arbitrary distribution, however the introduction of a small number of air particles in the domain would lead to sharp density variation at the interface with the liquid particles, which could lead to numerical instabilities [99].

As it was discussed above, the compressibility of the mixture is highly influenced and governed by the gas (air) component. An initial investigation was performed with both changing and constant liquid density, in order to assess the effect on the pressure evaluation. The pressure equation used, follows the assumption that the processes in the mixture behave in an adiabatic manner. The equation for the pressure is given as:

$$\frac{P}{\rho^{\gamma}} = \frac{P_0}{\rho_0^{\gamma}}, \qquad \textbf{(7-2)}$$

where γ is the adiabatic index and is equal to 1.4, subscript 0 represent the old state and ρ is the density.

The graph of Figure 7-1 shows the variation in pressure, which is negligible. This suggests that the compressibility of the mixture is controlled by the gas content to a greater degree when compared to the compressibility of the liquid. Obviously, once the pressure increases to significant levels, the compressibility of the liquid should also be considered. This leads to the next assumption of the method. Just as with the initial gas fraction (percentage of air in the particle), the user is able to define a minimum limit of gas content, below which the mixture no longer contains air but is thereafter treated as pure water.

Given the fact that the SPH method cannot deal with strong density variations [99] and based on the fact that the densities of the gas and water components are significantly different, it was considered appropriate to also set a maximum limit for the gas content. The maximum volume gas content is capped in the SPH code at 70% air. This is done in order to avoid any strong discontinuities which could lead to numerical instabilities within the code.

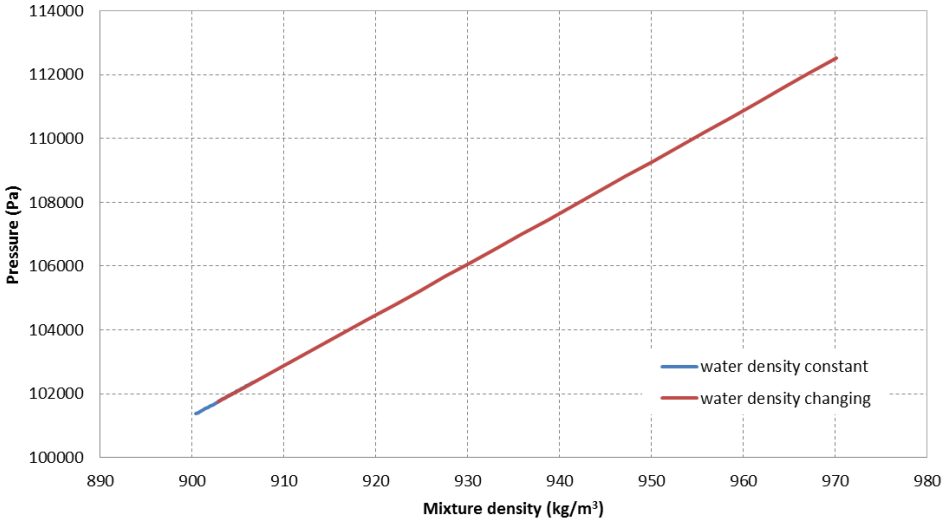

Figure 7-1: Variation in the pressure with and without consideration of the liquid's (water) compressibility.

As mentioned above, in the proposed model, each SPH particle is considered to be seeded with a portion of gas. In the SPH method the mass of the particle is taken as constant throughout the computation. Depending on whether the particle is in tension or compression, the corresponding changes in the volume are computed.

It has also been established that any changes in the mixture properties of the aerated model can be considered to be driven by the gas content. As such, it is necessary to define a mass fraction for each particle, which depends on the gas content, the mixture density and the gas density. Since the mass remains constant these values are the original values set by the user and the gas mass fraction is given as [74]:

$$f_g = \frac{\beta_0 * \rho_{g0}}{\rho_0}, \tag{7-3}$$

where ρ_{g0} is the initial density of the gas component, β_0 is the initial gas content (gas volume fraction) and ρ_0 is the initial mixture density, based on the initial density of the gas, the initial gas volume fraction and a constant water density.

The mixture density is given as in the cavitation model:

$$\rho = \beta\rho_g + (1-\beta)\rho_l\,, \tag{7-4}$$

and the gas volume fraction is:

$$\beta = \frac{\rho_l - \rho}{\rho_l - \rho_g}. \tag{7-5}$$

In order to evaluate the gas density, it is essential to use an additional closure equation for the system. This is [74]:

$$\frac{1}{\rho} = \frac{f}{\rho_g} + \frac{1-f}{\rho_l}. \tag{7-6}$$

Combining equations (7-4) and (7-6) leads to the following equation for the gas density:

$$\rho_g = \frac{\rho f_g \rho_l}{\rho_l + (f_g - 1)\rho}. \tag{7-7}$$

Finally, the speed of sound of the mixture, given in equation (7-8) uses the same equation as in the cavitation approach. The only difference is that the gas density changes depending on whether the mixture is in compression or tension [49]. A full derivation of the mixture speed of sound is given in Appendix C.

$$C = \left\{\left[\beta\rho_g + (1-\beta)\rho_l\right] * \left[\frac{\beta}{\rho_g c_g^2} + \frac{1-\beta}{\rho_l c_l^2}\right]\right\}^{-1/2}. \tag{7-8}$$

Figure 7-2 shows the dependence of the speed of sound of the mixture on the gas content, as an SPH water particle is in tension. It follows the theoretical description that the speed of sound of a mixture reaches values lower than the speed of sound of either the components (water and air). In the graph of Figure 7-2 it is assumed that the initial point is a particle with a gas content of 10% and a corresponding mixture speed of sound of approximately 40 m/s.

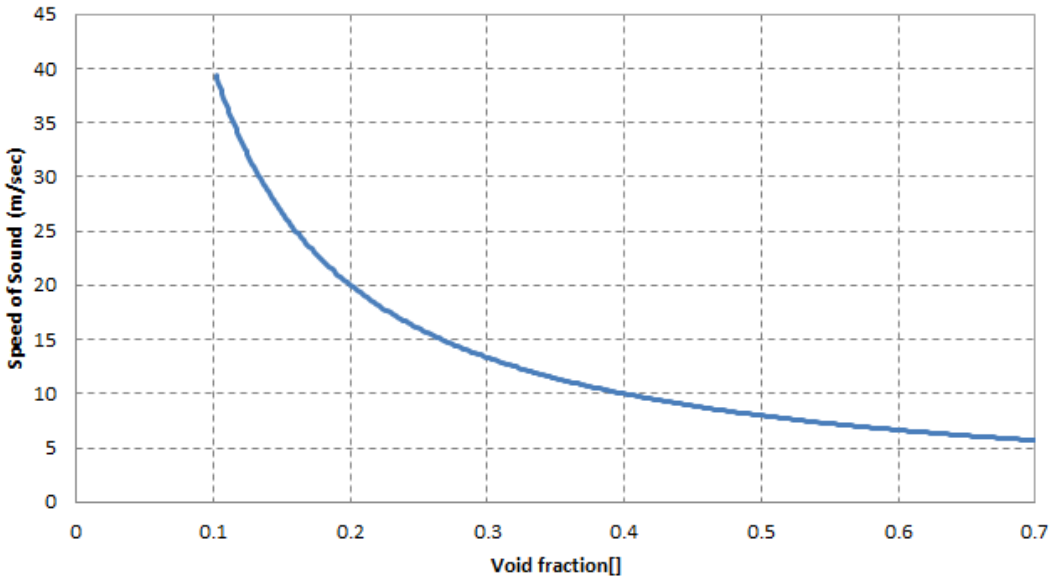

Figure 7-2: Speed of sound of a mixture of water and gas for a volume fraction of 10% up to 70%.

7.2 Methodology Implementation

In this section, the essential input parameters and the structure of the method within the MCM code will be discussed.

The main structure of the MCM code includes the following main routines.

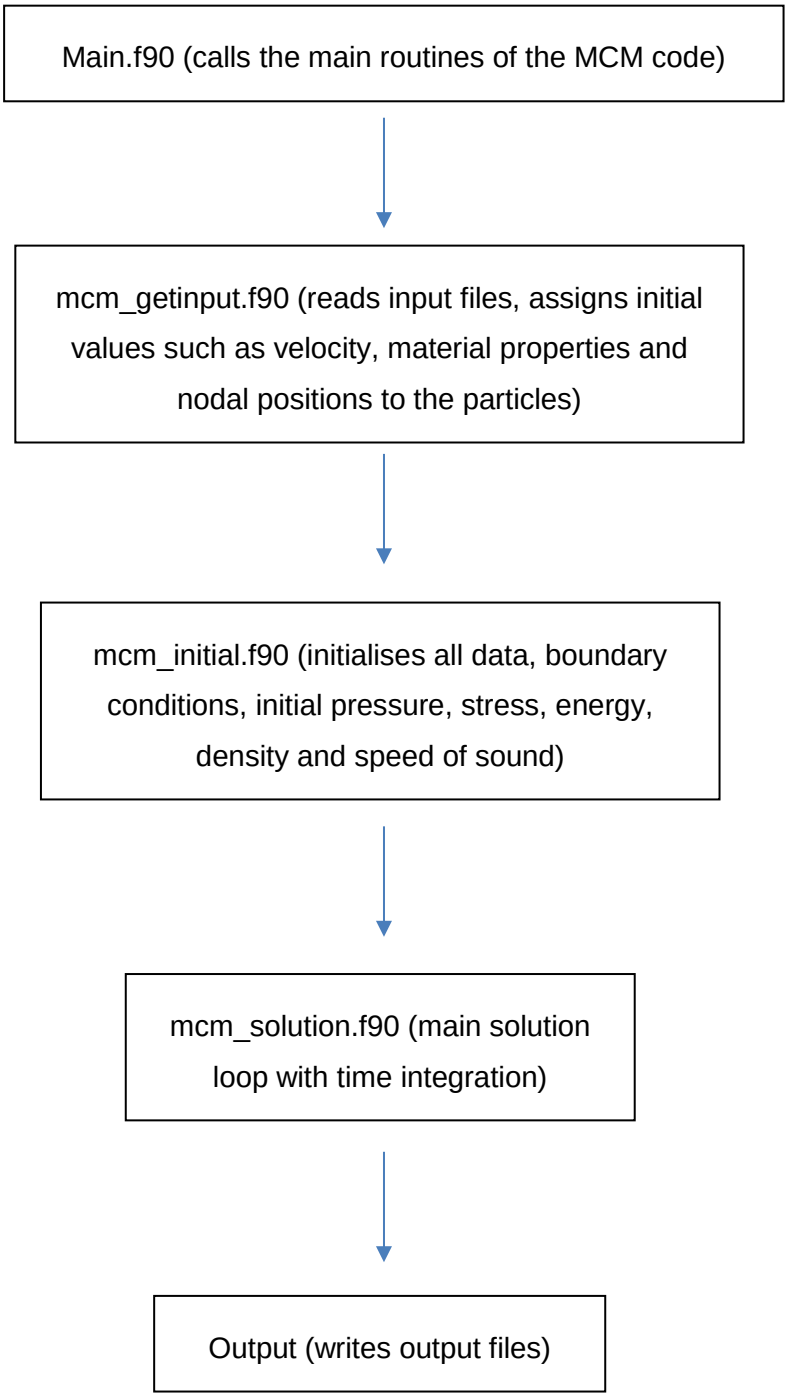

For the aeration model implementation the following subroutines have been modified.

- Mcm_initial.f90
    - Mcm_initialise_database.f90
    - Mcm_calcmass.f90
    - Mcm_eoscalc.f90
    - Mcm_eos13p.f90
    - Mcm_eos13c.f90
- Mcm_solution.f90
    - Mcm_rhoupd.f90
    - Mcm_eos28c.f90
    - Mcm_eqos13.f90
    - Mcm_eqos28.f90

mcm_initialise_database.f90 initialises the input data. All of the parameters that are used in the MCM code are initialised in this subroutine and are usually given an original value of zero.

mcm_calcmass.f90 calculates the particle masses by dividing the material's mass equally among the particles. The gas mass fraction, f_g, is estimated in this subroutine. This is done because it is necessary for the later stages of the code to have the actual mass of each component, which is updated at each timestep. Using this initial mixture density and the gas fraction given in the input file, we can determine the actual gas and water mass of each particle based on equation (7-3). Once the gas mass fraction is calculated, the mass of each of the mixture components, the water and air components, is calculated. The inputs used are given in the table below.

Table 7-1: Input parameters for mcm_calcmass.f90

Input Parameter	**Description**
gasfraction	Initial gas content/particle
rholiquid	Water density
rhogas	Air density
rho0	Initial input mixture density

The initial density for the mixture should be calculated following the example below:

Assuming that the flow has the characteristics of Table 7-2 the initial mixture density using equation (7-4) is 900.1225 kg/m^3 with a total particle mass of 4.713x10^{-4} kg.

Table 7-2: Initial input example

gasfraction	0.1
rholiquid	1000 kg/m^3
rhogas	1.225 kg/m^3

mcm_eoscalc.f90 selects the appropriate equation of state as assigned in the input file. It also calculates the initial density and internal energy. The initial density of the mixture and the gas content is estimated based on the input file and for the purposes of this project it provides the same initial densities as read in the input file. The internal energy uses the gas content density as read from the input file and the mass of the gas component as calculated in mcm_calcmass.f90. This is due to the negligible effect of the water density in the mixture as observed in Figure 7-1. If the aeration model is not active and the particles are pure water then no change in the subroutine occurs.

mcm_eos13p.f90 is the subroutine that calculates the initial pressure when the ideal gas equation of state is used. This subroutine has been modified to include the adiabatic equation of state of equation (7-2). When using the adiabatic equation of state (7-2) there is one issue that needs to be resolved. The initial pressure is used to determine the pressure at the next step. If the initial pressure is zero then the updated pressure at subsequent steps will always be zero. To overcome this an initial pressure is defined in the input file. For this project it is always equal to atmospheric pressure. This allows the initial pressure to be computed and not give a zero value. Once the pressure is estimated then the pressure is reduced by whatever initial pressure has been read from the input file (i.e. $P=P_{ad}-P_{atm}$).

mcm_eos13c.f90 is the subroutine that calculates the speed of sound when the ideal gas equation of state is used. It has been modified to consider the aeration model. If the aeration model is active but the gas volume fraction is zero, which means that the particles have compressed beyond the minimum allowable gas volume fraction, and they have been switched to being pure water, then the Murnaghan equation of state as given below is called.

$$p = B\left(\left(\frac{\rho}{\rho_0}\right)^{\gamma} - 1\right), \quad \textbf{(7-9)}$$

where *B* is the bulk modulus, ρ is the density at the current timestep, ρ_0 is the density at the previous timestep and γ is a coefficient.

The bulk modulus and coefficient γ need to be additional inputs in the input file, which are read directly when this equation of state is activated in the subroutine **mcm_eos28p.f90**. This is because the main line of the input file that reads the inputs for the equation of state, are already occupied with the adiabatic/ideal gas equation of state.

If the aeration model is active and the gas volume fraction is not zero, the mixture speed of sound is calculated as given by equation (7-8).

mcm_rhoupd.f90 is the subroutine that updates the density based on the continuity equation. If the aeration model is active, then the gas density is updated based on equation (7-7). Once the gas density is updated, the gas volume fraction is also updated based on equation (7-5).

The first time (per particle) that the gas fraction reaches the minimum limit, the gas fraction is set to zero, the initial density is set to the liquid density and the mass of the particle is set as the mass of the liquid component. Then the density is updated with an inverted Murnaghan equation of state using the current pressure. At that point, the input for equation (7-9) are used since the equation of state changes. The code determines if this is the first timestep that each particle is filled only with liquid, in which case the above inverted Murnaghan equation is used. In the subsequent timesteps the density of these particles updates based on the continuity equation as for a pure liquid flow.

mcm_eqos13.f90 is the subroutine that calculates the pressure at each particle based on the equation of state. For the aeration implementation the ideal gas subroutine eqos13 has been modified. The same philosophy as for the changes in **mcm_eos13p.f90** is applied. If the particles have switched to pure water, after they have reached the specified minimum gas volume fraction, **mcm_eqos28.f90** is used. This subroutine updates the pressure based on equation (7-9).

The parameters necessary as input are given in Table 7-3.

Table 7-3: Input parameters for aerated water model and description

Input Parameter	Description
gasfraction	Initial gas content/particle
rholiquid	Water density
rhogas	Air density
gaslimitmax	Maximum limit for the gas fraction (set at 0.7)
gaslimitmin	Minimum limit for the gas fraction (below which the flow is pure water)
B	Bulk modulus (as in the Murnaghan equation of state)
gamma	Gamma parameter for the Murnaghan equation of state
Adiabatic flag	Flag that activates the adiabatic pressure equation (7-2)
p0	The initial pressure that is used in the case of the adiabatic pressure formula (need for a value to initialise the pressure).

The flow chart below shows the solution loop performed for each MCM particle.

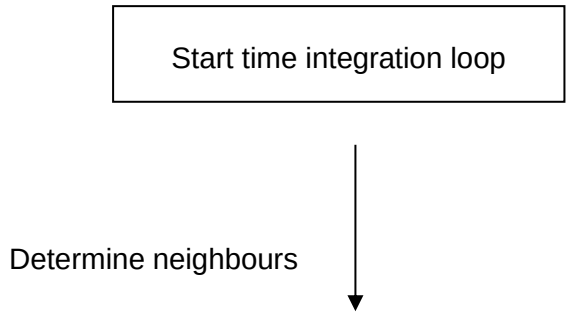

Strain rates

$gradv_{ij}=gradv_{ij}+Vol_j(v_j-v_i)dwdx$

$E_{ij}=0.5(gradv_i+gradv_j)$

$R_{ij}=0.5(gradv_i-gradv_j)$

$Tr(E_{ij})=E_{ii}+E_{jj}+E_{kk}$

If aeration is active and particle is a mixture of gas and liquid

If aeration is active and particle has been compressed, for the first time, and has a gas fraction smaller than the input-defined minimum limit

Density update

$$\rho_g = \frac{\rho f_g \rho_l}{\rho_l + (f_g - 1)\rho}$$

$$\beta = \frac{\rho_l - \rho}{\rho_l - \rho_g}$$

Density update

$$\rho_0 = \rho_l$$

$$\rho = \rho_0 / V_0$$

$$m = m_l$$

$$\rho = \rho(((P + B)/B)^{1/\gamma})$$

$$\rho = \rho/(1 - tr(E_{ij})dt)$$

Material strength and stress tensor

The stress tensor for hydrostatic pressure (for water)

$$\begin{bmatrix} \sigma_{ii} - \frac{1}{3}tr(E_{ij}) & 0 & 0 \\ 0 & \sigma_{jj} i \frac{1}{3}tr(E_{ij}) & 0 \\ 0 & 0 & \sigma_{kk} - \frac{1}{3}tr(E_{ij}) \end{bmatrix}$$

If aeration model is active and the gas fraction is greater than zero

If aeration model is active and the gas fraction is equal to zero

Speed of sound

The speed of sound is calculated by the following:

$c=(\alpha\rho_g +(1- \alpha)\ \rho_0)((\ \alpha/(\ \rho_g(c_g^2)))+((1- \alpha)/(\ \rho_0\ c_l^2)))^{-0.5}$

Speed of sound

The speed of sound is calculated by the following (Murnaghan):

$$c = \sqrt{B\gamma/\rho_l}$$

Calculate trial value for internal energy

Update pressure and internal energy:

Select the appropriate Equation of State. If the aeration model is active and the gas fraction is greater than zero the the pressure is calculated with the adiabatic equation:

$$P = \frac{P_0 \rho_g^{\gamma}}{\rho_{g0}^{\gamma}}$$

If the aeration model is active but the particle has reverted back to pure fluid then the Murnaghan Equation of State is called:

$$p = b((\rho/\rho_0)^{\gamma} - 1.0)$$

Then update the internal energy:

$$e = e_{try} - 0.5 p \Delta V$$

Update stress tensor with pressure and calculate critical timestep, calculate acceleration update boundary conditions, calculate total energy and update velocity and position of particle

End of time integration loop

7.3 2D Test Case

The first test case is a 2D column of particles that impacted a boundary at a variety of velocities. The purpose of this simple test case was to establish the influence of the different parameters such as initial and minimum gas fraction, velocity and equation of state on the results.

The column is 4 m long and 0.5 m wide, consisting of 20451 particles. Initially the 2D test was performed with pure water content. This formed the basis of the initial comparison. The velocity of the column was 0.001 m/s and the particle spacing was chosen at 0.01 m. The Murnaghan equation of state, (7-9), was used with $B=5.5\times10^8$ Pa and $\gamma= 4$. The results are shown in Figure 7-3 - Figure 7-4. The results exhibited a typical behaviour of a pressure wave travelling as the column impacts a rigid boundary (located at the bottom). The table below shows the main input parameters.

Table 7-4: Input data for 2D water column tests.

Height, m	4.0
Width, m	0.5
No of particles	20451
Particle spacing, m	0.01
Smoothing length, m	0.013
Velocity, m/s	0.001
Density, kg/m^3	1000
Mass, kg	2045.1

The pressure results corresponded to a material with a density of 1000 kg/m^3 and a speed of sound of approximately 1483 m/s. Initial pressure of the fluid column is zero, so the results can be considered as computed in gauge terms. The pressure has been measured at five elements along the length of the water column. These elements and their vertical distance from the bottom of the column are given below.

Table 7-5: Five particles and their corresponding vertical distance from the bottom of the column. Used for pressure readings.

Particle	Distance from the bottom, m
18526	0.15
18097	0.47
15684	0.85
13211	1.12
13238	1.39

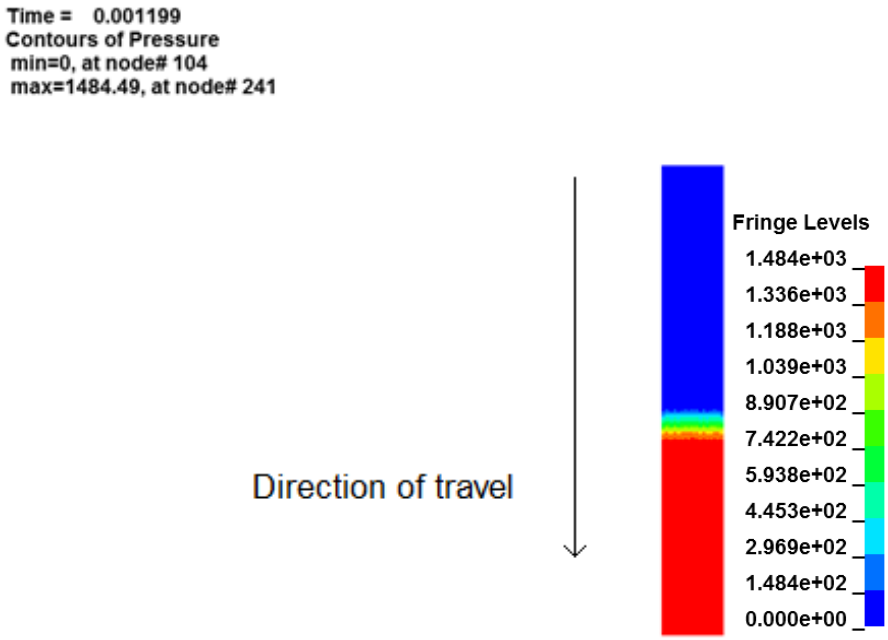

Figure 7-3: Pure water pressure results at t=0.0012 s. Maximum pressure corresponds to the theoretical value for a quasi-compressible fluid like water. Fringe levels show pressure in Pa.

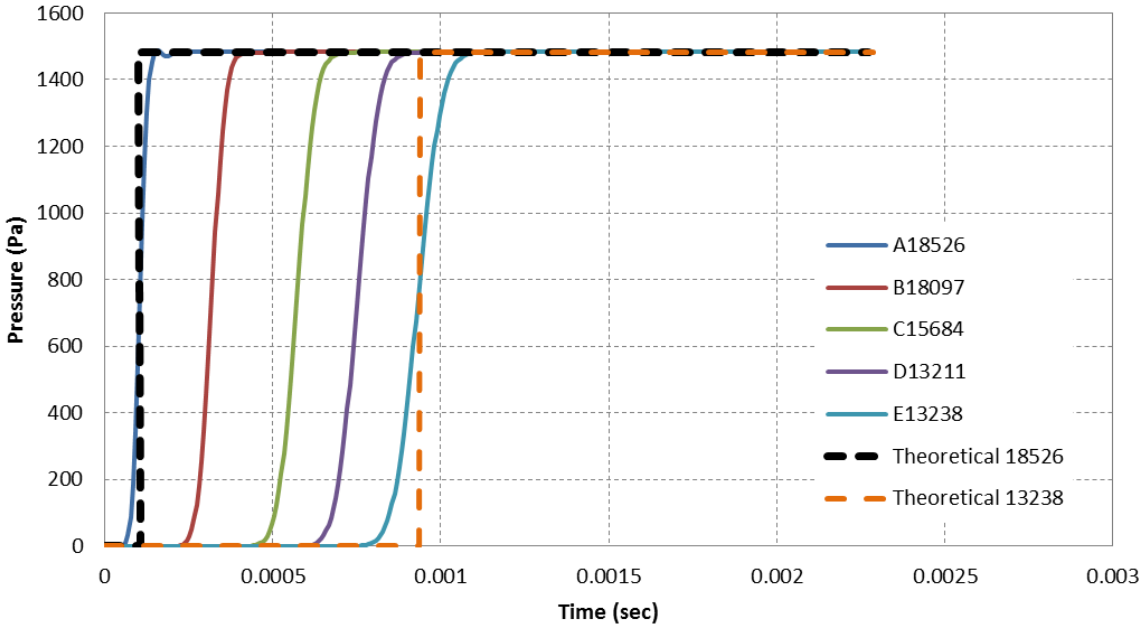

Figure 7-4: Change in pressure distribution along the length of the column for pure water. Theoretical wave propagation pressure of 1483 Pa for particle 18526 shows that the simulation follows the theoretical estimate.

Consider the plane wave impedance equation [103]:

$$p = \rho c v \,, \tag{7-10}$$

where ρ is the density, c is the speed of sound and v is the velocity of the fluid.

The pressure wave should peak at the 1483 Pa as is shown in Figure 7-4. The theoretical curves for the first and last particle, at 0.15 m and 1.39 m from the bottom of the column has also been included. The results between the analytical and the numerical simulations show good agreement.

The same test was performed with the aerated model described before. The test was performed with the ideal gas equation of state, which is already given in the MCM code in the following form:

$$p = \rho(\gamma - 1)e\,, \qquad \textbf{(7-11)}$$

where e is the internal energy of the particle and γ=1.4 is the adiabatic index, which is typical for a diatomic gas like air.

Next the aeration model was tested using the ideal gas equation of state. The input parameters for the aerated column are given in Table 7-6.

Table 7-6: Aerated water model input parameters for 2D column.

Initial gas volume fraction	0.1
Water density, kg/m^3	1000
Gas (air) density, kg/m^3	1.225
Particle spacing, m	0.01
Minimum gas volume fraction	0.001
Initial pressure, Pa	101325
Velocity, m/s	0.001

The results for the ideal gas equation of state tests are shown in Figure 7-5 - Figure 7-8.

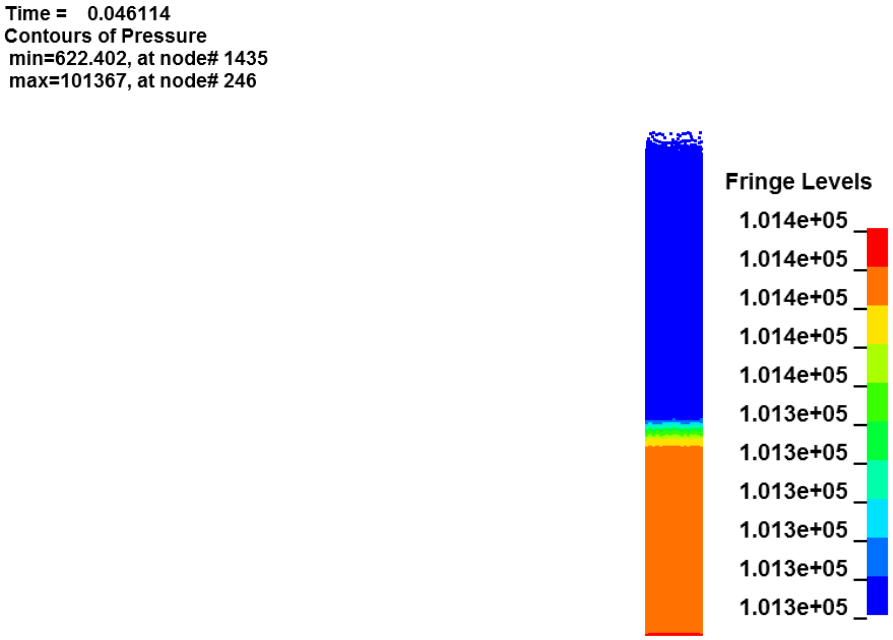

Figure 7-5: Pressure distribution for aerated water model in 2D column with ideal gas equation of state. Fringe levels show pressure in Pa. initial velocity of 0.001 m/s. Initial gas volume fraction of 10%.

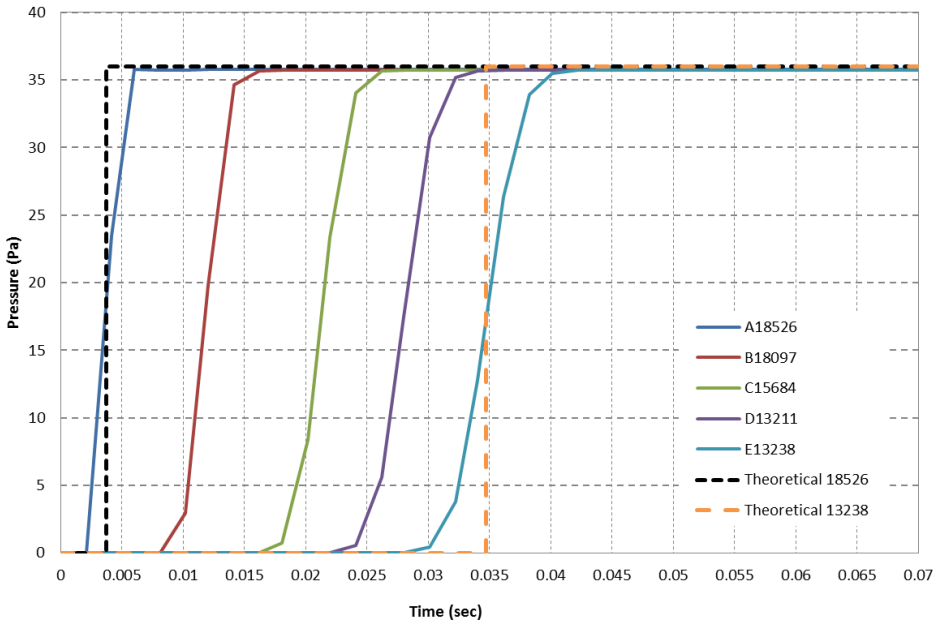

Figure 7-6: Change in pressure distribution along the length of the column for aerated water model with the ideal equation of state (7-11). Theoretical wave propagation pressure of 36 Pa for particle 18526 shows that the simulation follows the theoretical estimate. Initial velocity of 0.001 m/s and initial gas volume fraction of 10%.

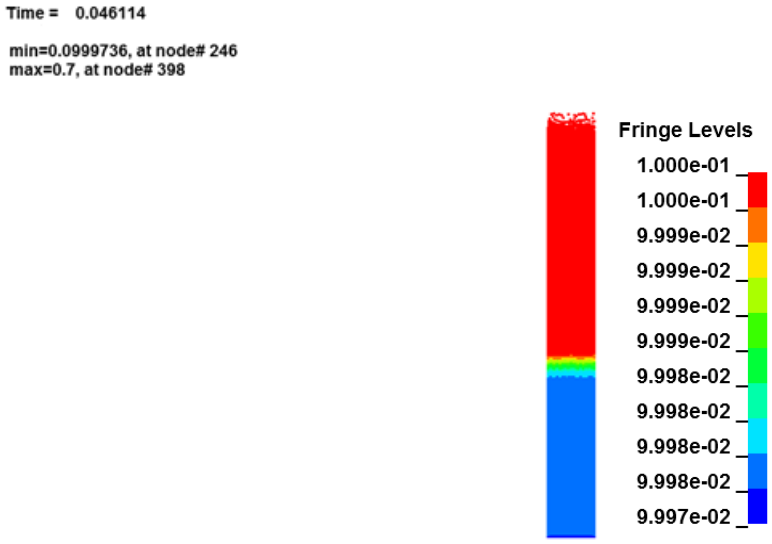

Figure 7-7: Gas volume fraction evolution in 2D column with ideal gas equation of state for the pressure evaluation. Fringe levels show gas volume fraction values. Initial gas volume fraction of 10%

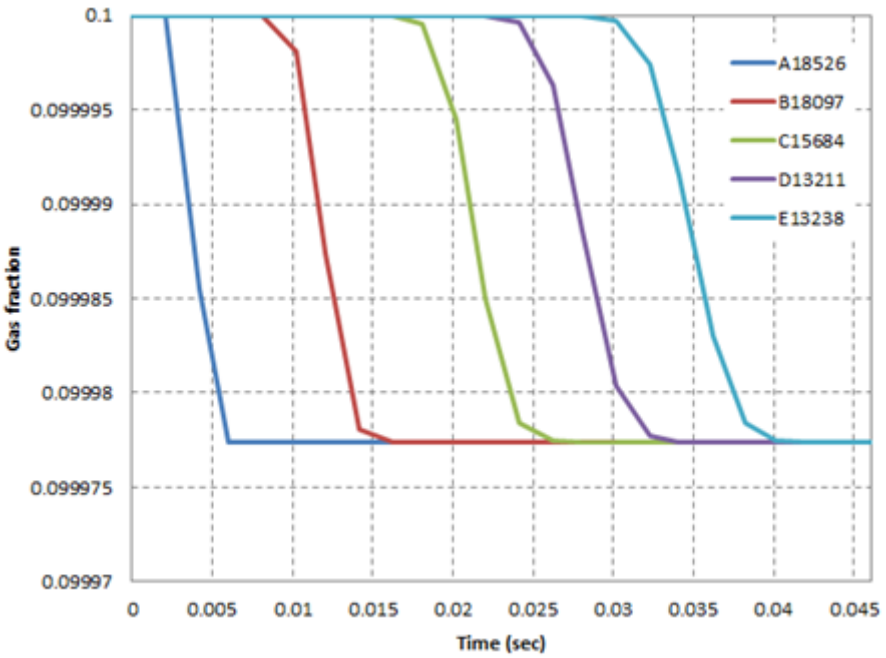

Figure 7-8: Gas fraction at various points along the length of the 2D column with the ideal gas equation of state.

The differences in the pressure between Figure 7-4 and Figure 7-6 are due to the differences between the mixture and the pure water models. In the pure water model

the speed of sound is 1483 m/s, as opposed to the mixture's speed of sound of around 40 m/s. This means that the propagation of the pressure wave will be slower in the aerated model than the pure water model. Indeed, comparing the pressure plots above indicates that, for a 10% initial gas volume fraction, the peak pressures appear at a later stage. Furthermore, the maximum peak pressures in the aerated model are significantly lower when compared to the pure water model. This can again be attributed to the lower speed of sound of the mixture when compared to the pure water. Considering the plane wave impedance equation (7-10), then the pressure wave should peak at the values given in Table 7-7.

Table 7-7: Estimated pressure peaks for the pure water and aerated models.

Input	Pure water model	Aerated model
density, kg/m^3	1000	900
Velocity, m/s	0.001	0.001
Theoretical speed of sound, m/s	1483	40
Propagation pressure, Pa	1483	36

The theoretical curves for the first and last particle, at 0.15 m and 1.39 m from the bottom of the column has also been included. The results between the analytical and the numerical simulations show good agreement.

The gas fraction reduced as the particles compressed, which is also expected. As the pressure wave propagated through the column, the variation in the gas content is evident. Behind the pressure wave, when the pressure has settled, the gas content remained constant, whereas the drop seen in Figure 7-8 corresponds to the transition of the pressure wave through the column. Due to the low velocity and small minimum gas fraction set in the input file, the particles never managed to become pure water.

The results for the same test case with the adiabatic equation of state, equation (7-2), are identical to that of Figure 7-6.

Finally, it must be noted that the particles at the top of the column underwent an unphysical behaviour in that they moved away from the column. This is due to the fact that there was an initial pressure of 1 atm present. The adiabatic equation of state

given in equation (7-2) would provide a zero pressure if the initial pressure was set to zero. To overcome the problem, the adiabatic equation of state was modified in the MCM code in order to offset the pressure by any value given as input initial pressure. The results of Figure 7-9 - Figure 7-10 show the correct particle behaviour for zero initial pressure.

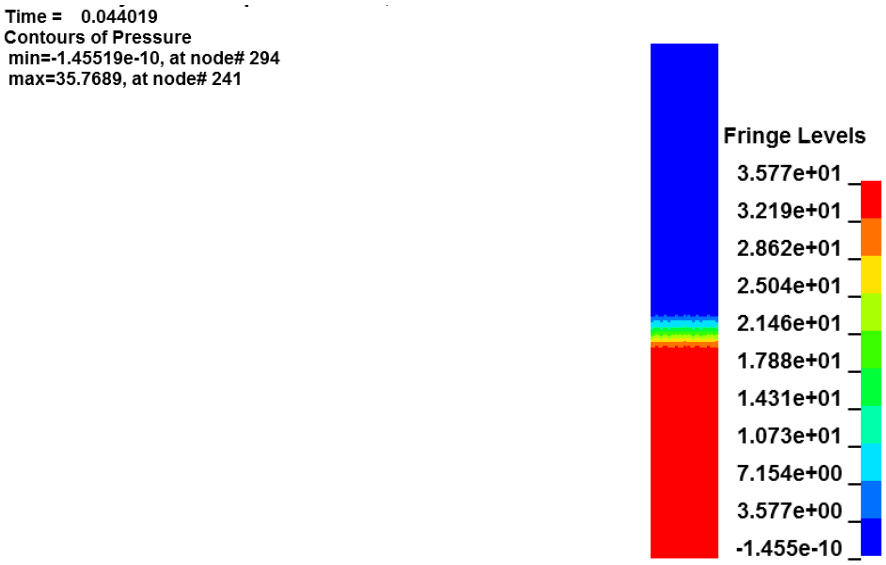

Figure 7-9: Pressure distribution for initial pressure of zero with offset in the adiabatic formula. The results show the correct behaviour and no particles are detached at the top from the main fluid column. Fringe levels show pressure in Pa. Note: the pressure levels are in gauge terms as opposed to the pressure results of Figure 7-5. Initial velocity of 0.001 m/s.

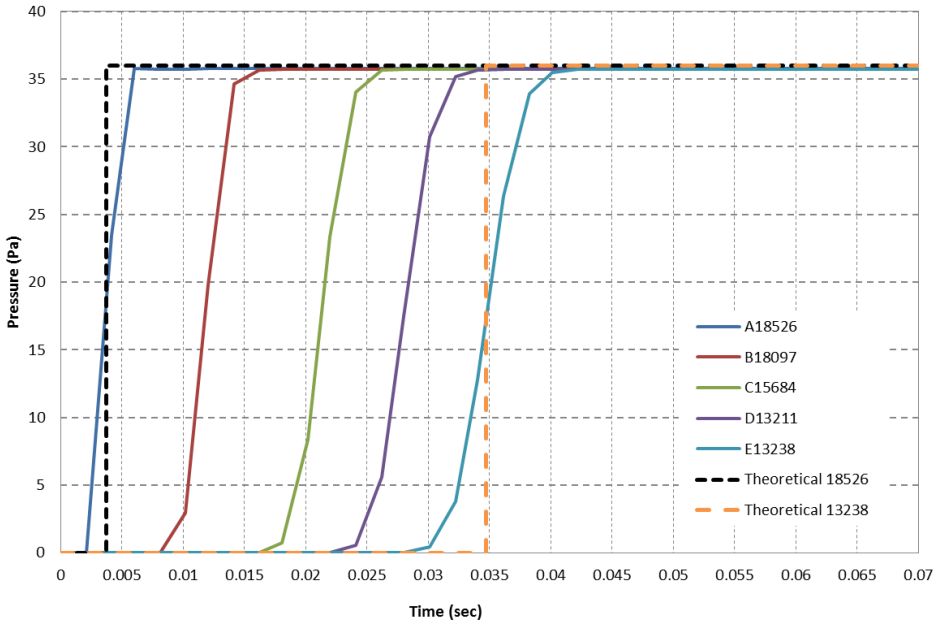

Figure 7-10: Change in pressure distribution along the length of the column for aerated water model with the adiabatic equation of state (7-2). Theoretical wave propagation pressure of 36 Pa for particle 18526 shows that the simulation follows the theoretical estimate. Initial velocity of 0.001 m/s and initial gas volume fraction of 10%.

The pressure values were the same as in the previous example, however there was no particle disturbance at the top of the column. As it is expected, the gas fraction variations remained the same as in the previous test cases. The tests so far were concerned with small velocities and hence small variations in the gas fraction and pressure waves.

Next, the same test case was considered but with a velocity of 1 m/s. It provides a better comparison between the ideal and adiabatic equations of state. The pressure and gas fraction results for the adiabatic equation of state are shown in Figure 7-11 and Figure 7-12.

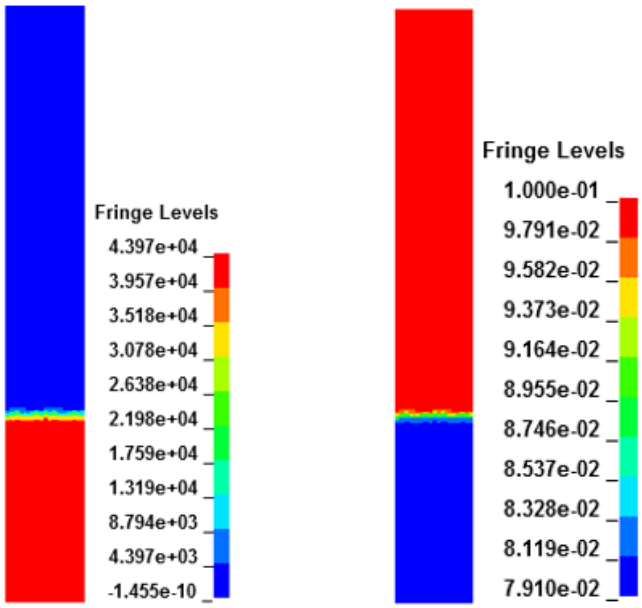

Figure 7-11: Pressure evolution (left) and gas fraction evolution (right) for 2D column at 1 m/s with adiabatic equation of state and initial gas volume fraction of 10% (plot taken at t=0.028 s). Fringe levels on the left show pressure in Pa and on the right the gas volume fraction.

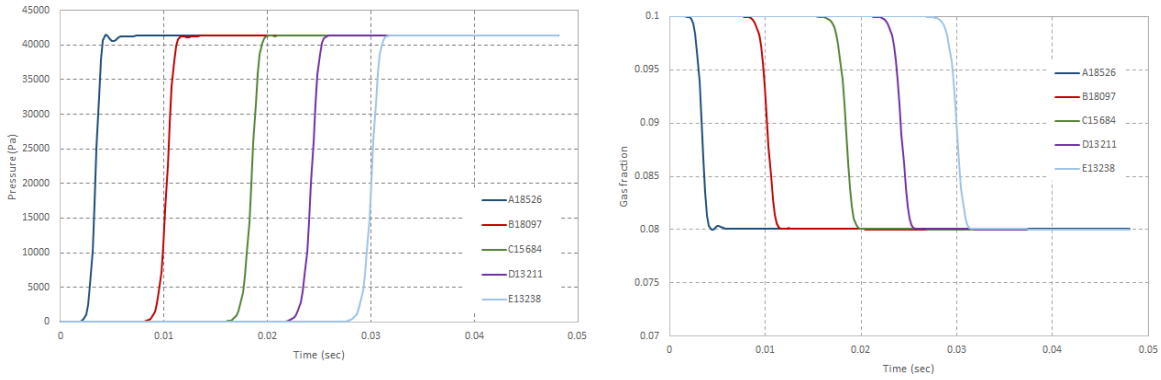

Figure 7-12: Pressure (left figure) and gas volume fraction (right figure) along various points for 2D column at 1 m/s and initial gas volume fraction of 10% with adiabatic equation of state. Gas fraction reduction is more severe than in the previous case, as expected for more severe impacts.

Term *c* in equation (7-10) can only be considered as the speed of sound of the fluid if *v*<<*c*, in which case the wave propagation velocity is equal to the speed of sound. For a 10% gas fraction, the speed of sound of the mixture would be 40 m/s (using equation (7-8). This suggests that, for v=1 m/s, the assumption that *v*<<*c* is not valid. In order to

assess the pressure peaks of Figure 7-12, the propagation velocity from the model was used directly in equation (7-10). This is given in Table 7-8.

Table 7-8: Estimated pressure peaks for the aerated model for 1m/s impact velocity and initial gas volume fraction of 10%.

Input	Aerated model
density, kg/m^3	900
Velocity, m/s	1
Propagation velocity at particle 13238 (1.39 m from the bottom), m/s	45.9
Propagation pressure, Pa	41310

The propagation pressure, calculated from equation (7-10), with a propagation velocity of 45.9 m/s compares well with the numerical results. If the estimated speed of sound was used (40 m/s) instead of the propagation velocity of the model, then the pressure peak would have been 36000 Pa. This is approximately 16% less than the pressure peak in Figure 7-12. Comparing the rise time of the pressure wave between Figure 7-10 and Figure 7-12, it can be seen that the speed of the compression wave has also increased by approximately 16%. A 16% increase in the speed of the compression wave means that the propagation velocity increases from a theoretical 40 m/s to approximately 46 m/s. This compares well with the propagation velocity of Table 7-8. In turn the propagation pressure increases by approximately 16%, from 36000 Pa to the more accurate 41760 Pa. This also compares well with the propagation pressure of Table 7-8. These results demonstrate that equation (7-10) can assume that the propagation velocity is equal to the speed of sound only if $v<<c$.

The gas volume fraction evolution showed the dependency of the gas content on the severity of the impact, as it is expected. Comparison between the gas volume fraction reduction in the original test case and the latest one (i.e. with impact velocity of 0.001 m/s and 1 m/s) shows that the higher velocity impacts would cause a more significant compression of the particles and as a result reduce the gas volume fraction content in each particle.

The results for the ideal gas law are shown in Figure 7-13.

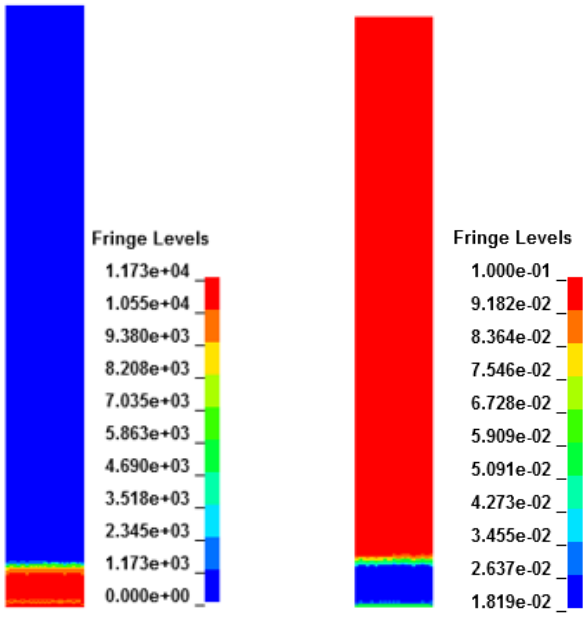

Figure 7-13: Pressure evolution (left) and gas evolution (right) for 2D column at 1 m/s with ideal equation of state (plot taken at t=0.028 s). Fringe levels on the left show pressure in Pa and on the right the gas volume fraction. Initial gas volume fraction of 10%.

The results for the ideal gas show that the wave propagation was slower compared to the test with the adiabatic equation of state. Moreover, comparing the maximum pressure it is observed that the ideal gas law underestimated the results.

The above tests indicate that using the adiabatic equation of state can provide more accurate results, corresponding to pressure values closer to the theoretical estimates.

Next a set of simulations was performed with a higher initial gas volume fraction (20%), in order to establish its influence on the pressure peaks. The parameters remain the same as in the previous test cases, however the initial density changes in order to account for the higher initial gas volume fraction. The difference in the initial density is shown in Table 7-9. It is expected that the pressure should be smaller. The results are shown in Figure 7-14 and Figure 7-15.

Table 7-9: Initial density and speed of sound variation depending on the initial gas volume fraction.

Initial gas volume fraction, %	Density, kg/m^3	Theoretical speed of sound, m/s
0	1000	1483
10	900	40
20	800	20

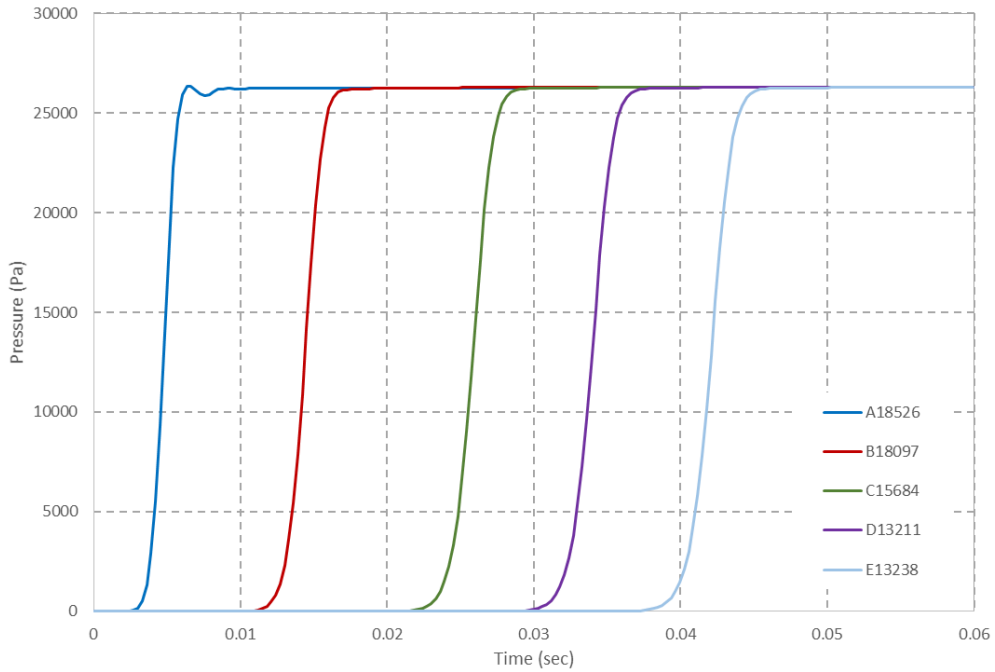

Figure 7-14: Pressure points for 2D column at 1 m/s with adiabatic equation of state and initial gas fraction of 20%. The pressure peaks are lower when compared to the peak values for an initial gas content of 10%. Initial velocity of 1 m/s.

Following equation (7-10) and the propagation velocity of the model, the pressure for the mixture at 1.39 m from the bottom can be estimated. This is given in Table 7-10.

Table 7-10: Estimated pressure peaks for the aerated model for 1m/s impact velocity and initial gas volume fraction of 10%.

Input	Aerated model
density, kg/m^3	800
Velocity, m/s	1
Propagation velocity at particle 13238 (1.39 m from the bottom), m/s	31.7
Propagation pressure, Pa	25340

The pressure peaks were lower compared to the test cases with an initial gas content of 10%. Moreover, the peak values took longer to reach their maximum indicating a less severe pressure wave. This follows the theory which suggests that the presence of air in the water reduces impact forces and provides a less pronounced peak. The theoretical estimate for the propagation pressure provided a peak value of 25340 Pa, which compares well with the simulation results. Once again, using the theoretical speed of sound as the wave propagation velocity would have led to a peak pressure of 16000 Pa, which is 60% less than the model predictions. These results further demonstrate that equation (7-10) can assume that the propagation velocity is equal to the speed of sound only if $v<<c$.

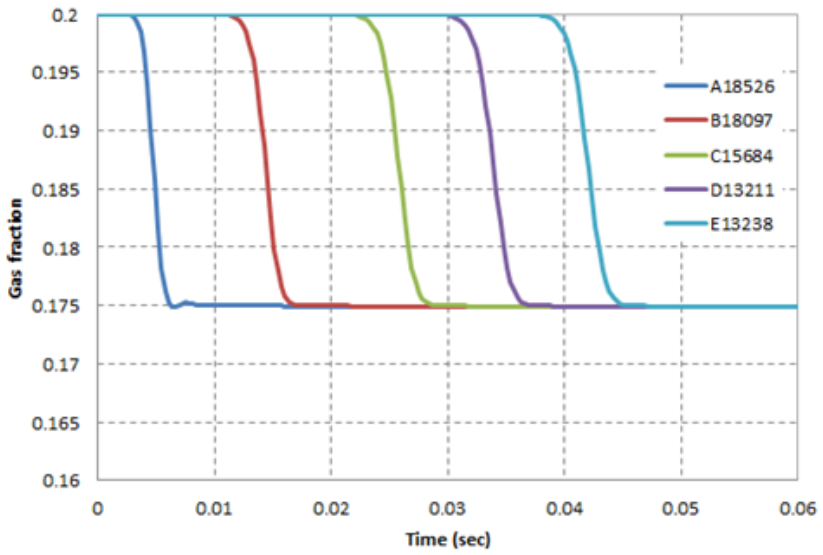

Figure 7-15: Gas fraction points for 2D column at 1 m/s with adiabatic equation of state and initial gas fraction of 20%.

As far as the gas fraction is concerned, its value should reduce with increasing compression, which means that higher velocity impacts should compress the particles further reducing the amount of gas present in them. This can be seen in Figure 7-16 where the same column with initial gas fraction of 20% was tested with velocities of 5 and 10 m/s.

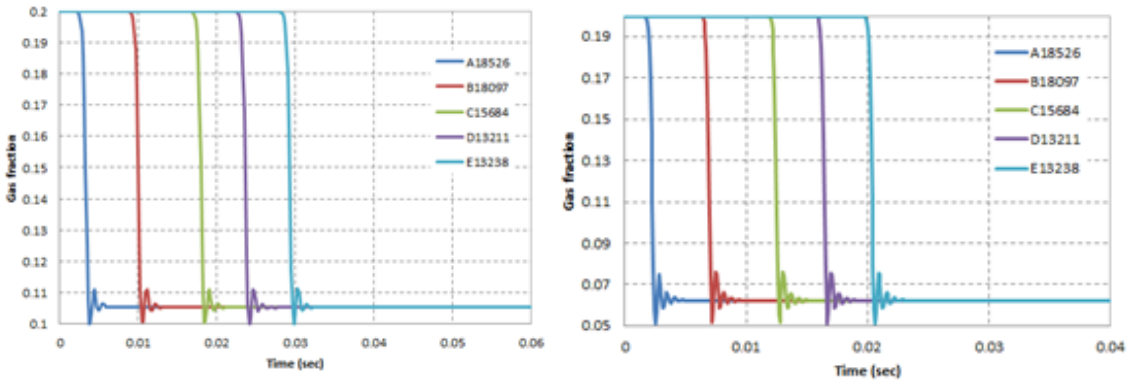

Figure 7-16: Gas fraction reduction for velocities of 5 m/s (left) and 10 m/s (right) for the 2D column test with the adiabatic equation of state and an initial gas content of 20%. The particles compress more with the 10 m/s impact case leading to a reduction in the gas content.

There are three main findings with respect to the simulations performed above. Firstly, the adiabatic equation of state appears to provide more accurate pressure results when compared to the alternative ideal gas equation of state. This was checked against the plane wave propagation equation for a fluid for different impact velocities. For the higher impact velocities (1 m/s) the propagation velocity should be used, in the plane wave propagation equation, instead of the speed of sound of the mixture. Secondly, the higher gas content leads to slower wave propagation and lower pressure peaks. This is in accordance with theory, suggesting that the cushioning effect is more profound with higher levels of air. Finally, the above simulations correctly predicted a higher reduction of the gas fraction as the velocity increases, which is expected because the particles are compressed more in such cases.

7.4 Drop Test

In this section a validation case is considered. Experiments of a drop test of a guided circular plate, made of steel, of varying mass and with various velocities onto aerated water have been performed by Walkden [104]. The results of these experiments have been collected and analysed by Bullock et al. [49].

The experimental test cases used three different impact velocities, 1.98 m/s, 2.8 m/s and 3.43 m/s. Two different masses were considered, 1.35 kg and 1.85 kg. Finally, the levels of aeration in the water domain ranged from 0% (pure water) up to 17.5%.

The aim of this validation case is to show that the aeration model, described above, provides a reasonable peak pressure reduction with increasing levels of aeration in the water domain.

7.4.1 Simulation Model

For the validation purposes the heavier mass of 1.85 kg and the highest impact velocity of 3.43 m/s were selected. The overall model is shown in Figure 7-17. The structure is considered rigid and the element size was chosen carefully, in order to match closely with the SPH particle spacing (Figure 7-18).

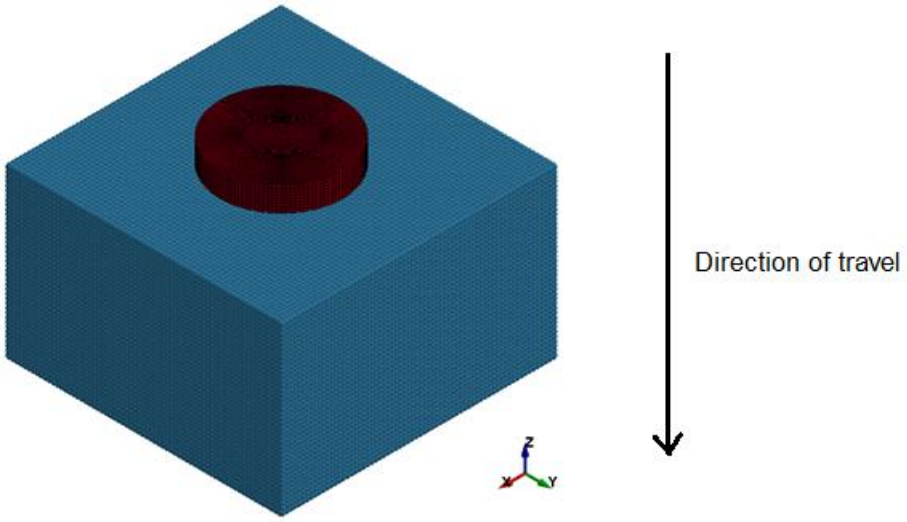

Figure 7-17: Overall drop test set-up for aeration validation case.

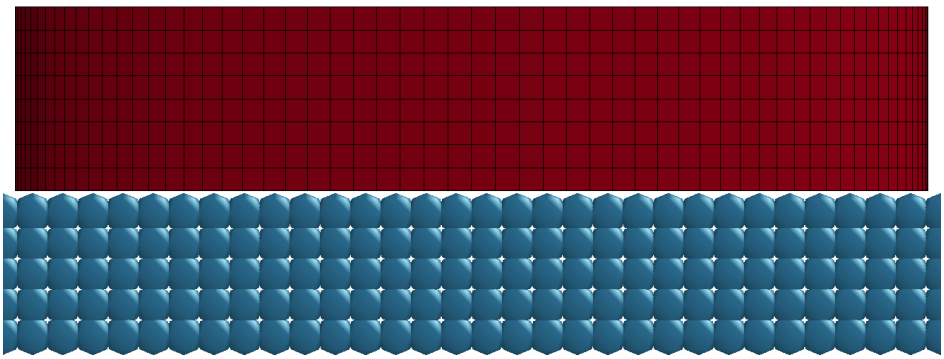

Figure 7-18: Relative SPH particle – finite element spacing.

The main input parameter for the circular plate are given in the table below.

Table 7-11: General input data for circular plate for drop test in aerated water.

Diameter, m	0.09
Height, m	0.018
No of elements (Rigid Solids)	30240
Vertical velocity, m/s	3.43
Mass, kg	1.85
Boundary conditions	Only vertical motion allowed and fully constrained in rotations

The main input parameters for the water domain are given in the table below.

Table 7-12: General input data for water domain for drop test in aerated water.

Length, m	0.2
Height, m	0.12
Width, m	0.2
No of particles	189584
Particle spacing, m	0.003
Smoothing length, m	0.0039
Density, kg/m^3	1000
Mass, kg	4.8

No symmetry planes or gravity has been applied to the model. The adiabatic formula (7-2) was used with $\gamma = 1.4$.

As far as the aeration test cases in this validation section are concerned, two separate case with 5% and 10% initial gas volume fraction were considered. The input parameters for these cases are given in Table 7-13.

Table 7-13: Aerated water model input parameters for drop test in aerated water.

Initial gas volume fraction	0.05	0.1
Initial mixture density density, kg/m^3	950.0	900.13
Liquid (water) density, kg/m^3	1000	1000
Gas (air) density, kg/m^3	1.225	1.225
Particle spacing, m	0.003	0.003
Minimum gas volume fraction	0.001	0.001
Maximum gas volume fraction	0.7	0.7
Mixture mass	4.56	4.32

7.4.2 Simulation Results

The figure below shows the pressure results for the pure water (with 0% aeration) and the results with 5% and 10% aeration. The results focus on the initial stages of the impact. This is because the aim is to capture the reduced pressure peaks as the aeration levels increase.

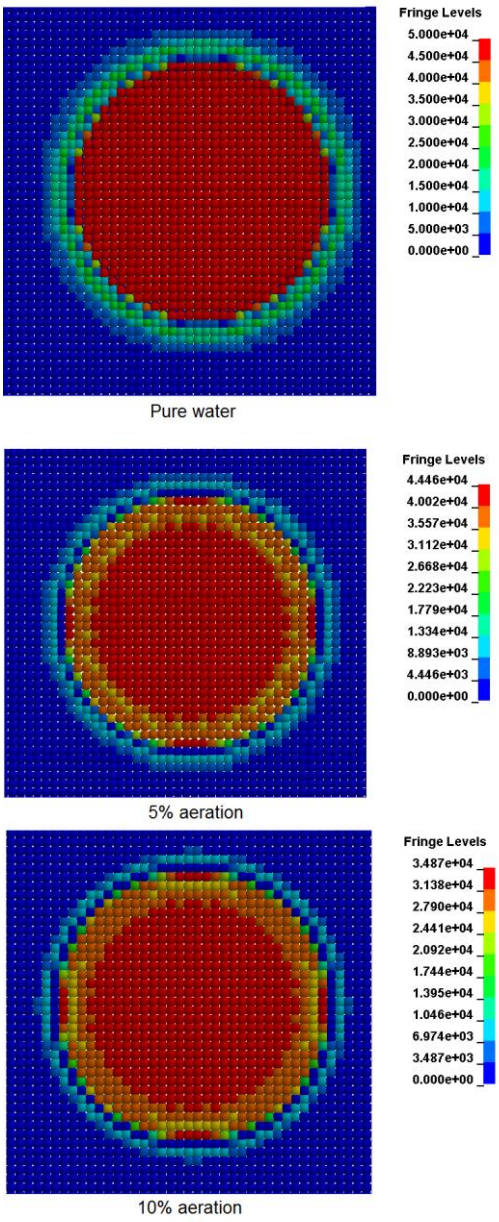

Figure 7-19: Top view of pressure plots at 0.00074 s. Plots neglect the plate in order to show the pressure results. Results show a reduced peak pressure as the aeration levels increase. Fringe levels show pressure in Pa.

The results show that as the aeration levels increase, there is a drop in the peak pressures as expected. This is shown in the figure below, where a comparison of the peak pressures at the centre of the water domain is plotted.

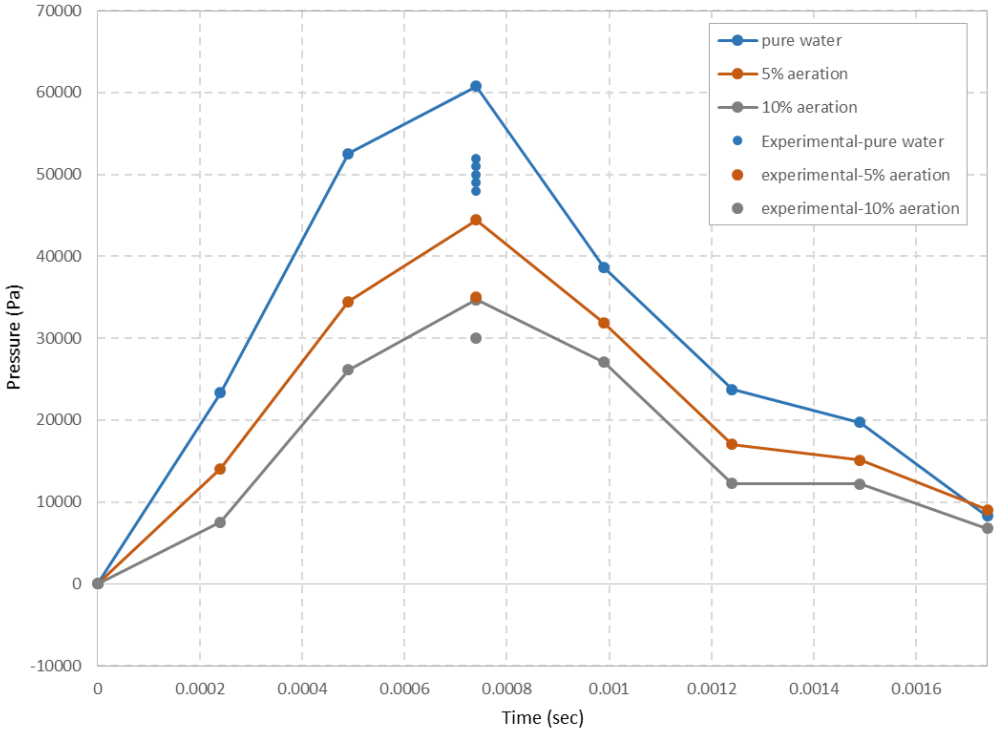

Figure 7-20: Pressure evolution for circular plate impact on water. Pure water, 5% aeration and 10% aeration cases were considered and compared to experimental results by Walkden [104]. Comparison shows good agreement, especially for the 10% aeration case.

The pressure results of Figure 7-20 compare relatively well with the experimental results. The difference in the results are possibly due to the reduced water model. This was done in order to reduce the computational costs, since the aim of this validation case was to show the reduced peak pressure that occur at the start of the impact. Nevertheless, some noise and rebound of pressure waves from the edges of the water domain can influence the results further towards the centre of the water domain.

Secondly, the contact definition was chosen so that there is no particle penetration during the impact. Softer contact stiffness could be further investigated, as long as there is no penetration.

Finally, the particle spacing, chosen at 0.003 m, provided pressure predictions with an error of 16%-27% when compared to the experimental results. Further work on this test case could involve a finer particle distribution, along with an equally more detailed Finite Element model.

For completeness, the gas volume fraction is shown in the figure below for the 5% and 10% aeration cases. The results show the reduction in the gas volume fraction immediately below the circular plate. This is the expected behaviour since the particles beneath the plate are compressed.

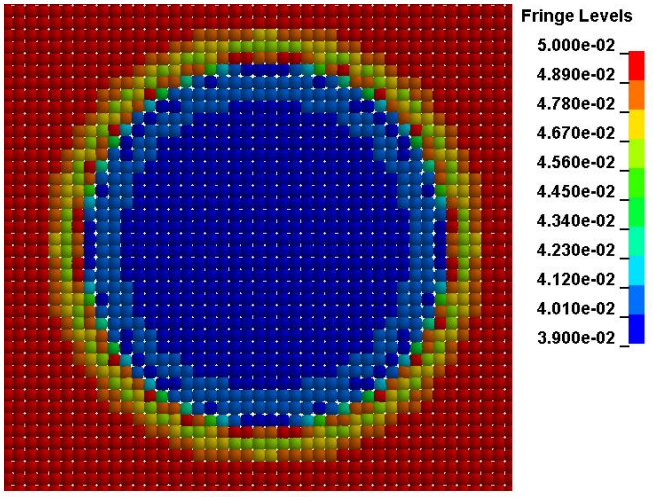

5% aeration

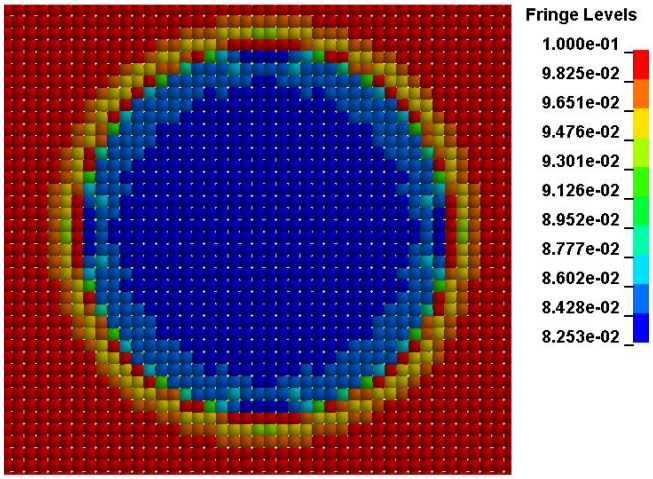

10% aeration

Figure 7-21: Top view of gas volume fraction plots at 0.00074 s. Plots neglect the plate in order to show the pressure results. Results show a reduction in gas content as the particles compressed. Fringe levels show gas volume fraction.

7.5 Inclined Plate

In this section, a more realistic and complicated example was tested for the aerated model. The same plate example, as in Section 6.7 (Figure 6-28), was used. The plate test cases include the structure, impacting the water with an inclination of 4° and 10° at a horizontal velocity of 40 m/s and a vertical velocity of -1.5 m/s. In both inclination

tests the initial gas volume fractions range from 0.05 to 0.2. Even though there are no experimental results for the effect of aeration, these results can provide added confidence in the aeration model, with respect to complicated fluid-structure interaction problems. All the boundary conditions set out in Section 6.7 remain in place.

7.5.1 4° Inclination

The water model consists of 19200 particles with a spacing of 0.05 m and a total length of 6 m. The main input parameters for the water domain are given in Table 7-14. The details of the structure are given in section 6.7. For an inclination of 4°, the pressure levels for the pure water model are given in Figure 7-22.

Table 7-14: General input data for water domain for plate impact at 4° inclination.

Length, m	6.0
Height, m	0.4
Width, m	1.0
No of particles	19200
Particle spacing, m	0.05
Smoothing length, m	0.06
Density, kg/m^3	1000
Mass, kg	2420

The Murnaghan equation of state was used. The parameters are given below. Since the flow velocities of the simulations were not expected to reach values close to the speed of sound it was beneficial to employ a reduced compressibility. This increased the critical time step, while maintaining the incompressible nature of the liquid.

Table 7-15: Murnaghan EOS input data.

Bulk Modulus B, MPa	1.5
Parameter γ, -	7.0

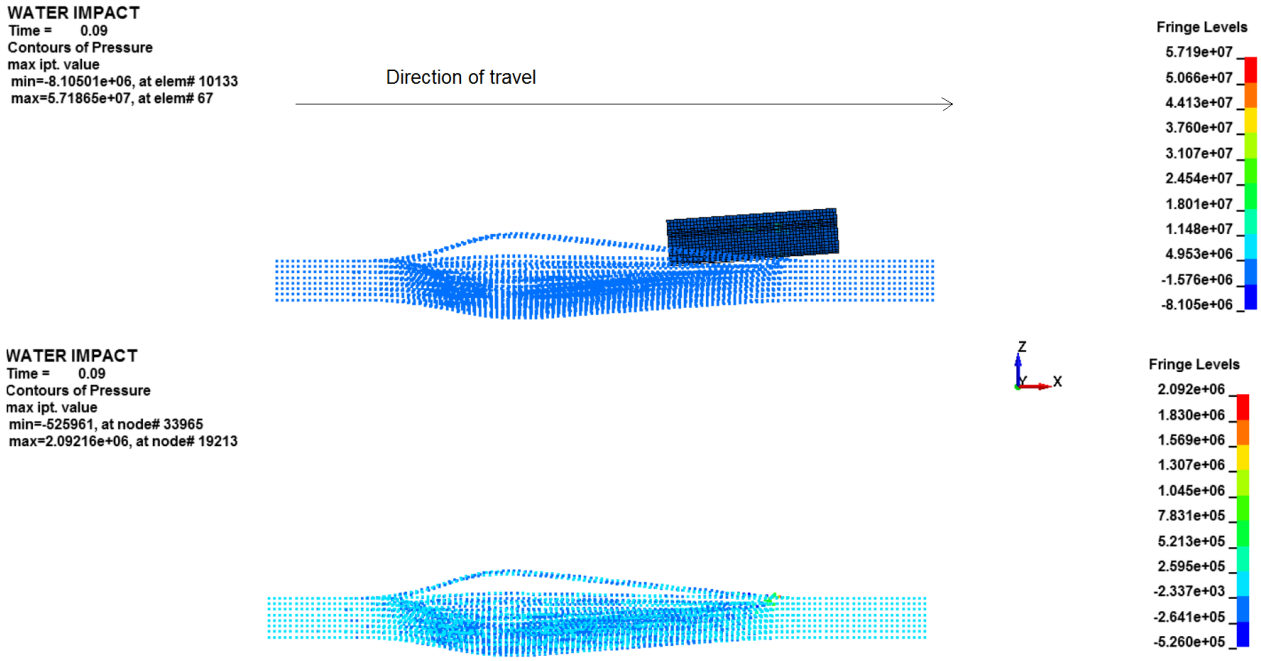

Figure 7-22: Global behaviour for pure water model at 4° inclination. Side view of model at 0.09 s. Forward velocity of the structure is 40 m/s and vertical velocity of the structure is -1.5 m/s. Fringe levels show pressure in Pa. Top figure shows complete set-up and bottom figure shows pressure levels for the water domain only.

Next the aeration model was tested. The necessary inputs are given in Table 7-16.

Table 7-16: Aerated water model input parameters for plate impact tests at 4° inclination.

Initial gas volume fraction	0.05	0.1	0.2
Initial mixture density density, kg/m^3	950.0	900.13	800.3
Liquid (water) density, kg/m^3	1000	1000	1000
Gas (air) density, kg/m^3	1.225	1.225	1.225
Particle spacing, m	0.01	0.01	0.01
Minimum gas volume fraction	0.001	0.001	0.001
Maximum gas volume fraction	0.7	0.7	0.7
Mixture mass, kg	2280	2160.3	1920.6

Similar global behaviour, to the pure water test case, was observed for the aerated test cases in Figure 7-23-Figure 7-25. Since there were no experimental data available, the interest in this section is primarily on the changes in the water model and how that affects the forces imparted on the structure. Direct comparison of the pressure levels would not be correct, as the peak pressures are not experienced at the same locations.

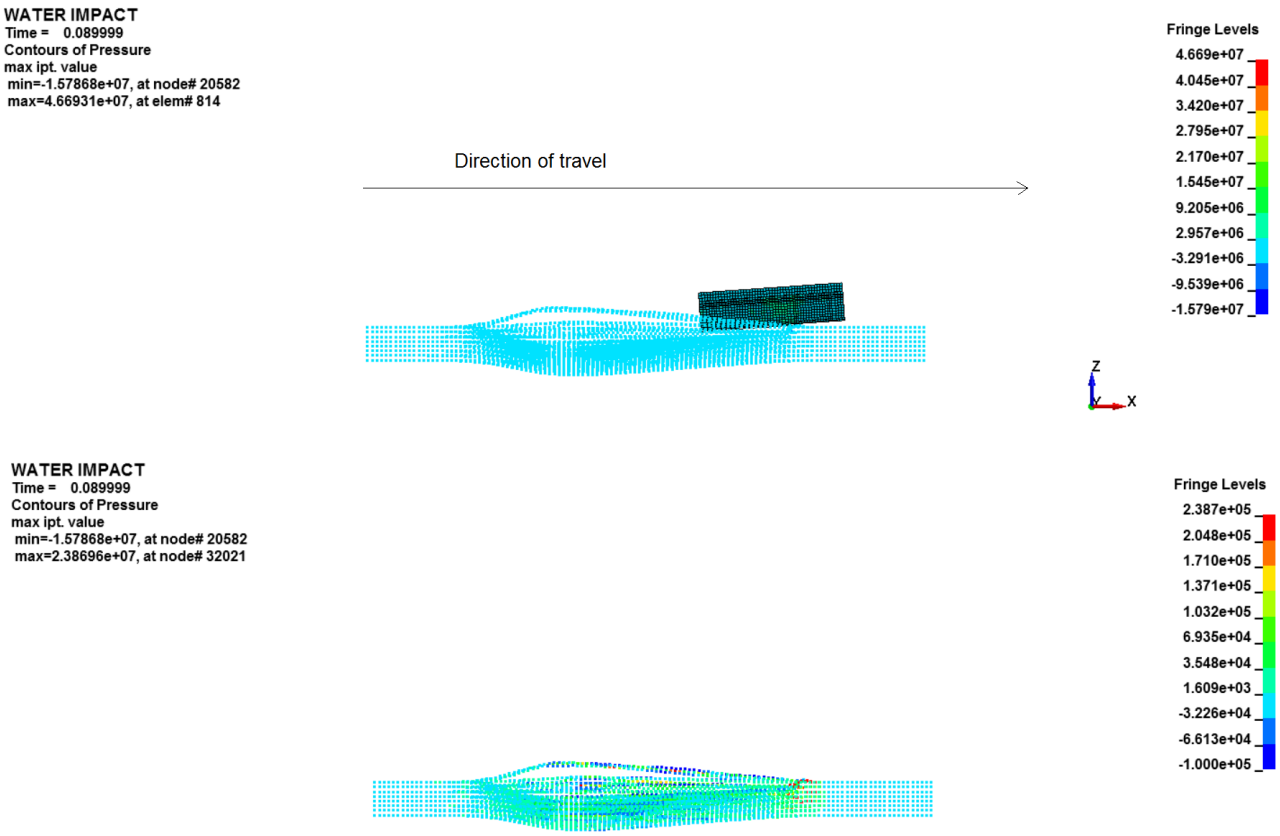

Figure 7-23: Global behaviour of structure for aeration levels of 5% for 4° inclination. Side view of model at 0.09 s. Forward velocity of the structure is 40 m/s and vertical velocity of the structure is -1.5 m/s. Fringe levels show pressure in Pa. Top figure shows complete set-up and bottom figure shows pressure levels for the water domain only.

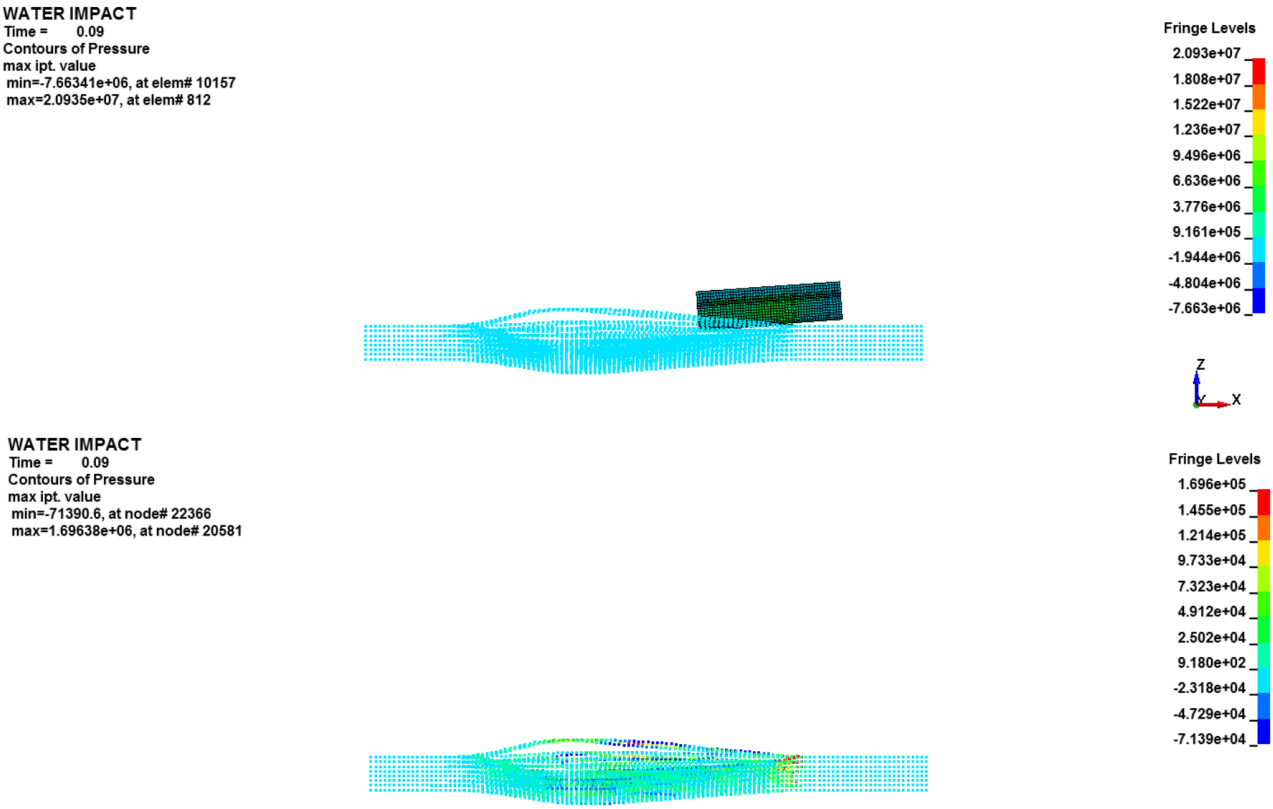

Figure 7-24: Global behaviour of structure for aeration levels of 10% for 4° inclination. Side view of model at 0.09 s. Forward velocity of the structure is 40 m/s and vertical velocity of the structure is -1.5 m/s. Fringe levels show pressure in Pa. Top figure shows complete set-up and bottom figure shows pressure levels for the water domain only.

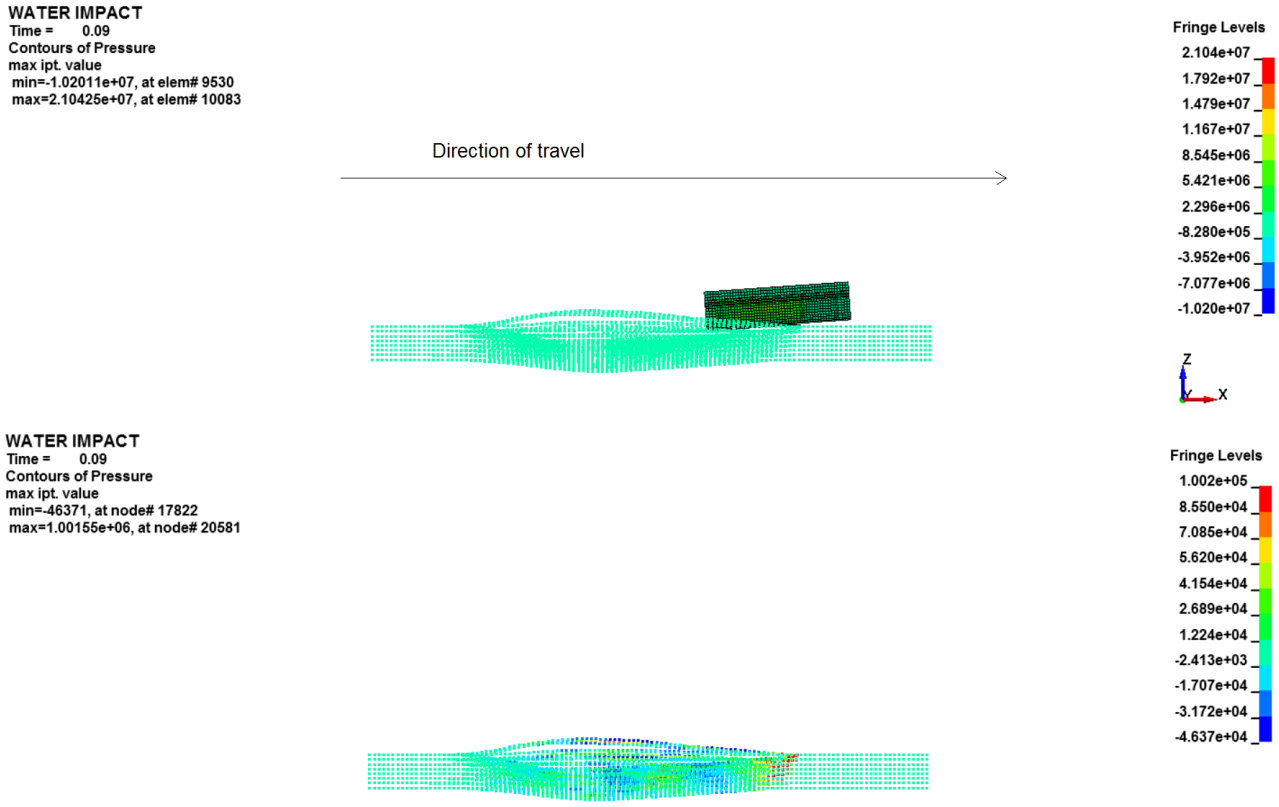

Figure 7-25: Global behaviour of structure for aeration levels of 20% for 4° inclination. Side view of model at 0.09 s. Forward velocity of the structure is 40 m/s and vertical velocity of the structure is -1.5 m/s. Fringe levels show pressure in Pa. Top figure shows complete set-up and bottom figure shows pressure levels for the water domain only.

A better understanding of the effect of aeration on the structure was found through the force acting on it. The overall contact force acting on the Finite Element model is shown in Figure 7-26.

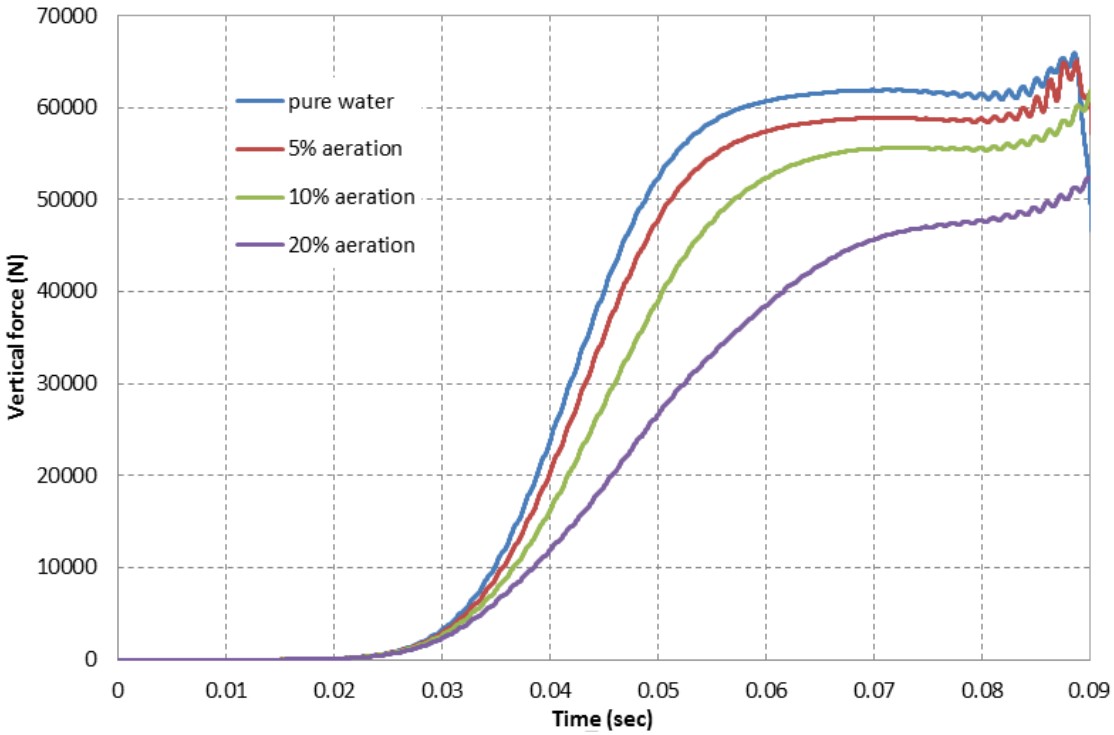

Figure 7-26: Vertical force acting on the structure for the original (pure water) model, 5%, 10% and 20% aeration models for impact of plate at 4° inclination.

In general, the force graphs follow a similar trend when compared to the original (pure water) model. However, as the gas content increased, the slope of the force graphs reduced. This is due to the fact that, as in experimental results for simpler shapes, the presence of air in the water acted as a cushioning factor. The compression of the air prior to the actual impact was found to provide less abrupt peaks. In this model, the presence of air in a mixture approach followed a similar behaviour. Moreover, the peak forces in the graph were consistently reduced as the gas (air) content increased. The oscillations present, were due to the potential increase in the vibration on the plate. Next, the pressure at the centre of the plate was compared for all four case.

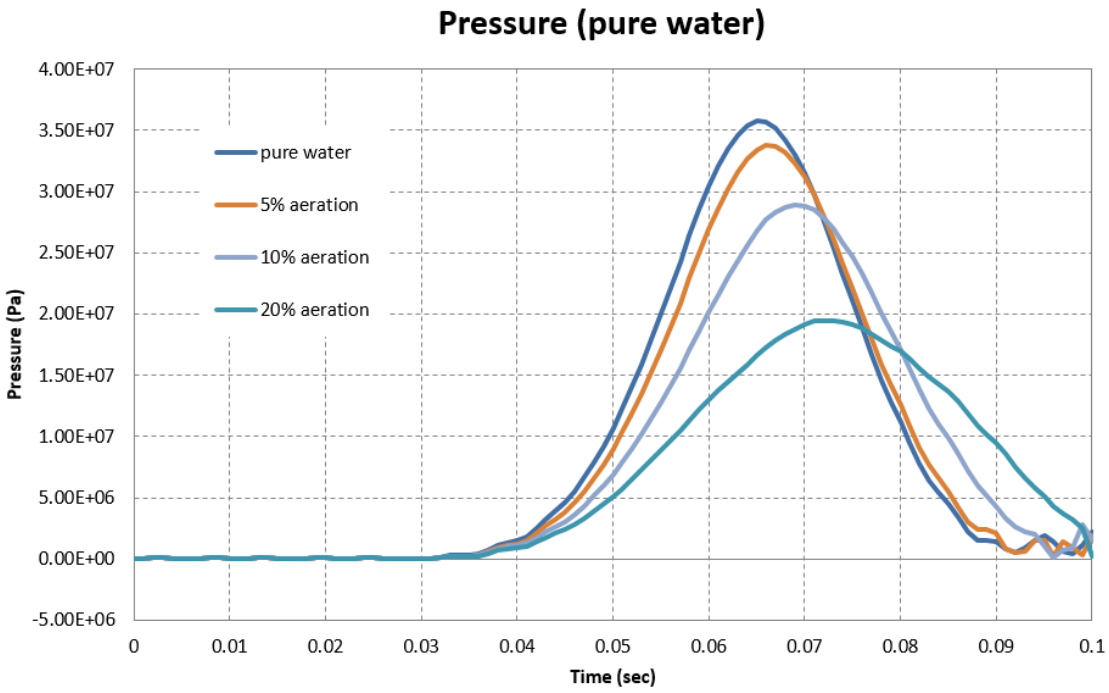

Figure 7-27: Pressure acting on the centre of the plate for the pure water model, 5%, 10% and 20% aeration models.

The pressure results show that the peak pressures became lower as the aeration increases, especially for the 10% and 20% cases. This is in accordance with the force behaviour, discussed previously, as well as with the theory. Moreover, a clearer observation with respect to the pressure pulse can be made. For the pure water case the initial pressure peak at the first point of impact lasted for 0.05 s. The duration was the same for the 5% aeration case, however it progressively increased to 0.055 s and 0.06 s for the 10% and 20% aeration cases respectively. This suggests that maybe a 5% aeration combined with the relatively coarse particle distribution is too low to show any significant difference.

Overall, the results for this test case indicate that the presence of air will reduce the pressures imparted on the structure. Even though there are no experimental results for comparison, the above behaviour is expected following the simulations on simple angled shapes performed by [42] [43]. The low angle of the plate, as well as the fact that it is a flat section, further suggest that the presence of air will play a role. Its significance however requires experimental results.

7.5.2 10° Inclination

The same case as before was modelled but in this set-up with an inclination of 10°. In this case, the water model consists of 32000 particles with a spacing of 0.05 m and a total length of 10 m. The same equation of state and boundary conditions as in Section 7.5.1 were used. The pressure results for the pure water case are shown in Figure 7-28.

Table 7-17: General input data for water domain for plate impact at 10° inclination.

Length, m	10.0
Height, m	0.4
Width, m	1.0
No of particles	32000
Particle spacing, m	0.05
Smoothing length, m	0.06
Density, kg/m^3	1000
Mass, kg	4000

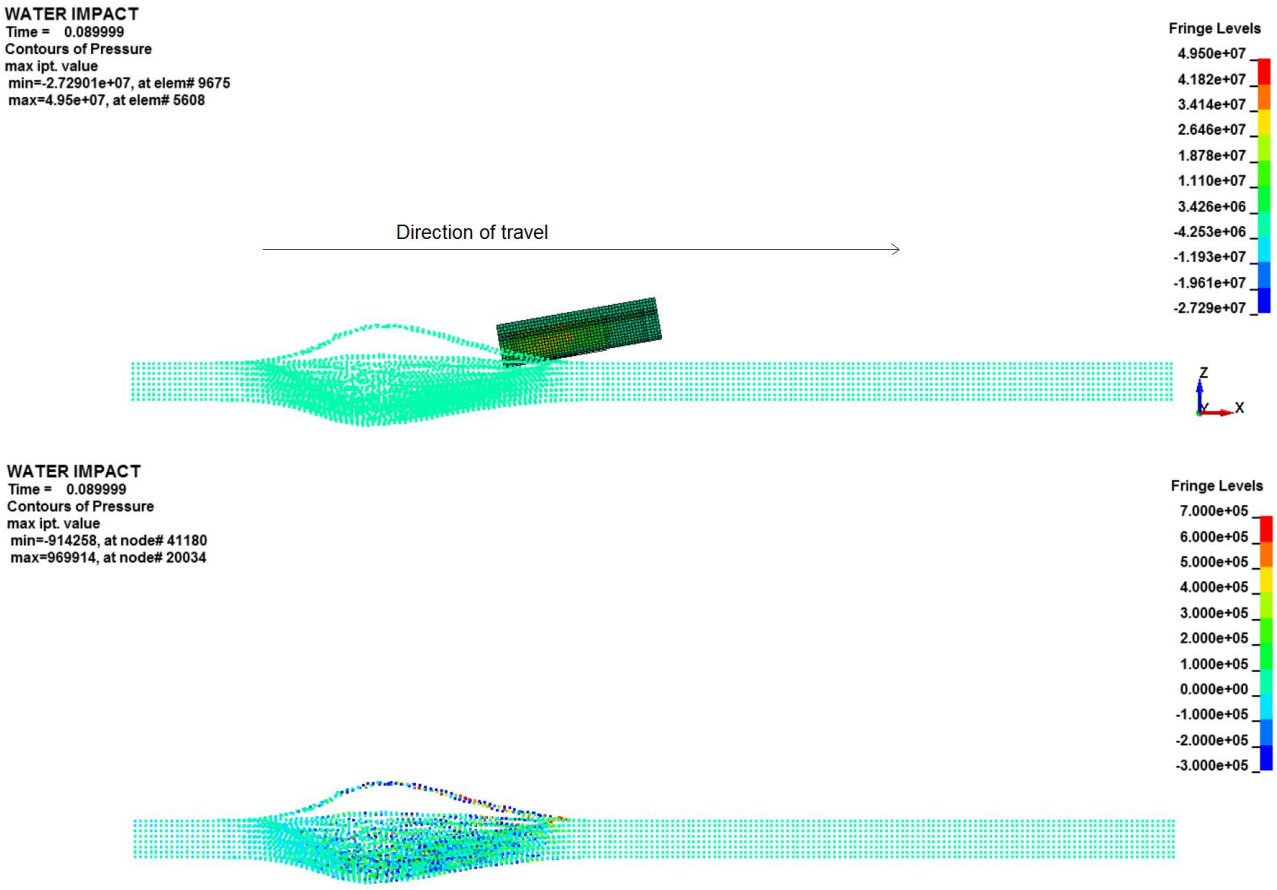

Figure 7-28: Global behaviour for pure water model at 10° inclination. Side view of model at 0.09 s. Forward velocity of the structure is 40 m/s and vertical velocity of the structure is -1.5 m/s. Fringe levels show pressure in Pa. Top figure shows complete set-up and bottom figure shows pressure levels for the water domain only.

The overall behaviour of the structure remained the same, however the water domain suffered from greater disturbances compared to the 4° inclination. The fact that this feature appears to this extent in the higher inclination test case, suggests that it was related to the positioning of the structure rather than the way the water is model. Since the impact was concentrated in a smaller area of the structure, it is expected that the water deformation in the vicinity will be more severe.

Another aspect that needs to be discussed is the deformation of the particles at the bottom of the water domain. This was present in both the 4° and 10° inclination impacts. Since there was no boundary applied on the bottom of the water domain, the particles were allowed to move outwards freely. The reason for the choice of this depth

was purely the computational cost of such simulations. Extending the depth would lead to a better description in the boundary.

Next the aeration model was tested. The necessary inputs are given in Table 7-18.

Table 7-18: Aerated water model input parameters for plate impact tests at 10° inclination.

Initial gas volume fraction	0.05	0.1	0.2
Initial mixture density, kg/m^3	950.0	900.13	800.3
Liquid (water) density, kg/m^3	1000	1000	1000
Gas (air) density, kg/m^3	1.225	1.225	1.225
Particle spacing, m	0.01	0.01	0.01
Minimum gas volume fraction	0.001	0.001	0.001
Maximum gas volume fraction	0.7	0.7	0.7
Mixture mass	3800.3	3600.5	3201

Similar global behaviour, to the pure water test case, was observed for the aerated test cases in Figure 7-29-Figure 7-31. Since there were no experimental data available, the interest in this section is primarily on the changes in the water model and how that affects the forces imparted on the structure. Direct comparison of the pressure levels would not be correct as the peak pressures are not experienced at the same locations.

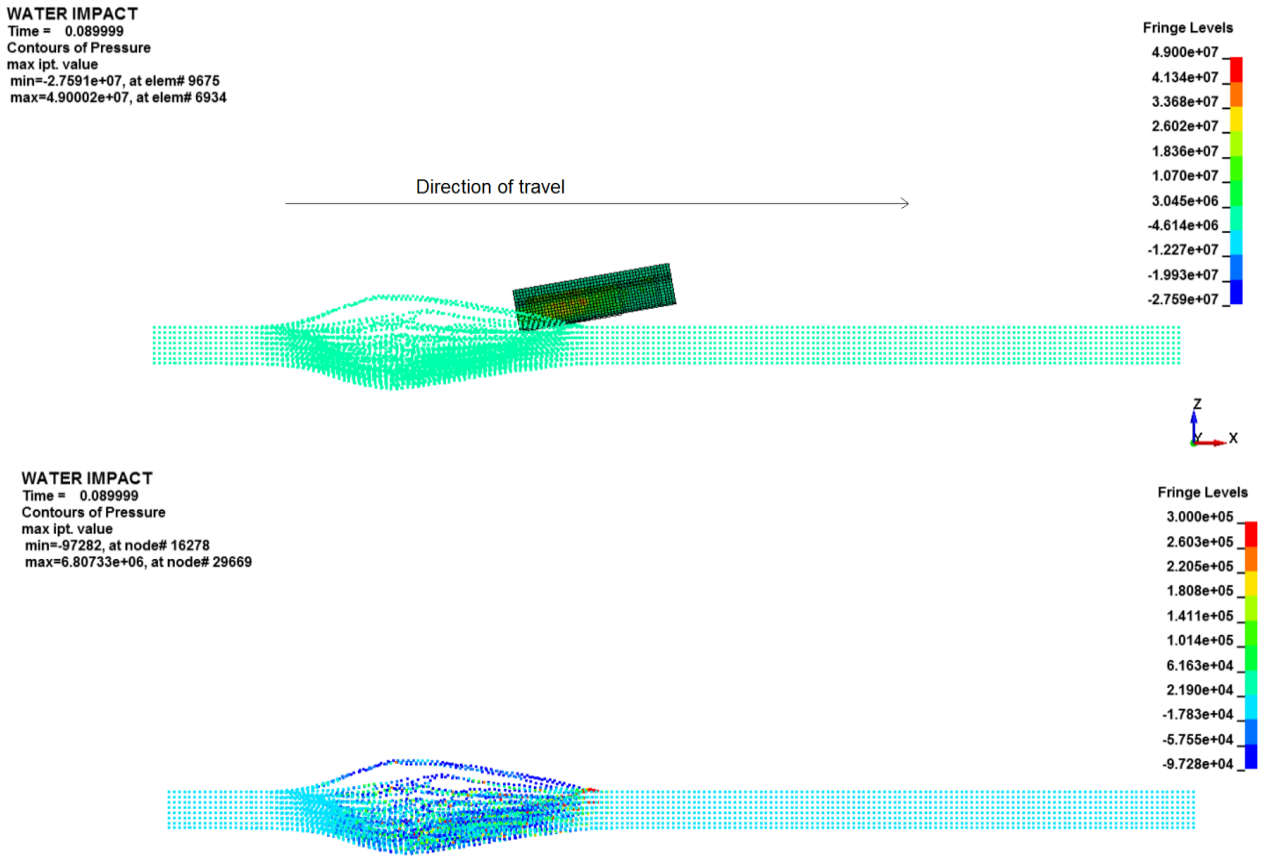

Figure 7-29: Global behaviour of structure for aeration levels of 5% for 10° inclination. Side view of model at 0.09 s. Forward velocity of the structure is 40 m/s and vertical velocity of the structure is -1.5 m/s. Fringe levels show pressure in Pa. Top figure shows complete set-up and bottom figure shows pressure levels for the water domain only.

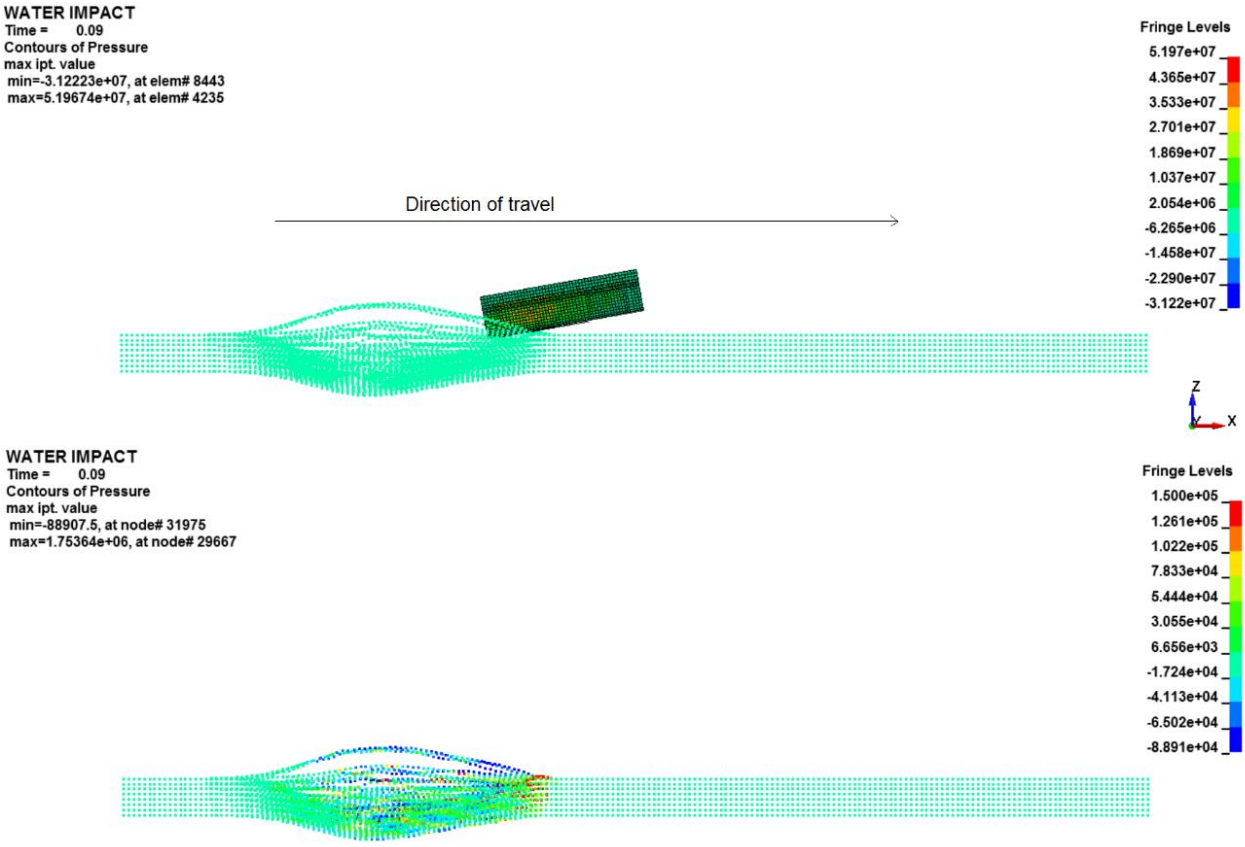

Figure 7-30: Global behaviour of structure for aeration levels of 10% for 10° inclination. Side view of model at 0.09 s. Forward velocity of the structure is 40 m/s and vertical velocity of the structure is -1.5 m/s. Fringe levels show pressure in Pa. Top figure shows complete set-up and bottom figure shows pressure levels for the water domain only.

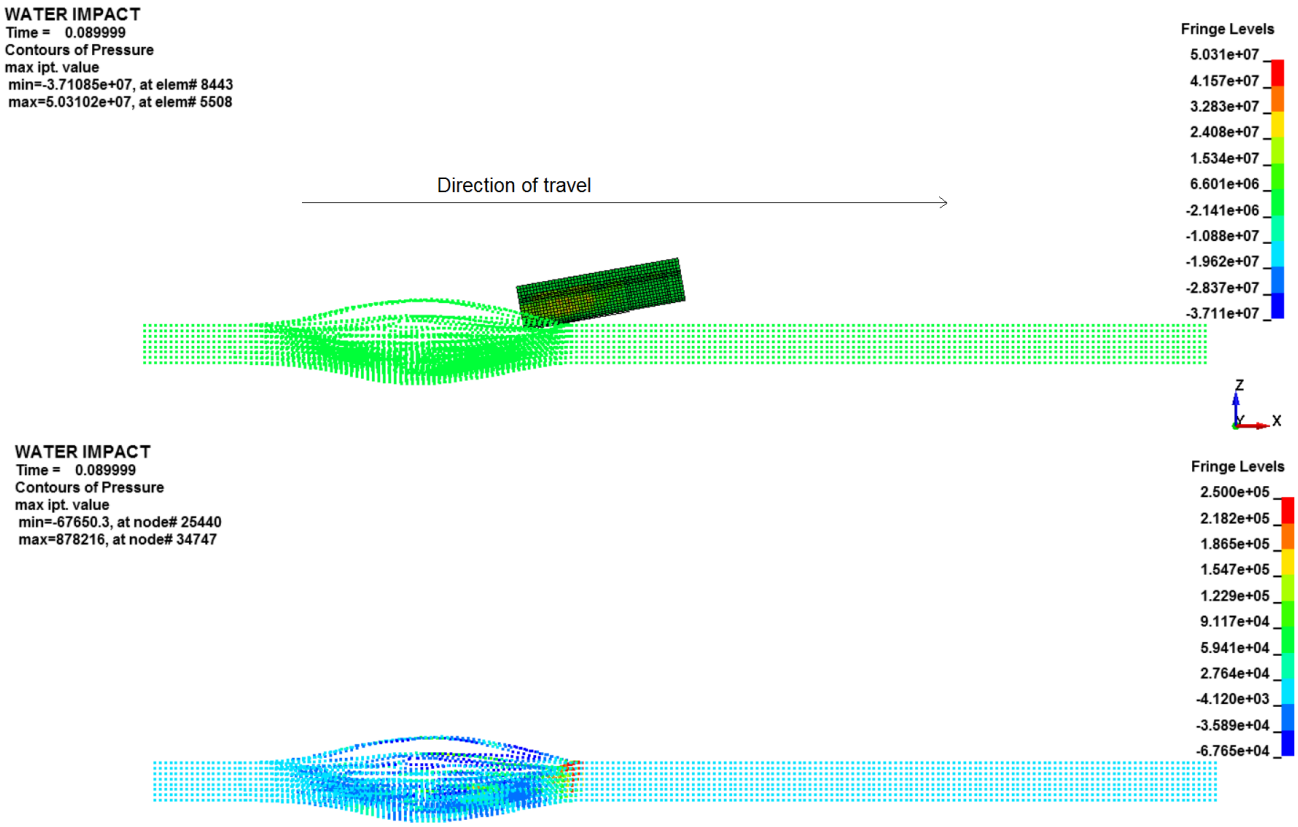

Figure 7-31: Global behaviour of structure for aeration levels of 20% for 10° inclination. Side view of model at 0.09 s. Forward velocity of the structure is 40 m/s and vertical velocity of the structure is -1.5 m/s. Fringe levels show pressure in Pa. Top figure shows complete set-up and bottom figure shows pressure levels for the water domain only.

The force graph of Figure 7-32 for the 10° inclination is similar in trend as in the 4° case. As the aeration levels increased, the force peaks reduced and the slope of the force graph was not as abrupt as in the pure water case.

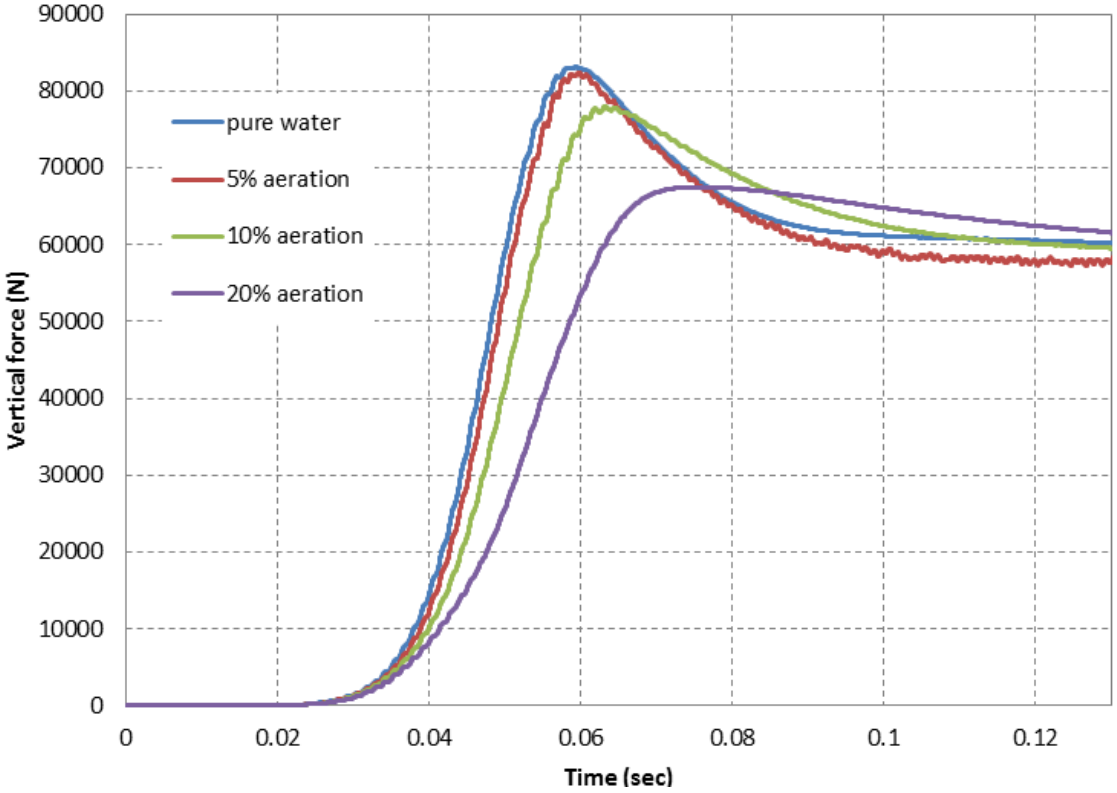

Figure 7-32: Vertical force acting on the structure for the original (pure water) model, 5%, 10% and 20% aeration models for impact of plate at 10° inclination.

With respect to the pressure at the middle of the structure, shown in Figure 7-33 and Figure 7-34, there are two points that need to be discussed. Firstly, the peak values were found to be higher, when compared to the 4° inclination. One possible explanation for this, is the increase in the angle of impact, which leads to a smaller wetted surface. This would lead to higher contact forces (as it is indeed the case from Figure 7-32) and as a consequence higher pressure values.

The second observation, from the pressure results, is that there was no significant difference in the peak values. To the contrary, the pressure reached an initial peak value of around 50 MPa in all of the cases. The most likely explanation for this is the configuration of the test case at a higher angle of impact. The elements chosen for the pressure results were located in the centre of the plate, which was possibly further from any direct contact with the water and were certainly not located close to the first point of contact.

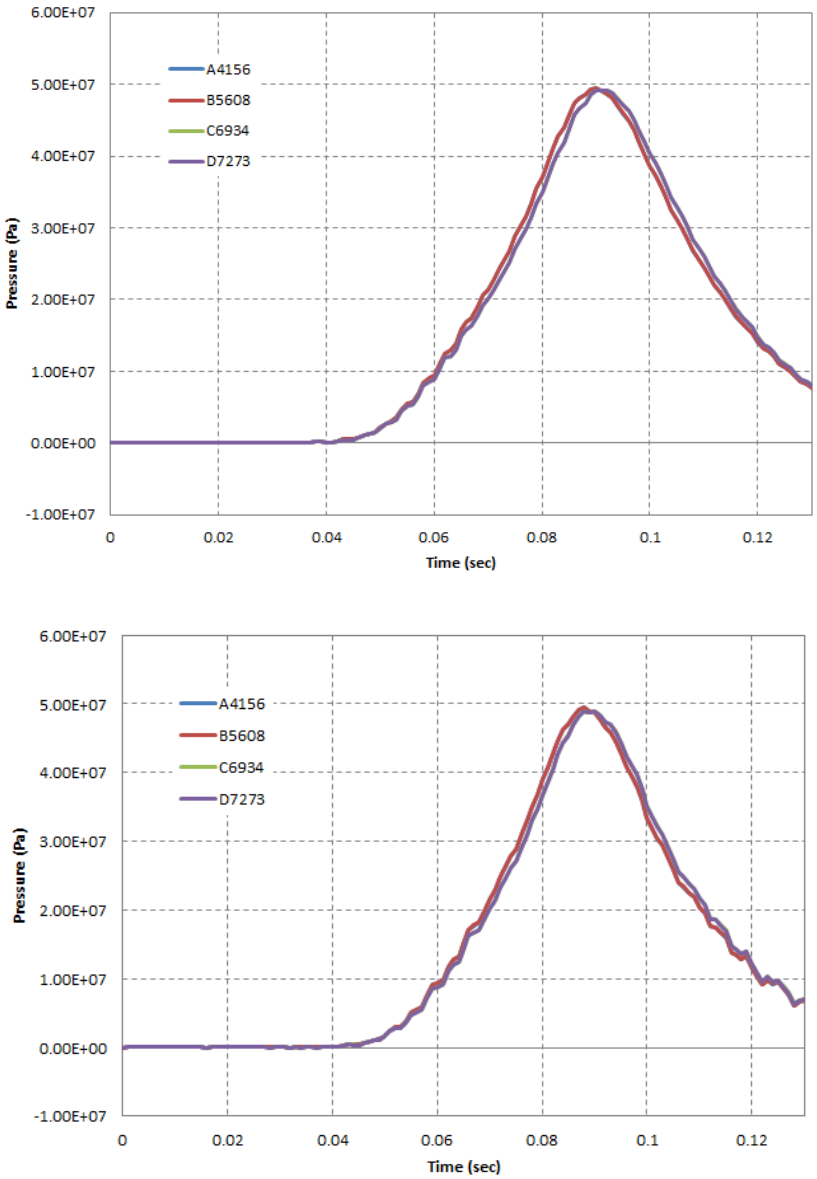

Figure 7-33: Pressure results for four elements (4156, 5608, 6934 and 7273) at the centre of the impacting plate for pure water (top figure) and 5% (bottom figure) aeration at 10° inclination.

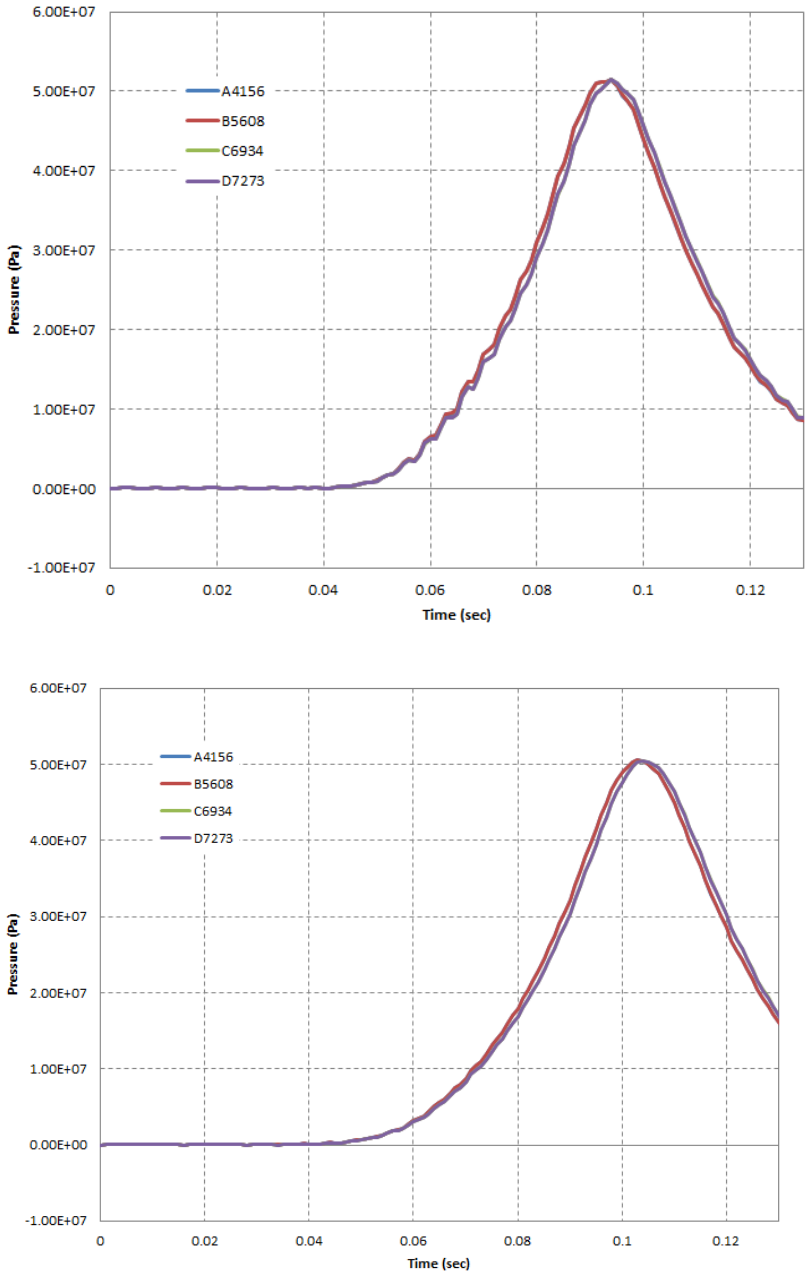

Figure 7-34: Pressure results for four elements (4156, 5608, 6934 and 7273) at the centre of the impacting plate for 10% (top figure) and 20% (bottom figure) aeration at 10° inclination.

A pressure comparison is given in Figure 7-35 between the original (pure water) and the aerated model. In this case, the pressure was taken at an element in the middle of the trailing edge of the plate that is in direct contact with the water. The trend of the results is much closer to the results obtained in the 4° inclination test cases. The pressure peak was at its highest when the pure water is considered and it reduced as the aeration levels increase. Finally, the duration of the initial impact peak was larger

for the higher levels of aeration. This final set of results suggests that the initial choice of the elements in the middle of the plate for the higher inclination test case was not the most appropriate, as it failed to capture the effect of aeration on the structure.

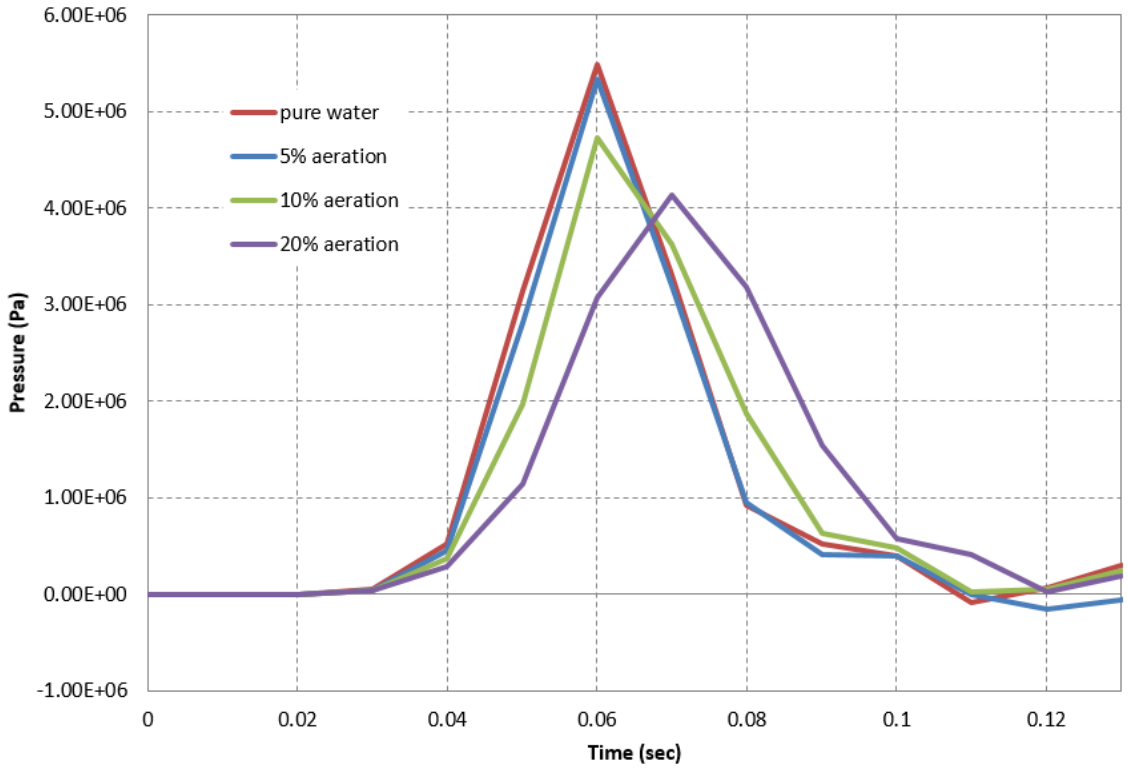

Figure 7-35: Pressure results for an element at the trailing edge of the plate for the pure water model, 5%, 10% and 20% aeration models for impacting plate at 10° inclination.

7.6 NACA2929 J-Body

In this section, a fuselage shape is considered and it is taken from a paper by McBride et al. [2]. Their investigation looked into a variety of fuselage shapes including the J-body and their effect in the general behaviour upon ditching. The experimental set-up consisted of catapulting the fuselage model at a pitch angle of 10° and a horizontal velocity of 9.144-18.288 m/s (30-60 ft/s). The fuselage of the J-body was swept up, with a tendency to increase suction forces, fineness ratio of 9, and a circular cross section. The reduction in forward velocity, the change in attitude and the change of the height of the centre of gravity were recorded.

The aim of this set of simulations is to provide further confidence in the aeration model. Furthermore, the testing of a complete fuselage should allow for the investigation of the overall dynamics of the fuselage, as a consequence of the presence of air in the water. Moreover, the following test case was considered in simulations by Streckwall et al. [26] at TUHH, allowing for an initial comparison of the fluid-structure interaction of this fuselage to other numerical tools. Streckwall et al. [26] used some generic aircraft models to simulate ditching events. A hybrid approach was used in order to estimate the forces on a section, using an enhanced momentum method based on the von Karman and Wagner theories. The authors also made use of a RANS solver in order to model the interaction of the structure with the free surface and the subsequent behaviour of the fuselage.

The fuselage model consists of 15000 rigid shell elements. The initial conditions of the model include the application of gravity and an initial forward velocity of 12.192 m/s (40 ft/s) and a vertical velocity of 0.7 m/s. With respect to the water model it consists of 647500 particles having a total length of 4.1 m, a width of 0.4 m and a depth of 0.2 m. The particle spacing was chosen at 0.008 m, which is fine enough to allow for an accurate description. It must be noted that one of the limitations of this model is the computational cost involved in such long runs. The length of the water model was chosen as stated above purely to avoid excessive computations. Figure 7-36 shows the initial set-up of the structure. Table 7-19 and Table 7-20 shows the input parameters for the structure and water domain models.

Table 7-19: General input data of the structure for fuselage water impact.

No of elements (Rigid Shell)	14828
Element thickness, m	0.002
Mass, kg	5.67
X coordinate of centre of mass	10.5
Y coordinate of centre of mass	0.0
Z coordinate of centre of mass	0.14
Horizontal velocity, m/s	12.192
Vertical velocity, m/s	0.7
Gravity, m/s^2	9.81
Boundary condition	Constrained in the lateral direction (y-axis)

Table 7-20: General input data of the water domain for fuselage water impact.

Length, m	4.1
Height, m	0.4
Width, m	0.2
No of particles	647500
Particle spacing, m	0.008
Smoothing length, m	0.01
Density, kg/m^3	1000
Mass, kg	328.0

The Murnaghan equation of state was used, using the same principle as in Sections 7.5.1 and 7.5.2. The parameters are given below.

Table 7-21: Murnaghan EOS input data.

Bulk Modulus B, MPa	1.5
Parameter γ, -	7.0

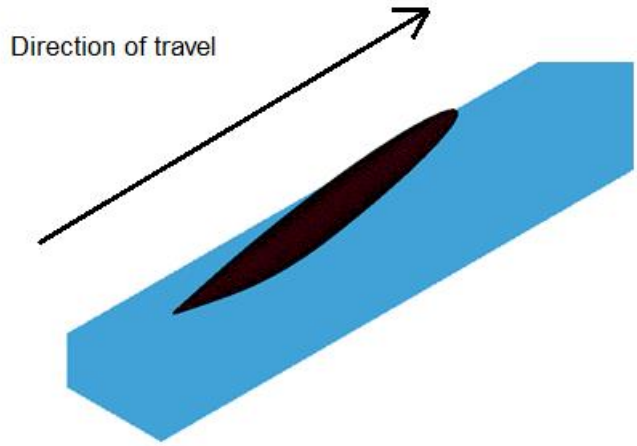

Figure 7-36: Initial set-up of fuselage structure.

The test cases followed the same initial gas fraction choices from the previous simulations, which are an initial gas content of 5%, 10% and 20%. Table 7-22 shows the aeration parameters that were used.

Table 7-22: Aeration parameters for fuselage water impact.

Initial gas volume fraction	0.05	0.1	0.2
Mixture density, kg/m^3	950.0	900.13	800.3
Mixture mass, kg	311.6	295.2	262.5
Minimum gas volume fraction	0.001	0.001	0.001
Maximum gas volume fraction	0.7	0.7	0.7
Gas density (air), kg/m^3	1.225	1.225	1.225
Liquid density (water), kg/m^3	1000	1000	1000

The pressure evolution of the pure water is shown first in Figure 7-37.

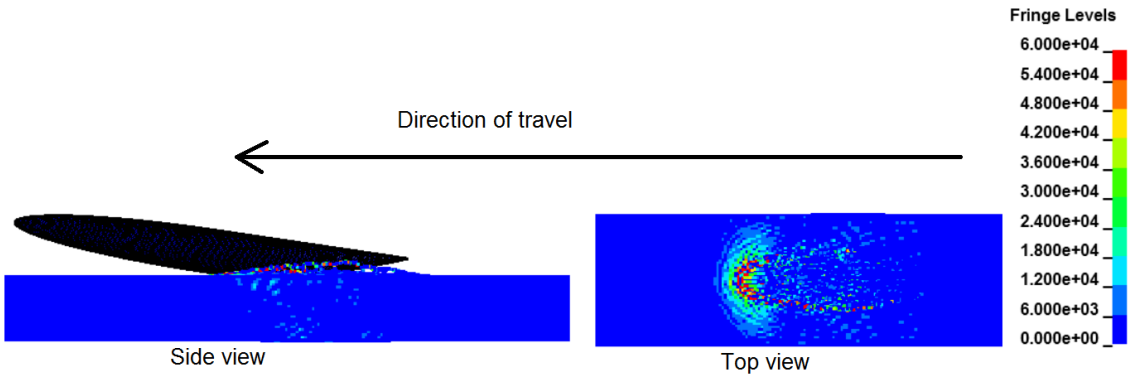

Figure 7-37: Impact evolution for the pure water case at 0.04 s. Fringe levels show pressure in Pa. Peak pressure was 190 kPa

With respect to the aerated cases the results are shown in Figure 7-38- Figure 7-40. To maintain consistency, the impact evolution in all the simulations were taken at the same time.

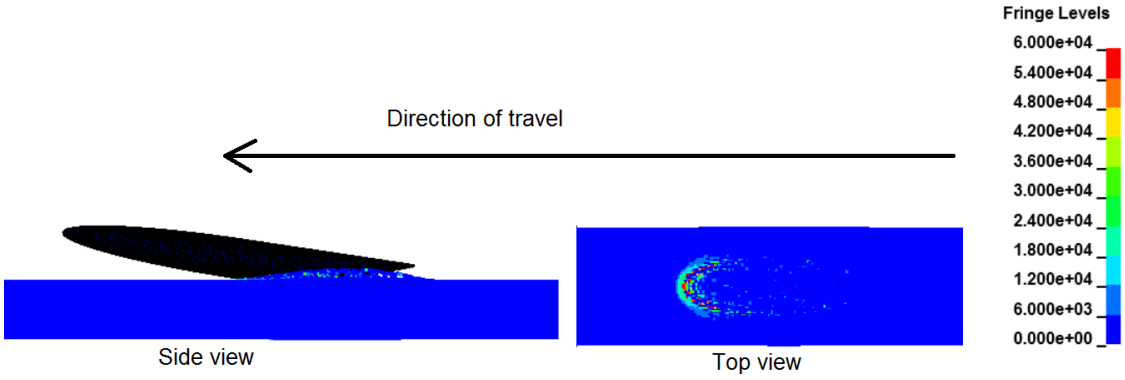

Figure 7-38: Impact evolution for the 5% aerated water at 0.04 s. Fringe levels show pressure in Pa. Peak pressure was 129 kPa.

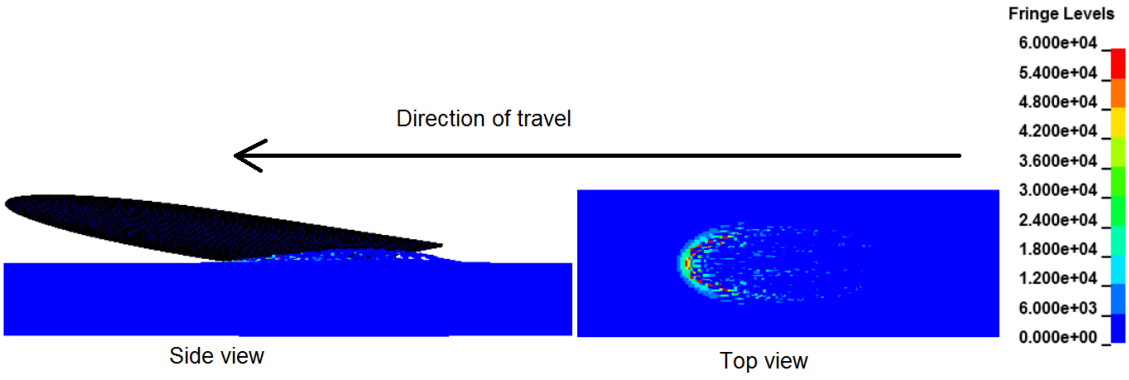

Figure 7-39: Impact evolution for the 10% aerated water at 0.04 s. Fringe levels show pressure in Pa. Peak pressure was 93.6 kPa.

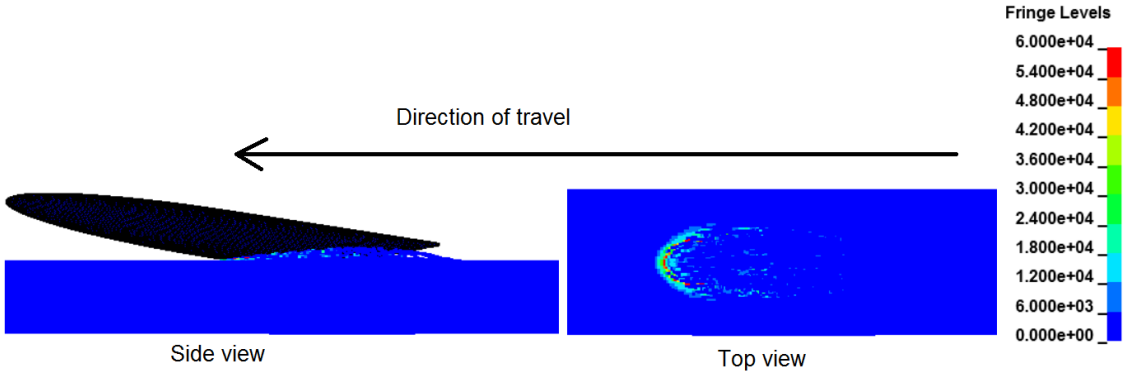

Figure 7-40: Impact evolution for the 20% aerated water at 0.04 s. Fringe levels show pressure in Pa. Peak pressure was 90.5 kPa.

The impact evolution results showed a general trend of reduced peak pressures when compared to the initial pure water model.

As far as the trajectory is concerned, the fuselage after the initial impact followed a relatively horizontal course, see Figure 7-41. Experimental results from McBride et al. [2] indicate that the fuselage should pitch up as a result of suction forces at the rear section of the fuselage. However, the lack of any discrete air particles in the above method did not allow the phenomenon of suction to be modelled. This led to inaccuracies in the general behaviour of the fuselage. Moreover, this model did not experience any skipping, which compares well with the experimental data.

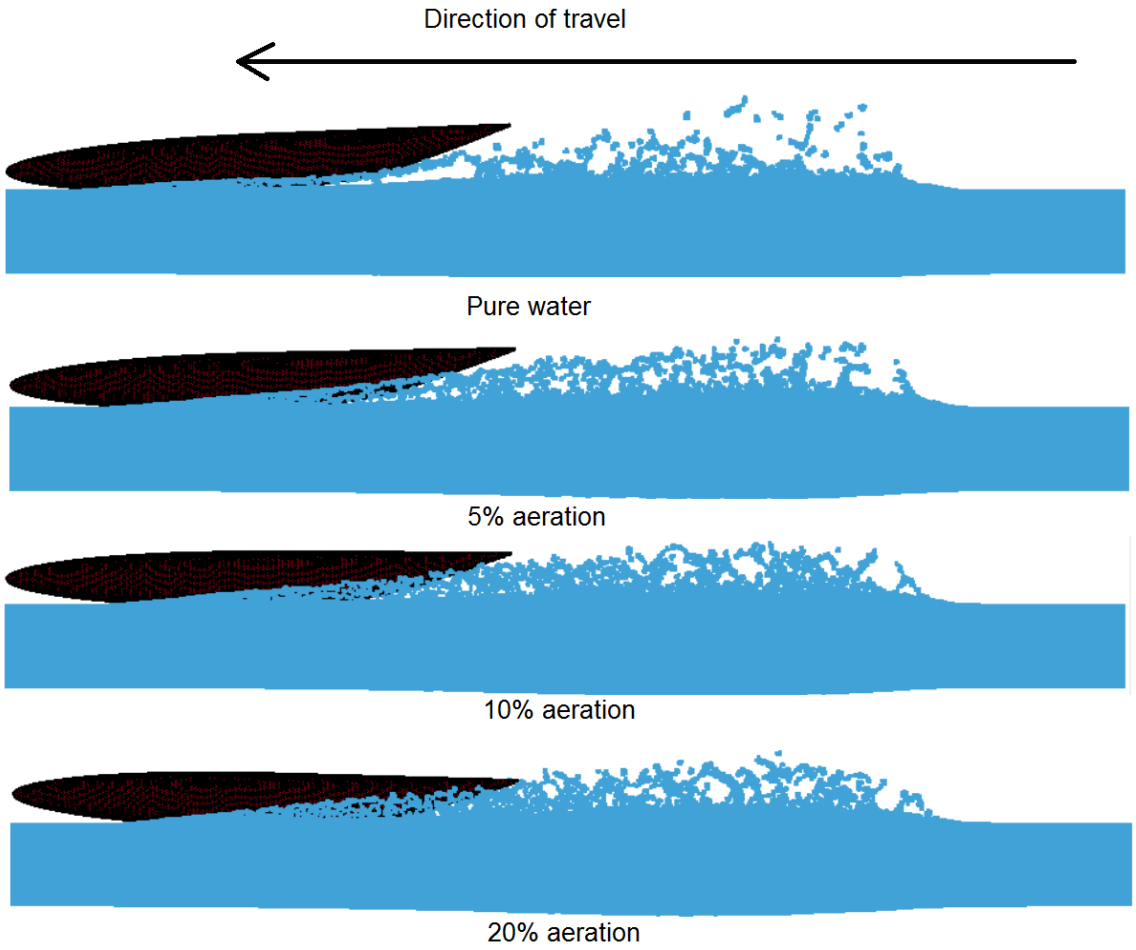

Figure 7-41: Impact evolution of fuselage on pure and aerated water (5%, 10% and 20%) at 0.12 s. The fuselage does not experience any pitching up motion, which is the expected experimental behaviour [2]. This is due to the lack of suction modelling.

With respect to the gas fraction and its evolution, it is expected to change as the fuselage progresses. The most significant change in the gas content should appear in the vicinity of the contact of the fuselage with the flow domain, since this is the area where there most abrupt pressure changes occur. Due to the relative small depth of the water, the sound waves caused by the impact travelled to the bottom and caused pressure changes at the boundary. This led to changes in the gas content. This issue can be avoided with an increase in depth, at the expense of computational costs.

Figure 7-42 shows the gas content at the end of the simulation (0.24 s). The figure shows the top of the water without the fuselage so that the gas content range can be visible. As the fuselage skidded forward it compressed the water directly beneath it. The front section also compressed the particles directly in its path. Hence, indicated

with the blue fringe levels are the particles that are compressed and so the gas content reduced. On the other hand, as the particles were displaced and moved further away into the spray, they experienced lower pressures leading the particles to go into tension. This was accompanied by an increase in the gas content. A finer particle distribution would be ideal for a better description of the spray. This description compared well with experimental evidence, where the spray in usually a mixture of water and air.

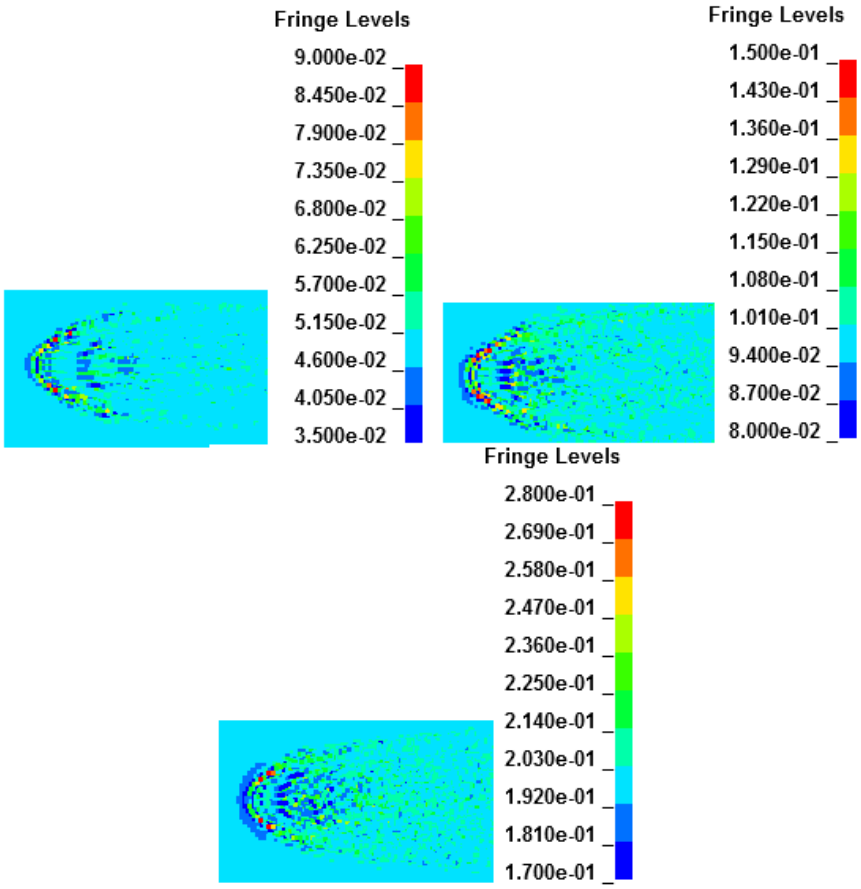

Figure 7-42: Gas content at t=0.24 s for 5% (top left), 10% (top right) and 20% (bottom) aeration. Top view with fuselage section blanked. Direction of travel from right to left.

Next a comparison of the position and velocity is considered with respect to the pure water model, as well as the numerical results provided by Streckwall et al. [26] from TUHH. The vertical velocity, pitch attitude and CG height are shown in Figure 7-43 - Figure 7-47.

As far as the vertical velocity is concerned, the initial reduction was not as severe for the aerated cases when compared to the pure water case. Since the presence of air leads to less severe loading of a structure a lower deceleration was also expected. The 20% aeration case provided the best fit, when compared to the results obtained from the TUHH simulations. It must be noted that the hydrodynamic loading obtained in the TUHH simulations was derived from the von Karman method, however there are no additional details with respect to the water model.

Once the vertical velocity became negative, the magnitude of the velocity was greater for the aerated cases. As it was observed in the plate impact case, this could be caused by the lower contact forces as the aeration levels increased.

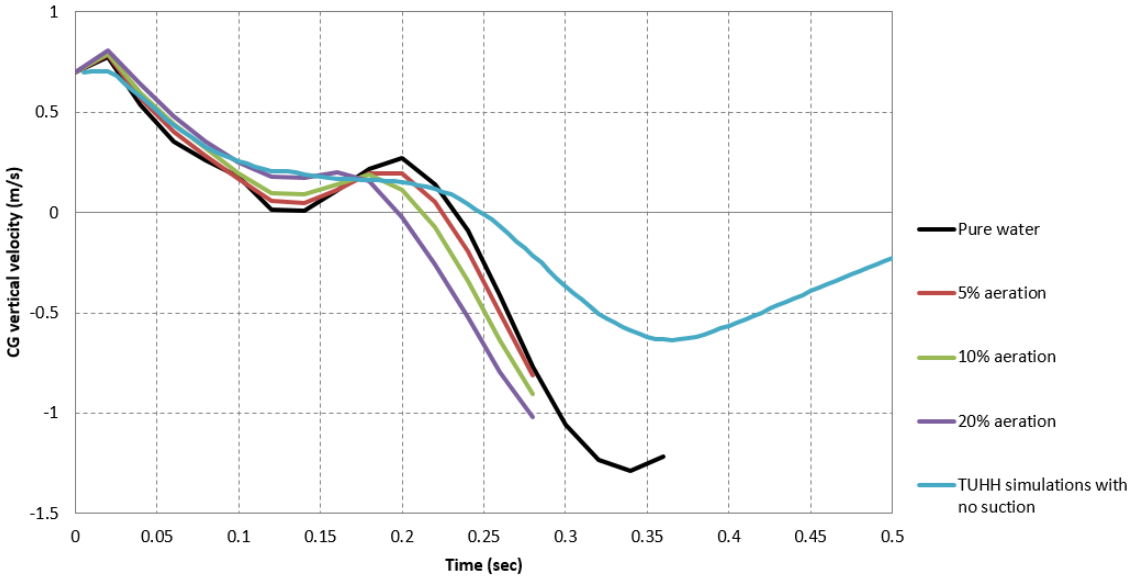

Figure 7-43: Vertical velocity comparison for pure water, aerated cases (5%, 10% and 20%) and TUHH simulations with no suction.

Next, the horizontal velocity and the effect of aeration are considered. For these results TUHH has provided experimental data as well. Due to the small timescales of the simulations, compared to the experimental investigation by McBride et al. [2], it was not possible to obtain accurate enough information directly from the paper hence the available extracted data from TUHH were used. From Figure 7-44 it is established that the simulations failed to capture the reduction of the horizontal velocity compared to the experiments. This was due do the lack of any suction modelling. In experimental work, as the aircraft skids along the water, it experiences a pitching up moment caused by negative pressure building up at the rear of the fuselage. This leads to a drop in its

forward velocity. In the current simulations there was no distinct layer of air and hence no atmospheric pressure that could allow for the development of such a pitching up moment.

The use of an aeration model did not influence the horizontal velocity significantly. This is expected, since the effects of air entrapment are far more pronounced in vertical impacts of flat objects. When there is a high forward velocity component, such as in the case of ditching and a circular cross section, such as in this specific body, means that the angled impact approach allows for part of the air to escape. For completeness, in Figure 7-45 a closer look in the effect of aeration on the forward velocity shows that as the aeration levels increased, the horizontal velocity reduced at higher rates.

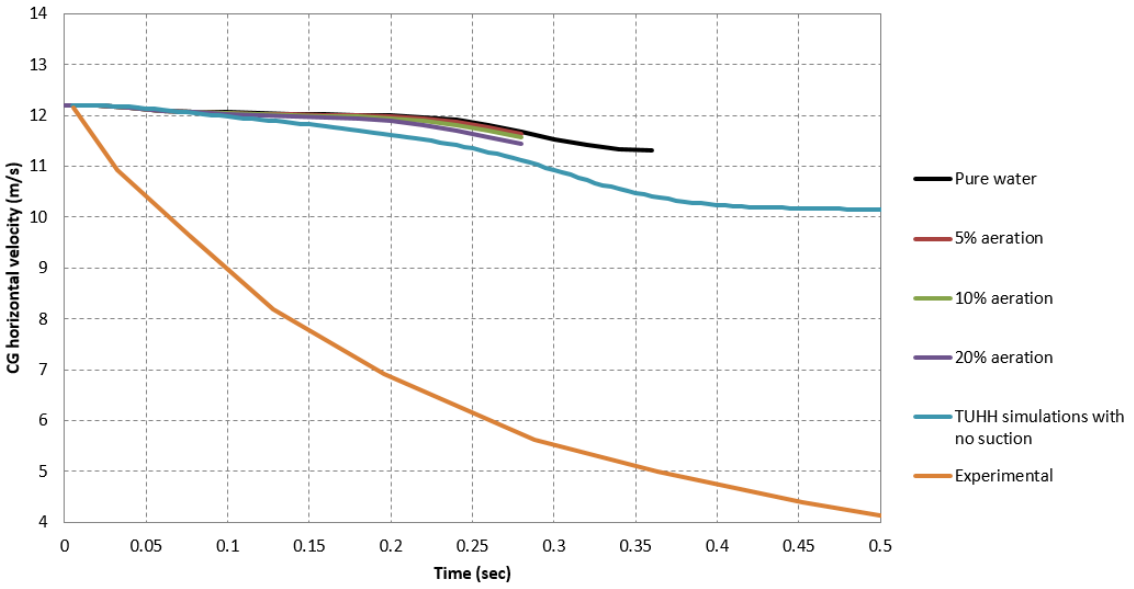

Figure 7-44: Horizontal velocity comparison of pure water, aerated cases (5%, 10% and 20%), experimental data [2] and TUHH simulations with no suction.

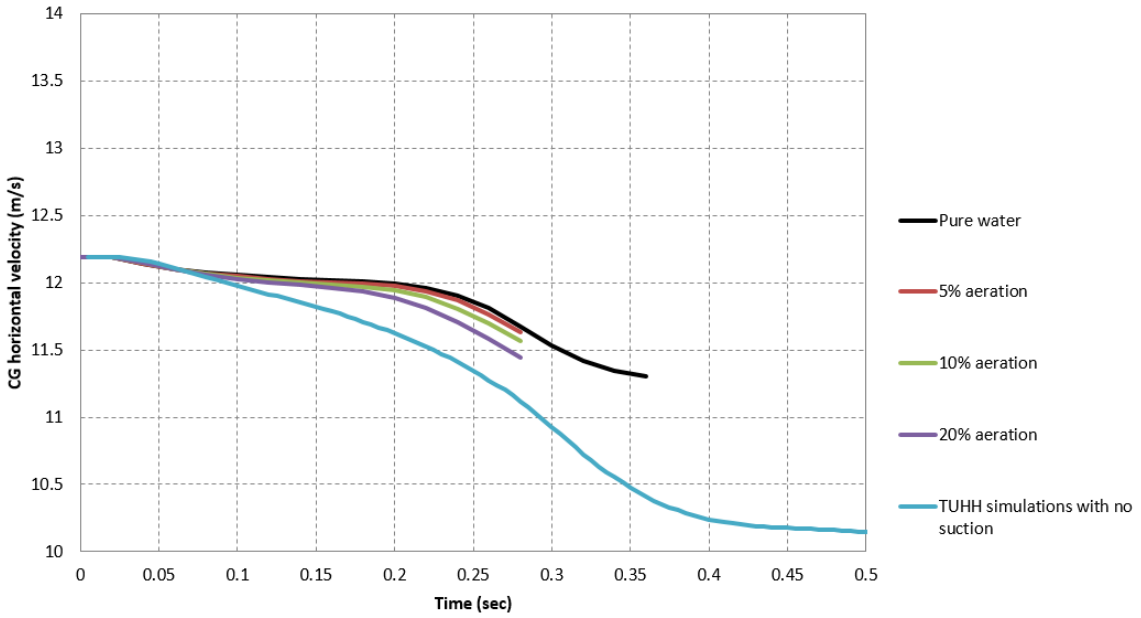

Figure 7-45: Zoomed in section of the horizontal velocity comparison of pure water, aerated cases (5%, 10% and 20%), experimental data [2] and TUHH simulations with no suction.

As a result of the lack of suction modelling, the pitch attitude and the height of the CG of the fuselage did not compare well with respect to the experimental data, as shown in Figure 7-46 - Figure 7-47. With respect to the pitch attitude, the numerical results predicted that the fuselage would attain an almost horizontal profile before pitching up, however experimental results indicate that the attitude should increase from an earlier stage. Even though the higher gas content simulations tend to close the gap between the experimental and numerical predictions it still did not provide accurate enough results.

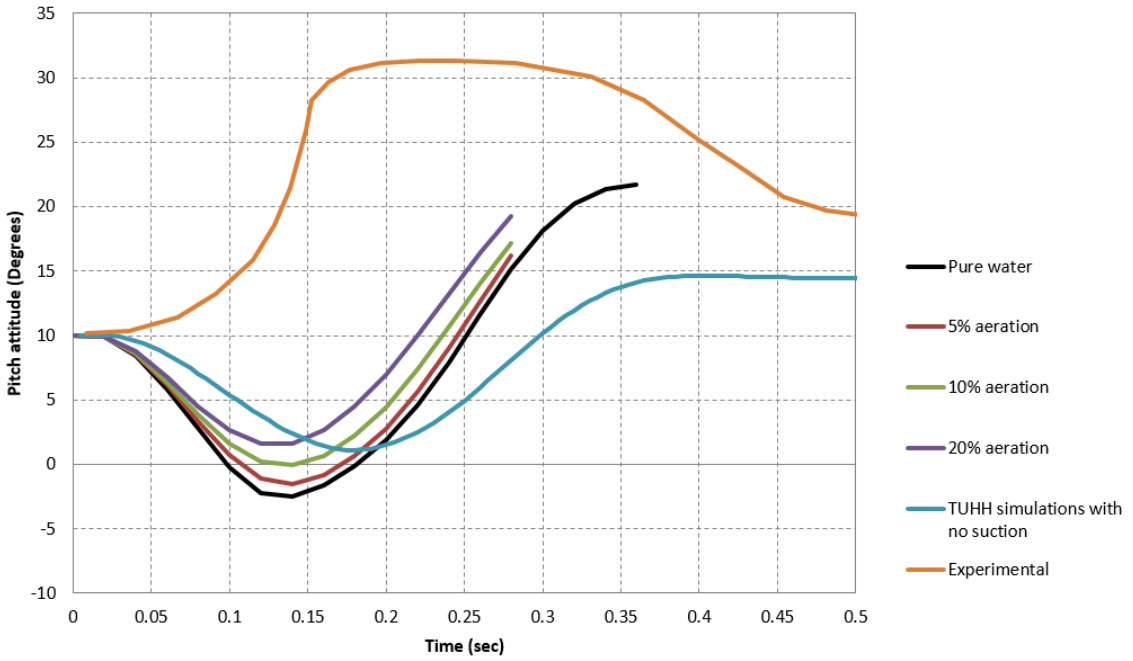

Figure 7-46: Pitch attitude comparison for pure water, aerated cases (5%, 10% and 20%), experimental data [2] and TUHH simulations with no suction.

With respect to the CG height, the comparison shows that the fuselage would dive deeper as the aeration level increased compared to the pure water case. This is in accordance with the fact that the structure would sustain lower contact forces. The experimental results indicate that the height of the centre of gravity should increase due to the pitching up of the fuselage, however similar to the comparison made previously, the numerical predictions fail to match with the experiments due to the lack of suction modelling.

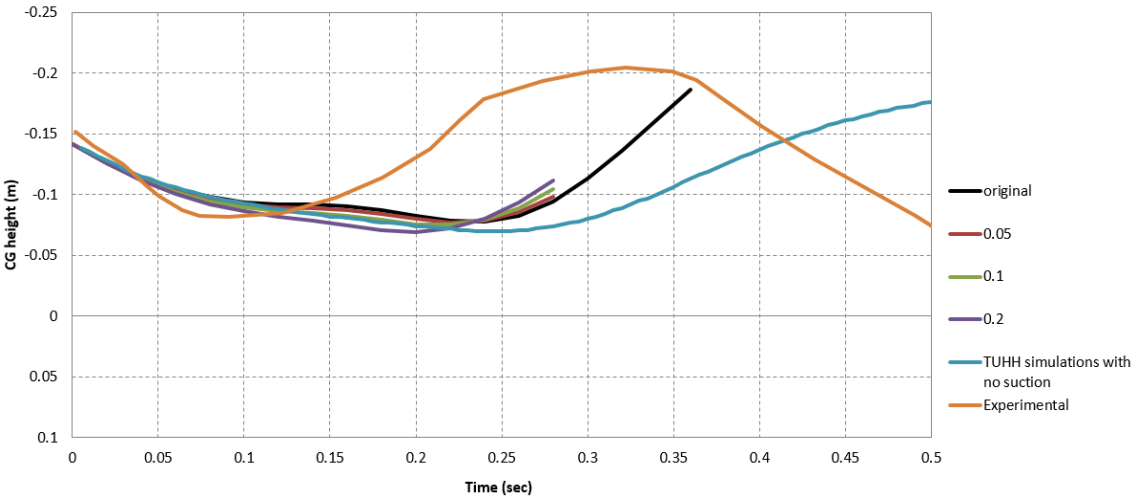

Figure 7-47: CG (Centre of Gravity) height comparison for pure water, aerated cases (5%, 10% and 20%), experimental data [2] and TUHH simulations with no suction.

Even though the aeration model changed the pressure imparted on the fuselage, it did not provide any significant change to its overall dynamics. Unlike the flat plate example, the circular cross section of the fuselage means that the effect of air will not be as severe. One of the most important outcomes of this test case is that suction forces are far more important for a fuselage with a circular cross section and are important for predicting the correct overall behaviour of the body.

7.7 Conclusions

The theory governing a mixture of water and air was described, establishing the effect of the presence of gas on the density and speed of sound of the mixture. Moreover, the effect of aerated water on the pressures imparted on a structure was outlined. A methodology was developed for the SPH code, where the aerated water mixture is governed by the gas content, while the liquid is considered fully incompressible. Additionally, it was shown that the adiabatic equation of state provides more accurate pressure results when compared to the alternative ideal gas equation of state. This was checked against the plane wave propagation equation for a fluid. For the higher impact velocities (1 m/s) the propagation velocity should be used, in the plane wave propagation equation, instead of the speed of sound of the mixture. The 2D validation test cases showed that the maximum pressures were closer to the theoretical value with the adiabatic equation of state.

Three example test cases were considered, increasing in complexity, in order to evaluate the method and also to enhance the confidence in the approach. In the first example a circular plate is dropped in aerated water of varying gas fraction content. The simulation results were compared directly to the experimental results available. The results showed good agreement with respect to the reduction of the peak impact pressures, as the gas volume fraction increases. The discrepancies in the results are thought to be due to the small fluid domain, which can lead to pressure waves rebounding from the edges, as well as the particle spacing. Further investigations, could be performed in order to determine whether more accurate pressure peaks can be achieved.

Next, a plate supported by a guiding structure was considered impacting the mixture at an angle and high forward velocity. The pressures imparted on the structure showed that, as the gas content increases, the pressures reduce and the pulse of the peak impact is longer providing a smoother impact profile.

Finally, a fuselage shape impacting the mixture was tested and compared against both experimental and other numerical results. With respect to the methodology employed, the results showed lower pressure peaks with increasing gas content, however comparison to experimental results showed the influence that the suction forces have on the global behaviour of the structure.

It can be concluded that, for any accurate comparison between experimental and numerical results, the addition of air particles or an artificial atmospheric pressure surrounding the fuselage is paramount, if the correct behaviour is to be predicted.

During the impact phase of an aircraft, a low pressure area under the rear of the fuselage can develop (as described in Chapter 4), allowing for the formation of a suction force which acts as a downwards force that pulls the fuselage skin further into water. This immersion can cause extended local deformations on the rear section of the fuselage. The presence of air particles, at atmospheric pressure, surrounding the fuselage can provide a physical description of the phenomenon. As the pressure drops at the aft section of the fuselage, the surrounding particle will submerge the aft section of the fuselage into the water domain, leading to a pitching up moment. This will lead to a reduced forward velocity and a change in the global behaviour of the fuselage.

Practically, this was not possible to be done as part of this project, due to the computational cost of introducing a large number of air particles in the simulation.

Moreover, the modelling complexity of introducing air particles would need to be investigated before performing more complicated simulations, thus increasing the overall resources required.

The next chapter will investigate the ability of the code to model the phenomenon of ricochet. This is due to the similar nature of impact to ditching, as both are forward velocity impacts. Moreover, the availability of experimental results means that an assessment of the numerical results is achievable.

8 Ricochet Modelling

This chapter deals with the phenomenon of ricochet. The reason for this is the fact that ricochet, as it will be described, is a problem with similar characteristics to ditching, in that it deals with the water impact of structures that have high forward velocity. The interest in ricochet also stems from the availability of experimental data for spheres, at least allowing for an assessment of the code in dealing with such impacts. This will complement the previous chapters, for which experimental results (for the plate impacts shown before) were not made available in time.

The phenomenon of ricochet of projectiles upon impact with a liquid surface has been studied extensively in the past. Even though initial interest in the ricochet and its effects has been focused on military operations, there has also been a general interest in the investigation of the phenomenon given its complex nature. Investigations of ricochet of spheres off water have taken place in the past [105] [106] [107] providing theoretical and experimental results.

A description into the existing theories for the phenomenon of ricochet is given along with experimental results. Furthermore, an analytical solution that depends on the impact velocity is provided for a cylindrical projectile. This complements the existing analytical solutions for a spherical projectile. Finally, the numerical results are presented for 2D and 3D cases respectively. A series of simulations have been performed that include a variety of angles and velocities. These are compared to the theoretical results and applicable experimental results.

8.1 Ricochet Theory and Experimental Data

Ricochet is described as the rebound of an object one or more times from a surface, either a liquid or a solid one. The earliest recordings of ricochet date back to the 16th century, showing the application of the phenomenon in military operations. An overview of these initial recordings can be found in [108]. During WWII the ricochet of projectiles off water was also considered by Wallis, with the concept of the “bouncing bomb”, designed to cause damage on dams.

The angle of impact, the velocity and the densities of the projectile and the surface target are some of the parameters that can influence the behaviour of the projectile. The main characteristics of ricochet are that the projectile usually retains its shape with no significant deformations, while the impacted surface is penetrated. Moreover, its

trajectory is governed by the vertical component of the pressure acting upwards, producing a lift force on the projectile [108].

Similar impact scenarios can describe the phenomenon of bouncing and broaching. Bouncing is the rebound of the projectile due to the elastic deformations, while broaching is described as the rebound of a projectile after it has been completely submerged [108]. Figure 8-1 shows the different paths that the projectile can follow during impacts with a liquid surface.

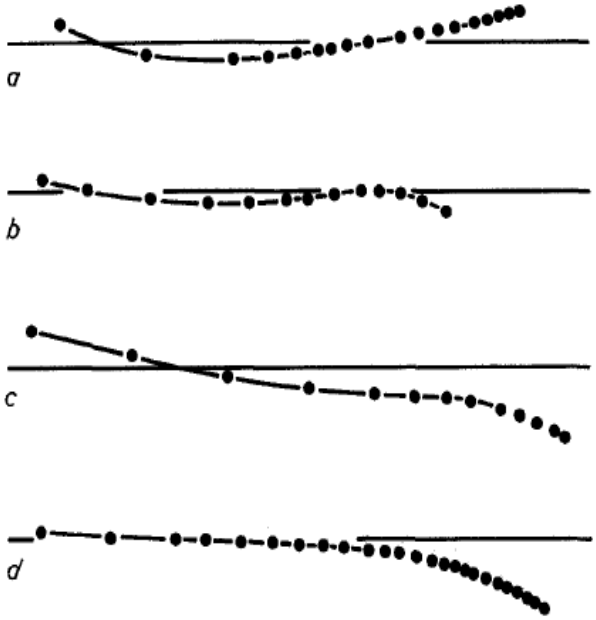

Figure 8-1: Different cases of water impact. Case a) describes the phenomenon of ricochet, case b) the phenomenon of broaching and cases c) and d) the phenomenon of sinking. Figure reproduced from Johnson [108].

The projectile can have a range of angles for which ricochet can occur. There is a maximum angle however, beyond which the projectile will submerge rather than ricochet. With respect to the maximum angle for ricochet to occur, there have been several theoretical estimates. The first one, proposed by Birkhoff et al., is for a sphere and as it is shown in equation (8-1), depends on the density of the projectile and the target. The main assumption employed in this approach is that the pressure on a surface area is $p = 1/2\rho u^2 cos^2\beta$, where u is the speed of the sphere and β is the angle of the outward normal of the surface area with respect to the line of forward motion. The characteristics of the projectile during impact are shown in Figure 8-2. Moreover, the pressure is only applied to the submerged parts of the projectile [105]. A detailed derivation of equation (8-1) is given by Johnson et al. [105].

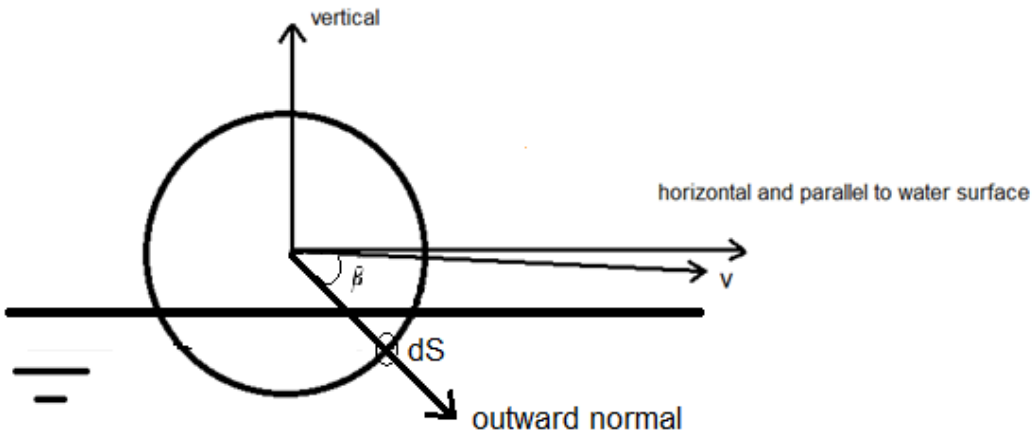

Figure 8-2: Partially submerged projectile during oblique impact. *v* is the velocity of impact and line of forward motion, *dS* is the surface area and *β* is the angle of the outward normal of the surface area with respect to the line of forward motion.

$$\theta_c = 17.5° \sqrt{\frac{\rho}{\rho'}}, \tag{8-1}$$

where ρ is the density of the liquid surface, ρ' is the density of the projectile and subscript c denotes the critical condition for ricochet.

Equation (8-1) implies that the mass of the projectile is neglected, which is acceptable for high velocity impacts, where the hydrodynamic forces are high enough. Furthermore, the application of backspin on the projectile, known to increases the lift and subsequently the maximum angle for ricochet, is not considered [109] [107].

An alternative approach proposed by Hutchings [106] takes into account the effect of spin, which was compared to a non-spinning sphere. Spinning of the projectile, in an anticlockwise manner, with respect to its centre of gravity, is called backspin. It can increase the maximum angle of impact at which the object can achieve ricochet. Furthermore, cylindrical projectiles were also considered including spin. The main difference in this approach is the use of the Rayleigh pressure formula and a larger wetted area over which this pressure is applied. The main assumption of the Rayleigh formula is the fact that it considers steady-state laminar flow across an inclined plate.

The Rayleigh pressure formula is given as [106]:

$$p = \frac{\pi cos\beta}{4 + \pi cos\beta}\rho u^2 , \tag{8-2}$$

where β is the angle of the outward normal from the surface area with respect to the line of forward motion.

Hutchings then derived the following equation for the critical angle of ricochet for cylinders while taking into account the spin of the projectile:

$$\theta_c = 18.7 * \left(\left(1 + \frac{1.6a\omega}{u}\right)^{0.5} \Big/ \sqrt{\sigma} \right), \tag{8-3}$$

where a is the radius, ω is the angular velocity, u is the projectile's velocity and σ is the specific gravity.

Assuming no angular velocity (no spin), equation (8-3) provides a similar result to the one of equation (8-1).

Another theoretical approach, taking into account the effect of the projectile's weight and the impact velocity, is proposed by Soliman et al. [107] for a sphere. Equation (8-4) shows the relationship between the impact velocity, the critical angle from the Birkhoff et al. theory, the weight of the projectile and the angle of impact, θ_g.

$$\theta_g^2 = \frac{\rho}{10\rho'} - \frac{4ag}{\bar{u}^2} , \tag{8-4}$$

where $\bar{u}$ is the mean velocity and a is the radius of the sphere.

Tests were carried out by Soliman et al. [107] in a tank measuring 1.82 m in length and 0.3 m in depth and width. The sphere that was tested was 0.0254 m in diameter and was made of steel. Figure 8-3 shows the range of velocities tested and a comparison between theoretical and experimental results. Figure 8-3 shows the dependency of the results on a variety of depths for the water tank. There is good agreement between the experimental results and the theoretical estimate, even though the theory overestimates the range of ricochet. This can be attributed to the fact that the authors used the entry velocity instead of the mean velocity of the sphere. This being said, the theoretical estimates show that ricochet will not occur for angles higher than 7°, following closely the initial theory of Birkhoff et al., stating that the critical angle for ricochet of steel sphere is between 7° and 9° [105]. The main difference between the two approaches, as shown in equation (8-1), is that the original theory of Birkhoff et al. does not depend on the velocity of the projectile.

The results of Figure 8-3 show that for a given angle, the velocity is influenced by the depth. In particular, the smaller the depth the smaller the velocity needed. Finally, it must be noted that the exit angle of the sphere should be less than the entry angle and approach [107]:

$$\theta_{exit} \cong 0.9 * \theta_{in} \, . \qquad \textbf{(8-5)}$$

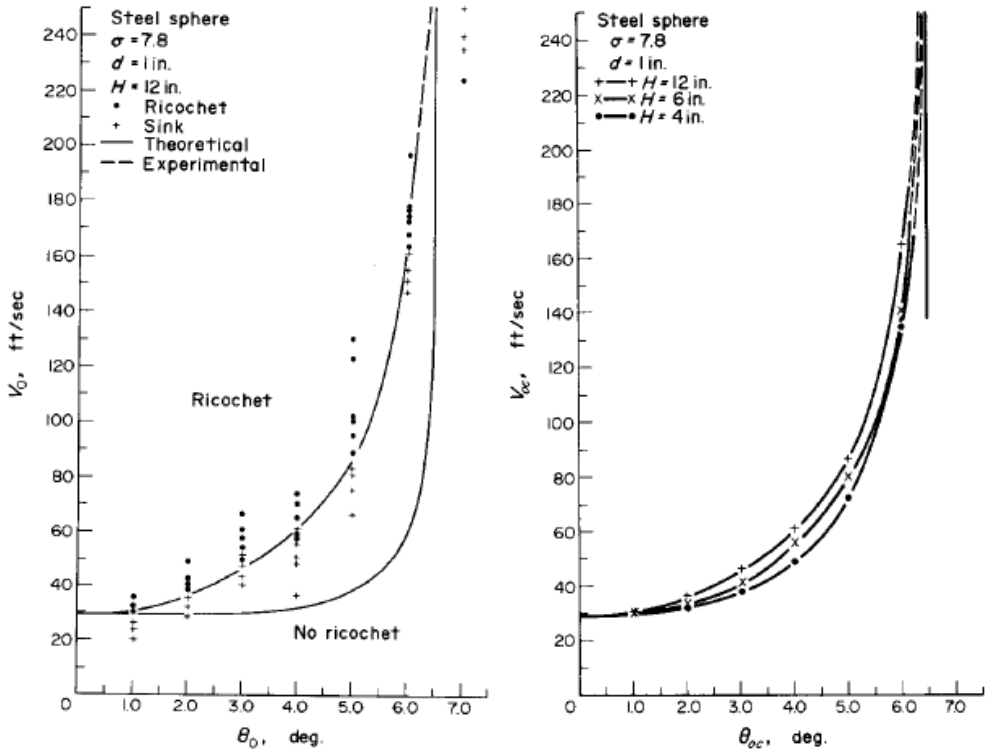

Figure 8-3: Experimental results for ricochet and sink cases depending on velocities and angles (left) and dependency of depth on ricochet (right). Tests carried out in a tank with steel spherical projectiles. The maximum angle at which ricochet can be achieved was determined to be approximately 6°. Figure reproduced from Soliman et al. [107].

Kirk derived an approximate analytical solution for the bouncing bomb that was designed by Wallis during WWII. The author considered a 5 ft long and 4 ft diameter bomb with a spin rate of 500 rpm. It was found, from first principles, that the impact velocity from a drop height of 60 ft would be 328 ft/s and the impact angle would be 10.7° [110]. The effect of backspin, as discussed previously, is responsible for the increase in the maximum angle at which ricochet can be achieved, when compared to a non-spinning projectile.

The literature above has shown the interest for the critical angle of spheres with and without spin as well as cylinders with spin, however there is a lack of a theoretical curve that links the velocity of the impact to the angle, as in Figure 8-3, for a cylinder without spin.

Next, the derivation of a theoretical estimate for the critical angle of a non-spinning cylinder and its influence on the velocity will be described. Hutchings [106] developed a

theoretical estimate for a spinning cylinder, however the coupling of the angular and linear velocities, shown in equation (8-3), does not allow for the derivation of the critical angle of a non-spinning cylinder by just neglecting the angular component. The derivation below, given by Hutchings [106], starts from the definition of the lift force for a spherical projectile. Using this basis, the derivation continues with the lift force for a spinning cylindrical projectile. Finally, a simplification of this derivation allows the estimation of the lift force for a non-spinning cylindrical projectile. In Figure 8-4 the partially submerged spherical projectile is shown, along with the angles of the wetted area. According to Hutchings, the wetted area, given by angle Φ_w, is equal to $2\Phi_0$ for $0 \leq \Phi_0 \leq {}^{\pi}/_{2}$ and π for $\Phi_0 > {}^{\pi}/_{2}$, thus taking into account the effect of the forward splash once the cylinder has submerged to depths greater than its radius.

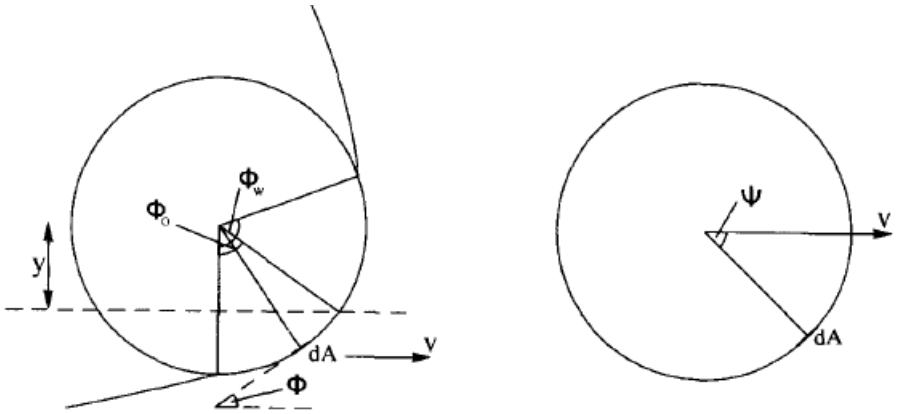

Figure 8-4: Generalised case of a partially submerged sphere and the wetted area angles. Left figure shows the elevation view and right figure shows a plan view. Φ and Ψ indicate the longitude and latitude at the element dA respectively. Figure reproduced from Hutchings [106].

The velocity of the flow normal to the element dA is given as:

$$v\, sin\varphi\, cos\psi\,. \qquad \textbf{(8-6)}$$

Using the basic equation (8-2):

$$p = \frac{\pi sin\varphi\, cos\psi}{4 + \pi sin\varphi\, cos\psi}\rho v^2\,. \qquad \textbf{(8-7)}$$

According to Hutchings [106] the pressure is integrated over the wetted area and φ is between 0 and π and ψ is between -π/2 and π/2. Therefore, the denominator of

equation (8-7) will be between 4 and 7.1. Hutchings proposed that the denominator of equation (8-7) can be assumed as a fixed value of 5.

The lift force, which is the vertical component of the pressure distribution, described by equation (8-7), on element dA of a spherical projectile is given as [106] :

$$dL = \frac{\pi}{5}\rho\, v^2\, sin\varphi\, cos\psi\, cos\varphi\, dA\,. \qquad \textbf{(8-8)}$$

Next consider a cylindrical projectile with backspin as shown in Figure 8-5 [106].

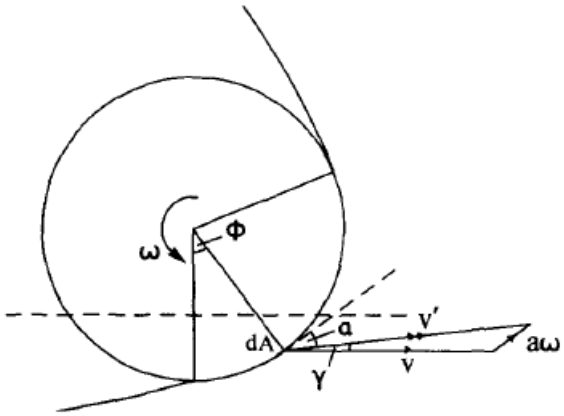

Figure 8-5: Elevation view of partially submerged cylindrical projectile with backspin. ω is the angular velocity of the spinning projectile, v is the velocity of the centre of mass, v' is the velocity of the surface element relative to the water, α is angle between v' and the surface of the cylinder, γ is the angle between v and v' and Φ is the angle between the vertical axis and the surface element dA.

The lift acting on surface element dA is:

$$dL = \frac{\pi sin\alpha}{4+\pi sin\alpha}\rho\, v'^2\, cos\varphi\, dA\,, \qquad \textbf{(8-9)}$$

where

$$v'^2 = (v + a\omega cos\varphi)^2 + (a\omega sin\varphi)^2\,, \qquad \textbf{(8-10)}$$

and

$$sin\alpha = sin\varphi cos\gamma - cos\varphi sin\gamma\,. \qquad \textbf{(8-11)}$$

Assuming that the backspin velocity is small compared to the velocity of the projectile's centre of mass, $\omega \ll v$, and neglecting second order terms [106]:

$$v'^2 \approx v^2 + 2\, a\omega v cos\varphi\,, \tag{8-12}$$

$$sin\gamma \approx \gamma \approx \frac{a\omega}{v} sin\varphi\,, \tag{8-13}$$

and

$$sin\alpha \approx sin\varphi - \frac{a\omega}{v} sin\varphi cos\varphi\,. \tag{8-14}$$

The above equation suggests that angle γ, the angle between the velocity of the projectile's centre of mass and the velocity of the surface element relative to the water, is small.

For $dA = ald\varphi$, where *l* is the length of the cylinder and a is the radius, the lift acting on a surface element becomes:

$$dL = \frac{\pi}{5}\rho al(v^2\, sin\varphi + a\omega sin\varphi cos\varphi)cos\varphi\; dA\,. \tag{8-15}$$

The above equation uses the same principle with respect to the denominator of the lift force equation as for the spherical projectile in equations (8-7) and (8-8).

For a non-spinning cylinder the lift force on the element dA is given as:

$$dL = \frac{\pi}{5}\rho\; v^2\; sin\varphi\; cos\varphi\; d\varphi\,. \tag{8-16}$$

The above equation is a simplification of equation (8-15) since no angular velocity is taken into account.

Integration of equation (8-16) over the wetted area gives the total lift force:

$$L = \frac{\pi}{10}\rho\; a\; l\; u^2\; sin^2\varphi_w\,. \tag{8-17}$$

Lift can also be described as:

$$L = m\frac{dy^2}{dt^2}. \tag{8-18}$$

Based on the assumption that the impact angles are small, it can be assumed that the velocity $u = dx/dt$ is constant leading to the following relationship [106]:

$$\frac{d^2y}{dt^2} \approx u^2 \frac{d^2y}{dx^2}. \quad \textbf{(8-19)}$$

Combining equations (8-17)-(8-19):

$$mu^2 \frac{d^2y}{dx^2} = \frac{\pi}{10} \rho\, a\, l\, u^2\, sin^2\varphi_w\,. \quad \textbf{(8-20)}$$

The angle of the wetted area can also be written with respect to the radius a and the vertical coordinate y:

$$sin^2\varphi_w = (2sin\varphi_0 cos\varphi_0)^2 = \frac{4(a^2-y^2)y^2}{a^4}. \quad \textbf{(8-21)}$$

Equation (8-20) then becomes:

$$mu^2 \frac{d^2y}{dx^2} = \frac{\pi}{10} \rho\, a\, l\, u^2 \frac{4(a^2-y^2)y^2}{a^4}\,. \quad \textbf{(8-22)}$$

In order to get a relationship between the angle and the velocity, the weight of the projectile should be considered, otherwise the velocity term disappears. This would lead to an equation relating only to the densities of the water and the cylinder similar to equation (8-1). The addition of the weight was also included in the work of Soliman et al. [107] leading to equation (8-4). By adding the weight of the cylinder and defining that the mass, *m*, is $m = V\rho'$, where *V* is the volume:

$$\rho'\pi a^2 l u^2 \frac{d^2y}{dx^2} = \frac{4\pi}{10} \rho\, a\, l\, u^2 \frac{(a^2-y^2)y^2}{a^4} - \rho'\pi a^2 l g \quad \textbf{(8-23)}$$

$$\frac{d^2y}{dx^2} = \frac{4\rho}{10\rho'} \frac{(a^2-y^2)y^2}{a^5} - \frac{g}{u^2}. \quad \textbf{(8-24)}$$

Using the chain rule, the fact that $\frac{dy}{dx} = tan\theta_c \approx \theta_c$ at the start of the impact ($y = a$) and integrating gives:

$$\int_{\theta_c^2}^{0} d\left(\frac{dy}{dx}\right)^2 = \int_a^0 \frac{8\rho(a^2-y^2)y^2}{10a^5\rho'} dy - \int_a^0 \frac{2g}{u^2} dy \quad \textbf{(8-25)}$$

$$\int_{\theta_c^2}^{0} d{\theta_c}^2 = \int_a^0 \frac{8\rho(a^2-y^2)y^2}{10a^5\rho'} dy - \frac{2g}{u^2}(0-a) \quad \textbf{(8-26)}$$

$$-\theta_c^2 = \int_a^0 \frac{4\rho(a^2y^2)}{5a^5\rho'} dy - \int_a^0 \frac{4\rho y^4}{5a^5\rho'} dy + \frac{2ga}{u^2}. \quad \textbf{(8-27)}$$

Equation (8-27) leads to the definition of the critical angle for a cylinder:

$$\theta_c^2 = \frac{4\rho}{\rho'}\left(\frac{1}{15} - \frac{1}{25}\right) - \frac{2ga}{u^2}. \quad \textbf{(8-28)}$$

Equation (8-28) has a similar form to that for a sphere in equation (8-4). Figure 8-6 shows the differences between the theoretical results of Soliman et al. [107] for a sphere without spin (equation (8-4)) and the results for a cylinder given in equation (8-28).

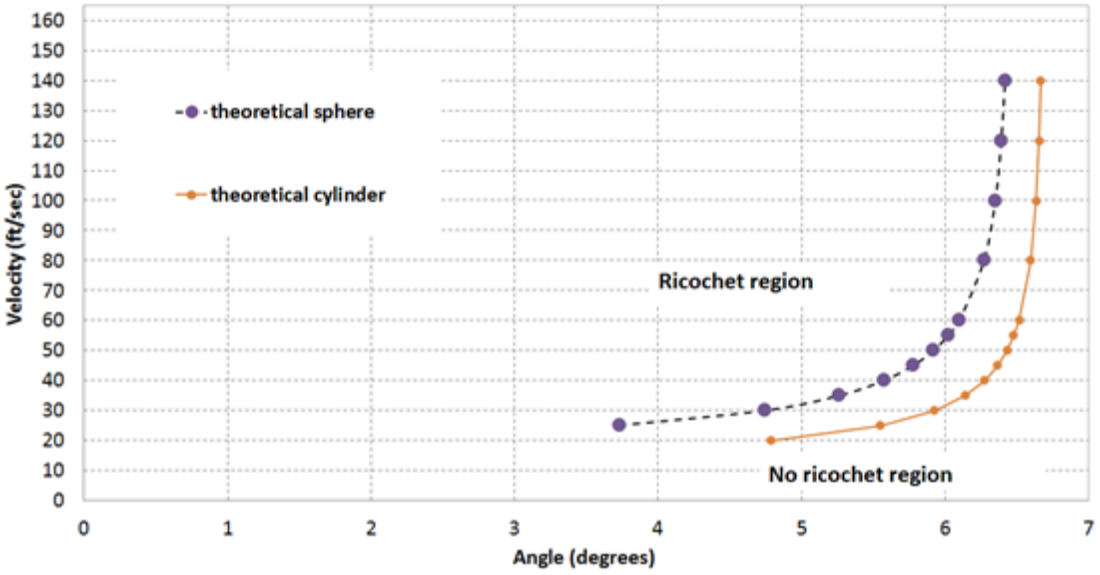

Figure 8-6: Theoretical critical angle as a function of velocity for a sphere and a cylinder with no spin. Theoretical results for a sphere are taken from Soliman et al. [107].

The asymptotic behaviour of the curves is due to the squared velocity term of equation (8-4) and (8-28). Both these theoretical estimates have been performed for a steel projectile with density of 7800 kg/m^3. Reducing the density of the impactor would lead to an increase in the theoretical critical angle for ricochet by 40% for both the sphere and the cylinder. Similarly, reducing the radius of the sphere or the cylinder would lead to an increase in the theoretical critical angle by almost 1%. The main differences between the two theoretical curves are caused by the difference in the initial pressure formula used, as well as the wetted surface area. In equation (8-4) the authors started the theoretical derivation from the fact that the pressure on an element is $\left(\frac{1}{2}\right)\rho(ucos\beta)^2$, where β is the angle between the velocity and outward normal on the element however, the derivation for the cylinder made use of equation (8-2). The comparison shows that the trends of the curves are in good agreement with the results for the sphere. Based on equation (8-1) the critical angle is 6.26°, while based on equation (8-3) and assuming that ω=0 the critical angle is 6.69°. This is the same as the result of equation (8-28), if the velocity term is neglected. So far there only existed an equation for the critical angle of a cylinder that was coupled to the angular velocities however, equation (8-28) provides an equation that would provide similar results to the Birkhoff et al. theory but includes the influence of the velocity. It must be noted that the drag force, which is not taken into account in the above analytical solution, would act in

the opposite direction of the projectile's motion, leading to an upward motion and possibly subsequent resurfacing and/or ricochet. This suggests that the theoretical curve for the critical ricochet angle may show sinking instead of ricochet for certain velocity and angle combination, thus leading to a more conservative approach.

8.2 Initial 3D Sphere Ricochet

The simulations in this section are based on the test cases of Soliman etl.al [107]. The ability of the current coupled code to model a fluid-structure interaction, which includes both horizontal and vertical components of velocity, for a simpler structure will be compared to the experimental results of Figure 8-3.

A sphere of 0.0254 m in diameter was modelled consisting of solid rigid elements with steel properties, given in Table 8-1. The sphere had a total mass of 0.065 kg and Table 8-2 shows the set of velocity and angle combinations that were tested.

Table 8-1: Dimensions and properties of the 3D sphere for the water impact simulations.

Diameter, m	0.0254
Density, kg/m^3	7800
Young's Modulus, Pa	2.1x10^{11}
Mass, kg	0.065
Poisson's ratio, -	0.33

Table 8-2: Combination of velocities and angles tested for water impact of 3D sphere simulations.

Initial velocity (ft/s)	Angle (°)
100	7.5
100	5
80	6.5
70	4
60	6.5
60	3
40	6
40	5
40	2
30	6
30	5
20	11
20	6
20	5
18	10
15	7
15	6
14	7
12	6
10	5

The water model consists of 18711 particles. Table 8-3 shows the main characteristics of the water domain.

Table 8-3: Water domain dimensions and properties for water impact of the 3D sphere simulations.

Length, m	0.4
Depth, m	0.05
Width, m	0.1
Particle spacing, m	0.005
Smoothing length, m	0.0065
Water density, kg/m^3	1000
Mass, kg	2.0

Figure 8-7 shows the initial pressure distribution under gravity.

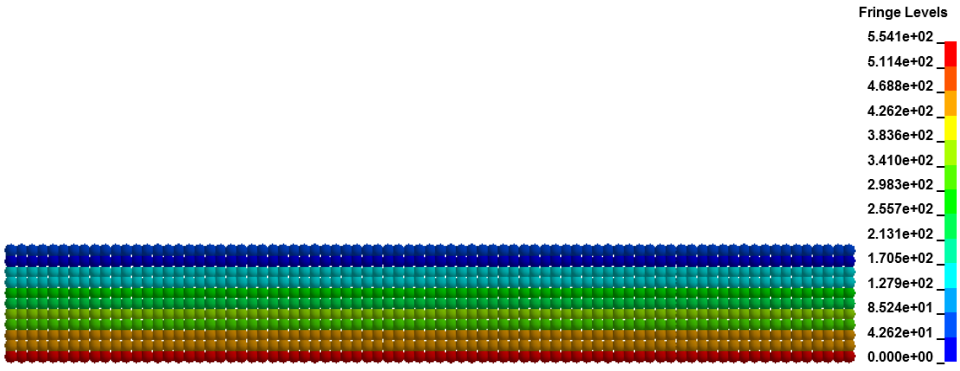

Figure 8-7: Initial pressure distribution for the water domain under gravity. Fringe levels show pressure in Pa.

The final set-up for the ricochet experiments is shown in Figure 8-8.

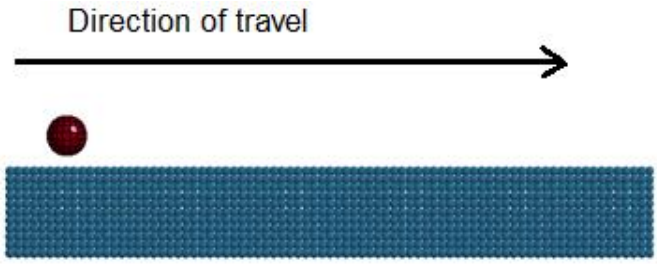

Figure 8-8: Side view of FE sphere and SPH water particles set-up.

A sensitivity study was used to select an appropriate contact stiffness and avoid penetration of particles in the sphere. Figure 8-9 shows the different contacts and cross sections that helped identify the ideal stiffness. Given these results, an initial contact stiffness of K=1 kg/m^4 s^2 was chosen. The contact stiffness is a parameter that affects the contact between the FE structure and the SPH particles. A higher value of K means that the contact is harder and the deformation of a structure more severe. In the test cases investigated in this chapter the structure is a rigid body. As such, no deformations are expected, however the correct value of the contact stiffness can help to avoid potential particle penetration as shown in Figure 8-9.

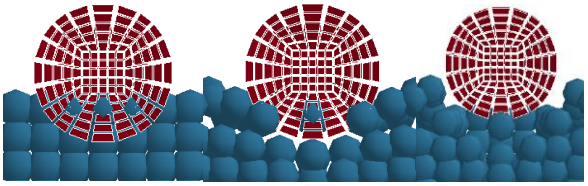

a) b) c)

Figure 8-9: Stiffness variations: a) K=0.01 kg/m^4 s^2, b) K=0.1 kg/m^4 s^2, c) K=1 kg/m^4 s^2. Particle penetration shown for the lower values of the contact stiffness. Figure shows a cut across the FE structure and the SPH particles in order to show potential particle penetration.

Next a range of simulations was performed and some of the results are shown in Figure 8-10. The trajectory of the sphere and the angle of the exit of the sphere from the water domain will be discussed.

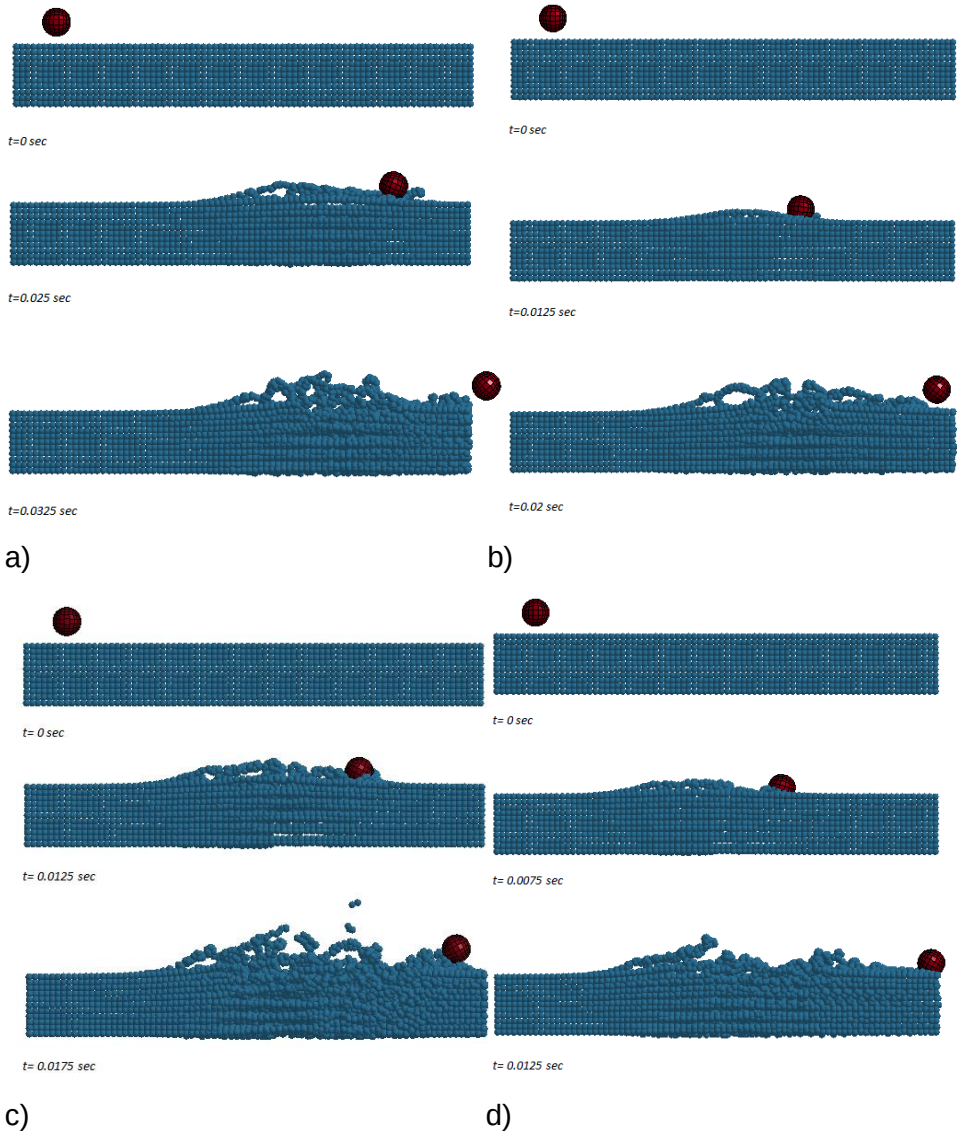

Figure 8-10: Water impact simulations of a rigid steel sphere: a) 40 ft/s at 2°, b) 60 ft/s at 3°, c) 70 ft/s at 4° and d) 100 ft/s at 5°. Direction of travel from left to right.

With respect to the trajectory of the sphere for the above simulations, it is evident that there was no sinking. The sphere penetrated the water surface reaching a minimum point and then resurfaced and continued on an upward trajectory. This trend is equivalent to the trajectory of Figure 8-1(a). The contact that the coupled code uses, treats the finite element nodes as particles and if they are within a distance of 2*h* from an SPH particle then a node to node contact is used.

Next, the investigation of the exit angles was considered. Theoretically, this angle should be less than the impact angle for ricochet cases. Table 8-4 shows the set-up angle for the simulation, the actual angle prior to contact and the exit angle for the various simulations. All measurements were taken from the centre element of the sphere. The results compare well with the theoretical estimates (considering the actual impact angle, θ_{in}), apart from the lower velocity case. This could be because of the increased influence of the gravity for smaller angles of impact.

Table 8-4: Impact and exit angles for the various ricochet simulations.

Velocity (ft/s)	**Set-up angle (°)**	$\boldsymbol{\theta_{in}}$**(°)**	$\boldsymbol{\theta_{exit}}$**(°)**	Maximum $\boldsymbol{\theta_{exit\ theory}}$**(°)**
40	2	2.55	2.6	2.3
60	3	3.1	2.44	2.8
70	4	4.1	2.74	3.7
100	5	5	3.8	4.5

Further simulations have been performed in order to check the ability of the coupled code to correctly predict the sinking of the sphere. The results provided by [107] will be used for comparison purposes. A cross section of the first test at 10 ft/s with an angle of 5° is shown in Figure 8-11.

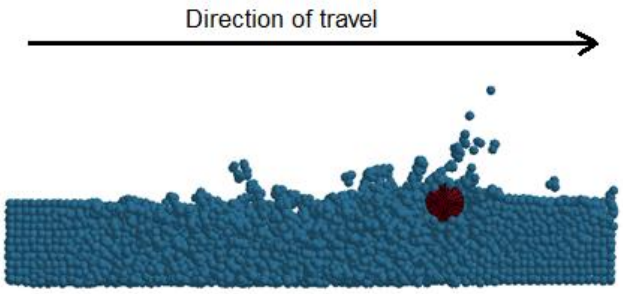

Figure 8-11: Cross sectional cut of sphere impact with initial velocity of 10 ft/s and an impact angle of 5°.

The sphere followed a trajectory similar to Figure 8-1(d). As the sphere impacted the water it begun to spin, as in the ricochet cases above. The average vertical velocities remained negative and as the forward velocity decreased, the sphere started to penetrate the water domain at an increased rate. Figure 8-12 shows a selection of the

remaining results. None of these cases resulted in sinking, which is the behaviour observed in the experimental results by Soliman et al. [107]. The vertical velocities become positive producing an upward trajectory of the sphere and an eventual ricochet.

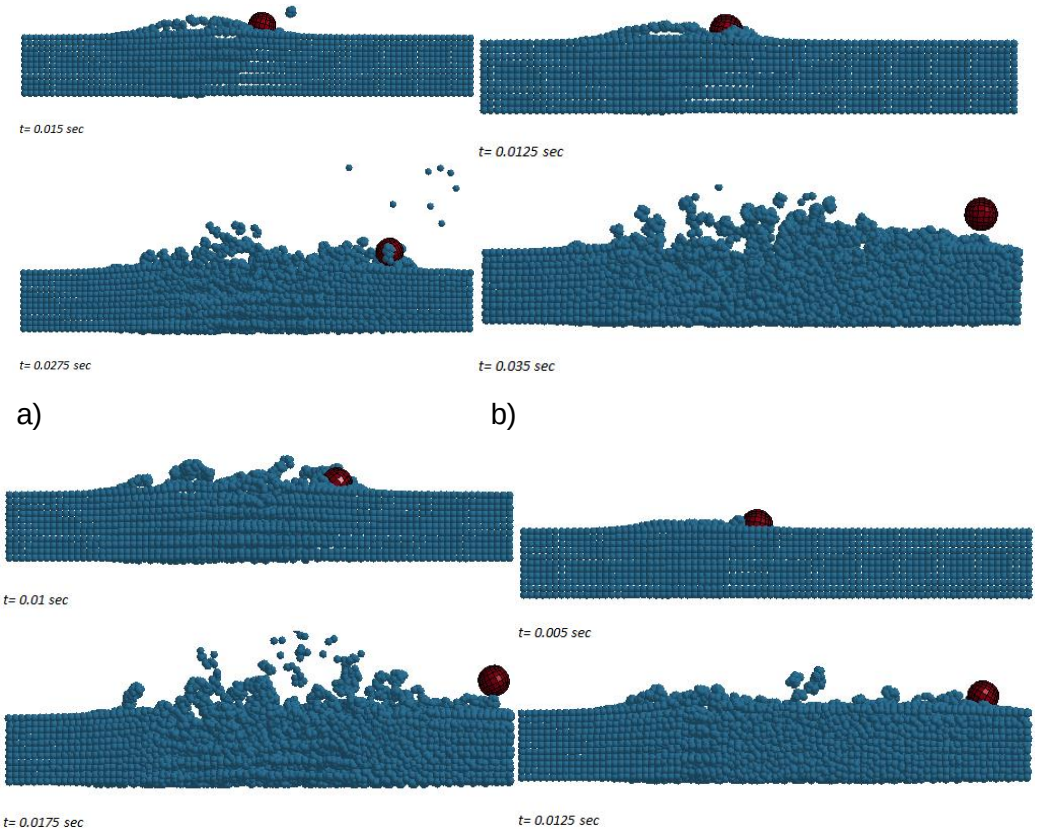

Figure 8-12: Water impact simulations of a rigid steel sphere: a) 40 ft/s at 5°, b) 40 ft/s at 6°, c) 80 ft/s at 6.5° and d) 100 ft/s at 7.5°. Results suggest that the sphere will ricochet contrary to experimental evidence that suggest that the sphere should sink. Direction of travel from left to right.

The reasons for the discrepancies in the sphere's behaviour are further investigated in the following sections of this chapter with the use of simpler 2D models. The effect of the particle distribution and potentially reduced decelerations are discussed.

The total set of simulations tested is shown in Figure 8-13. The continuous line shows the experimental results taken from Figure 8-3. The square points represent the simulations where ricochet occurred and the triangle points are the non-ricochet case.

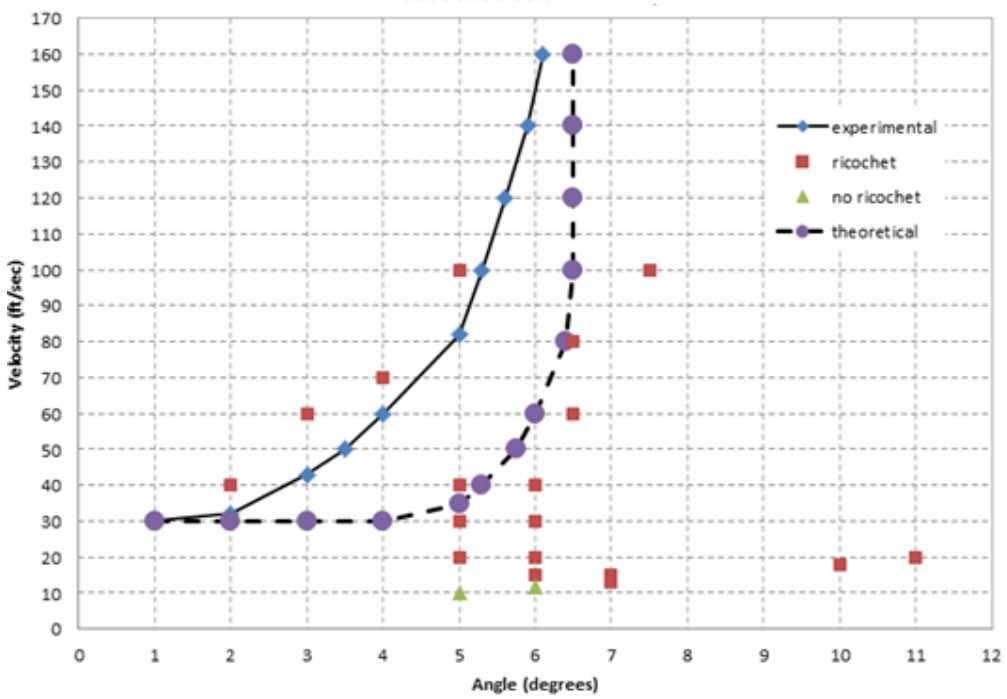

Figure 8-13: Complete set of 3D sphere water impact simulations. Comparison between experimental [107] and simulation results. Experimental and theoretical curves have been taken from Figure 8-3.

The sphere example showed that the code fails to predict the correct behaviour. Potentially reduced deceleration experienced by the projectile can be one reason for this discrepancy. The most straightforward approach to consider the effects of the deceleration is to account for the drag force that the projectile can experience, when travelling in a steady-state condition through a liquid. The difficulty with such an analysis at this stage, is that the sphere never reaches such a condition. An additional concern is the relatively coarse particle distribution. Further simulations are necessary in order to investigate the effect of the particle distribution.

8.3 Cylinder Mesh Sensitivity Analysis

Given the computational cost of performing such simulations, it was decided to perform the mesh sensitivity analysis of a 2D cylindrical problem, as it allowed for a reduced model size and hence computational cost. Given the theoretical estimate of the critical angle, shown in Figure 8-6, it would be computationally advantageous to start the simulations with these 2D models.

8.3.1 Water Domain Model

In order to determine the influence of the particle spacing, three particle densities were initially used: 0.002 m, 0.001 m and 0.0005 m. The dimensions given in the experimental results are prohibitively large, when the computational time is considered. Hence, a smaller domain that is 0.4 m long, 0.1 m in width and 0.05 m in depth was defined. Table 8-5 shows the number of particles for the respective particle spacing and the smoothing length used based on equation (8-29). The density of water has been taken as 1000 kg/m^3. The smoothing length for the simulations has been defined as:

$$h = 1.3d\,, \tag{8-29}$$

where *d* is the particle spacing.

Table 8-5: Particle spacing options used for the cylinder mesh sensitivity analysis.

Particle spacing (m)	Number of particles	Smoothing length (m)
0.002	10251	0.0026
0.001	40501	0.0013
0.0005	161001	0.00065

In order to account for the effect of gravity on the water model, an initial static analysis was performed prior to the ricochet tests. This provided correct estimates of the initial pressure in the water domain. The Murnaghan equation of state was employed:

$$p = B\left(\left(\frac{\rho}{\rho_0}\right)^{\gamma} - 1\right), \tag{8-30}$$

where $\gamma = 4$ and *B* is the bulk modulus. Accounting for the true compressibility of the liquid (Table 8-6), the value of *B* can be calculated from:

$$B = \frac{\rho_0 c^2}{\gamma} = 5.5\text{x}10^8\ \text{Pa}\,. \tag{8-31}$$

Since the flow velocities of the simulations were not expected to reach values close to the speed of sound it was beneficial to employ a reduced compressibility of *B*=5.5x10^6

Pa. This increased the critical time step, while maintaining the incompressible nature of the liquid.

Table 8-6: Input values for evaluation of true compressibility.

Denisty, kg/m^3	1000
Speed of Sound, m/s	1482.9
γ, -	4

Figure 8-14 shows the initial pressure distribution under gravity for the water domain. Table 8-7 shows the maximum and minimum pressures in the fluid.

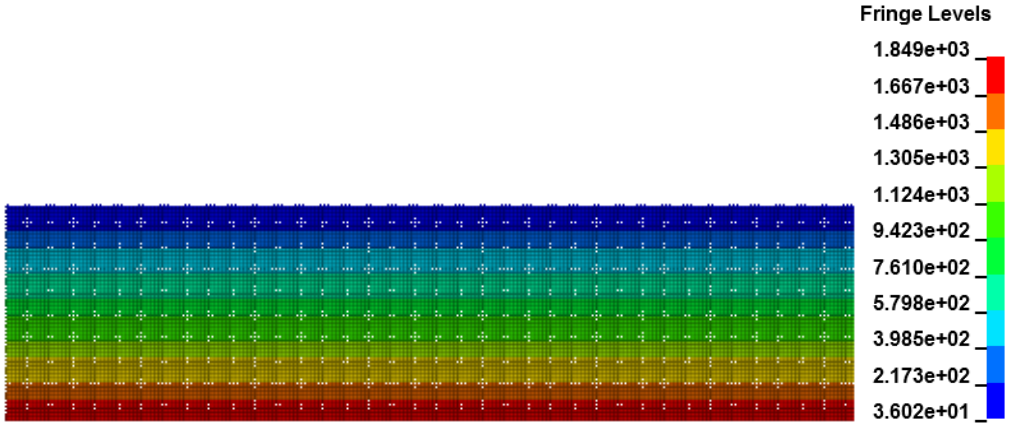

Figure 8-14: Side view. Pressure distribution on the water domain under gravity. Fringe levels show pressure in Pa.

Table 8-7: Pressure extremes for the 3 different particle spacing options for the water under gravity.

Particle Spacing (m)	Maximum Pressure (Pa)	Minimum Pressure (Pa)
0.0005	1814.06	5.909
0.001	1849	36.02
0.002	1826	13.88

The maximum pressures were significantly larger than the theoretical hydrostatic pressure of 981 Pa. This discrepancy was only present in 2D simulations. Due to the 3D nature of the FE solver, the water domain has been designed as a single layer of SPH particles (2D) but with the third dimension present. This means that the support

domain needed for the approximation in the SPH method is insufficient for the third dimension, since there are no particles present there. The reason for this modelling decision was the fact that the correct estimation of the mass of the water domain is needed for the coupled simulations at later stages (the FE code does not allow for a pure 2D model so a quasi-2D case will be developed below). Simply changing the water model from 2D to 3D would cause numerical errors due to the change in the mass estimation of the water.

8.3.2 2D Cylinder Model

With respect to the projectile it was assumed that it is an infinitely long cylinder. Since the material used for the projectile is rigid, it was more convenient to model a hollow cylinder with shell elements. To compensate for the reduced mass of the hollow projectile, the density was artificially increased from 7800 kg/m^3 to the values given in Table 8-8, depending on the particle spacing of the water. The mesh of the projectile followed closely the particle spacing of the water domain, so that the node spacing of the projectile follows the particle spacing of the water domain. This is appropriate because the contact definition treats the FE nodes as particles. The only boundary condition on the projectile is that it was constraint in the lateral direction. Figure 8-15 shows the mesh of the projectile for the different particle spacing options.

Table 8-8: Dimensions and material properties for steel cylinder.

Element Spacing, m	0.002	0.001	0.0005
Density, kg/m^3	37289.8931	18638.27	9318.20671
Young's Modulus, Pa	2.1x10^{11}	2.1x10^{11}	2.1x10^{11}
Poisson's ratio, -	0.33	0.33	0.33
Diameter, m	0.0254	0.0254	0.0254
Thickness, m	0.00127	0.00127	0.00127

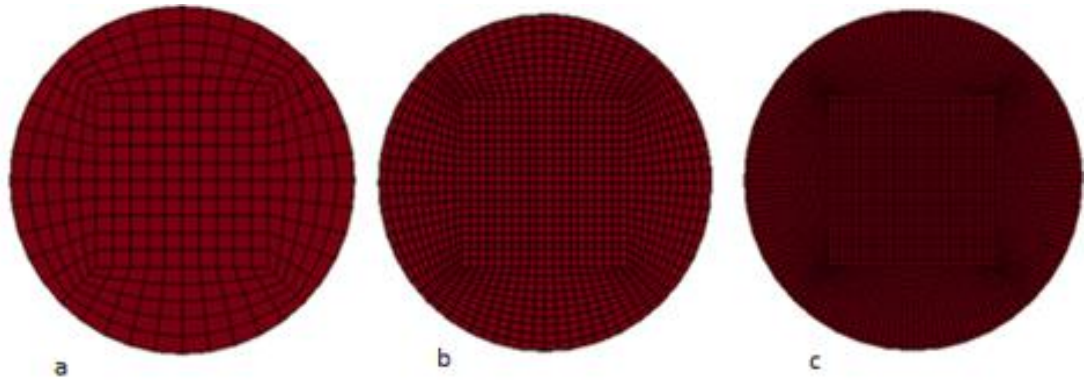

Figure 8-15: Side view of steel cylinder. Finite Element mesh sizes for a) 0.002 m, b) 0.001 m, c) 0.0005 m particle spacing.

In order to determine the particle spacing influence on the phenomenon, an initial velocity of 9.144 m/s (30 ft/s) at an inclination of 7° was chosen. This set of initial parameters should, according to the left graph of Figure 8-3, demonstrate a clear sinking of the projectile. Figure 8-16 shows the projectile's behaviour over time for the three particle spacing options. It is seen that for the coarser particle spacing of 0.002 m the projectile did not sink. Less pronounced upward motion was noticed for the medium particle spacing of 0.001 m, where there was more prolonged ploughing of the water before the projectile's vertical velocity became positive. The behaviour of the projectile follows roughly the sinking pattern of Figure 8-1(d), suggesting that this level of particle detail is necessary to achieve the correct behaviour.

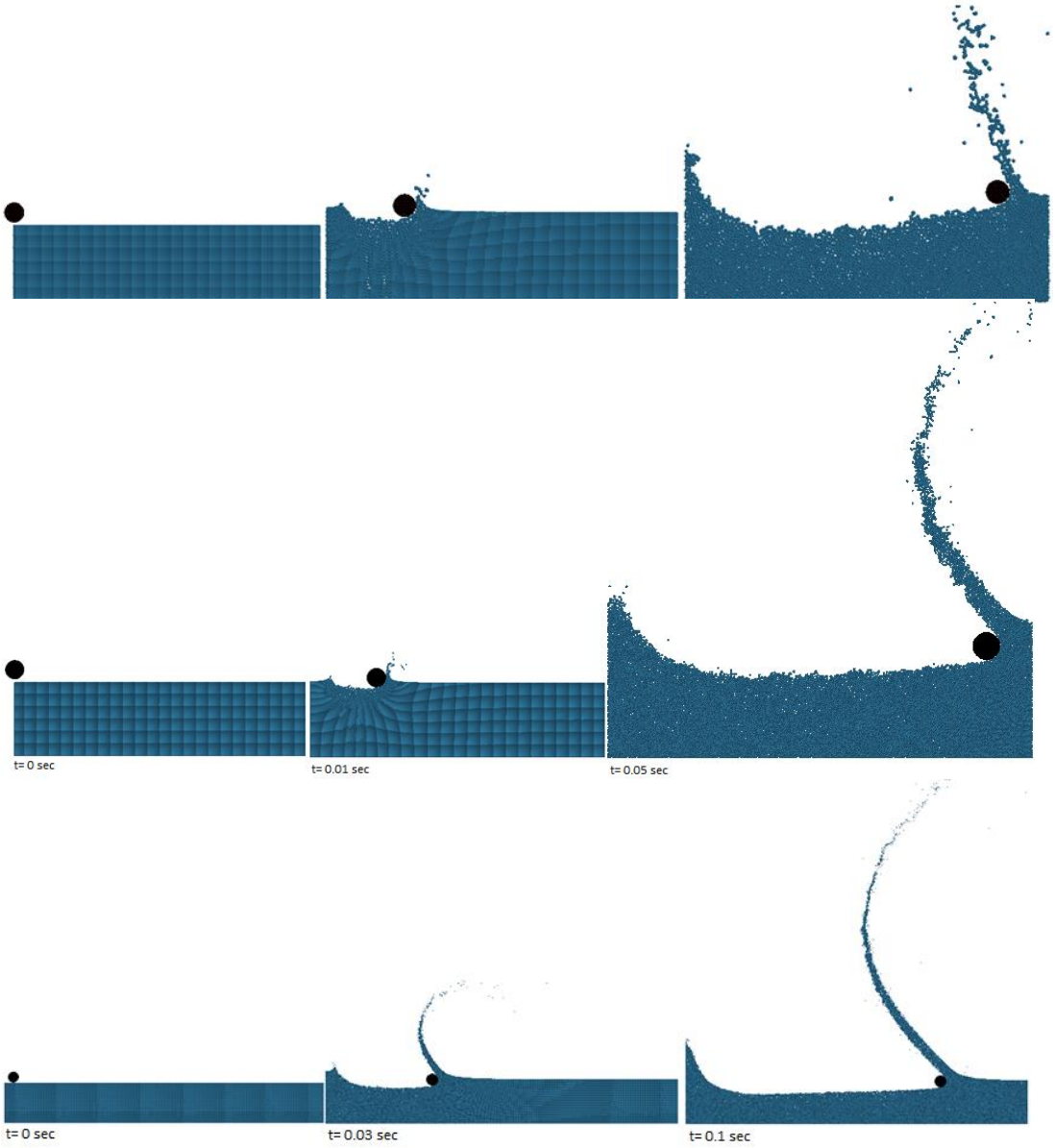

Figure 8-16: Side view. Cylinder impact on the water for the three different particle spacing at initial velocity of 30 ft/s and an inclination of 7°. Top figure is for 0.002 m, middle for 0.001 m and bottom for 0.0005 m of particle spacing. Direction of travel from left to right.

In order to determine the convergence of the results and specifically the particle spacing, it would be beneficial to show the response of the projectile upon impact in a water domain with further refined particle spacing. The projectile's properties are shown in Table 8-9. Figure 8-17 shows the trajectory of the projectile in a water domain with particle spacing of 0.00025 m and the results, from a phenomenological perspective, appeared similar to that of the 0.0005 m spacing. Overall, it is obvious that

the finer particle spacing can provide a more detailed splash during impact and a more consistent behaviour of the projectile.

Table 8-9: Material properties for steel cylinder for refined case with particle spacing of 0.00025 m.

Particle Spacing, m	0.00025
Density, kg/m^3	4659.01053
Young's Modulus, Pa	2.1x10^{11}
Poisson's ratio, -	0.33

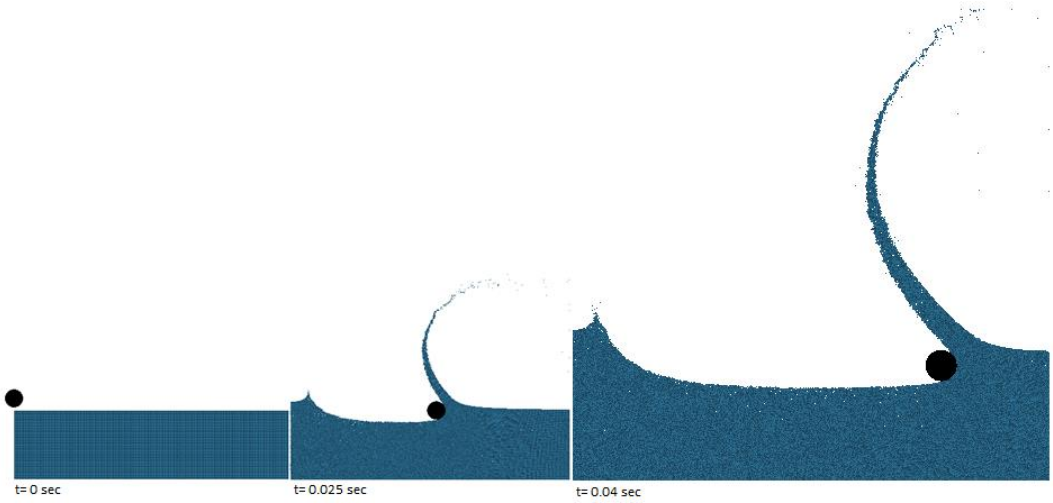

Figure 8-17: Side view. Cylinder impact on the water with initial velocity of 30 ft/s and an inclination of 7°. Water particle spacing of 0.00025 m. Direction of travel from left to right.

Figure 8-18 and Figure 8-19 show the vertical displacement and velocities of the simulations above. This can complement the phenomenological results, shown above. The displacement graph suggests that the simulations with the two finer particle options did not produce any ricochet, as the displacements never became positive. The velocity graph shows that for coarser particle spacing options the vertical velocity increased into positive regions leading to the ricochet of the projectile. As the particle spacing reduced, this trend diminished and for the particle spacing options of 0.0005 m and 0.00025 m the velocity attained an almost constant value. For the majority of these initial simulations the length of the water domain was 0.4 m but for the particle spacing option of 0.0005 m the simulations were doubled in length, in order to check the

influence of the length. Both the displacements and velocities were the same irrespective of the length of the water, apart from the boundaries where the contact forces could be unrealistic and any results should be treated with caution. The convergence of the two finer models suggests that the best choice between computational costs and accuracy of the phenomenon would be a particle spacing of 0.0005 m.

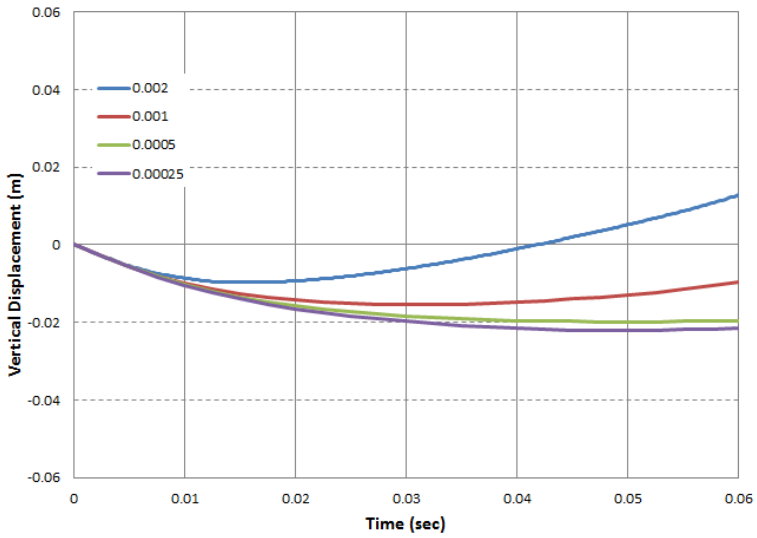

Figure 8-18: Cylinder impact on the water for the three different particle spacing at initial velocity of 30 ft/s and an inclination of 7°. Vertical displacement analysis for the different particle spacing options. Results show a convergence for the finer particle distribution of 0.0005 m and 0.00025 m.

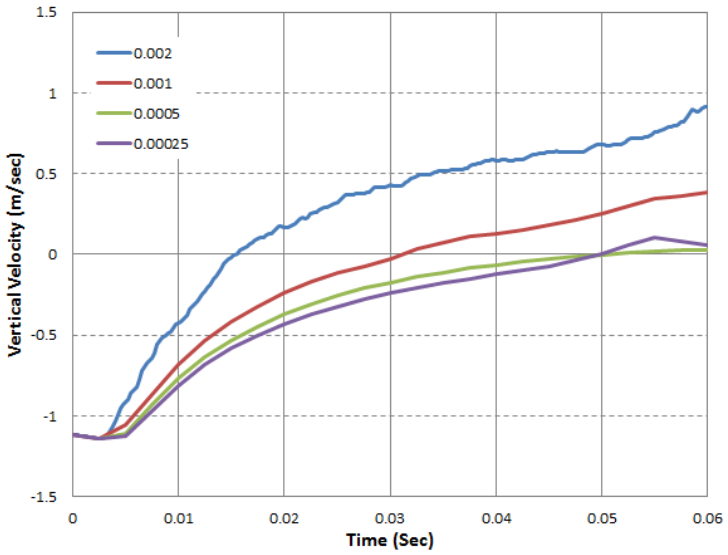

Figure 8-19: Cylinder impact on the water for the three different particle spacing at initial velocity of 30 ft/s and an inclination of 7°. Vertical velocity analysis for the different particle spacing options. Results show a convergence for the finer particle distribution of 0.0005 m and 0.00025 m.

For all the above, the contact stiffness was selected high enough, such that there is no penetration between the particles and the projectile and also it is low enough so that the particles are not unrealistically distant from the projectile. Numerically, the contact force depends not only on the stiffness, but also on the particle density of the model. The contact treats both finite element nodes and SPH particles as particles. Coarser particle spacing would provide noisier contact forces. For a given contact stiffness value of K=1, Figure 8-20 shows the contact force/unit area based on the projected area of the 2D object and the particle spacing. The contact force for a constant projected area was of the same magnitude but, as expected, the signal was noisier for the coarser of the two simulations. The choice of a constant stiffness value was based on the fact that it prevented penetration of particles, while maintaining close proximity of the interface particles to the projectile.

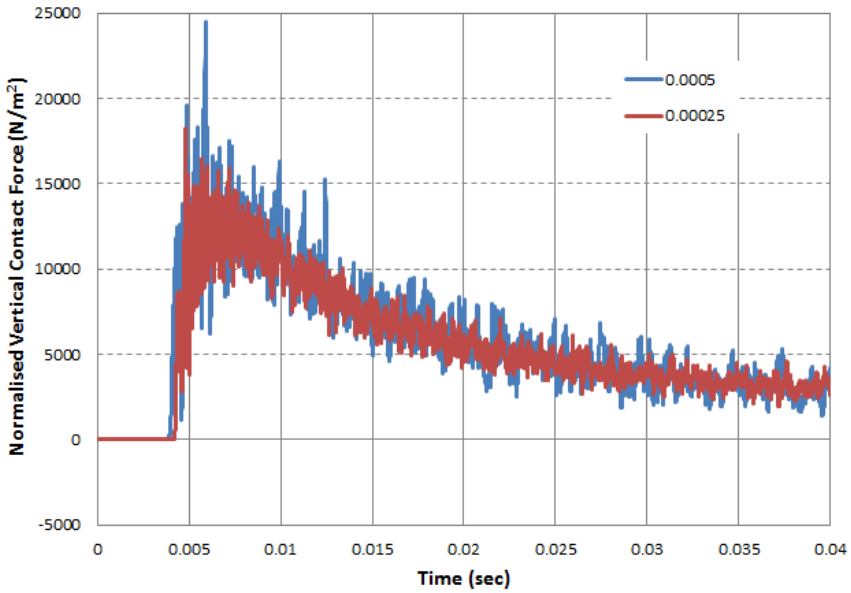

Figure 8-20: Vertical contact force comparison for the finer particle spacing options.

The theoretical vertical velocity has also been derived from equations (8-19) and (8-24). The aim is to establish whether the theoretical equation can provide an asymptotic behaviour similar to that of Figure 8-19. In order to determine the vertical velocity of a cylinder, with an initial velocity of 9.144 m/s (30 ft/s) at 7° inclination, the following timeframes were used.

Table 8-10: Discreet distances, times and vertical velocities for theoretical vertical velocity calculation of cylinder with diameter of 0.0254 m. Initial velocity of 9.144 m/s (30 ft/s) at 7° inclination.

Distance of centre of gravity from water surface (m)	Time (sec)	Vertical velocity (m/s)
0.0254	0	-1.11
0.024342	0.014689	-0.97274
0.023283	0.020773	-0.79441
0.021167	0.029378	-0.59411
0.02032	0.032182	-0.39754
0.01905	0.035981	-0.21426
0.016933	0.041547	-0.06397
0.0127	0.050884	0.021575
0	0.071961	0.164273

The time was estimated with the use of:

$$t = \sqrt{\frac{2h}{g}}, \tag{8-32}$$

where *h* is the distance of the centre of gravity of the cylinder from the surface of the water (initial taken as $\mathrm{h(t = 0) = 0.0254\ m}$). The major drawback of this approach, is that the hydrodynamic drag experienced by the cylinder during the impact cannot be analytically estimated. However, this approach allows the definition of discreet heights and times of a free falling object, which are used for determining the theoretical vertical velocity from equations (8-19) and (8-24).

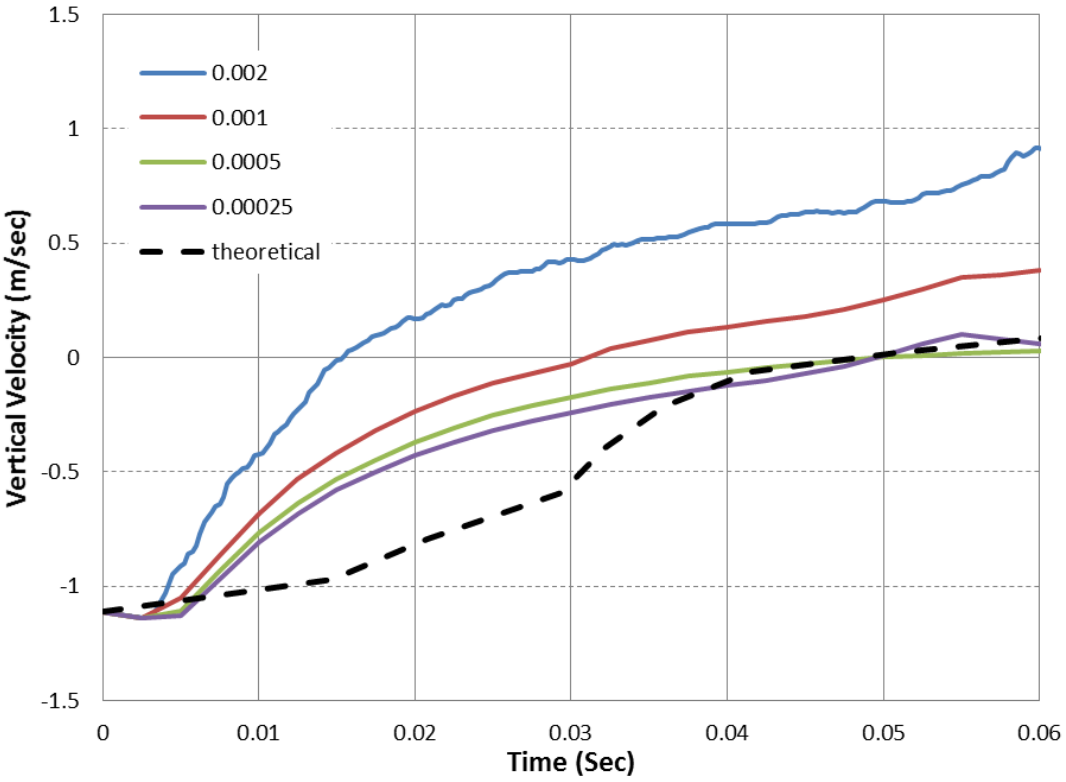

Figure 8-21: Theoretical vertical velocity for a cylinder with diameter of 0.0254 m and an initial velocity of 9.144 m/s (30 ft/s) at 7° inclination.

The graph follows the points of Table 8-10, as calculated from equations (8-19) and (8-24). The first point to note in Figure 8-21 is the slope of the vertical velocity until 0.03 s. The almost linear slope is due to the fact that the hydrodynamic drag is not considered in equation (8-24). As such, the cylinder experiences only the effect of gravity. Since this is constant, the vertical velocity follows a linear trend failing to capture any asymptotic behaviour. The effect of the drag force would be to reduce the vertical velocity further, approaching the numerical results. After 0.035 s, the theoretical curve matches the numerical results more accurately. One potential explanation for that, is that as the vertical velocity approaches zero, the effect of the drag reduces and the velocity is influenced to a higher degree by gravity.

8.3.3 2D Cylinder Ricochet Simulations

In these simulations the mass of the 2D non-spinning projectile was calculated for a cylinder with a length equal to the particle spacing, in effect considering a slice of an infinitely long cylinder. The same Finite Element model was used as the one for the

sensitivity analysis. For a steel cylinder with length of 0.0005 m the mass should be $1.976x10^{-3}$ kg. In order to match this mass with a hollow cylinder, the density was increased artificially to 9318.20671 kg/m^3 as given in Table 8-8. The water domain was 0.8 m long and 0.1 m deep. The dimensions and properties of the cylinder and the water domain are given in Table 8-11 and Table 8-12.

Table 8-11: Dimensions and properties of 2D cylinder for water impact simulations.

Diameter, m	0.0254
Thickness, m	0.00127
Density, kg/m^3	9318.20671
Mass, kg	$1.976x10^{-3}$

Table 8-12: Dimensions and properties of water domain for water impact of 2D cylinder simulations.

Length, m	0.8
Depth, m	0.1
Width, m	equal to the particle spacing
Particle spacing, m	0.0005
Smoothing length, m	0.00065
Water density, kg/m^3	1000

Figure 8-22 shows the overall results obtained for a variety of simulations. The results show that the coupled code overestimated the ricochet behaviour as the velocities and angles increased. As explained above, Hutchings [106] used the Rayleigh pressure formula, which assumes steady-state flow on a plane lamina. The same formula was used for the derivation of the theoretical curve for the cylinder, which is the orange curve of Figure 8-22. However, it is clear that depending on the pressure formulae that

were used by previous analyses, the critical angle will differ slightly but not enough to explain the discrepancies. Another parameter that could influence the accuracy of the predictions is the drag experienced by the projectile. This, as it will be shown later, could be lower than what a steady solution would provide, allowing for a higher velocity to be maintained. The fact that the simulations did not capture any splash on the sides of the projectile may have influenced the deceleration.

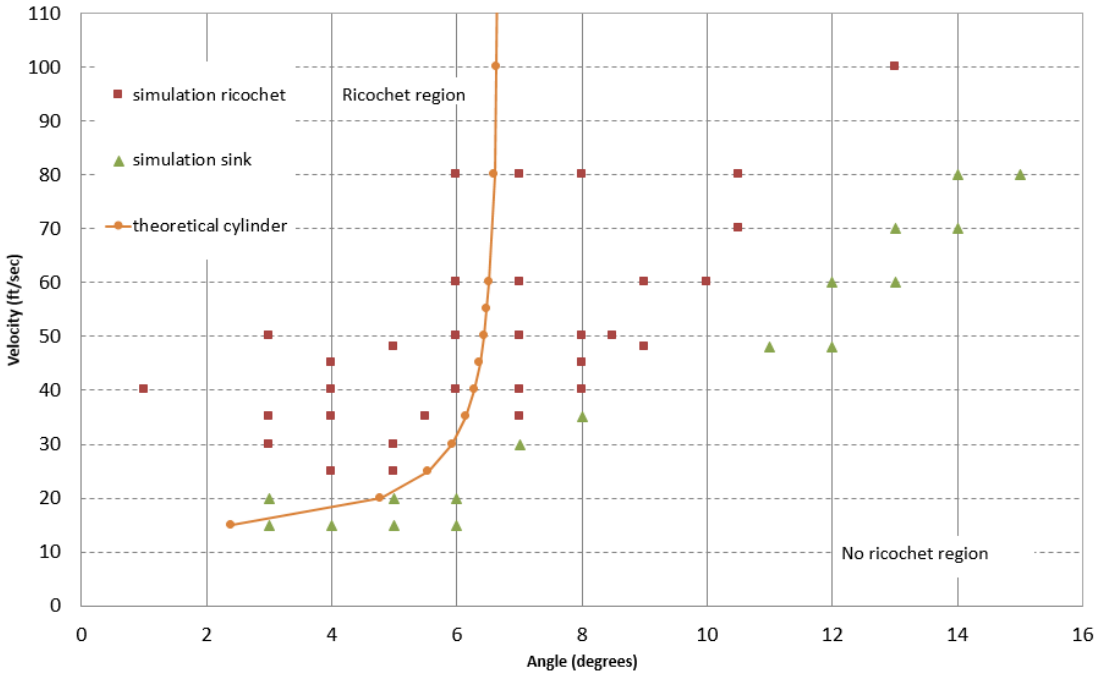

Figure 8-22: Overall set of water impact of 2D steel cylindrical projectiles. Comparison is made to the theoretical curve for ricochet for a 2D cylinder. Good comparison can be made for the low velocity impacts. Deviation from the theoretical curve occurs for high velocity cases.

Figure 8-23 shows the impact of the projectile for the cases of 15 ft/s at 6° inclination and for 40 ft/s at 7°.

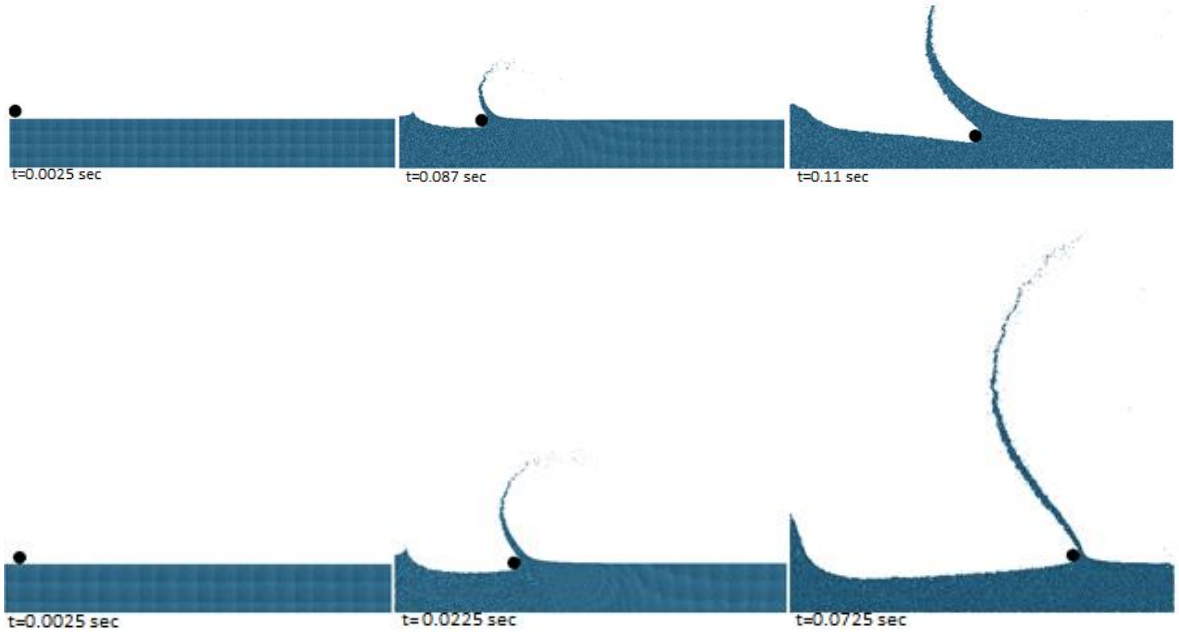

Figure 8-23: Side view. Water impact of 2D steel cylindrical projectile: top: 15 ft/s at 6° (indicating sinking), bottom: 40 ft/s at 7° (indicating ricochet). Direction of travel from left to right.

The 2D cylinder simulations agree with the critical velocity for the lower impact test cases but predict ricochet above the critical angle for higher velocities.

In the following section a 3D analysis was performed in order to investigate whether the correct water pressure can influence the predictions. The 3D cylinder simulation was performed with a relatively small water domain, with only 6 particles in width. Due to the prohibitive computational cost of these 3D analyses, the water model was developed with a particle spacing of 0.001 m. This was shown to provide inaccurate projectile behaviour in the 2D case, however the correct initial pressure distribution and its influence should be investigated with these 3D cases. The 3D model consists of 243006 particles and it is 0.4 m in length, 0.1 m in depth and 0.006 m in width. Similarly to the 2D case, applying an initial gravity gives the pressure distribution shown in Figure 8-24. The 3D analysis did not suffer from the wrong pressure as in the 2D case before.

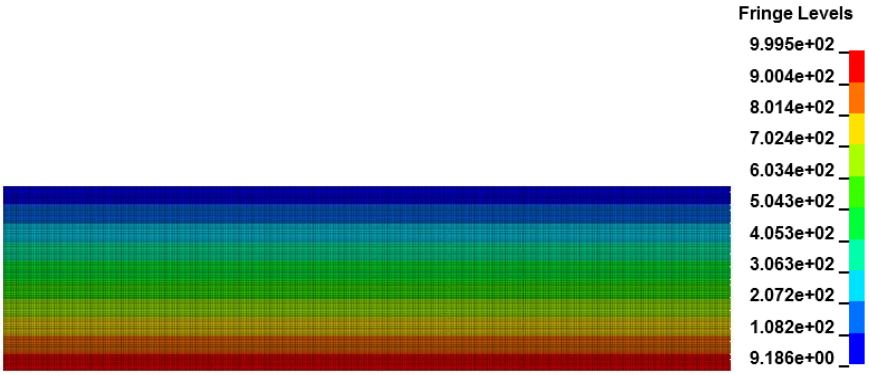

Figure 8-24: Initial pressure distribution for the 3D model. Fringe levels show pressure in Pa.

The projectile was modelled with 5120 shell elements and since it was assumed to be rigid it was modelled as a hollow cylinder, keeping the computational costs low. As a consequence, the density of the cylinder was increased, in order to have the correct mass, to 94947.2503 kg/m^3. The cylinder's diameter was the same as that for the 2D cases (0.0254 m) and its height was the same as the width of the water domain (0.006 m). Figure 8-25 shows the projectile's trajectory for an initial velocity of 9.144 m/s (30 ft/s) and an inclination of 7°. Based on the theoretical results of Section 8.1, this combination of velocity and angle should result in a clear sinking however, the results showed that the projectile would ricochet.

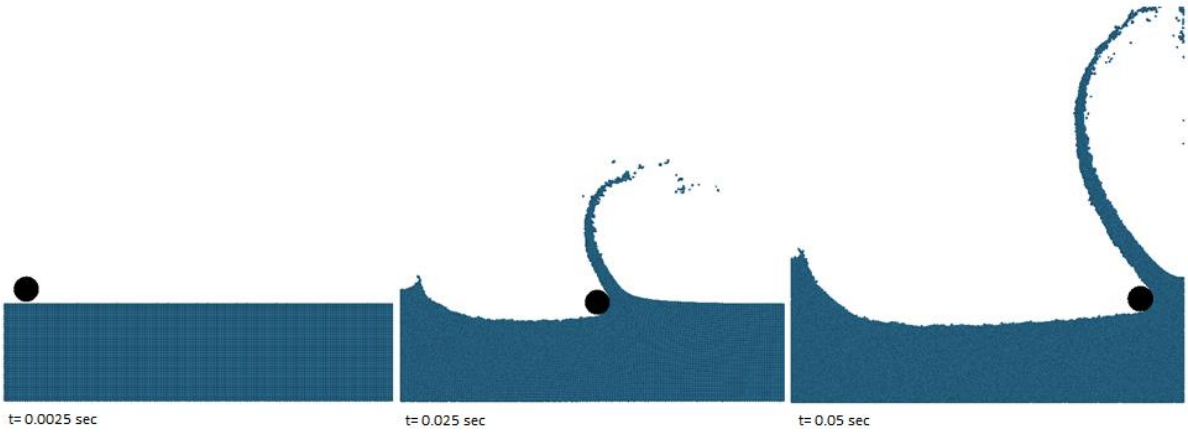

Figure 8-25: Side view. Water impact of 3D steel cylindrical projectile at 30 ft/s and an inclination of 7°. Direction of travel from left to right.

In the 2D analysis the effect of drag was discussed as one of the potential reasons for the deviation between the experimental and numerical results. Since it has been established that the water pressure did not affect the overall behaviour of the cylinder

significantly, the next factor to investigate is the horizontal drag and its influence on the trajectory of the cylinder. A comparison between the drag experienced by the 3D cylinder and a theoretical estimate of the drag of a cylinder is expected to provide different results. This would be due to the fact that the theoretical estimate assumes a steady-state flow around the body, a condition that is not true especially for the initial impact of the cylinder in the above simulations. Nevertheless, this comparison should provide an indication about the effect of the drag on the deceleration of the projectile. For the velocity of 9.144 m/s and the projected area of the 3D simulations above the Reynolds Number was in the region of $\mathrm{Re} \cong 2.3\mathrm{x}10^5$. This means that the coefficient of drag for the cylinder would be close to unity, leading to a drag force of $\mathrm{F} = 6.3\mathrm{N}$ [111]. Figure 8-26 shows the horizontal contact force on the 3D cylinder. The contact force (drag) showed a relatively steady behaviour between 0.02 and 0.05 s. After that point, the boundary deficiency of the SPH method affected the contact force and consequently the projectile's behaviour. The contact force between 0.02 and 0.05 s was not as low as the theoretical estimate, as it was expected. This was not only due to the fact that this was not a steady-state flow over the cylinder, but also because, as it can be seen from Figure 8-25, there was no water surrounding the projectile. From this analysis it appears that there was no significant forward deceleration, thus allowing the projectile to maintain its momentum and lead to ricochet.

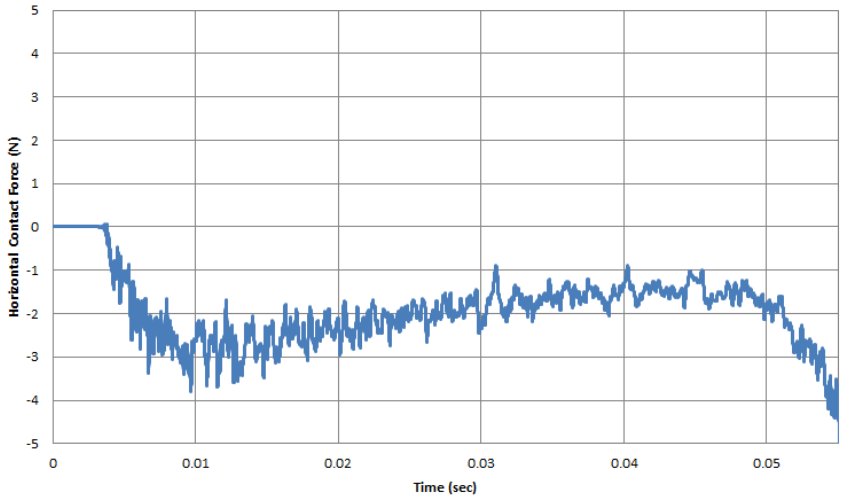

Figure 8-26: Horizontal component of the contact force on the 3D steel cylinder. Results indicate that there is no significant forward deceleration to slow the projectile down. As a consequence, the projectile maintains its momentum that leads to ricochet.

The main observations about the cylinder mesh sensitivity and ricochet analyses are that the particle spacing of the fluid has a significant effect on the behaviour of the projectile. The decelerations experienced by the cylinder are not as high as they steady-state solution provides. This was attributed to the lack of any water on the sides of the cylinder during the event. This appeared to have a more significant effect for the higher velocities range, where the numerical predictions deviate from the theoretical estimates. Even though the coarser 2D simulations were performed with an initially wrong pressure distribution in the water (due to gravity), the subsequent 3D test case showed no significant change to the projectile's displacement, incorrectly predicting ricochet. Given the influence of the particle spacing on the overall behaviour of the cylindrical projectiles, it was decided to perform additional simulations with a more detailed water and sphere model.

8.4 Final 3D Sphere Ricochet

The following simulations were performed with a particle spacing of 0.001 m compared to the 0.005 m used before. Even though the cylinder analysis showed that this particle spacing may not be adequate for the correct behaviour to be predicted, it was considered a compromise between computational costs and accuracy. Figure 8-27 shows the water model and the sphere finite element.

With respect to the water domain, the dimensions were altered in order to reduce the number of particles. The length of the water domain is 0.4 m and both the height and width are 0.05 m. For a particle spacing of 0.001 m this leads to a total of 1043001 particles. The MPI parallel version of the code was used in order to reduce the computational cost of these simulations. The material properties and the equation of state for the water remained the same, as for the previous simulations. The tables below show the dimensions and properties of the sphere and water.

Table 8-13: Dimensions and properties of 3D sphere for water impact simulations.

Diameter, m	0.0254
Density, kg/m^3	7900
Young's Modulus, Pa	2.1x10^{11}
Mass, kg	0.065
Poisson's ratio, -	0.33

Table 8-14: Dimensions and properties of water domain for water impact of 2D cylinder simulations.

Length, m	0.4
Depth, m	0.05
Width, m	0.05
Particle spacing, m	0.001
Smoothing length, m	0.0013
Water density, kg/m^3	1000

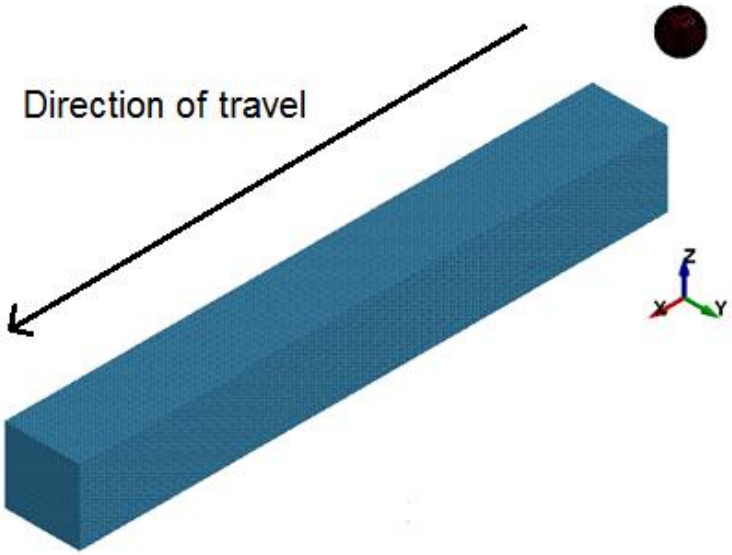

Figure 8-27: Initial position of the 3D steel sphere and the water domain with a particle spacing of 0.001 m.

The overall results of the test cases performed are shown in Figure 8-28.

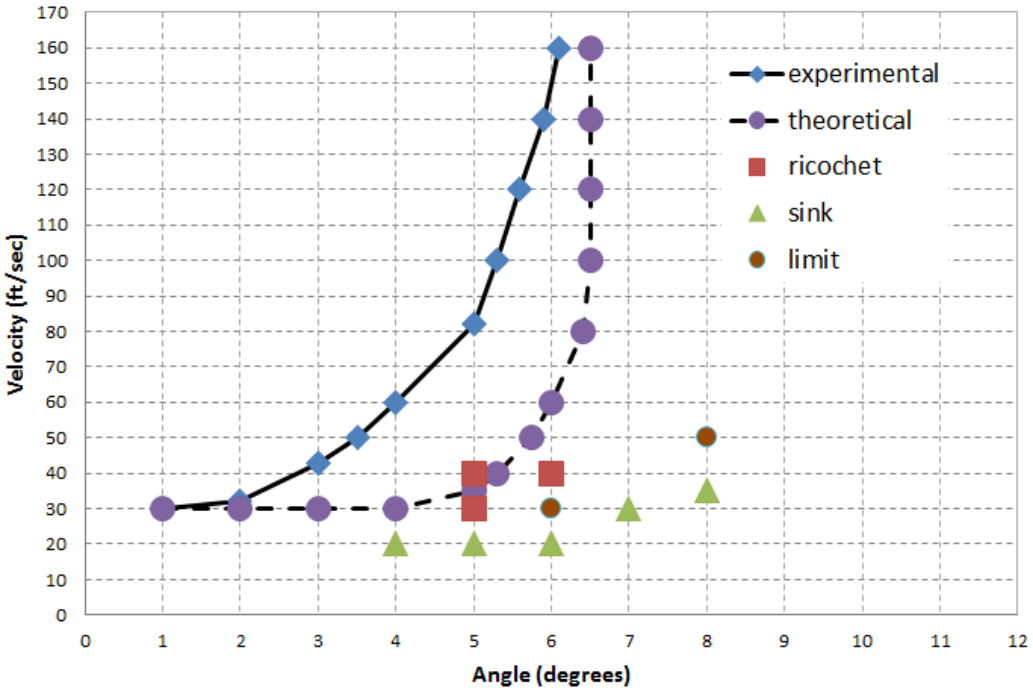

Figure 8-28: Overall results for the water impact of a 3D steel sphere and a water particle spacing of 0.001 m. Comparison is made with experimental and theoretical results taken from Figure 8-3 [107].

Due to the large number of particles and the relatively short water domain, any combinations of higher velocities and angle would have led to inconclusive results as to whether the sphere would ricochet or not. Hence, in this section the simulations were confined in the lower range of velocities and angles and tried to capture an improved behaviour and trend, compared to the coarser models. The results show better agreement with the finer models of Section 8.2, as it is expected. The comparison with the coarser results of Figure 8-13 shows that sinking occurred at velocities of 20 ft/s (Figure 8-29) for a range of angles, whereas for the coarser model this occurred only in the region of 10 ft/s. Moreover, for the velocities up to 40 ft/s there was a more reasonable pattern suggesting that for increasing velocities, the ricochet angle also increased. However, the computational restrictions of the finer models did not allow for a conclusive result at higher velocities, since that would require a far larger water domain. As the velocities increase, the curve deviates from the experimental and theoretical results, which can be due to the drag experienced by the projectile influencing the deceleration of the sphere at the higher velocities range.

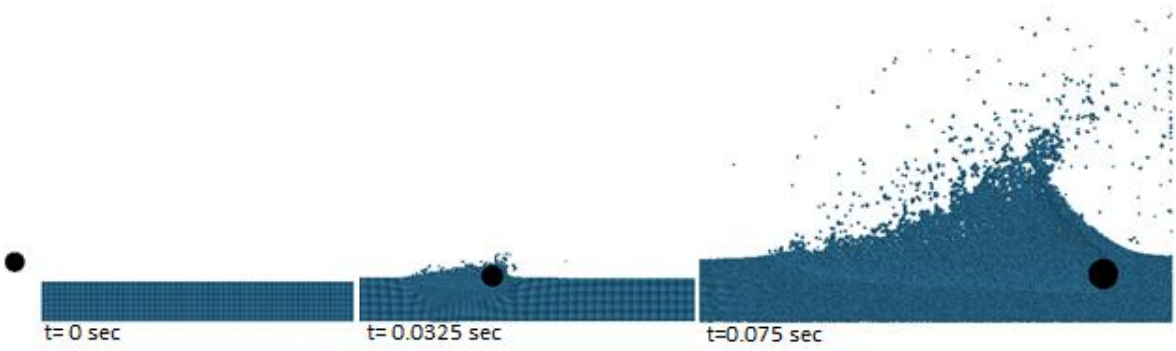

Figure 8-29: Side view cut. Cross section of 3D steel sphere impacting water domain at 20 ft/s and 6° inclination. The sphere sinks as the simulation progresses following the theoretical and experimental results by Soliman et al. [107].

8.5 Conclusions

This chapter investigated the phenomenon of ricochet, based on the fact that it is characterised by the same high forward velocities as a ditching event. The simplicity of the structure, compared to the more complex plate impacts of the previous chapters, combined with the availability of results made this phenomenon an ideal candidate. The main aims of this study were to assess the ability of the code to simulate impacts

characterised by high forward velocity and identify aspects that can be crucial for the accurate prediction of the structure's behaviour.

An overview of the ricochet theory and the SPH formulation was presented. A theoretical estimation of the critical angle of a non-spinning cylinder, with respect to the specific density and the velocity, was also derived. The analytical solution for the 2D cylinder does not consider the effect of drag. As a result, the theoretical curve of the vertical velocity of the projectile is not capable of producing an asymptotic curve as shown in the simulation results. Additionally, it must be noted that the drag component would act in the opposite direction of the projectile's motion, leading to an upward motion and possibly subsequent resurfacing and/or ricochet. This suggests that the theoretical curve for the critical ricochet angle may show sinking instead of ricochet thus leading to a more conservative approach.

2D and 3D simulations of a rigid cylinder were performed with the use of a couple FE-SPH code. The sensitivity analysis showed that the overall behaviour of the projectiles was significantly affected by the particle spacing. The particle spacing was found to play an important role as to whether the projectile is predicted to ricochet.

Simulations of a steel sphere impacting the water surface were also performed based on experimental results by Soliman et al. [107]. The simulation results showed good agreement with the experimental results by Soliman et al. [107] for the lower velocity impact cases. The simulations failed to predict the correct behaviour for combinations of higher velocities and angles. Once again, the particle spacing had a considerable effect on the overall behaviour of the projectile.

Apart from the influence of the particle spacing, it was found that the contact force between the projectile and the water and consequently the drag force acting on the 2D and 3D projectile, can be less than the theoretical values for a steady-state solution, leading to less severe deceleration of the object. It must be noted that an accurate analytical solution for the drag force of a submerging cylinder is not possible due to the continuous change of wetted area, velocity and coefficient of drag.

One possible reason for the inaccurate predictions could be the lack of air present in the simulations. However, based on the geometry of the projectiles, both the sphere and the 2D cylindrical object, the effects of air should not be significant. Moreover, as it was observed in Section 7.5, the effects of air on the position of the centre of gravity of a curved cross section of a fuselage does not provide any significant changes.

With respect to the low decelerations, especially in the case of the 2D cylindrical projectile, they could be attributed to the lack of any particles on the sides of the projectile. Even in the 3D cases, the modelling technique used, which allowed for a reduced computational cost, meant that the projectile's width was the same as the water domain and thus did not consider the effects of water on the sides of the projectile. This alone however, cannot fully explain the inaccurate prediction for the 3D sphere behaviour, where the water domain's width was larger than the diameter of the sphere. The lack of friction in the contact approach of the SPH code should also be considered as a potential reason.

The effect of spin was discussed in theory as it can alter the maximum angle of ricochet considerably. Indeed, the sphere model exhibited that behaviour after impact, however the contact treatment in the SPH method means that it would not affect the overall behaviour. More specifically, the contact algorithm in SPH treats the finite element nodes as particles, while they are within a distance of *2h*, equal to the support domain of the kernel, and applies a node to node contact. Since the projectiles had a uniform mesh, this means that any rotation would not change the contact force between the projectile and the water.

Finally, the depth of the water domain could have been a factor in the behaviour of the projectiles. As it was observed in the plate impact simulations, in Section 5.3 and partially in Section 6.7, the depth of the water domain can have an effect on the recorded accelerations and the reflected waves from the bottom boundary can influence the forces imparted on the structure at the free surface.

The main outcomes of the above study with respect to the water modelling with SPH are that the particle density is the most significant parameter than influences the predictions. Moreover, for the majority of these simulations the modelling was driven by the need for reduced computational resources. The results however, indicate that for an accurate prediction of high forward velocity water impacts, including that of ditching, a finer particle distribution is necessary. For the case of the 3D sphere specifically, a longer water domain would also be necessary for more accurate predictions at the higher velocities range, further increasing the computational cost.

9 Conclusions and Future Work

9.1 Conclusions

This thesis aimed to improve the numerical capabilities to predict the structural loading of high speed, low angle impacts, such as during an aircraft ditching event and more specifically to improve the meshless SPH code, in order to improve the fluid model used for fluid-structure interactions with forward velocities, such as ditching.

The first objective of this project was to understand the phenomenon of ditching including an accident, experimental and numerical review and to assess the factors that influence the accurate prediction of the loading of the structure.

An overview of the original theories of water impact were discussed. These theories applied to simple rigid objects, namely wedges, and pressure formulae were derived based on the wetted area of the object. Further review of accidents resulted in two main conclusions. Firstly, any structural damage was highly dependent of the sea state, as well as the configuration of the aircraft. Secondly, most fatalities occur due to drowning, which shows the importance of avoiding fuselage rupture during such events.

A review of experimental work was performed showing the relevant full scale and model tests. This research showed the number of parameters that can affect the ditching behaviour of airliners, which are the pitch attitude, the velocity, the sea state, the fuselage shape and the flap/landing gear position. It also provided an understanding of the possible damage that can be caused by suction forces on the fuselage, namely the damage sustained at the forward section of the fuselage. An investigation into the state-of-the-art of the numerical simulation showed that the majority of the cases considered were for vertical drops of simple shapes, which led to accurate enough predictions. Moreover, ditching simulations have been performed to a lesser extent. The main conclusions of this investigation are that for the vertical impacts, the lack of air modelling can lead to inaccurately large pressures and that for the aircraft ditching simulations, the simplified water model led to inaccurate loading predictions. Cavitation, suction and the presence of air were considered as the main phenomena that the current water models lack. As a result, for an accurate description of ditching, the investigation of these phenomena needed to be performed.

The second objective of this project was to develop a more detailed understanding of how cavitation, suction and the presence of air affects the flow and the structural loading in such cases.

A literature review on these phenomena was performed. The effect of an air pocket was found to provide a cushioning effect during impact, reducing the pressure peaks and providing a longer pressure pulse. This was more profound for flat objects, which followed closely the numerical investigations reviewed previously.

Suction was determined to be one of the most significant forces acting on an aircraft, which can result in severe secondary damage. It was found that the omission of this phenomenon from the numerical simulations can lead to inaccurate attitude predictions.

Cavitation was finally investigated in more detail, as it is difficult to assess its influence with model impacts, due to scaling effects. The different types of cavitation were investigated. Transient cavitation was found to be the one of interest in this project, as it is caused by the tension experienced by the fluid. A modelling review showed that the majority of the simulations were concerned with the attached cavitation taking place over symmetric bodies, such as cylinders and hydrofoils. In these modelling attempts the interest lies with the general evolution of the flow, rather than its effects on the structural loading. With respect to ditching, an accurate modelling of cavitation can lead to reduced forces (and pressures) experienced by the body, as the fluid is not allowed to reach inaccurately high negative pressures.

The third objective of this project was to develop and implement a physical cavitation model that can improve the predictions for the loading of the structure and investigating the parameters that can influence these predictions.

A one-fluid homogeneous mixture approach for cavitation modelling was implemented, considering the correct vapour pressure, the evolution of the mixture's properties and accounting for the cavitation nuclei growth and reduction. This was an improvement to the SPH code, which at the time was able to consider cavitation by using an arbitrary cut-off pressure value. Initial numerical validation cases showed that the method is sensitive to the nuclei population, which affects the extent of cavitation. Further simulations of plates impacting the water under high forward velocity were performed, which highlighted the influence of the size of the water domain. A small enough water domain can lead to wave reflection and artificial cavitation dominating the domain.

Larger water domains for the simple plate examples led to less noisy results, however this was not the case for the more detailed plate model, where an even larger domain was deemed necessary.

The fourth objective of this project was to develop and implement an aerated water model in order to investigate the effect of air on the loading of the structure.

The effects of air in the form of a cavity between the structure and the water surface were deemed less significant than the effects of suction and cavitation for aircraft ditching, however the effect of suspended air particles in the water due to the fractioning of such a cavity was an area of interest. The literature review performed earlier indicated a gap in this aspect, with the inaccurate predictions of numerical simulations of both simple structures as well as fuselage sections. In order to bridge this gap, the effect of aerated water on the pressures imparted on a structure was investigated with the implementation of a mixture approach, governed by the gas content, while the liquid was considered fully incompressible. Test cases of increasing complexity were performed, including plate impacts and a fuselage section, which provided a comparison of the applied method with results obtained by TUHH as well as experimental results. The main outcomes of the simulations were that the presence of air reduces the pressure peaks and allows for a longer pressure pulse, thus providing a smoother impact profile. This was found to be dependent of the level of aeration, as expected from theory. With respect to aircraft ditching however, the comparison between experimental and numerical results showed that the effect of air does not improve the overall dynamics of the aircraft considerably. It was concluded that the effects of suction are far greater in capturing the correct behaviour of this specific fuselage. However, the increased computational cost and the increased modelling complexity of introducing distinct air particles were the two factors that did not allow for the modelling of suction in this project.

The fifth objective of this project was to investigate angled water impact cases that will allow the assessment of the water model.

The phenomenon of ricochet was examined as a simpler test case with experimental and theoretical results available for comparison. The fact that ricochet deals with high forward velocity impacts of structures at an angle is the main reason why this phenomenon was chosen, as it deals with similar initial conditions as a ditching event. The theoretical investigation into ricochet provided a clearer understanding of the

relation between velocity and angle and specifically that a higher angle of impact is necessary for ricochet to occur, as the velocity increases. Moreover, it became clear from literature that a theoretical estimate relating the angle of impact with the velocity for a non-spinning cylinder was not available and hence it was derived.

The SPH code was employed for the water modelling of both cylinders and spheres in 2D and 3D simulations. Results fitted fairly well for the lower velocity impacts, however for higher velocities the results were not accurate.

The conclusions of this investigation are that the particle spacing significantly affects the trajectory of the projectile and should be taken into account for future simulations. Moreover, the depth of the water domain could also be a reason for the inaccurate predictions. This was shown to affect the results of the plate impacts from the previous models as well, suggesting that potential wave reflection can lead to inaccurate pressure predictions at the free surface. Finally, the lack of any friction in the contact definition, along with the lack of water particles on the sides of the cylinder test cases, could explain the lower decelerations experienced by the projectile.

9.2 Future Work

The areas of future work should focus on the following:

- For cavitation, a larger combination of nuclei populations and water domain sizes should be tested. The water domain should be large enough so that there is no influence from reflected waves, until at least the leading edge of the plate comes into contact with the water.
- Comparison of experimental results should take place with respect to cavitation, based on the results provided by INSEAN, one of the SMAES partners.
- Implement a suction model by either introducing air particles at atmospheric pressure or by including a contact definition in the SPH code, similar to the one provided by [21]. For the first option, a less complicated analysis should be performed to assess the ability of the code to deal with water and air particles at different pressures.
- An analysis should be performed to weigh the computational cost of such a complex set of simulations against the benefits. An alternative numerical method, the Arbitrary Lagrangian Eulerian (ALE) Finite Element method, should be considered as it can incorporate two materials.

- An investigation into the addition of friction in the contact definition between the SPH particles and the finite elements should be performed. Additional tests for larger water domains, in length and depth, should be considered for the ricochet test cases and a comparison between experiments, theory and numerical analysis should be performed.

REFERENCES

[1] EASA, “Certification Specifications for Large Aeroplanes CS-25 Amendment 2,” European Aviation Safety Agency, 2006.

[2] E. E. McBride and L. J. Fisher, “Experimental investigation of the effect of rear - fuselage shape on ditching behavior,” NACA TN 2929, 1953.

[3] E. E. McBride, “Preliminary investigation of the effects of external wing fuel tanks on ditching behavior of a sweptback - wing airplane,” NACA TN 3710, 1956.

[4] A. G. Smith, C. H. Warren and D. F. Wright, “Investigations in the Behaviour of Aircraft When Making a Forced Landing on Water (Ditching),” Ministry of Supply Aeronautical Research Council Reports and Memoranda, 1957.

[5] M. F. Steiner, “Accelerations and bottom pressures measured on a B-24D airplane in a ditching test,” NACA Memorandum Report No. L4K14, Washington, 1944.

[6] W. C. Thompson, “Ditching investigation of a 1/30 - scale dynamic model of a heavy jet transport airplane,” NASA TM X-2445, 1972.

[7] T. von Karman, “The impact of seaplane floats during landing,” NACA TN 321, 1929.

[8] H. Wagner, “Planing of Watercraft,” NACA TN 1139, 1948.

[9] H. Wagner, “Landing of seaplanes,” NASA TM No.622, 1931.

[10] C. Busch and N. A. Lange, “Ditching of Aircrafts: Simulations and Experimental Investigation,” Presentation Ecole Centrale Marseille, 2007.

[11] L. J. Fisher and E. L. Hoffman, “Model ditching investigation of the Douglas DC-4 and DC-6 airplanes,” NACA RM SL 9K02a, 1949.

[12] L. J. Fisher and E. L. Hoffman, “Ditching investigations of dynamic models and effects on design parameters of ditching characteristics,” NACA Report 1347,

Washington, 1958.

[13] W. Mayo, “Theoretical and experimental dynamic loads for a prismatic float having an angle of dead rise of 22 1/2,” NACA RB No.L5F15, Washington, 1946.

[14] M. Anghileri, L.-M. L. Castelletti, E. Francesconi, A. Milanese and M. Pittofrati, “Rigid body water impact - experimental and numerical simulations using the SPH method,” *International Journal of Impact Engineering,* vol. 38, pp. 141-151, 2011.

[15] M. Anghileri, L. M.-L. Castelletti and E. Francesconi, “Water Impact: Experimental Tests and Numerical Simulations Using Meshless Methods,” in *6th European LS-DYNA Users' Conference*, Gothenburg, Sweden, 2007.

[16] E. G. Candy, N. E. Kirk and P. J. Murrell, “Airframe water impact analysis,” *International Journal of Crashworthiness,* vol. 5, no. 1, pp. 51-62, 1998.

[17] G. Colicchio, M. Greco, M. Miozzi and C. Lugni, “Experimental and numerical investigation of the water - entry and water - exit of a circular cylinder,” in *International Workshop on Water Waves and Floating Bodies*, Zelenogorsk, Russia, 2009.

[18] E. Francesconi and M. Anghileri, “A numerical - experimental investigation on crash behaviour of skin panels during a water impact comparing ALE and SPH approaches,” in *7th European LS-DYNA Conference*, Salzburg, Austria, 2009.

[19] G. Oger, M. Doring, B. Alessandrini and P. Ferrant, “Two - dimensional SPH simulations of wedge water entries,” *Journal of Computational Physics,* vol. 213, pp. 803-822, 2006.

[20] C. M. Seddon and M. Moatamedi, “Review of water entry with applications to aerospace structure,” *International Journal of Impact Engineering,* vol. 32, pp. 1045-1067, 2006.

[21] M. Siemann, D. Kohlgrueber, L. B. Montanes and H. C. Manez, “Ditching Numerical Simulations: Recent Steps in Industrial Applications,” in *Aerospace Structural Impact Dynamics International Conference*, Wichita, Kansas, 2012.

[22] C. Judge, A. Troesch and M. Perlin, “Initial water impact of a wedge at vertical

and oblique angles," *Journal of Engineering Mathematics,* vol. 48, pp. 279-303, 2004.

[23] J. Allen, "Impact measurements on a large model of a representative landplane fuselage on water," Aeronautical Research Council, London, 1956.

[24] R. E. Zimmermann, J. C. Warrick, A. D. Lane, N. A. Merritt and A. O. Bolukbasi, "Aircraft Crash Survival Design Guide. Volume III: Aircraft Structural Crash Resistance," U.S. Army Aviation Research & Technology Activity Report USAAVSCOM TR 89-D-22C, 1989.

[25] W. L. Mayo, "Analysis and modification of theory for impact of seaplanes on water," NACA, Report No. 810, Washington, 1945.

[26] H. Streckwall, O. Lindenau and L. Bensch, "Aircraft ditching: a free surface/ free motion problem," *Archives of civil and mechanical engineering,* vol. VII, no. 3, pp. 177-190, 2007.

[27] CAA, "Safety Sense Leaflet 21c Ditching," CAA, 2008.

[28] CAA, "Global Fatal Accident Review 1980-1996," CAA, 1998.

[29] CAA, "Global Fatal Accident Review 1997-2006," CAA, 2008.

[30] A. A. Patel and R. P. Greenwood, "Transport water impact and ditching performance," DOT/FAA/AR-95/54,US Department of Transportation, 1996.

[31] R. A. Johnson, "Study on Transport Airplane Unplanned Water Contact," DOT/FAA/CT-84/3, US Department of Transportation, 1984.

[32] NTSB, "Aircraft Accident Report: Overseas National Airways, Inc. Douglas DC-9,N935F operating as Antilliaanse Luchtvaart Maatschappij Flight 980 near St. Croix, Virgin Islands May 2 1970," NTSB, Washington D.C., 1971.

[33] NTSB, "Special study. Passenger survival in turbojet ditching (A critical case review)," NTSB, Washington D.C., 1972.

[34] Civil Aeronautics Board, "The Flying Tiger Line inc., Lockheed 1049H, N 6923C, ditching in the North Atlantic September 23, 1962," Civil Aeronautics Board,

Washington D.C., 1964.

[35] E. Widmayer and O. B. Brende, “Commerical jet transport crashworthiness,” NASA, CR-165849, 1982.

[36] NTSB, “Loss of thrust in both engines after encountering a flock of birds and subsequent ditching on the Hudson river US Airways flight 1549 Airbus A320-214 N106US Weehawken, New Jersey, January 15, 2009,” NTSB, Washington D.C., 2010.

[37] ANSV, “FINAL REPORT Accident Involving ATR 72 Aircraft Registration Marks TS-LBB ditching off the coast of Capo Gallo (Palermo Sicily),” ANSV, 2005.

[38] W. Sottorf, “Experiments with planing surfaces,” NACA TM No. 661, 1929.

[39] J. M. Shoemaker, “Tank tests of flat and V-bottom planing surfaces,” NACA TN No. 509, Washington, 1934.

[40] W. C. Thompson, “Model ditching investigation of a jet transport airplane with various engines installations,” NACA RM L56G10, 1956.

[41] W. C. Thompson, “Rough-water ditching investigation of a model of a jet transport with the landing gear extended and with various ditching aids,” NACA TN D-101, 1959.

[42] H. Climent, L. Benitez, F. Rosich, F. Rueda and N. Pentecote, “Aircraft ditching numerical simulation,” in *25th International Congress of the Aeronautical Sciences*, 2006.

[43] N. Pentecote, D. Kohlgruber and A. Kamoulakos, “Simulation of water impact problems using the smoothed particle hydrodynamics method,” in *Proceedings of the International Crashworthiness and Design Symposium*, GRRT, 2003.

[44] K. Hughes, J. Campbell and R. Vignjevic, “Application of the finite element method to predict the crashworthy response of a metallic under floor structure onto water,” *International Journal of Impact Engineering,* vol. 35, pp. 347-362, 2008.

[45] R. Ortiz, G. Portemont, J. L. Charles and J. F. Sobry, “Assessment of explicit F.E.

capabilities for full scale coupled fluid/structure aircraft ditching simulations," in *ICAS*, 2002.

[46] R. Ortiz, J. L. Charles and J. F. Sobry, "Structural loading of a complete aircraft under realistic crash conditions: generation of a load database for passenger safety and innovative design," in *24th International Congress of the Aeronautical Sciences,*, Yokohama, Japan, 2004.

[47] G. Wittlin, M. Smith and M. Rihards, "Airframe water impact analysis using a combined MSC/DYTRAN - DRI/KRASH approach," in *American Helicopter Society 53rd Annual Forum*, Virginia Beach, Virginia, USA, 1997.

[48] D. H. Peregrine and L. Thais, "The effect of entrained air in violent water wave impacts," *Fluid Mechanics,,* vol. 325, pp. 377-397, 1996.

[49] G. N. Bullock, A. R. Crawford, P. J. Hewson, M. A. Walkden and P. A. Bird, "The influence of air and scale on wave impact pressures," *Coast Engineering,* vol. 42, pp. 291-312, 2001.

[50] A. Korobkin, "Entry problem for body with attached cavity," in *Proceedings of 11th International Workshop on Water Waves and Floating Bodies*, Hamburg, 1996.

[51] O. M. Faltinsen, "Hydroelastic Slamming," *Marine Science and Technology,* vol. 5, pp. 49-65, 2000.

[52] O. M. Faltinsen, "Hydrodynamics of High - Speed Marine Vehicles", New York: Cambridge University Press, 2005.

[53] A. Korobkin, "Elastic response of catamaran wetdeck to liquid impact," *Journal of Ocean Engineering,* vol. 28, no. 8, pp. 687-714, 1998.

[54] G. G. Lewison, "On the reduction of slamming pressures," *Trans. RINA,* vol. 112, pp. 285-306, 1970.

[55] B. Peseux, L. Gornet and B. Donguy, "Hydrodynamic impact: Numerical and experimental investigations," *Journal of Fluids and Structures,* vol. 21, pp. 277-303, 2005.

[56] R. Panciroli, S. Abrate , G. Minak and A. Zucchelli, "Hydroelasticity in water-entry

problems: Comparison between experimental and SPH results," *Composite Structures,* vol. 94, no. 2, pp. 532-539, 2012.

[57] R. F. Young, "Cavitation", London: Imperial College Press, 1999.

[58] R. T. Knapp, J. W. Daily and F. G. Hammitt, Cavitation, New York: McGraw - Hill, 1970.

[59] J. P. Franc, "Physics and Control of Cavitation," 2006. [Online]. Available: http://www.rto.nato.int/abstracts.asp. [Accessed 10 01 2011].

[60] L. Zardoni, "Cavitation Modelling for DYNA3D," MSc Thesis, Cranfield University, 2005.

[61] G. Sandberg, "A new finite element formulation of shock - induced hull cavitation," *Computer methods in applied mechanics and engineering,* vol. 120, pp. 33-44, 1995.

[62] C. Brennen, "Cavitation and Bubble Dynamics", Oxford Engineering Series 44, New York: Oxford University Press, 1995.

[63] P. Eisenberg , "Cavitation," in *On the mechanism and prevention of cavitation*, Washington, Navy Dept., David W. Taylor Model Basin, 1950, pp. 121-128.

[64] J. P. Franc and J. M. Michel, "Fundamentals of Cavitation", Dordrecht: Kluwer Academic Publishers, 2004.

[65] R. E. Franklin, "A note on the radius distribution function for microbubbles of gas in water," in *ASME FED-Vol.135 Cavitation and Multiphase Flow Forum* , Los Angeles USA, 1992.

[66] F. Caupin and E. Herbert, "Cavitation in water: a review," *Comptes Rendus Physique,* vol. 7, pp. 1000-1017, 2006.

[67] K. Davitt, A. Arvengas and F. Caupin, "Water at the cavitation limit: Density of the metastable state and size of the critical bubble," *EPL,* vol. 90, pp. 16002(1)-16002(6), 2010.

[68] S. A. Sedgewick and D. H. Trevena, "Limiting negative pressure of water under

dynamic stressing," *Journal of Physics D: Applied Physics,* vol. 9, no. 14, pp. 1983-1990, 1976.

[69] D. Trevena, "Cavitation and the generation of tension in liquids," *Journal of Physics D: Applied Physics,* vol. 17, no. 11, pp. 2139-2164, 1984.

[70] J. Pellicer, V. Garcia-Morales and M. J. Hernadez, "On the demonstration of the Young-Laplace equation in introductory physics courses," *Physics Education,* vol. 35, no. 2, 2000.

[71] A. Kubota, H. Kato and H. Yamaguchi, "A new modelling of cavitating flows: a numerical study of unsteady cavitation on a hydrofoil section," *Journal of Fluid Mechanics,* vol. 240, pp. 59-96, 1992.

[72] C. E. Brennen, "Fission of collapsing cavitation bubbles," *Journal of Fluid Mechanics,* vol. 472, p. 153.166, 2002.

[73] I. Senocak, "Computational methodology for the simulation of turbulent cavitating flows," University of Florida, 2002.

[74] A. K. Singhal, M. M. Athavale, H. Li and Y. Jiang, "Mathematical basis and validation of the full cavitation model," *Journal of Fluids Engineering,* vol. 124, pp. 617-624, 2002.

[75] G. R. Liu and M. B. Liu, "Smoothed particle hydrodynamics: a meshfree particle method", Singapore: World Scientific Publishing, 2003.

[76] L. X. Zhang, W. G. Zhao and X. M. Shao, "A Pressure based Algorithm for Cavitating Flow Computations," *Journal of Hydrodynamics,* vol. 23, no. 1, pp. 42-47, 2011.

[77] B. Pouffary, R. Fortes Patella and J. L. Reboud, "Numerical Simulation of Cavitating Flow Around a 2D Hydrofoil: A Barotropic Approach," in *Fifth International Symposium on Cavitation (CAV2003)*, Osaka, Japan, 2003.

[78] B. Pouffary, "Numerical Modelling of Cavitation," 2006. [Online]. Available: http://www.rto.nato.int/abstracts.asp. [Accessed 18 10 2011].

[79] E. Goncalves and R. F. Patella, "Numerical Simulation of Cavitating Flows with

homogeneous models," *An International Journal: Computers and Fluids,* vol. 38, pp. 1682-1696, 2009.

[80] Y. Tamura and Y. Matsumoto, "Improvement of bubble model for cavitating flow simulations," *Journal of Hydrodynamics,* vol. 21, no. 1, pp. 41-46, 2009.

[81] W. F. Xie, T. G. Liu and B. C. Khoo, "Application of a one-fluid method for large scale homogeneous unsteady cavitation: the modified Schmidt model," *An International Journal: Computers and Fluids,* vol. 35, pp. 1177-1192, 2006.

[82] C. Ying, L. Chuan-jing and W. Lei, "Modelling and computation of unsteady turbulent cavitation flows," *Journal of Hydrodynamics,* vol. 18, no. 5, pp. 559-566, 2006.

[83] Q. W. Ma and D. J. Andrews, "On techniques for simulating effects of cavitation associated with the interaction between structures and underwater explosions using LS-DYNA," in *3rd European LS-DYNA Conference*, Paris France, 2001.

[84] G. Wang, I. Senocak, W. Shuyy, T. Ikohagi and S. Cao, "Dynamics of attached turbulent cavitating flows," *Progress in Aerospace Sciences,* vol. 37, pp. 551-581, 2001.

[85] B. Huang, G. Wang and H. Yuan, "A cavitation model for cavitating flow simulations," *Journal of Hydrodynamics,* vol. 22, no. 5, pp. 798-804, 2010.

[86] T. Liu, B. Khoo and W. Xie, "Isentropic one-fluid modelling of unsteady cavitating flow," *Journal of Computational Physics,* vol. 201, pp. 80-108, 2004.

[87] Y. Chen, L. Chuang-jing and L. Wu, "Modelling and computation of unsteady turbulent cavitation flows," *Journal of Hydrodynamics,* vol. 18, no. 5, pp. 559-566, 2006.

[88] R. A. Gingold and J. J. Monaghan, "Smoothed particle hydrodynamics: theory and application to non - spherical stars," *Monthly Notices of the Royal Astronomical Society,* vol. 181, pp. 375-389, 1977.

[89] J. J. Monaghan, "Smoothed particle hydrodynamics," *Reports on Progress in Physics,* vol. 68, pp. 1703-1759, 2005.

[90] J. W. Swegle, S. W. Attaway, M. W. Heinstein, F. J. Mello and D. L. Hicks, “An analysis of smoothed particle hydrodynamics,” SAND93-2513, Sandia National Laboratories, 1994.

[91] P. W. Randles and L. D. Libersky, “Smoothed Particle Hydrodynamics: Some recent improvements and applications,” *Computer Methods in Applied Mechanics and Engineering,* vol. 139, pp. 375-408, 1996.

[92] T. De Vuyst, R. Vignjevic and J. C. Campbell, “Coupling between meshless and finite element methods,” *International Journal of Impact Engineering,* vol. 31, pp. 1054-1064, 2005.

[93] R. Vignjevic, *Review of development of the smooth particle hydrodynamics (SPH) method,* Crashworthiness,Impact and Structural Mechanics (CISM), Cranfield University, UK, 2010.

[94] J. Campbell, “Lagrangian hydrocode modelling of hypervelocity impact on spacecraft,” Ph.D. Thesis, Cranfield University, UK, 1998.

[95] J. J. Monaghan and R. A. Gingold, “Shock simulation by the particle method SPH,” *Journal of Computational Physics,* vol. 52, pp. 374-389, 1983.

[96] T. A. I. De Vuyst, “Hydrocode modelling of water impact,” Ph.D. Thesis, Cranfield University, 2003.

[97] G. W. Thomson, “The Antoine Equation for Vapor-Pressure Data,” *Chemical Review,* vol. 38, no. 1, pp. 1-39, 1946.

[98] M. Frobenius, R. Schilling, R. Bachert, B. Stoffel and G. Ludwig, “Three - dimensional unsteady cavitation effects on a single hydrofoil and in a radial pump - measurements and numerical experiments (Part two : numerical experiments),” in *Fifth International Symposium on Cavitation (CAV2003)*, Osaka, Japan, 2003.

[99] A. Valizadeh, M. Shafieefar, J. J. Monaghan and S. Salehi Neyshaboori, “Modeling two-phase flows using SPH method,” *Journal of Applied Sciences,* vol. 8, no. 21, pp. 3817-3826, 2008.

[100] O. Coutier-Delgosha, R. Fortes-Patella and J. L. Reboud, “Evaluation of the

turbulence model influence on the numerical simulations of unstead cavitation," *Journal of Fluids Engineering,* vol. 125, pp. 38-45, 2003.

[101] L. R. Aparici, "Model development for guided water impact tests to support the study of aircraft ditching," Cranfield University, Cranfield, UK, 2012.

[102] J. F. Zhao and W. Iahr, "Investigation of the compressibility of extra-high-velocity aerated flow," *Journal of Hydraulic Research,* vol. 38, no. 5, pp. 351-358, 2000.

[103] F. B. Jensen, W. A. Kuperman, M. B. Porter and H. Schmidt, "Chapter 2: Wave propagation theory," in *Computational Ocean Acoustics, Modern Acoustics and Signal Processing*, Springer, 2011, pp. 65-153.

[104] M. J. A. Walkden, "Model wave impulse loads on caisson breakwaters: aeration, scale and structural response," University of Plymouth, Plymouth, 1999.

[105] W. Johnson and S. R. Reid, "Ricochet of spheres off water," *Journal of Mechanical Engineering Science,* vol. 17, no. 2, pp. 71-81, 1975.

[106] I. M. Hutchings, "The ricochet of spheres and cylinders from the surface of water," *International Journal of Mechanical Science,* vol. 18, pp. 243-247, 1976.

[107] A. S. Soliman, S. R. Reid and W. Johnson, "The effect of spherical projectile speed in ricochet off water and sand," *International Journal of Mechanical Science,* vol. 18, pp. 279-284, 1976.

[108] W. Johnson , "Ricochet of non-spinning projectiles, mainly from water part 1: some historical contributions," *International Journal of Impact Engineering,* vol. 21, no. 1-2, pp. 15-24, 1998.

[109] W. Johnson, "The ricochet of spinning and non-spinning spherical projectiles mainly from water part 2: an outline of theory and warlike applications," *International Journal of Impact Engineering,* vol. 21, no. 1-2, pp. 25-34, 1998.

[110] C. L. Kirk, *The Dynamics of the Bouncing Bomb,* Personal Communication, 2013.

[111] R. L. Daugherty, J. B. Franzini and E. J. Finnemore, "Fluid Mechanics with Engineering Applications", Singapore: Mc Graw Hill, 1989.

[112] G. E. Mase, "Schaum's outline series theory and problems of continuum mechanics", McGraw-Hill, 1970.

[113] G. A. Holzapfel, "Nonlinear solid mechanics: A continuum approach for engineering", Wiley, 2000.

Appendix A SPH Derivations

A.1 Mass

Mass is written as:

$$m = \rho dV \,. \qquad \textbf{A- 1}$$

Total mass can be expressed as:

$$\int_V \rho dV \,. \qquad \textbf{A- 2}$$

Accounting for the rate of change:

$$\frac{d}{dt}\int_V \rho dV \,. \qquad \textbf{A- 3}$$

The derivative can be moved inside the integral and with the use of Reynolds Transport Theorem:

$$\frac{d}{dt}\int_V \rho dV = \int_V \frac{d}{dt}\rho \, dV + \int_S \rho \boldsymbol{u}\hat{n} \, dS \,, \qquad \textbf{A- 4}$$

where the surface integral represents the rate of transport of mass (flux) across the surface, *S*. Using the Divergence Theorem:

$$\frac{d}{dt}\int_V \rho dV = \int_V \frac{d}{dt}\rho \, dV + \int_V div(\rho \boldsymbol{u}) \, dV \,. \qquad \textbf{A- 5}$$

For conservation of mass the above equation must equal zero:

$$\int_V \frac{d}{dt}\rho \, dV = -\int_V div(\rho \boldsymbol{u}) \, dV \,, \qquad \textbf{A- 6}$$

and

$$\frac{d\rho}{dt} = -\rho div \boldsymbol{u} \,, \qquad \textbf{A- 7}$$

which can be rewritten as:

$$\frac{d\rho}{dt} = -\rho \frac{\partial \boldsymbol{u}}{\partial x} \,. \qquad \textbf{A- 8}$$

Writing the above in the kernel approximation [93] [94]:

$$< \frac{d\rho}{dt} >= -\int_V \rho' W \frac{\partial \boldsymbol{u}'}{\partial x'} dx' , \qquad \textbf{A- 9}$$

where the dash is for the variable estimated at point x'. The above equation is of the general form:

$$\int_V f(x') \frac{\partial g(x')}{\partial x'} W dx' . \qquad \textbf{A- 10}$$

Expanding with the use of Taylor series for $x' = x$ [94]:

$$\int_V f(x') \frac{\partial g(x')}{\partial x'} W dx' \qquad \textbf{A- 11}$$
$$= \int_V \left\{ f(x) \frac{\partial g(x)}{\partial x} + (x' - x) \frac{d}{dx} \left(f(x) \frac{\partial g(x)}{\partial x} \right) + \cdots \right\} W dx' .$$

Since $W((x - x'), h) = W(|x - x'|, h)$ i.e. is an even function then the second term of the Taylor series expansion is an odd function leading to:

$$\int_V (x' - x) \frac{d}{dx} \left(f(x) \frac{\partial g(x)}{\partial x} \right) W dx' = 0 . \qquad \textbf{A- 12}$$

Neglecting the higher order terms and for $x' = x$:

$$\int_V f(x') \frac{\partial g(x')}{\partial x'} W dx' = f(x') \frac{\partial g(x')}{\partial x'} , \qquad \textbf{A- 13}$$

and

$$f(x') \frac{\partial g(x')}{\partial x'} = f(x) \int_V \frac{\partial g(x')}{\partial x'} W dx' . \qquad \textbf{A- 14}$$

Using equation (A- 14) to simplify equation (A- 9) leads to:

$$< \frac{d\rho}{dt} >= -\rho \int_V W \frac{\partial \boldsymbol{u}'}{\partial x'} dx' . \qquad \textbf{A- 15}$$

Integrating by parts leads to:

$$< \frac{d\rho}{dt} >= -\rho W \boldsymbol{u}' + \rho \int_V \boldsymbol{u}' \frac{\partial W}{\partial x'} dx' . \qquad \textbf{A- 16}$$

The first term on the RHS can also be written as:

$$\rho W\boldsymbol{u}' = \rho \int_V \frac{d(W\boldsymbol{u}')}{dx'} dx' \,, \qquad \textbf{A- 17}$$

and with the use of Green's Theorem:

$$\rho \int_V \frac{d(W\boldsymbol{u}')}{dx'} dx' = \rho \int_S W\boldsymbol{u}' n dS \,. \qquad \textbf{A- 18}$$

For a problem where the kernel is not cut by the boundaries, any surface term should be equal to zero. Neglecting the surface integral term:

$$< \frac{d\rho}{dt} >= \rho \int_V \boldsymbol{u}' \frac{\partial W}{\partial x'} dx' \,. \qquad \textbf{A- 19}$$

Moving on to the particle approximation:

$$\frac{d\rho_i}{dt} = \rho_i \sum_{j=1}^{N} \frac{m_j}{\rho_j} \boldsymbol{u_j} \frac{\partial W_{ij}}{\partial x_i} \,. \qquad \textbf{A- 20}$$

An extension to the above equation includes the velocity difference of the particles. Using the fact that the kernel is zero at infinity [94]:

$$\rho \boldsymbol{u} \int_V \frac{\partial W}{\partial x'} dx' = 0 \,. \qquad \textbf{A- 21}$$

Representing the above in the particle approximation form:

$$\rho_i \boldsymbol{u_i} \sum_{j=1}^{N} \frac{m_j}{\rho_j} \frac{\partial W_{ij}}{\partial x_i} = 0 \,, \qquad \textbf{A- 22}$$

which can be subtracted from equation (A- 20) to give:

$$\frac{d\rho_i}{dt} = \rho_i \sum_{j=1}^{N} \frac{m_j}{\rho_j} (\boldsymbol{u_j} - \boldsymbol{u_i}) \frac{\partial W_{ij}}{\partial x_i} \,. \qquad \textbf{A- 23}$$

A.2 Momentum

Momentum is defined as mu and the rate of change of momentum is:

$$\frac{d}{dt}\int_V \rho \boldsymbol{u} dV \,. \qquad \textbf{A- 24}$$

Using the Reynolds Transport Theorem:

$$\frac{d}{dt}\int_V \rho \boldsymbol{u} dV = \int_V \frac{d}{dt}\rho\, \boldsymbol{u} dV + \int_S \rho \boldsymbol{u}\boldsymbol{u}\hat{n}\, dS \,. \qquad \textbf{A- 25}$$

Using the Divergence Theorem:

$$\frac{d}{dt}\int_V \rho \boldsymbol{u} dV = \int_V \frac{d}{dt}\rho\, \boldsymbol{u} dV + \int_V div(\rho \boldsymbol{u}\boldsymbol{u})\, dV \,. \qquad \textbf{A- 26}$$

Based on Newton's Second Law, any change in momentum is due to a force acting on the body:

$$\frac{d}{dt}\int_V \rho \boldsymbol{u} dV = \int_V \frac{d}{dt}\rho\, \boldsymbol{u} dV + \int_V div(\rho \boldsymbol{u}\boldsymbol{u})\, dV = \int_S \boldsymbol{\sigma}\hat{n}\, dS \,, \qquad \textbf{A- 27}$$

which using the Divergence Theorem:

$$\begin{aligned} \frac{d}{dt}\int_V \rho \boldsymbol{u} dV &= \int_V \frac{d}{dt}\rho\, \boldsymbol{u} dV + \int_V div(\rho \boldsymbol{u}\boldsymbol{u})\, dV \\ &= \int_V div\boldsymbol{\sigma}\, dV \,, \end{aligned} \qquad \textbf{A- 28}$$

and

$$\frac{d}{dt}(\rho \boldsymbol{u}) + div(\rho \boldsymbol{u}\boldsymbol{u}) = div\boldsymbol{\sigma} \,. \qquad \textbf{A- 29}$$

Expanding the LHS:

$$\frac{d\rho}{dt}\boldsymbol{u} + \frac{d\boldsymbol{u}}{dt}\rho + \boldsymbol{u}(\rho div\boldsymbol{u} + \boldsymbol{u} grad\rho) = div\boldsymbol{\sigma}. \qquad \textbf{A- 30}$$

Rearranging:

$$\frac{d\boldsymbol{u}}{dt}\rho + \boldsymbol{u}\left(\frac{d\rho}{dt} + \rho div\boldsymbol{u} + \boldsymbol{u} grad\rho\right) = div\boldsymbol{\sigma}. \qquad \textbf{A- 31}$$

Noting that:

$$\rho div\boldsymbol{u} + \boldsymbol{u} grad\rho = div(\rho\boldsymbol{u}) , \qquad \textbf{A- 32}$$

then:

$$\frac{d\boldsymbol{u}}{dt}\rho + \boldsymbol{u}\left(\frac{d\rho}{dt} + div\rho\boldsymbol{u}\right) = div\boldsymbol{\sigma} . \qquad \textbf{A- 33}$$

The second term on the LHS vanishes since it is the conservation of mass leading to:

$$\frac{d\boldsymbol{u}}{dt}\rho = div\boldsymbol{\sigma} , \qquad \textbf{A- 34}$$

$$\frac{d\boldsymbol{u}}{dt} = \frac{1}{\rho} div\boldsymbol{\sigma} = \frac{1}{\rho}\frac{\partial\boldsymbol{\sigma}}{\partial x} . \qquad \textbf{A- 35}$$

Using the Quotient Rule [93] [94]:

$$\frac{d\boldsymbol{u}}{dt} = \frac{\partial}{\partial x}\left(\frac{\boldsymbol{\sigma}}{\rho}\right) + \frac{\boldsymbol{\sigma}}{\rho^2}\frac{\partial\rho}{\partial x} . \qquad \textbf{A- 36}$$

In the kernel format:

$$< \frac{d\boldsymbol{u}}{dt} >= \int_V W\frac{\partial}{\partial x'}\left(\frac{\boldsymbol{\sigma}'}{\rho'}\right)dx' + \int_V W\frac{\boldsymbol{\sigma}'}{\rho'^2}\frac{\partial\rho'}{\partial x'}dx' . \qquad \textbf{A- 37}$$

Using the same procedure as in the conservation of mass (with the Taylor series expansion):

$$< \frac{d\boldsymbol{u}}{dt} >= \int_V W\frac{\partial}{\partial x'}\left(\frac{\boldsymbol{\sigma}'}{\rho'}\right)dx' + \frac{\boldsymbol{\sigma}}{\rho^2}\int_V W\frac{\partial\rho'}{\partial x'}dx' . \qquad \textbf{A- 38}$$

Following the same procedure as in the conservation of mass, i.e. integrating by parts, making use of Green's Theorem and neglecting the surface terms:

$$< \frac{d\boldsymbol{u}}{dt} >= -\int_V \left(\frac{\boldsymbol{\sigma}'}{\rho'}\right)\frac{\partial W}{\partial x'}dx' - \frac{\boldsymbol{\sigma}}{\rho^2}\int_V \rho'\frac{\partial W}{\partial x'}dx' . \qquad \textbf{A- 39}$$

Moving on to the particle approximation:

$$\frac{du_i}{dt} = -\sum_{j=1}^{N}\frac{m_j}{\rho_j}\frac{\boldsymbol{\sigma_j}}{\rho_j}\frac{\partial W_{ij}}{\partial x_i} - \frac{\boldsymbol{\sigma_i}}{\rho_i^2}\sum_{j=1}^{N}\frac{m_j}{\rho_j}\rho_j\frac{\partial W_{ij}}{\partial x_i} . \qquad \textbf{A- 40}$$

The above is equivalent to:

$$\frac{du_i}{dt} = -\sum_{j=1}^{N} m_j \left(\frac{\boldsymbol{\sigma_j}}{\rho_j^2} + \frac{\boldsymbol{\sigma_i}}{\rho_i^2}\right) \frac{\partial W_{ij}}{\partial x_i}. \quad \textbf{A- 41}$$

A.3 Energy

Multiplying the momentum by velocity gives [112]:

$$\int_V \rho \boldsymbol{u}\boldsymbol{u} dV = \int_V \boldsymbol{u} div\boldsymbol{\sigma}\, dV\,, \quad \textbf{A- 42}$$

where:

$$\int_V \rho \boldsymbol{u}\boldsymbol{u} dV = \frac{d}{dt}\int_V \frac{\rho \boldsymbol{u}\boldsymbol{u}}{2} dV = \frac{dK}{dt}\,, \quad \textbf{A- 43}$$

which is the rate of change of the kinetic energy.

Noting that the stress σ tensor is symmetric and that [113]:

$$div\left(\boldsymbol{\sigma}^{\boldsymbol{T}}\boldsymbol{u}\right) = div(\boldsymbol{\sigma}\boldsymbol{u}) = \boldsymbol{u} div\boldsymbol{\sigma} + \boldsymbol{\sigma}\colon grad\boldsymbol{u}\,, \quad \textbf{A- 44}$$

then:

$$\frac{dK}{dt} + \int_V \boldsymbol{\sigma}\colon grad\boldsymbol{u}\, dV = \int_V div(\boldsymbol{u}\boldsymbol{\sigma})\, dV\,. \quad \textbf{A- 45}$$

The integral on the LHS is the rate of internal mechanical work and is the response of the volume to the stress. The time rate of change of internal energy *U* should be equal to the rate of internal mechanical work:

$$\frac{dU}{dt} = \int_V \boldsymbol{\sigma}\colon grad\boldsymbol{u}\, dV\,. \quad \textbf{A- 46}$$

In terms of specific internal energy [112]:

$$\frac{dU}{dt} = \frac{d}{dt}\int_V \rho E\, dV = \int_V \boldsymbol{\sigma}\colon grad\boldsymbol{u}\, dV\,. \quad \textbf{A- 47}$$

Then:

$$\rho \frac{dE}{dt} = \boldsymbol{\sigma}\colon grad\boldsymbol{u}\,, \quad \textbf{A- 48}$$

and rewritten it becomes:

$$\frac{dE}{dt} = \frac{\boldsymbol{\sigma}}{\rho}\frac{\partial \boldsymbol{u}}{\partial x} \ . \qquad \textbf{A- 49}$$

Using Monaghan's second golden rule of SPH means that [94]:

$$\frac{dE}{dt} = \frac{\boldsymbol{\sigma}}{\rho^2}\left(\rho^2 \frac{\partial}{\partial x}\left(\frac{\boldsymbol{u}}{\rho}\right) + \boldsymbol{u}\frac{\partial \rho}{\partial x}\right). \qquad \textbf{A- 50}$$

Using the Quotient and product rules:

$$\rho^2 \frac{\partial}{\partial x}\left(\frac{\boldsymbol{u}}{\rho}\right) = \frac{\partial}{\partial x}(\rho \boldsymbol{u}) - 2\boldsymbol{u}\frac{\partial \rho}{\partial x} \ . \qquad \textbf{A- 51}$$

which leads to:

$$\frac{dE}{dt} = \frac{\boldsymbol{\sigma}}{\rho^2}\frac{\partial}{\partial x}(\rho \boldsymbol{u}) - \frac{\boldsymbol{\sigma u}}{\rho^2}\frac{\partial \rho}{\partial x} \ . \qquad \textbf{A- 52}$$

In the kernel format:

$$< \frac{dE}{dt} >= \int_V \frac{\boldsymbol{\sigma}'}{\rho'^2}\frac{\partial}{\partial x'}(\rho' \boldsymbol{u}')W dx' - \int_V \frac{\boldsymbol{\sigma}'\boldsymbol{u}'}{\rho'^2}\frac{\partial \rho'}{\partial x'}W dx' \ . \qquad \textbf{A- 53}$$

Using the same procedure as in the conservation of mass (with the Taylor series expansion):

$$< \frac{dE}{dt} >= \frac{\boldsymbol{\sigma}}{\rho^2}\int_V \frac{\partial}{\partial x'}(\rho' \boldsymbol{u}')W dx' - \frac{\boldsymbol{\sigma u}}{\rho^2}\int_V \frac{\partial \rho'}{\partial x'}W dx' \ . \qquad \textbf{A- 54}$$

Following the same procedure as in the conservation of mass, i.e. integrating by parts, making use of Green's Theorem and neglecting the surface terms:

$$< \frac{dE}{dt} >= -\frac{\boldsymbol{\sigma}}{\rho^2}\int_V (\rho' \boldsymbol{u}')\frac{\partial W}{\partial x'} dx' + \frac{\boldsymbol{\sigma u}}{\rho^2}\int_V \rho' \frac{\partial W}{\partial x'} dx' \ . \qquad \textbf{A- 55}$$

Moving on to the particle approximation:

$$\frac{dE}{dt} = -\frac{\boldsymbol{\sigma_i}}{\rho_i^2}\sum_{j=1}^{N}\frac{m_j}{\rho_j}\rho_j \boldsymbol{u_j}\frac{\partial W_{ij}}{\partial x_i} + \frac{\boldsymbol{\sigma_i u_i}}{\rho_i^2}\sum_{j=1}^{N}\frac{m_j}{\rho_j}\rho_j \frac{\partial W_{ij}}{\partial x_i}. \qquad \textbf{A- 56}$$

Rearranging gives:

$$\frac{dE}{dt} = -\frac{\boldsymbol{\sigma_i}}{\rho_i^2}\sum_{j=1}^{N} m_j(\boldsymbol{u_j} - \boldsymbol{u_i})\frac{\partial W_{ij}}{\partial x_i}. \qquad \textbf{A- 57}$$

Appendix B Rayleigh-Plesset Equation

The following derivation of the Rayleigh-Plesset equation was provided by [59] [64]. Initially consider that any mass transfer is neglected meaning that the interface velocity is equal to:

$$\dot{R} = \frac{dR}{dt}. \qquad \textbf{B- 1}$$

The normal stresses at the interface are, for *r*=*R*:

$$t(R,t) = -p(R,t) + 2\mu\frac{\partial u}{\partial r}, \qquad \textbf{B- 2}$$

where μ is the kinematic viscosity and u is the velocity field. Based on the equilibrium equation (4-5) the balance of the forces is:

$$-t(R,t) = p_v + p_g(t) - \frac{2S}{R}. \qquad \textbf{B- 3}$$

The gas pressure can also be expressed in terms of its initial state as [59] [64]:

$$p_g(t) = p_{g0}\left[\frac{R_0}{R(t)}\right]^{3\gamma}, \qquad \textbf{B- 4}$$

where γ is the ratio of the heat capacities of the gas component.

Combining equations (B- 2) and (B- 3):

$$p(R,t) = p_v + p_{g0}\left[\frac{R_0}{R(t)}\right]^{3\gamma} - \frac{2S}{R} + 2\mu\left.\frac{\partial u}{\partial r}\right|_{r=R}, \qquad \textbf{B- 5}$$

which gives the pressure at the interface.

Density for an incompressible fluid (which is the case for low enough velocities compared to the speed of sound of the fluid) does not undergo significant changes. The rate of change of volume of a nucleus with radius *R* should be equal to the rate of change of volume for an arbitrary nucleus with radius *r*.

$$\frac{dV_R}{dt} = \frac{dV_R}{dR}\frac{dR}{dt} = \frac{dV_r}{dr}\frac{dr}{dt} \qquad \textbf{B- 6}$$

$$\frac{d}{dR}\left(\frac{4}{3}\pi R^3\right)\frac{dR}{dt} = \frac{d}{dr}\left(\frac{4}{3}\pi r^3\right)\frac{dr}{dt} \qquad \textbf{B- 7}$$

$$\frac{4}{3}\pi R^2\frac{dR}{dt} = \frac{4}{3}\pi r^2\frac{dr}{dt} \qquad \textbf{B- 8}$$

$$\frac{dr}{dt} = \left(R^2/r^2\right)\frac{dR}{dt} \qquad \textbf{B- 9}$$

$$u(r,t) = \left(R^2/r^2\right)\dot{R}\,. \qquad \textbf{B- 10}$$

Using the momentum equation in the Eulerian form:

$$-\frac{1}{\rho}\frac{\partial p}{\partial r} = \frac{\partial u}{\partial t} + u\frac{\partial u}{\partial r}\,. \qquad \textbf{B- 11}$$

Substituting equation (B- 9) leads to the following equation:

$$-\frac{1}{\rho}\frac{\partial p}{\partial r} = \ddot{R}\frac{R^2}{r^2} + 2\dot{R}^2\left[\frac{R}{r^2} - \frac{R^4}{r^5}\right], \qquad \textbf{B- 12}$$

which after integration from *r* to infinity, and considering the fact that $R(\dot{\infty}, t) = 0$:

$$\frac{p(r,t) - p_\infty(t)}{\rho} = \ddot{R}\frac{R^2}{r^2} + 2\dot{R}^2\left[\frac{R}{r} - \frac{R^4}{4r^4}\right]. \qquad \textbf{B- 13}$$

For *r*=*R*:

$$\frac{p(r,t) - p_\infty(t)}{\rho} = R\ddot{R} + \frac{3}{2}\dot{R}^2\,. \qquad \textbf{B- 14}$$

Substituting in equation (B- 5) and noting that for *r*=*R*, $u(r,t) = \left(R^2/r^2\right)\dot{R}$:

$$\rho\left[R\ddot{R} + \frac{3}{2}\dot{R}^2\right] = p_v - p_\infty(t) + p_{g0}\left[\frac{R_0}{R}\right]^{3\gamma} - \frac{2S}{R} - 4\mu\frac{\dot{R}}{R}. \qquad \textbf{B- 15}$$

Appendix C Mixture Speed of Sound

Consider the following bulk modulus equation of a mixture given as [49]:

$$\frac{1}{K_{ab}} = -\frac{1}{V_a + V_b}\left[\frac{dV_a}{dP} + \frac{dV_b}{dP}\right], \quad \textbf{C- 1}$$

where, *a* and *b* are the two components of the mixture, *V* is the volume and *P* is pressure.

The bulk modulus of each of the components is:

$$\frac{1}{K_a} = -\frac{dV_a}{dP}\frac{1}{V_a}, \quad \textbf{C- 2}$$

$$\frac{1}{K_b} = -\frac{dV_b}{dP}\frac{1}{V_b}. \quad \textbf{C- 3}$$

The above equations can be written as:

$$\frac{dV_a}{dP} = -\frac{V_a}{K_a}, \quad \textbf{C- 4}$$

$$\frac{dV_b}{dP} = -\frac{V_b}{K_b}. \quad \textbf{C- 5}$$

Equation (C-1) becomes:

$$\frac{1}{K_{ab}} = \frac{1}{V_a + V_b}\left[\frac{K_b V_a + K_a V_b}{K_a K_b}\right]. \quad \textbf{C- 6}$$

The volume fraction of the mixture can be written as:

$$\beta = \frac{V_a}{V_a + V_b}. \quad \textbf{C- 7}$$

Equation (C-6) can then be written as:

$$\frac{1}{K_{ab}} = \frac{K_b V_a + K_a V_b}{(V_a + V_b) K_a K_b} = \frac{\beta (K_b V_a + K_a V_b)}{V_a K_a K_b} = \frac{\beta}{K_a} + \frac{\beta V_b}{V_a K_b}. \quad \textbf{C- 8}$$

Additionally, from equation (C-7):

$$V_b = \frac{V_a (1 - \beta)}{\beta}. \quad \textbf{C- 9}$$

Combining equations (C-8) and (C-9):

$$\frac{1}{K_{ab}} = \frac{\beta}{K_a} + \frac{(1 - \beta)}{K_b}. \quad \textbf{C- 10}$$

The bulk modulus can also be written in terms of density and speed of sound as follows:

$$K = c^2 \rho. \quad \textbf{C- 11}$$

Substituting the above equation into equation (C-10), for each component of the mixture and rearranging, the speed of sound is:

$$\frac{1}{c_{ab}^2} = \rho_{ab} \left[\frac{\beta}{c_a^2 \rho_a} + \frac{(1 - \beta)}{c_b^2 \rho_b} \right]. \quad \textbf{C- 12}$$